



UNIVERSIDAD DE OVIEDO

Departamento de Ingeniería Eléctrica, Electrónica, de Computadores
y Sistemas

TESIS DOCTORAL

EMC: A mapping for the CMS experiment

Fernando José González Arteché

2004

CERN-THESIS-2004-027
16/04/2004



Acknowledgements

In a few lines I would like to thank to everybody that has helped me in the development of this thesis. During the last three years that I have been working on my PhD I have received the support of a lot of people that I would like to thank now. I hope I do not forget any of them along the following paragraphs.

First of all I would like to thank to my supervisors *Dr. Peter Sharp* and *Prof. Javier Gómez-Aleixandre Fernández* for their enthusiastic support during the development of the thesis. Thanks *Peter* for your help, you have always found time to talk to me; your office's door has always been open for me, no matter time or day. Thanks *Javier* for your help from the Electrical and Electronic Engineering Department of the University of Oviedo. Thanks to answer all my questions as well as for dealing with all official issues that I had with the University.

From FERMILAB, I would like to thank *Dr. Claudio Rivetta*. I do not know how to thank you. I think there are not enough words to thank you for the hundreds of e-mails that you have written to me in these years, for the long VRVS-conferences to discuss technical aspects of the project, for supporting me during the bad moments, for sharing with me your engineering knowledge, for your insights and support during the writing of the thesis, for your willingness to proof-read the chapters and for your fruitful suggestions and technical discussions. "*Muchas gracias flaco, te estaré eternamente agradecido*".

From CERN, I would like to express a warm "*thank you*" to *Dr. Fritz Szoncso* for his unconditional support during the bad moments, enthusiasm and fruitful technical discussions during coffee breaks. Also, I would like to thank you, *David Nisbet* for your fruitful discussions about technical aspects and thoughtful comments on different versions of the thesis. I would like to thank you for being patient and reading carefully the thesis, giving to the document the final English configuration. I would like to thank all members of the electronic pool too. Especially, I would like to thank *Bruno Allongue* and *Philippe Fontaine-Vive-Roux* for their support during the EMC tests carried out at CERN. Great thanks as well to *Dr. Horst Breuker*, *Dr. Robert Hammarstrom* and *Virginia Prieto* for the help that I have received from them during the thesis.

From the EMC department of the European Space Agency, I would like to thank *Dr. Antonio Ciccolessa* and *Philippe Langet* for the three-day meeting they spent with me. Especially, I thank you, *Antonio*, for devoting part of your time to talk to me by telephone or write e-mails, where you kindly answered me all technical questions.

Acknowledgements

You and your group have always been ready to offer me support and to give me useful suggestions.

Great thanks to the HCAL US group, *Ms. Terry Shaw, Mr. Sergey Los, Dr. John Elias, Terry Grozis* and to all other members for their support during the EMC tests performed at FERMILAB. Also from HCAL group I would like to thank to *Dragoslav-Laza Lazic* for his help during the preparation and coordination of the trip to FERMILAB.

From University of Oviedo I would like to thank *Prof. Guillermo Ojea Merín* and *Dr. Alberto Diez González* for their support from the Electrical and Electronics Engineering Department of the University of Oviedo. Thanks a lot Alberto for the "financial" help that I have received from your group.

I would like to thank my dear friends *Eduardo (gracias por haber tenido la paciencia de leer la tesis), Silvia* and *Barbara* for their support during the whole development of the Thesis. Also, great thanks family *Guerrero-van der Ploeg* for your support.

To my family, gracias *mama, Nacho, Yoyi, Natalia, Jofre y Atena* por vuestra ayuda incondicional todos estos años que he pasado lejos de casa.

Finally, I would like to thank a very special person. *Ana*, thanks for your unconditional support, love, and basically just for being yourself. Without your support I think that I would not have finished this project.

Contents

Introducción - Versión en castellano	1
Introduction	5
Chapter 1	
CMS detector	9
1.1 The Large Hadron Collider (LHC)	9
1.2 The Compact Muon Solenoid (CMS) experiment	10
1.3 Tracker Sub-system	13
1.3.1 Pixel detector	14
1.3.2 Silicon detector	15
1.3.3 Tracker Readout Electronics	17
1.3.3.1 APV Front End circuit.	17
1.3.3.2 Optical Link.	18
1.3.3.3 Front End Driver	18
1.3.3.4 Control System.	18
1.3.3.5 Low and High voltage PS distribution system.	18
1.4 Electromagnetic Calorimeter (ECAL)	20
1.4.1 ECAL Read out electronics	21
1.4.2 Pre-shower detector.	22
1.4.2.1 Pre-shower read-out electronics	23
1.5 MUON chambers sub-system.	24
1.5.1 Muon Sub-system read-out electronics	26
1.6 Super-conducting Magnet Sub-system	28
1.6.1 Super-conducting coil	29
1.6.2 Power supply system of Super-conducting solenoid	29
1.7 HCAL sub-system	30
1.7.1 System generalities	30
1.7.2 HCAL FEE	31
1.7.2.1 Introduction.	31
1.7.2.2 System configuration	32
1.7.2.3 Front-end electronics	33
1.7.2.4 Analogue signal conditioning	34
1.7.2.5 Dynamic range.	35
1.7.3 FEE Components	36
1.7.3.1 Overview.	36
1.7.3.2 Analogue conditioning and digitising ASIC-QIE	37
1.7.3.3 Channel control ASCI (CCA)	38
1.7.3.4 Data links.	38
1.7.3.5 Linear Rad-Tolerant Voltage Regulators	39
1.7.4 Front-end Electronics Readout Boxes (RBX).. . . .	39
1.7.4.1 Channel distribution per RBX	39
1.7.4.2 RBX layout	40
1.7.4.3 Power requirements per RBX	41
1.8 PS distribution system of CMS detector	42
1.8.1 Introduction.	42

1.9	Summary	44
1.10	References	44
Chapter 2		
Grounding & Shielding 47		
2.1	Grounding generalities	47
2.2	Grounding for fault and personnel protection.	49
2.2.1	System grounding or earthing	49
2.2.2	Equipment grounding	50
2.2.2.1	Standard equipment grounding	51
2.2.2.2	Isolated grounding	52
2.3	High frequency grounding configuration	54
2.3.1	Multipoint and single point grounding connections	57
2.3.1.1	Single point	57
2.3.1.2	Multipoint	58
2.3.2	Bonding and straps	59
2.3.3	Signal reference structure for non-continuous area	63
2.4	Shielding	63
2.4.1	Introduction.	63
2.4.2	Electromagnetic field shielding.	64
2.4.3	Electric field shielding	65
2.4.4	Magnetic field shielding	65
2.4.5	Cable shielding	66
2.5	CMS grounding	69
2.6	Summary	74
2.7	References	76
Chapter 3		
Conducted noise 79		
3.1	RF conducted noise	81
3.2	Switching mode power supplies.	82
3.2.1	Conducted RF emission of SMPS	83
3.2.2	Conducted noise measurements	85
3.2.2.1	Experimental set-up	85
3.2.2.2	Measurement results	88
3.3	Filter selection	90
3.3.1	Non ideal behavior of components.	91
3.3.1.1	Resistor	91
3.3.1.2	Capacitors	92
3.3.1.3	Inductors	93
3.3.1.4	Common mode chokes	94
3.3.2	Insertion loss	95
3.3.3	Filter characterization	96
3.3.4	Filter performance	99
3.3.4.1	Output filter performance.	100
3.3.4.2	Input filter performance	107
3.4	Stability problems with SMPS - Negative input impedance.	112
3.5	Harmonics.	118
3.6	Summary	121
3.7	References	122

Chapter 4	
Noise Propagation	125
4.1 Introduction to Multi-conductor Transmission lines (MTL)	125
4.2 Definitions of per-unit length parameters	127
4.2.1 Per unit length inductance matrix	127
4.2.2 Per unit length capacitance matrix	129
4.2.3 Per unit length resistance matrix	131
4.2.4 Per unit length conductance matrix	131
4.3 Parameters measurement procedure	132
4.3.1 Inductance	132
4.3.2 Capacitance	135
4.3.3 Resistance	138
4.4 Frequency domain solution of MTL systems	140
4.4.1 Solution of MTL incorporating the terminal conditions	144
4.5 Noise propagation in cables	146
4.5.1 Introduction	146
4.5.2 Common mode noise effects	149
4.5.3 Differential mode noise effects	152
4.5.4 Summary of noise propagation	155
4.5.5 CM and DM mode noise propagation in HCAL power supply distribution system	156
4.5.5.1 Introduction	156
4.5.5.2 Common mode noise propagation	157
4.5.6 Differential mode noise propagation	160
4.6 Shield models	162
4.6.1 Surface transfer impedance and admittance	162
4.6.2 Solution for the cable including the shield in the frequency domain	164
4.6.3 Susceptibility of HCAL power cable to shield currents	167
4.6.3.1 Introduction	167
4.6.3.2 Common mode	169
4.6.3.3 Differential mode	170
4.7 Summary	172
4.8 References	172

Chapter 5	
Susceptibility at early design stage	175
5.1 Introduction	175
5.2 Considerations about the noise in the FEE	176
5.3 Thermal noise	177
5.4 Susceptibility to CM currents	181
5.5 External electromagnetic fields	186
5.5.1 Introduction	186
5.5.2 Uniform plane-wave excitation of the line	189
5.5.3 Susceptibility to Electromagnetic fields of HF FEE	192
5.6 Summary	194
5.7 References	195

Chapter 6	
RF Susceptibility Test of FEE	197
6.1 Introduction	197
6.1.1 Injection of shield currents	198

6.1.2	Injection of CM currents in the central conductors.	199
6.1.3	Injection of DM currents in the central conductors	200
6.1.4	Injection of CM+DM currents in the central conductors.	201
6.2	Experimental set-up	202
6.2.1	HCAL FEE prototype	204
6.3	Susceptibility to shield currents	207
6.3.1	Noise distribution	207
6.3.2	Transfer function	210
6.3.3	Grounding configurations.	212
6.4	Susceptibility to CM power currents	216
6.4.1	Noise distribution	216
6.4.2	Transfer function	218
6.4.3	Common mode filter effects.	220
6.5	Susceptibility to DM power currents	222
6.6	DM and CM noise contributions to FEE output	224
6.6.1	Noise distribution and TF of CM + DM currents.	225
6.6.2	External noise contributions to the overall FEE noise.	227
6.6.3	Normalized noise level required at the output of the PS	229
6.7	Summary	235
6.8	References	236
Chapter 7		
Susceptibility to transient perturbation		237
7.1	Introduction	237
7.2	Voltage dips and short interruptions	240
7.2.1	Introduction.	240
7.2.2	HCAL FEE susceptibility test to voltage dips and short interruptions.	241
7.3	Surge or slow transients.	244
7.3.1	Introduction.	244
7.3.2	Transients in DC distribution	246
7.3.2.1	The Tracker DC power distribution system	247
7.3.2.2	Multi-module DC distribution	256
7.3.3	Surge test for the CMS detector.	264
7.3.3.1	Introduction.	264
7.3.3.2	Characterization of the HCAL FEE to surge test.	266
7.3.3.3	Protection stages for the CMS detector.	270
7.4	Burst or fast transients	271
7.5	Quenching effects	273
7.6	Summary	275
7.7	References	277
Conclusions		279
Thesis contribution and future work		283
Conclusiones - Versión en castellano		285
Objetivos de la tesis & Futuros Trabajos -Versión en castellano		291
Appendix A		
MTL		293
A.1	Internal impedances - Skin effect	293

A.2	Characteristic impedance	294
A.2.1	CM and DM characteristic impedance matrix	296
A.3	MTL programs validation	299
A.3.1	Ribbon cable	299
A.3.2	Field incident	301
A.4	References	302
Appendix B		
Transients 303		
B.1	Dynamic load impedances of Tracker FEE	303
B.2	Transient lumped model validation	304
B.3	ATO fuse data sheet	307
B.4	TVS validation	308
Appendix C		
Current probes 309		
Glossary 311		

Introducción - Versión en castellano

El Laboratorio Europeo de Física de Partículas, CERN, es el mayor centro de física de partículas del mundo. Dicho centro, formado por veinte países europeos, está situado en la frontera franco-suiza, al oeste de Ginebra. En el CERN se realiza investigación básica, con el objetivo de descubrir de qué está hecho nuestro Universo y a qué leyes obedece. Para ello, se estudia el comportamiento de los componentes más pequeños de la naturaleza: las partículas elementales. Con este fin, se realizan diferentes tipos de experimentos científicos utilizando aceleradores y detectores de partículas. En los aceleradores se llevan las partículas hasta altos niveles de energía y después se las hace colisionar entre ellas, pudiendo observarse lo que ocurre en los detectores.

Actualmente en el CERN se está realizando la construcción del más potente y largo acelerador de partículas del mundo llamado Large Hadron Collider (LHC). Este acelerador tiene como objetivo profundizar en el estudio de la estructura de la materia, recreando las condiciones que existieron en el Universo instantes después del "Big Bang". Junto con el acelerador, se está procediendo a la construcción de 4 detectores de partículas. El detector llamado CMS (Compact Muon Solenoid) es uno de ellos. Las dimensiones de este detector son de unos 30 metros de largo por 25 de diámetro, con un peso total aproximado de 13000 toneladas.

El detector CMS está dividido en 5 subsistemas, los cuales se encuentran emplazados en diferentes niveles dentro de la estructura del detector. Cada subsistema tiene una función diferente y maneja diferentes niveles de señal y potencia, siendo alimentados independientemente. En general, los experimentos de física de altas energías tienen como función identificar partículas y medir su energía usando diversos tipos de sensores y dispositivos ópticos. En el experimento de CMS, la señal eléctrica detectada es amplificada y procesada por el FEE (front end electronics), el cual se comunica con el sistema de adquisición de datos mediante fibra óptica. Dicho sistema se encuentra localizado a unos 120 metros del detector. La electrónica del detector CMS está diseñada para procesar señales de pocos milivoltios para su posterior digitalización sincronizada a 40 MHz. Parte de esta electrónica se encuentra situada en la sección interna del detector teniendo que soportar una elevada radiación protónica y un altísimo campo magnético de unos 4 Tesla.

Todos los datos del FEE son transmitidos al sistema de adquisición por fibra óptica, con lo que se evitan problemas de integridad de señal generados por ruido. El problema aparece intrínsecamente en el detector debido al elevado número de

interacciones electromagnéticas entre los diferentes subsistemas. Los principales problemas de interferencia electromagnética se pueden encontrar en la conexión entre el sistema de alimentación y el FEE y en el propio FEE. Los elementos más importantes a tener en cuenta antes de integrar la electrónica del detector son, por un lado, la definición de los niveles de ruido y transitorios dentro de cada subsistema, y por otro, cómo imponer estos niveles al sistema electrónico mediante medidas normalizadas. CMS necesita generar una especificación tanto para la emisión como para la inmunidad al ruido que permitan integrar el detector de una forma segura. Describir el escenario electromagnético de CMS es de crucial importancia para fijar y resolver problemas referentes a interferencias electromagnéticas, puesta a tierra y blindajes. Esta tesis se centra en los estudios de EMC realizados en el experimento CMS con el fin de definir la base de una futura norma de EMC para el detector. Fundamentalmente estos estudios están enfocados a la cuantificación de la sensibilidad del FEE al ruido conducido acoplado a través de los cables de entrada y salida de la electrónica, así como del ruido generado por las fuentes de alimentación. Asimismo, se consideran la magnitud y los efectos de los transitorios en el sistema de potencia.

Los estudios de EMC en CMS se han basado en los estándares industriales, comerciales y militares existentes, así como en reglas de las agencias espaciales (ESA y NASA). Dichos estándares han sido adaptados a los requerimientos de la electrónica de CMS basándose en medidas y estudios de EMC en prototipos de los componentes del sistema de distribución. El principal objetivo de estos estudios es definir buenas topologías en los componentes del sistema, niveles de emisión e inmunidad, así como niveles de transitorios. Estos análisis permitirán realizar la integración del detector de forma que el correcto funcionamiento del detector esté asegurado. Además, esta tesis es la base de futuros estudios que posteriormente darán lugar a los futuros estándares de EMC en física de altas energías.

La gran complejidad del detector CMS hace que no se pueda analizar cada sistema en detalle, sin embargo, las reglas generales obtenidas a partir algunos subsistemas, como son el Tracker y HCAL, pueden ser extendidas al resto del experimento. Los estudios de EMC se han centrado en el sistema de distribución de potencia, al considerar CMS como un sistema aislado en donde la única conexión galvánica es a través de los cables del sistema de potencia. Para ello, se ha estudiado de forma simplificada, habiéndose desglosado en tres partes: FEE, cables y fuentes de alimentación.

El FEE es el componente más sensible del sistema y será caracterizado por la susceptibilidad al ruido conducido. En las fuentes de alimentación es necesario caracterizar sus niveles de emisión. Esto es especialmente importante en los convertidores DC-DC, los cuales, debido a sus altas emisiones radiadas y conducidas, necesitan de un adecuado filtrado y blindaje con el fin de reducir sus emisiones a niveles que puedan ser tolerados por la electrónica. Los cables son generalmente el medio de acoplamiento del ruido entre unos sistemas y otros.

Afortunadamente, la tecnología actual permite reducir el volumen de cables en CMS, al estar conectados el FEE y el sistema de adquisición de datos por fibra óptica. Esto reduce notablemente el nivel de inmunidad del FEE, lo que permite una simplificación notable de la integración de la electrónica del detector. No obstante, el estudio de los efectos del ruido de modo común y diferencial en cables largos de potencia constituye un importante punto a analizar. Estos efectos son cruciales para la transmisión de ruido dentro del FEE y han de ser tenidos en cuenta en el diseño del cableado y en la selección del tipo de cable (cable trenzado, blindado) a instalar en el detector.

La tesis doctoral ha sido desarrollada en tres etapas diferentes, las cuales corresponden, aproximadamente, a los trabajos realizados en cada uno de los tres años que ha durado el trabajo realizado en el CERN. Durante el primer año, la tesis se ha centrado en los estudios del sistema de distribución de potencia de CMS, en concreto en los subsistema Tracker y HCAL, y en el diseño, de la electrónica de estos sistemas. Se realizaron una serie de ensayos preliminares para evaluar las emisiones conducidas de los convertidores DC-DC. Los resultados obtenidos han sido usados para determinar la atenuación de ruido necesaria en el sistema.

En el caso del sub-detector Tracker, se piensan instalar las fuentes de alimentación en la sala anexa a la caverna (counting room). Esto hace que la fuentes estén situadas a unos 100 o 120 metros de distancia y la energía sea suministrada a través de unos cables especiales. Los principales parámetros y características del cable han sido definidos basándose en medidas y en modelos de cables. El principal objetivo de este análisis ha sido definir los modelos adecuados que posteriormente nos permitan estudiar la estabilidad del sistema de distribución y la respuesta a perturbaciones en la corriente de carga, así como la propagación del ruido de alta frecuencia entre las fuentes de alimentación y el FEE.

Durante el segundo año, los estudios se han enfocado en el desarrollo e implementación de los ensayos de EMC, que constituirán la base de la propuesta del plan de EMC para CMS. Los ensayos han sido diseñados basándose en recomendaciones de los ingenieros de la Agencia Espacial Europea (ESA). Estos ensayos fueron llevados a cabo en el laboratorio FERMILAB en Chicago (USA).

El FEE del subsistema "Very Forward HCAL" de CMS presenta una conexión bastante especial entre el detector y el FEE. Esta conexión se ha usado para estudiar la inmunidad de la electrónica a las señales de ruido de modo común, así como la inmunidad a campos electromagnéticos externos, durante la fase de diseño. El efecto de "crosstalk" en cables multi-conductores y el acoplamiento de campos externos y tensiones de modo común son igualmente analizados en este punto.

CMS planea distribuir potencia hasta la periferia del detector mediante un sistema trifásico de 400 Hz. En la periferia, convertidores AC-DC transformarán la tensión alterna en la apropiada baja tensión continua necesaria para operar la electrónica

del detector. También fueron analizadas las implicaciones que tiene este tipo de distribución en CMS.

Finalmente, los resultados obtenidos mediante los ensayos de EMC realizados en el FERMILAB han sido analizados durante el último año de tesis. La susceptibilidad del FEE a perturbaciones electromagnéticas ha sido definida. También durante este año se han analizado los efectos de la propagación de ruido en alta frecuencia a través de cables de potencia y sus implicaciones en la especificación final de los niveles de emisión de las fuentes de alimentación. Con el fin de completar la caracterización de las emisiones de las fuentes de alimentación, así como de los filtros a incluir en ella, se realizaron unos ensayos adicionales.

El documento de tesis esta organizado de la siguiente forma:

- Descripción del detector CMS (*Capítulo 1*)
- Puesta a tierra del detector. (*Capítulo 2*)
- Emisiones conducidas y filtrado de convertidores DC-DC. (*Capítulo 3*)
- Efectos en la propagación del ruido en cables de potencia. (*Capítulo 4*)
- Inmunidad del ruido en la fase de diseño. (*Capítulo 5*)
- Ensayo de susceptibilidad del FEE. (*Capítulo 6*)
- Transitorios en el sistema de distribución de CMS. (*Capítulo 7*)

Introduction

The Compact Muon Solenoid (CMS) is one of the four high-energy physics experiments under construction at CERN for the Large Hadron Collider (LHC) accelerator. The dimensions of the CMS detector are about 30 meters long and 25-meter diameter, with a total weight of around 13000 tons.

The CMS detector is divided in five sub-systems located at different layers of the structure. Each sub-system has distinct objectives and processes different signal and energy levels. In general, high-energy physics (HEP) experiments identify particle interactions and measure their energy using sensitive detection devices such as silicon and pixel detectors, wire chambers, scintillators and optical devices. In the CMS experiment, the detected electrical signal is amplified and processed by the front-end electronics (FEE), which communicate, via optical links, with the acquisition system located 120 meters away from the detector. The read-out electronics of the CMS experiment are designed to process signals of a few mV digitizing them synchronously at 40 MHz. Part of this electronics is located inside of a harsh environment with particle radiation and a DC magnetic field of 4 Tesla.

All the data from the FEE is transmitted to the acquisition system via optical fibers, avoiding that the electromagnetic interference (EMI) is coupled to the FEE from outside of the detector. The problem may appear in the detector itself, where a large amount of electromagnetic interactions exist among the electronic sub-systems. These interactions can be mainly found in the connection between the FEE and the power supply distribution and in the FEE itself. The two most important issues to address before integrating the electronic system into the detector are first, the definition of the maximum levels of the radio-frequency noise and the transient signals such that the FEE in each sub-system can operate achieving the performance goals and second, the definition of how to impose those levels to the electronic system using normalized measurements. Within this framework, CMS needs to generate a specification of both emission and immunity noise limits for the electronic equipment to be integrated into the experiment. Normalized tests for the equipment have to be defined to comply with those limits. Describing the electromagnetic (EM) environment of CMS is of major importance for determining and solving problems related to electromagnetic interference, grounding and shielding. This thesis addresses the EMC studies conducted for the CMS experiment to define the baseline of the future CMS EMC policy. The EMC studies are mainly focused on the quantification of the FEE sensitivity to conductive noise coupled through the input/output cables and the noise generated by power

supplies. Also, the magnitude and effects of transient signals disturbing the power supply system are introduced.

The EMC studies in CMS are based on existing industrial, commercial and military standards and rules applied by aerospace agencies. These standards have been adapted to the CMS electronic systems based on EMC measurements and EMC studies, which include immunity test conducted on the FEE and emission tests performed in different components of a power supply distribution system prototype. The goal of these EMC studies is to define good topologies, emission and immunity levels and transient levels. This allows the integration of electronic units of the CMS detectors in a safe way, such that will define future EMC standards required by HEP community.

Due to the complexity of the CMS experiment, it has not been feasible to analyze each subsystem in detail; nevertheless general rules emerging from particular subsystems, as the Hadron calorimeter (HCAL) and the Tracker, can be easily extended to the rest of the sub-detectors. The EMC study has been focused on the power supply distribution system, as CMS can be considered an isolated system with a sole galvanic connection done through the power supply system. For that purpose, a simplified scheme of the power supply system has been used in this research work to address EMC studies. Basically each sub-detector can be defined by these three constitutive elements:

- Front end electronic (FEE)
- Power supply (PS)
- Cables (C)

The FEE considers not only the amplification and the analogue to digital conversion stages but also includes the particle detector device itself. This complete equipment is the most sensitive part and has to be characterized by the susceptibility to conductive noise and transients. Power supplies are characterized by the EM emission, in particular, switching power supplies which generate high frequency noise that can be coupled to the sensitive electronics via radiation or conduction. Appropriate filtering and shielding may reduce the noise emission to levels that can be tolerated by the FEE. Cables in general are the conductive link to couple noise among sub-systems. The state of the art of technology nowadays allows reducing the cable network because almost all high-speed digital communication between the FEE and the acquisition system is performed via optical links. This fact highly improves the immunity level of FEE against interferences, making easier the complete integration of such a large detector. Nevertheless, the study of the common mode and differential mode noise effects in long power cables constitutes an important issue. These effects are crucial for the noise transmission from the power supplies to the FEE and have to be taken into account in the selection of the cable and the design of the cable layout in the detector.

In the doctoral work planning, the thesis development has been divided in three main parts, which correspond roughly to each of the 3 years of the Ph.D. During the first year, the study has been focused on the power supply system for CMS sub-detectors, in particular HCAL and Tracker, and on the electronic layout of these sub-systems. Using the Hadron calorimeter sub-system as experimental set-up, tests of conducted noise generated by DC-DC converters have been performed. Based on the obtained results, EMC filters have been evaluated to achieve a low noise distribution system.

In the case of the Tracker sub-detector, it is planned to supply low voltage between the control room and the detector (100-120 m.) using special multi-conductor cables with different sections having different properties. A characterization of these cables has been conducted based on cable models and measurements to define the characteristic parameters. The target is to define appropriated models to allow the analysis of the stability of the power distribution system, the response to load current perturbations and propagation of high frequency noise between the power supply and the sensitive front-end electronics.

During the second year, studies have been focused around the development and the implementation of the EMC tests, which will form the base line of the EMC proposal. Tests were designed based on recommendations given by EMC engineers of the European Space Agency (ESA). A set of measurements was conducted during the end of this year on CMS HCAL front-end electronics prototypes at FERMILAB, USA.

The front-end electronics of the CMS Very Forward Hadron Calorimeter (HF) sub-detector presents a special connection between the detector and the electronics. This connection has been used to study the noise susceptibility to common mode noise signals and external electromagnetic fields of the electronic system at the design stage.

A 400Hz AC system is proposed to distribute power to all CMS sub-detectors. It distributes high voltage to the periphery of the detector using a three-phase system. On the detector, step-down converters transform the AC high voltage to appropriated DC low voltages. The implications of this kind of distribution in the CMS detector have been also examined.

Finally during the last year, the results from the EMC tests have been analyzed. The tests had been carried out in December of the previous year at FERMILAB. The susceptibility of the FEE to EMI and perturbations has been defined. Also during this period the effects of high frequency noise propagation through the power cables and their implications in the final specifications of CM and DM emissions of the power supply have been analyzed. As a final step, a set of additional EMC tests on the power supply have been carried out with the aim of completing the characterization of the power supplies and output filters.

The thesis report is organized as follows

- CMS detector description (*Chapter 1*)
- Grounding issues (*Chapter 2*)
- Conducted emissions and filtering of switching power supply (*Chapter 3*)
- Noise propagation effects on cables (*Chapter 4*)
- Immunity of the FEE at design stage (*Chapter 5*).
- Susceptibility test of the FEE (*Chapter 6*)
- Transients on the power supply distribution system (*Chapter 7*)

Chapter 1

CMS detector

The Compact Muon Solenoid (CMS) is one of the four high-energy physics experiments under construction at CERN for the Large Hadron Collider (LHC) accelerator. In general, high-energy physics (HEP) detectors identify particle interactions and measure their energy using sensitive detection devices such as silicon and pixel detectors, optical devices, wire chambers, etc. The CMS and ATLAS calorimeters at LHC constitute the biggest detectors ever designed for HEP experiments. A short description of the main part of CMS detector and sub-systems is presented as well as some details about the new circular accelerator the LHC. Special attention is paid to two sub-systems of the CMS detector, as the EMC plan has been based on several preliminary studies of these subsystems. These systems are the Hadron Calorimeter (HCAL) and the Silicon Tracker Detector.

1.1 The Large Hadron Collider (LHC)

The Large Hadron Collider (LHC) [1] is under construction at CERN laboratory on the French-Swiss border west of Geneva, at the foot of the Jura mountains, in front of the Alps. Combined with the LHC are 4 experiments called CMS [2], ATLAS [3], LHCb [4], and Alice [5].

The LHC consist on a 27 km circular accelerator placed 100 meters under the ground, containing two beam pipes, capable of accelerating counter rotating bunches of protons with beam energies up to 7 TeV. The bunches are focused to collide within the experiments with centre of mass energies up to 14 TeV. High-energy LHC beams need high magnetic bending fields. To bend 7 TeV protons around the ring, the LHC must be able to produce magnetic fields of 8.36 Tesla by superconducting magnets.

LHC superconducting magnets will be operated at 1.9 K and will be capable to carry currents of 15,000 amps and withstand forces, which build up to hundreds of tons per meter in the coils as the field rises. The LHC will be made of 5,000 LHC superconducting magnets, which need a complex cryogenics system. In all, LHC

cryogenics will need 40,000 leak-tight pipe junctions, 12 million liters of liquid nitrogen will be vaporized during the initial cool down of 31,000 tons of material and the total inventory of liquid helium will be 700,000 liters. Figure 1.1 shows the layout of the LHC.

The Large Hadron Collider (LHC)

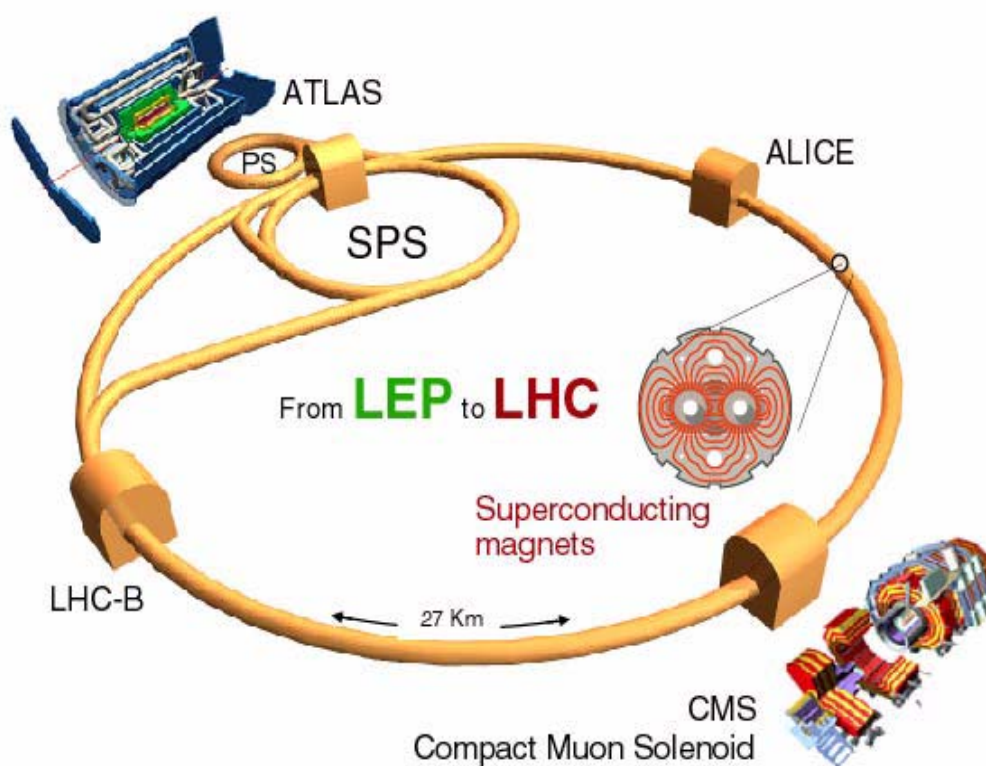


Figure 1.1: LHC layout.

1.2 The Compact Muon Solenoid (CMS) experiment

The goal of the CMS detector is to identify particles and measure their position momenta or energy. An illustration of the CMS detector showing the various sub-detectors and the super-conducting solenoid magnet is depicted in figure 1.2, while figure 1.3 shows the CMS detector cavern. The detector is organized in sub-systems as follows, from the interaction point to the periphery:

1. Tracker - (Silicon & Pixel detector)

The tracker is designed to measure precisely the momentum of the charged particles. It is configured by a highly segmented and layered charged particle detector involving millions of channels. Silicon pixel and strip sensors are used. The presence or not of a charged particle is recorded in each channel allowing the tracks to be reconstructed. The radius of curvature of the tracks in the magnetic field reveals the momentum of the particle.

2. Calorimeters

Electrons, protons and hadrons will be stopped by the calorimeters allowing the measurement of their energy. The first calorimeter layer is designed to measure the energies of electrons and photons with a high precision. Since these particles interact electromagnetically, it is called the electromagnetic calorimeter (ECAL). Particles, which interact via the strong interaction (hadrons), deposit most of their energy in the next layer, the hadronic calorimeter (HCAL). Neutrinos escape direct detection but their presence can be inferred as an apparent energy imbalance after the collision.

a. Electromagnetic Calorimeter (ECAL).

The electromagnetic calorimeter measures the energy of photons and electrons. Almost no photon nor electron originating from proton-proton interaction point pass beyond the ECAL.

b. Hadron Calorimeter (HCAL).

The hadronic calorimeter measures the energy of particles such as protons, pions, neutrons and kaons. Almost no hadrons generated from proton-proton interactions pass beyond the HCAL.

3. Superconducting Solenoid.

A long superconducting solenoid of 13m length and inner diameter 6m has been chosen to create a uniform magnetic field of 4 Teslas in the direction of the beam axis.

4. Muon detector.

The only particles generated from the proton-proton interactions to reach the muon detector are muons and neutrinos. The muons are detected directly but the neutrinos escape undetected. The presence of a neutrino is inferred by missing transverse energy.

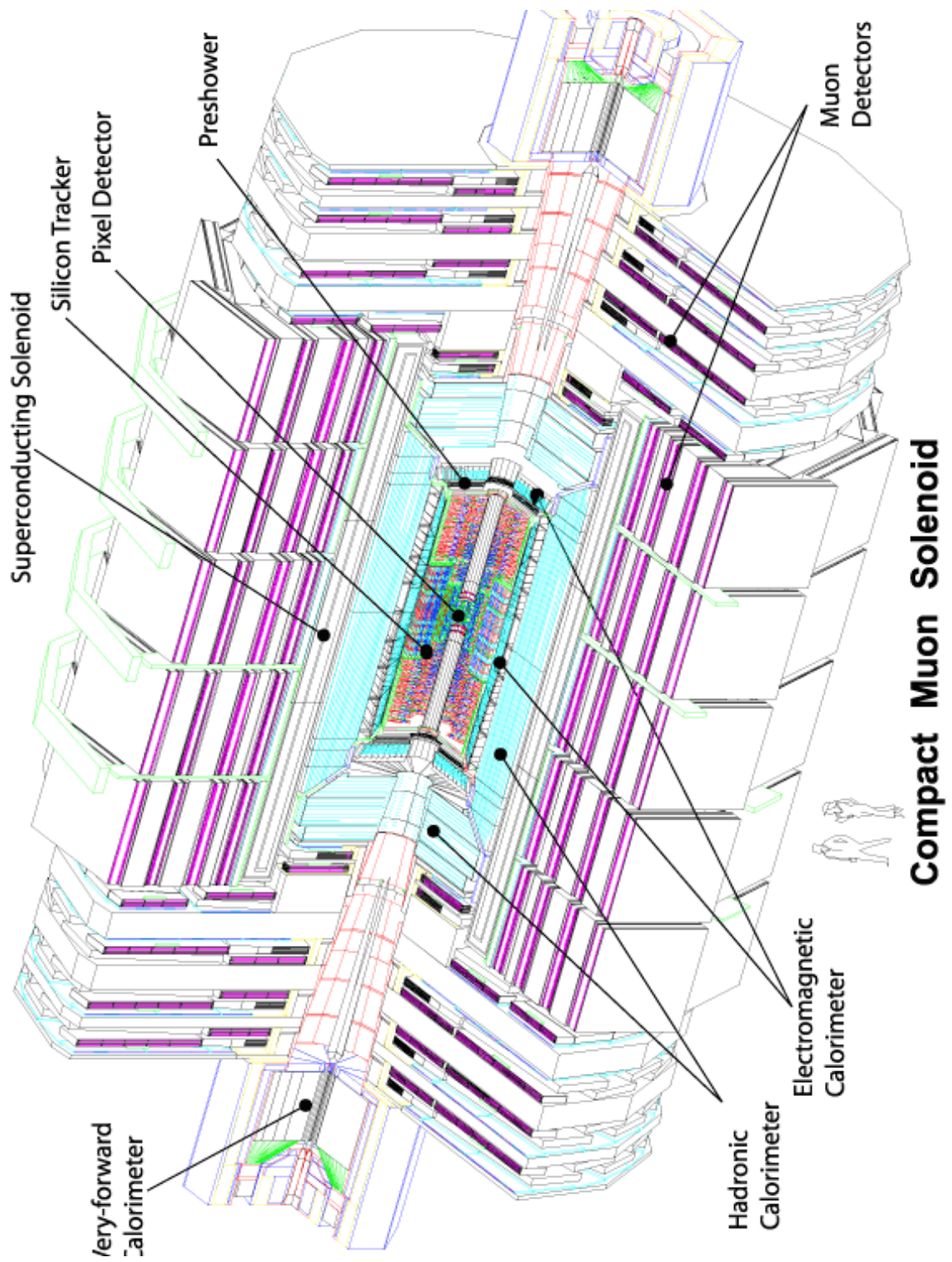


Figure 1.2: Complete layout of the CMS detector.

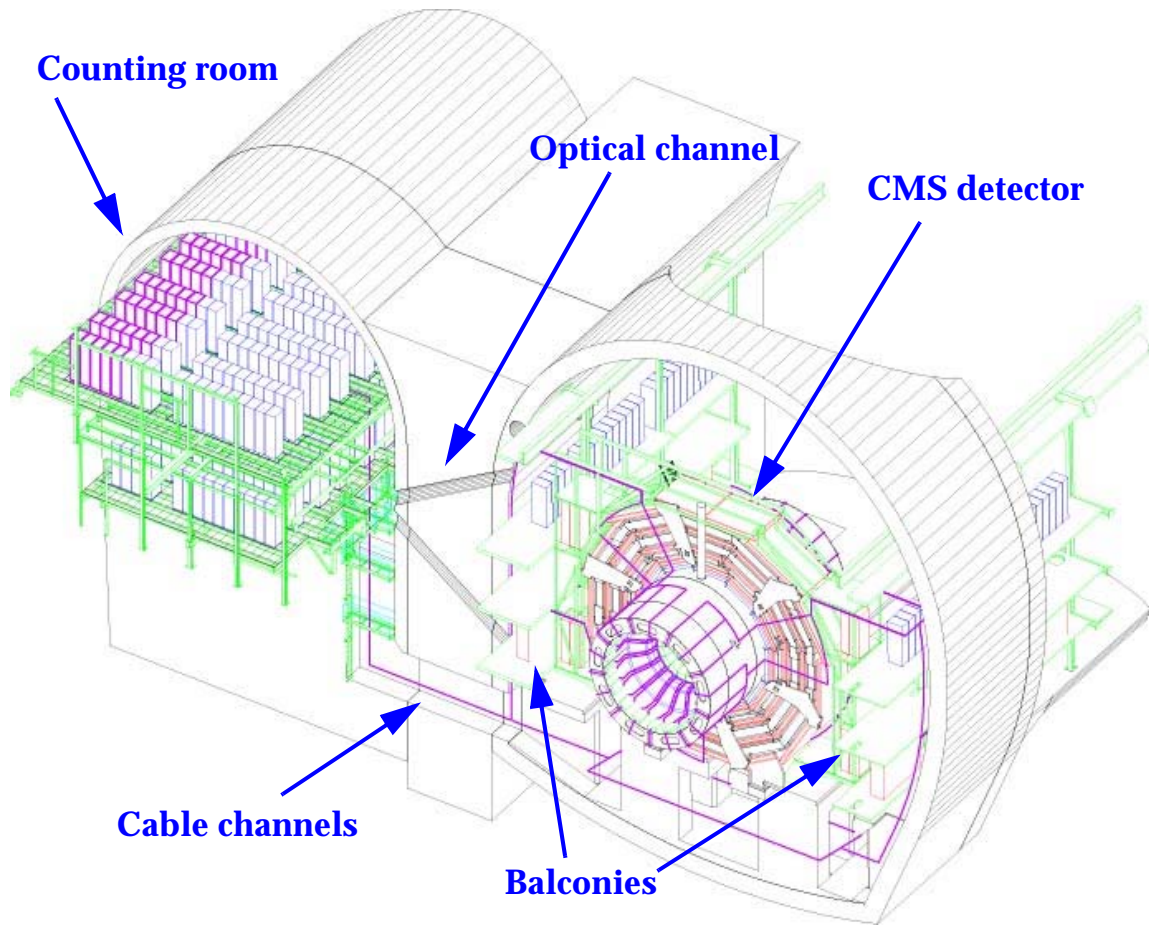


Figure 1.3: View of CMS detector cavern.

1.3 Tracker Sub-system

The tracker detector [6] is of the utmost importance for an experiment designed to address the full range of physics. The CMS tracking system is designed to reconstruct tracks of high- p muons, isolated electrons and hadrons with a high momentum resolution and a high efficiency. It is also designed to allow the identification of tracks coming from detached vertices.

The tracker system is embedded in a 4 Tesla magnetic field, which forces low- p particles into small radius helical tracks, resulting in reduced occupancy at larger radius. The presence or not of charged particles is recorded in each channel and the tracks reconstructed. The curvature radius of the tracks in the magnetic field reveals the momentum of the particle.

The layout of the tracker (Silicon & Pixel detector) [7] is shown in figure 1.4. This volume operates at a temperature around -20 degrees.

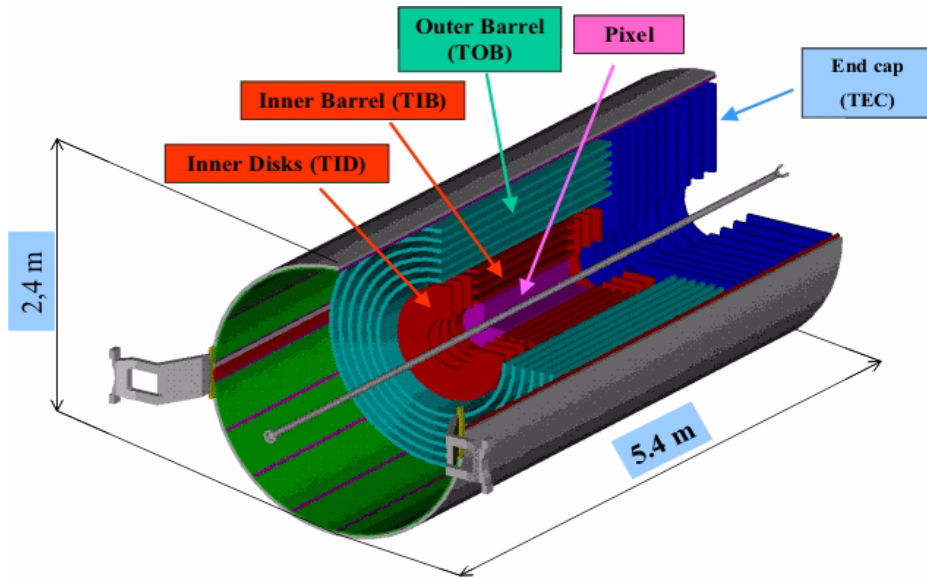


Figure 1.4: View of the Silicon and Pixel detector.

1.3.1 Pixel detector

At the smallest section of beam line (around 10 cm radius), the interaction region of the detector is surrounded by three layers of silicon pixel detectors. Two end-cap disks cover the distance from 6 to 15 cm of radius. A mechanical scheme is depicted in figure 1.5.

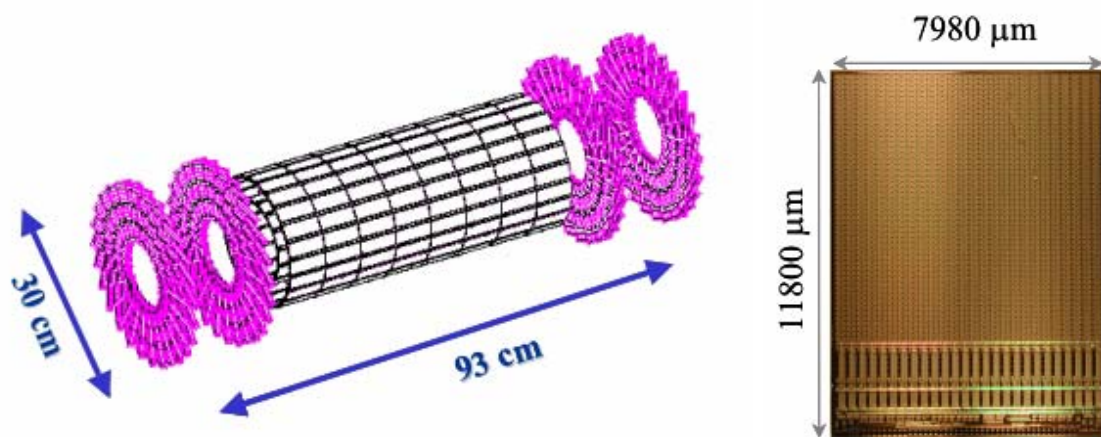


Figure 1.5: Pixel detector and pixel sensor.

The pixel layers are composed by modular detector units. Each module consists of a thin, segmented sensor plate with highly integrated readout chips connected to

them using the bump bonding technique. The cell size in the pixel detector is $150 \times 150 \mu\text{m}$ and the total number of the chips of the pixel detector is around 16000, which process the data from 45×10^6 pixels. Around 224 PS supplies the power to the FEE of pixel detector. These voltages are 2.5 V and 1.8 V and the maximum current per line will be less than 8 A. Also the pixel detector needs around 112 power supply units to supply the HV (+600V). These units deliver only a few mA.

1.3.2 Silicon detector

It is placed around the pixel detector. The cylindrical layers contain modules based on rectangular detectors and the end-cap disk carries up to four rings of wedged-shaped detector modules. Figure 1.6 depicts the geometry of the silicon detector.

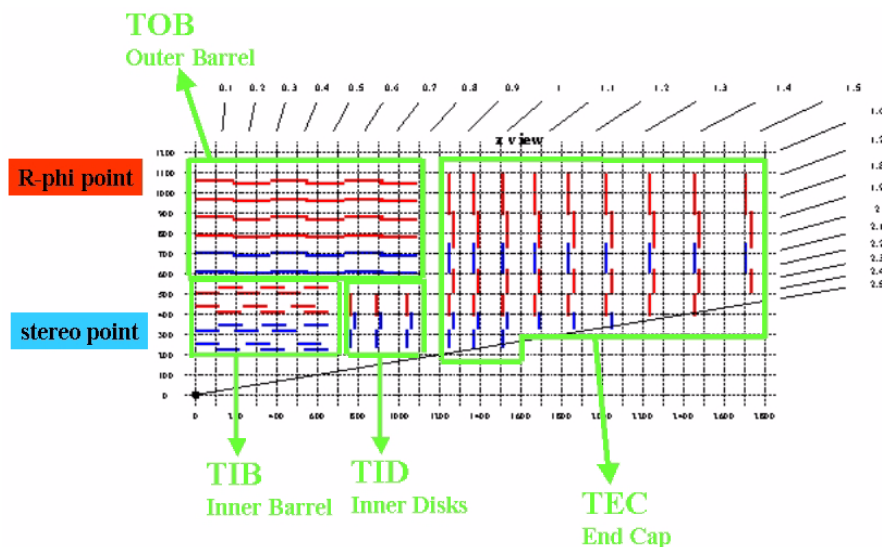


Figure 1.6: Geometry of the Silicon detector. It shows a quarter of the detector.

The detector module is the basic functional component of the silicon tracking system. Each module consists of three main elements:

- Single side or double side silicon sensors.
- Mechanical support (Carbon fiber frame).
- Readout hybrids Front end electronics.

A general layout of a module is shown in figure 1.7.

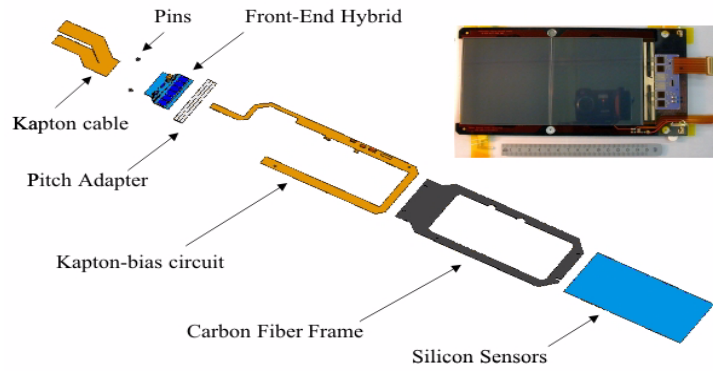


Figure 1.7: Silicon detector module layout.

These modules are grouped in leaders and petals, as it is shown in figure 1.8 and figure 1.9. Finally these leaders are mounted on two-structure wheel as it is shown in figure 1.4.



Figure 1.8: Leader structure.

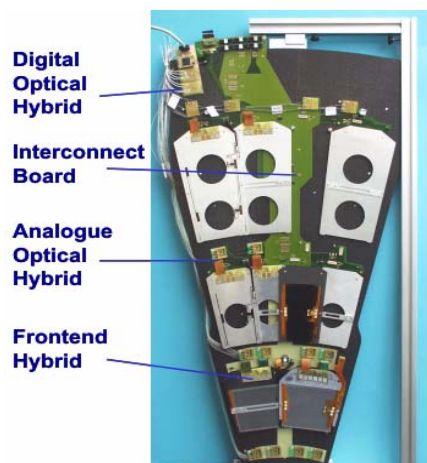


Figure 1.9: Petal structure.

1.3.3 Tracker Readout Electronics

A general block diagram of the front end electronic for the tracker [6] detector is shown in figure 1.10. The system processes analogue signals from 10 million channels of micro-strip tracker with minimal power and material. Electronic noise should be sufficiently low to ensure high efficiency and bunch crossing identification. Performance is ultimately limited by the speed and magnitude of detector signals and the radiation environment. It has four different parts; the detector or sensor, the APVs [8] and the control unit located in the central part of the calorimeter, and the front end controller and front end driver located in the counting room.

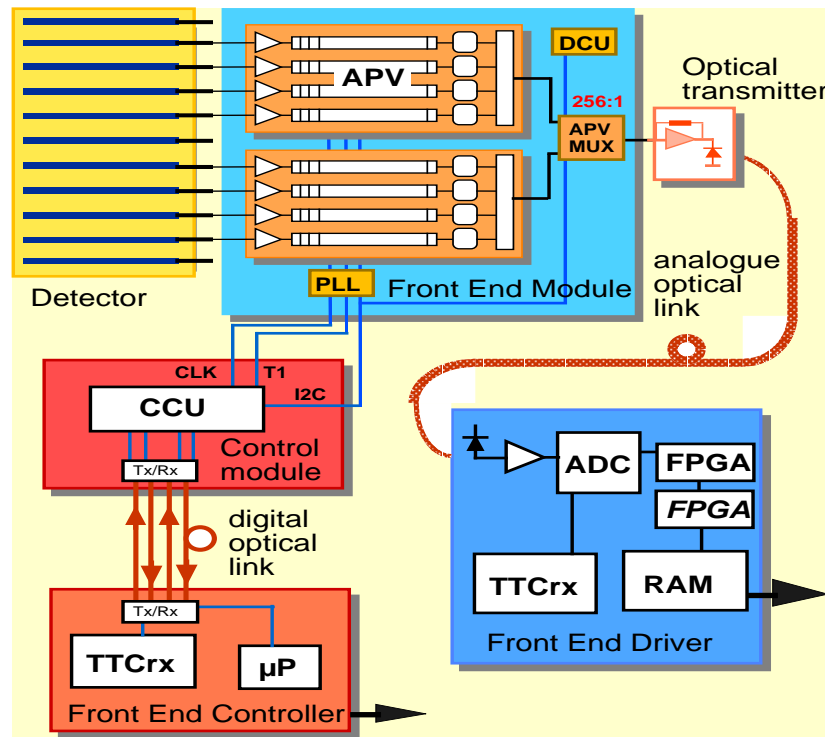


Figure 1.10: General block diagram of the readout system of the silicon detector.

1.3.3.1 APV Front End circuit.

Each micro-strip is read out by a charge sensitive amplifier whose output voltage is sampled at the LHC 40 MHz rate. Samples are stored in an analogue pipe line for a few ms and following a trigger, are processed by an analogue circuit using a weighted sum algorithm to measure signal amplitude and associate the bunch crossing with the hit. Pulse height data is multiplexed from a couple of front end chips, sending differential signals over a short twisted pair cable to a laser, where

electrical signals are converted to infrared and transmitted over 100 meter fibre optic cable to the counting room adjacent to the cavern.

1.3.3.2 Optical Link

The optical link [9] employs edge-emitting semiconductor laser transmitters operating at the telecommunications wavelength of 1310nm. Those lasers are assembled with single mode fibre pigtails in a low mass package developed in collaboration with industry. All link components have been shown to be extremely radiation hard. Minimum current is required before laser actions starts. Above threshold the light output power is extremely linear with the drive current.

1.3.3.3 Front End Driver

Pulse height data are received by a photodiode - amplifier and the front end driver which digitizes and processes the signals, including reordering and pedestal subtraction, and stores results in a local memory for the higher level data acquisition.

1.3.3.4 Control System

The front-end controller supervises and controls the front-end electronics and also it is the interface with the CMS Timing Trigger and command system. Digital optical links, using the same analogue link components, transmit triggers, clocks and control data. Internally digital transitions are recovered by photodiode-amplifiers and distributed electrically by a communication and control unit (CCU) to detector modules. Clocks are recovered by phase locked loop (PLL) chips on each module for high reliability and minimum phase jitter. CCU modules can be configured as rings to match the tracker topology and reduce cost

1.3.3.5 Low and High voltage PS distribution system.

Tracker sub-detector [10][11] has proposed several topologies to power-up the front-end electronics. In such proposals, the primary 400Hz AC distribution system is rectified and later, DC-DC converters transform with high efficiency the 48 V into the LV and HV required by the front-end (FE) electronics, which are locally regulated using sense wires. The final location of these converters is not yet defined, one proposal planned to locate the converters between 20-40 mts. from the front-end electronics. The other plan is to place both the rectifiers and the DC-DC converters in the counting room (100 or 120 meters far from the detector) due to the intense magnetic field that exists inside the detector.

1.3. Tracker Sub-system

The total number of tracker detector modules is 13884 and the total number of APV's is around 80000, (i.e 100 million of read-out channels.). Between 12 and 6 modules are grouped together to create a PS group, each of them is supplied by a PS unit. Tracker needs around 250 kW in order to work. About 2000 power supply units power the silicon tracker detector. Each of them supplies three different voltages (Table 1.1) to a specific group of modules.

	Voltage (V)	Max. current (A)
LV -1	+ 2.5 V	10
LV -2	+ 1.25	8
HV	+ 600	0.02

Table 1.1 Tracker power supply values per power channel.

Two different long and complex cables are used to supply the power from the DC-DC converters to the tracker FEE. These cables are split in three or two segments. The length as well as the type of cable is different for each segment. Basically three types of cable can be found in tracker sub-detector.

- Low impedance cable (LI)
- Multiservice cable (MSC) - Copper [12]
- Multiservice cable (MSC) - Aluminum

These complex cables have HV, LV, signal and control wires located inside an aluminum and copper braid shield. Figure 1.11 shows the schematics of the LIC and MSC copper cable.

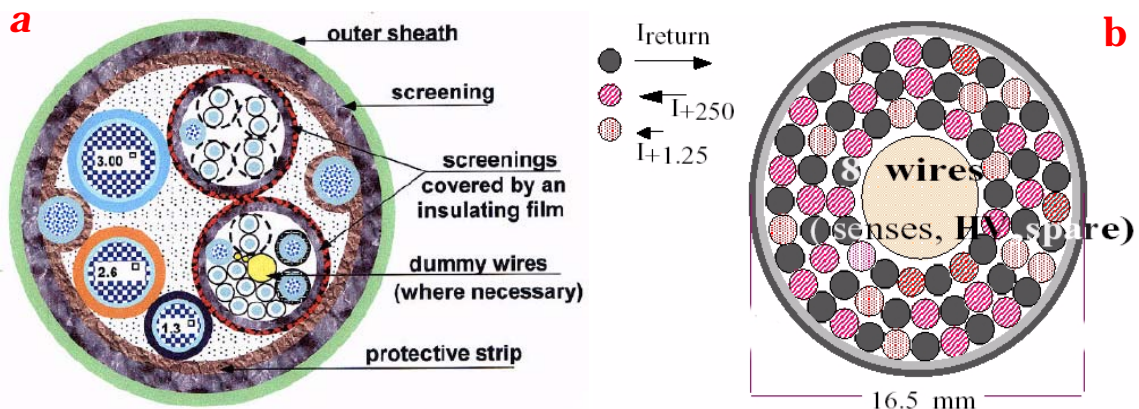


Figure 1.11: Tracker power cables a) MSC cable and b) LIC cable.

1.4 Electromagnetic Calorimeter (ECAL)

The CMS electromagnetic calorimeter [13] is composed by scintillating crystals and offers excellent performance for energy resolution since almost all of energy of electrons and photons is deposited within the crystal volume. CMS has chosen lead tungstate crystals, which have high density, a small Moliere radius and a short radiation length allowing a very compact calorimeter system.

The electromagnetic calorimeter system is placed around tracker detector in the 4 Tesla magnetic field. Electrons and protons will be stopped by the calorimeters allowing their energy to be measured. There are two different parts on this sub-detector:

- Electromagnetic calorimeter.
- Pre-shower detector.

The layout and some details of the ECAL system are shown in figure 1.12.

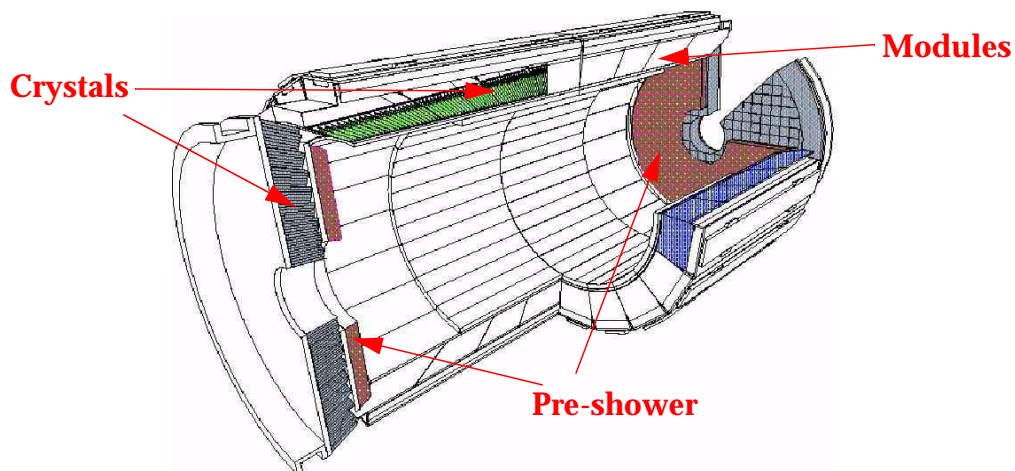


Figure 1.12: Interior view of the Electromagnetic calorimeter and Pre-shower detector.

The CMS electromagnetic calorimeter consists of over 76000 lead-tungsten crystals equipped with avalanche photodiode (APD) or photodiodes and associated electronics operating in a challenging environment, with a magnetic field of 4 Tesla, high radiation dose and difficult access for maintenance.

The detector module is the basic functional subunits of the ECAL system. Each module consists of three elements.

- Crystal
- Basket or mechanical support

- Readout electronics (FEE)

A general layout of a module is shown in figure 1.13:

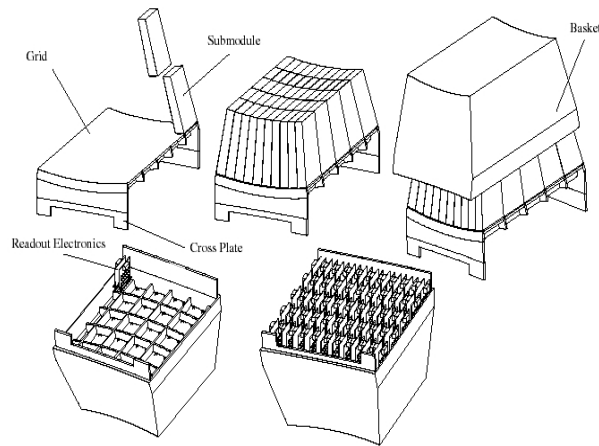


Figure 1.13: General layout of a ECAL module.

1.4.1 ECAL Read out electronics

A general block diagram of the front end electronic for the ECAL detector [14][15] is in figure 1.14. The first element in the front-end chain is the lead- tungsten crystal, which converts energy into light. The light is converted into a photocurrent by the APD. The relative low electric current delivered by the photodetector device is amplified, shaped and converted to a voltage waveform. This signal is then acquired and digitized. The resulting data is transmitted off the detector via optical fibre to the read out located in the counting room.

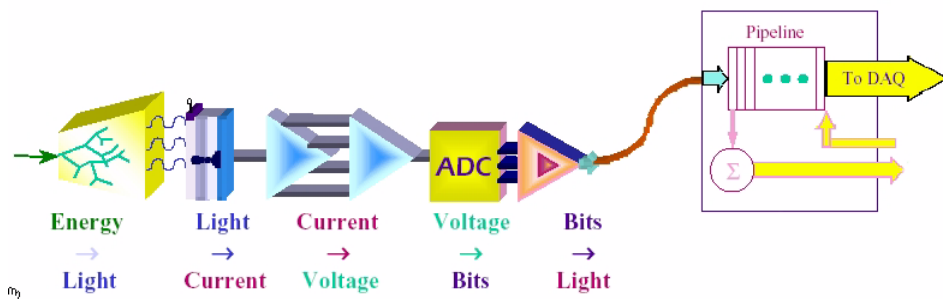


Figure 1.14: Scheme of the ECAL readout system.

The upper level read-out has four main functions:

- Formation of trigger tower energy sums
- Pipelining (Storing the data until arrive of level -1 trigger decision)
- Transmission of the data of the triggered event to the data acquisition system
- Providing interface functions for the 'on detector electronics'.

ECAL needs around 450 kW in order to work. About 750 power supply units [16] bias the ECAL front-end electronics. Each of them supplies 4.5 V with a maximum current of 100 A. This voltage is used to supply the power to a low voltage regulator board where LV regulators transform the input voltage into the final one required for the electronics, which is 2.5 V.

1.4.2 Pre-shower detector

CMS utilizes a pre-shower detector [13] in the endcap region. This region is shown in figures 1.12 and 1.15. Its main function is to provide a separation between two different particle decays ($\gamma - \pi^0$). The CMS pre-shower consists of two lead radiators having about 2 and 1 radiation length thick respectively, each one followed by a layer of silicon micro-strip detectors. Both layers of detectors have their strips orthogonal to each other. The first layer has vertical strips and measures the horizontal position of shower particles, whilst the second layer has horizontal strips to measure the vertical position of particles. The energy deposited in the silicon detectors is proportional to the energy deposited in the lead, so it can be used to apply a correction.

The pre-shower has a cylindrical shape about 18cm long (along the beam axis), the inner radius is approximately 45cm whilst the outer radius is about 120cm ($h = 1.65$). The total area to be covered by silicon detectors is about 16.4 square meters (Around half of the one used by the Tracker in CMS).

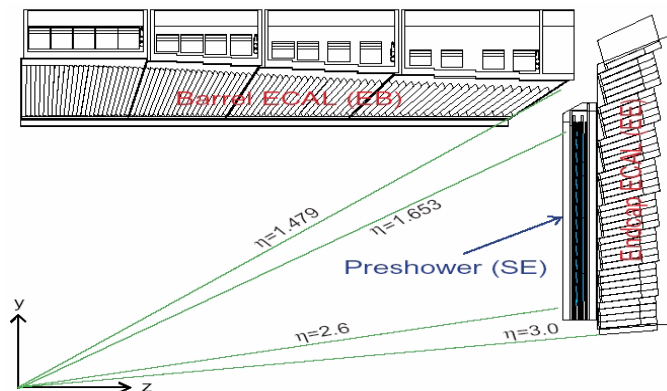


Figure 1.15: Location of the Pre-Shower in the end cap.

The silicon detectors used in the pre-shower do not have to present ultra-fine granularity like in the Tracker detector. A strip pitch around 2mm is sufficient for this application. To reduce the number of channels to a minimum, it has been chosen the largest detectors that are easily integrated.

The motherboard is the basic functional submit of the Pre-shower detector. Each module consists of three elements.

- Single side or double side detectors
- Mechanical support
- Readout hybrids (Front end electronics)

This module is shown in figure 1.16.

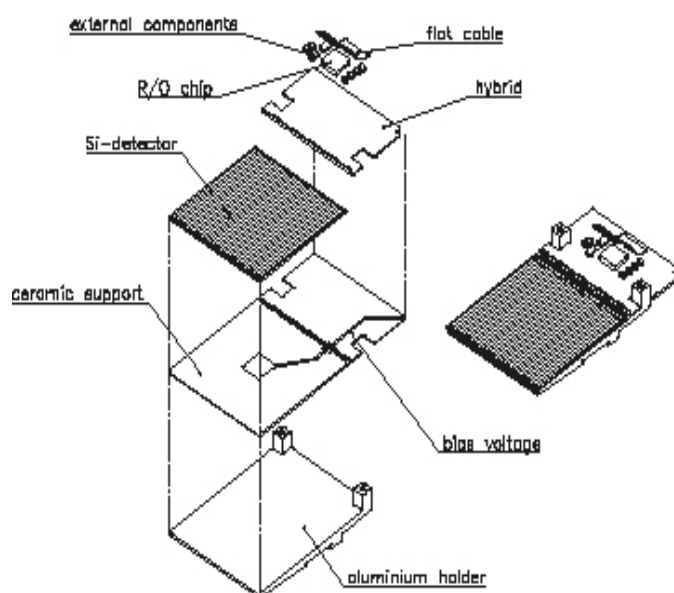


Figure 1.16: Pre-shower module layout.

1.4.2.1 Pre-shower read-out electronics

The basic requirements for the pre-shower electronics are: 1) the front-end must have a large dynamic range (due to the large fluctuation in particle energies to be measured), 2) low noise, and 3) a "*pipeline memory*" to store signals until a trigger signal arrives. The CMS ECAL and Tracker detectors require similar electronics, so some common parts have been adapted to the pre-shower needs. However, some parts for the front end electronics of the Pre-shower are such as the 'PACE' circuit [17] (Pre-shower Analog CMS Electronics). The PACE has 32 channels (one for each of the micro-strips on a single silicon detector) with 160 memory cells for each channel. The analog signals from the PACE are fed into an analog-to-digital converter (ADC) with a large dynamic range. A suitable ADC is the CRIAD, also

designed at CERN. The output digital signals are sent via optical cables to VME crates, located in the counting room. The VME electronics performs zero-suppression and some signal processing before feeding the data to the CMS data acquisition system (DAQ). The motherboard (MB) is located into the detector, while the DDU is located into the counting room.

Pre-shower needs around 21 kW in order to work. About 48 power supply units power the pre-shower detector. Each of them supplies the 4.5 V voltage required at the input of the FEE, where LV regulators transform the 4.5 V in the final low voltage required by the analog and digital part of the FEE.

1.5 MUON chambers sub-system

Muons are expected to provide clean signatures for a wide range of physics processes. The task of the muon system [18] is to identify muons and provide, in association with the tracker, a precise measurement of their momentum. In addition, the system provides fast information for triggering purpose. The muon detectors, placed behind the calorimeters and the coil, consist of four muon stations interleaved with the iron return yoke plates. They are arranged in concentric cylinders around the beam line in the barrel region, and in disks perpendicular to the beam line in the end caps. They are shown in light blue in figure 1.17.

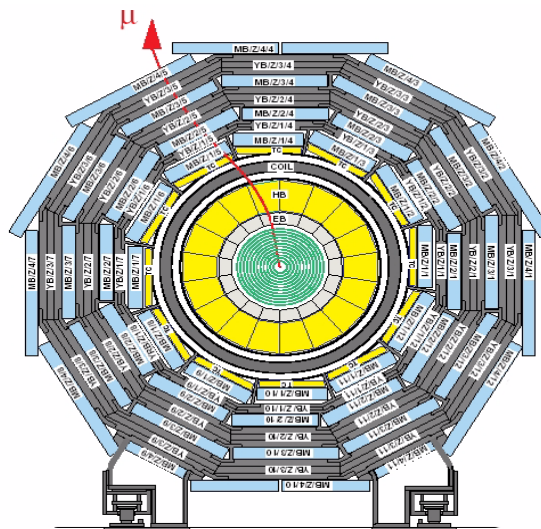


Figure 1.17: Layout of barrel muon disk (Blue colour).

CMS will use three types of gaseous particle detectors for muon identification: 1) Drift tubes (DT) in the central barrel region, 2) Cathode Strip Chambers (CSC) in the end cap region, and 3) Resistive Parallel Plate Chambers (RPC) in both the barrel

and end caps. The DT and CSC detectors are used to obtain a precise measurement of the position and thus the momentum of the muons, whereas the RPC chambers are dedicated to provide fast information for the Level-1 trigger.

1. Drift tubes.

Drift tubes are used in the barrel where the magnetic field is guided and almost fully trapped by the iron plates of the magnet yoke. Each tube contains a wire with large pitch (4 cm), and the tubes are arranged in layers. Only signals from the wires are recorded - resulting in a moderate number of electronics channels needed to read out the detectors. When an ionizing particle passes through the tube, it liberates electrons, which move along the field lines to the wire, which is at positive potential. The coordinate on the plane perpendicular to the wire is obtained with high precision from the time taken by the ionization electrons to migrate to the wire. This time (measured with a precision of 1ns), multiplied by the electron drift velocity in the gas, translates to the distance from the wire.

A DT layer is put together by gluing to an aluminum plate a set of parallel aluminum beams. The wires are stretched and held by the appropriate end plugs, and the layer is closed by another aluminum plate. Groups of four layers are grown in this way on a precision table. Copper strips are previously glued to the aluminum plates in front of the wire to shape better the electrostatic field. The largest DT chamber to be used in CMS will be 4 m x 2.5 m.

2. Cathode Strip Chambers.

CSCs are used in the end cap regions where the magnetic field is very intensive and very inhomogeneous. CSCs are multi-wire proportional chambers in which one cathode plane is segmented into strips running across wires. As avalanche is developed a wire induces a charge on several strips of the cathode plane. In a CSC plane, two coordinates per plane are made available by the simultaneous and independent detection of the signal induced by the same track on both the wires and the strips. The wires give the radial co-ordinate whereas the strip measures the angle. In addition to providing precise space and time information, the closely spaced wires make the CSC a fast detector suitable for triggering. The CSC modules containing six layers provide both robust pattern recognition for rejection of non-muon backgrounds and also efficient matching of external muon tracks to internal track segments.

Six layers CSC are built assembling together 7 Honeycomb panels. Three of them support two wire planes each, one on each face of the plate, wire at the same time. The other four plates have the etched strips. The two inner plates have strips on both faces, whereas the two outer plates (closing the chamber) have strips only on one face.

3. Resistive Parallel Plate Chambers.

RPCs are fast, gaseous detectors whose information is the base of the triggering process. RPCs combine good spatial resolution with time resolution of 1 ns, comparable to that of scintillators. The RPC is a parallel plate counter with two electrodes. It is made of plastic material with very high resistivity. This allows the construction and operation of very large and thin detectors that can operate at high rate with high gas gain. Resistive Parallel plate Chambers are fast gaseous detectors whose information is the base of the triggering process. The total number of chamber of the Muon system is around 1800.

1.5.1 Muon Sub-system read-out electronics

1. FEE - Cathode Strip Chambers.

Cathode and anode front-end boards (FEB) are mounted directly on the CSC modules. The data from the FEB are sent by cable to the readout motherboard, also mounted on the chamber. The motherboard serves as link between FEBs and the rest of the detector. It sends both the readout and trigger data to the central DAQ system and level-1 trigger system located into the counting room. It also receives the trigger, timing and control (TTC) signals from the counting room and distributes them to the FEBs. This connection is implemented using an optical link. A general layout of the readout system of CSC is shown in figure 1.18.

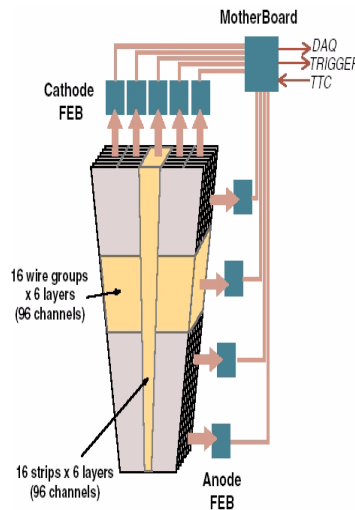


Figure 1.18: Readout structure of CSC.

2. FEE - Drift tubes.

The FEE is basically composed of both the read-out boards (ROB) and the read-out servers (ROS). All these units are housed in crates and are placed in racks on the

balconies (periphery of the detector). The FEE, placed inside the gas volume, will provide discriminated differential signals that are transmitted to the read-out boards (ROB) using a 25-m twisted-pair cable.

3. FEE - Resistive Parallel Plate Chambers.

A general scheme of the front-end control system and the data transmission interface to the optical link is shown in figure 1.19. The data from the front-end board (FEB) is sent, using flat cables, to a link board where it is processed and transmitted to the trigger processors. The FEBs are located close to the detector and are connected via an optical link, with both the RCP trigger crates and the network. It also supplies the LHC clock and broadcast test pulses to the FEB.

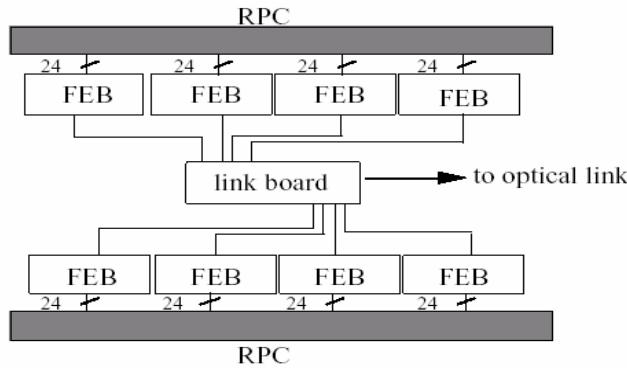


Figure 1.19: Layout of the front-end system and transmission interference.

Muon chambers need to operate about 250 kW and it will be provided by 3000 power supply units with different voltages and currents. A short summary of voltages and currents per sub-system are shown in table 1.2.

	Voltage	Max Current
HV - RPC	10 kV	0.2 mA
HV - CSC	5 kV	0.2 mA
HV - DT	4 kV	0.1 mA
LV-1	2.5 V	10 A
LV-2	3.5 V	42 A
LV-3	5.0 V	38 A
LV-4	6.5 V	56 A
LV-5	7 V	13.5 A

Table 1.2 Power requirements of Muon chambers.

1.6 Super-conducting Magnet Sub-system

The CMS magnet sub-system [19] consists on a super-conducting coil, the magnet yoke (barrel and end cap), a vacuum tank and ancillaries such as cryogenics, power supplies and process controls. The main parameters of this sub-system are: a magnetic field of 4 Tesla, a yoke diameter of 14m across flats, an axial yoke length including end caps of 21.6m and a total weight of about 11000 tons. It will be the largest super-conducting magnet system in the world. The energy stored into it, if liberated, will be large enough to melt 18 tons of gold. A general view of the magnet is depicted in figure 1.20a.

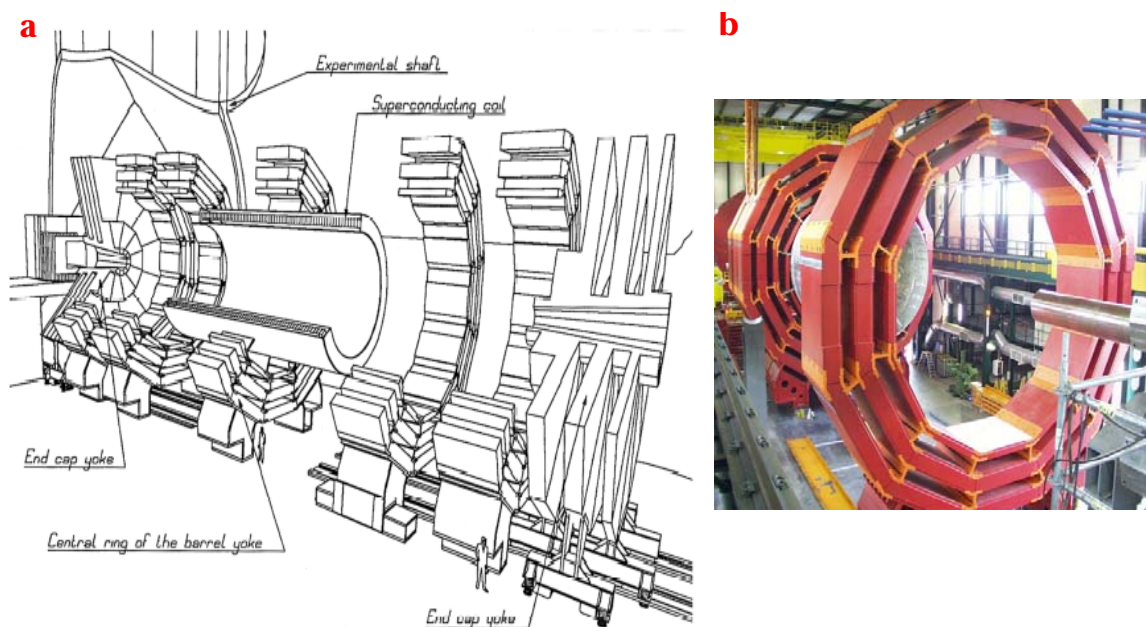


Figure 1.20: 4 Tesla CMS Magnet system.

The magnetic flux generated by the super-conducting coil is returned via a 1.5m thick saturated iron yoke (figure 1.20b). The yoke is divided into the barrel and the end cap yoke. The barrel yoke is a 12-sided cylindrical structure, divided into five rings. It is 13.2 m long, giving a total iron mass for the barrel of about 7000 tons. The central barrel ring, centered on the interaction point, supports the super-conducting coil. Each barrel ring is made up of three iron layers. Connecting brackets join together the steel plates forming the three layers and provide the required structural rigidity. The central barrel ring is the only stationary part around the interaction point and it is used to support the vacuum tank and the super-conducting coil. The other four-barrel rings and the end-cap disks slide on common floor rails, running in the beam direction, to allow insertion and maintenance of the muon stations.

1.6.1 Super-conducting coil

The super-conducting coil [20] consists of the coil itself and the ancillary sub-systems required for its operation and protection. The structure of the super-conducting coil is self-supporting, whereby magnetic forces are resisted where they are produced. The reinforced conductor of the four-layer CMS coil can sustain by itself all the induced magnetic forces.

Bellow some details of the magnet are shown.

Magnetic induction at interation point	4 Tesla
Magnetomotive force	42.20 MaT
Conductor peak magnetic field	4.6 T
Winding overall current density	$12.68 \frac{A}{mm^2}$
Stored energy	2.69 GJ
Magnetic radial pressure	6.4 Mpa
Axial compressive force at midplane	148 MN
Operating current	19.5 kA
Inductance	14.15 H
Total number of turns	2168
Turns per layer	542
Dump resistor	0.05 Ω
Dump voltage	1000 V
Dump time constant	283 s

Table 1.3 Magnet characteristics.

1.6.2 Power supply system of Super-conducting solenoid

A 2-quadrant thyristor power converter deliver a coil current of 20 kA at a maximum ramping voltage of 16 V. The current ramping time necessary to power up the magnet will be some hours.

The magnet can be discharged by different modes that vary from hours in normal operation up to around ten minutes during emergencies. In case of a main power failure, electrical power could be generated for helium recovery by using some of the stored magnetic energy.

1.7 HCAL sub-system

1.7.1 System generalities

The Hadronic Calorimeter (HCAL) [21] plays an essential role in the identification and measurement of quarks, gluons, and neutrinos by measuring the energy and direction of jets and of missing transverse energy flow in events. Missing energy forms a crucial signature of new particles, like the super-symmetric partners of quarks and gluons. For good missing energy resolution, a good calorimetry is required. The HCAL will also aid in the identification of electrons, photons and muons in conjunction with the tracker, electromagnetic calorimeter, and muon systems.

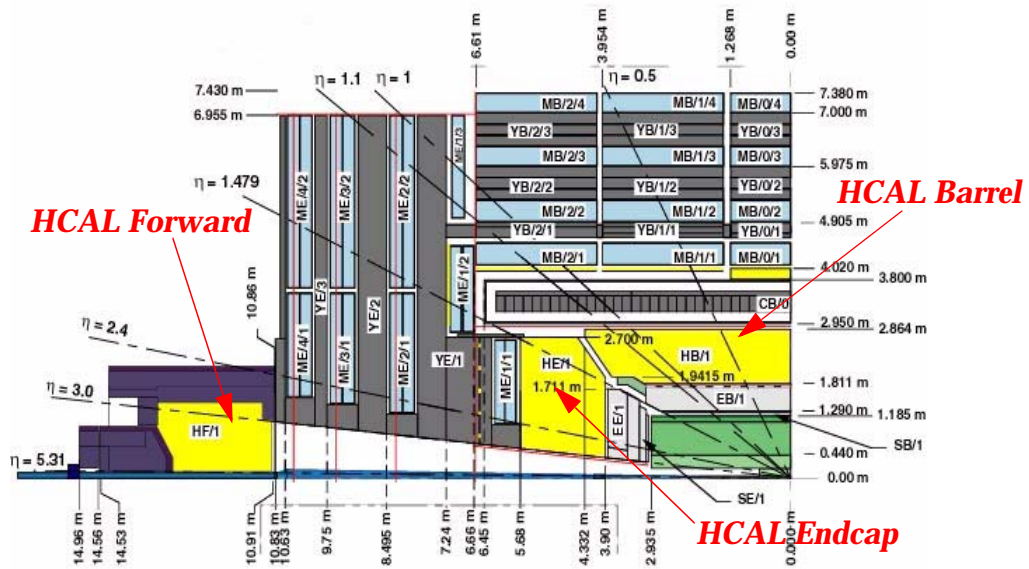


Figure 1.21: One-quarter view of the CMS detector showing the location of HCAL sub-system (in Yellow).

The hadron barrel (HB) and hadron end cap (HE) calorimeters are sampling calorimeters with 50-mm thick copper absorber plates interleaved with 4-mm thick scintillator sheets. Figure 1.21 depicts a view of the detector showing the location of the HCAL parts. Copper has been selected as the absorber material because of its

density. The HB is constructed of two half-barrels, each of 4.3 meter length. The HE consists of two large structures, situated at each end of the barrel detector and within the region of high magnetic field. Because the HCAL barrel inside the coil is not sufficiently thick to contain all the energy of high-energy showers, additional scintillation layers (HOB) are placed just outside the magnet coil. The full depth of the combined HB and HOB detectors is approximately 11-absorption length.

There are two hadronic forward (HF) calorimeters, one located at each end of the CMS detector, which complete the HCAL coverage. The HF detectors are situated in a harsh radiation field and cannot be constructed of conventional scintillator and wave-shifter materials. Instead, the HF is built of steel absorber plates; steel suffers less activation under irradiation than copper. Hadronic showers are sampled at various depths by radiation-resistant quartz fibers, of selected lengths, which are inserted into the absorber plates.

1.7.2 HCAL FEE

1.7.2.1 Introduction

The readout of the CMS hadron calorimeter is built through a chain of system elements beginning with photo-detectors coupled to the light produced in the calorimeter detection media and ending with memory storage of digitized results in an on-line processor farm. Electronics systems [22][23] are located in three different areas on the CMS experiment complex:

- In the control room at grade level 150 meters above the accelerator tunnels and caverns.
- In the shielded underground service room about 100 meters inward from the beam line (USC55).
- On or adjacent to the detector in the underground cavern centered on the beam line.

Signal processing functions required from the calorimeter readout electronics chain during colliding beam operations can be summarized as follows:

- Analogue signal conditioning of photo-detector responses
- Digitalization of conditioned analog signals at the beam-crossing rate of 40MHz.
- Transmission of digitized values from the detector to the control room using 1.6 Gbit optical links.
- Linearization and conversion of the front-end results into deposited energy values at 40MHz.
- Generation and transmission of filter-extracted first level trigger information at 40MHz.

- Pipeline storage of linearized energy values during the first level trigger decision interval at 40MHz.
- Buffering the linearized time samples at the average first-level trigger accept rate of 100 kHz
- Generation of the second level trigger information at 100 kHz.
- Formatting, organising and transferring of trigger and linearized time sample data to the event builder at 100 kHz.

All of the 40MHz signal processing operations at the very front end of the system are synchronous with the accelerator operations and are phase locked to the beam crossing. The higher levels of the readout system operate at an average "interesting event" rate of 100 kHz and are de-coupled from the synchronous, pipelined front ends by a set of de-randomising buffers. Other modes of operation of the readout system, e.g. data acquisition for the light flasher calibration system or determination of pedestal values are far less demanding.

1.7.2.2 System configuration

Partitioning of the readout chain is subject to several important global and space constraints, and is impacted strongly by considerations of maintainability. Access to the underground cavern is limited, regions along the sidewalls can be accessed on a twice a month basis. For the inner part of the detector access could be possible on a yearly basis with difficulty. The CMS first level trigger system can not be located on the surface because of the time delays introduced; it is located as close to the detector as possible in the adjacent underground service room. Sufficient radiation shielding is planned so that this area can be accessed during accelerator operation. The remainder of the data acquisition and trigger system is located on the surface due to the limited size of the shielded underground service room.

The HCAL sub-detector has electronics systems located on:

- The detector.
- The side walls of the collision cavern and the periphery of the detector.
- The underground service room or counting room.
- The surface.

Analogue signal conditioners and digitization electronics are located at the photo-detectors attached to the calorimeter elements; trigger and data acquisition electronics are located in the underground service room; and readout control, formatting, and interfaces to higher levels of the system are located on the surface. 1.6Gbit/s optical links connect the front-end electronics on the detector to the trigger and data acquisition systems in the counting room. Standard communication links bring the digitized data to the surface at the reduced rate corresponding to the first level trigger accepts. Low voltage power supplies are

located on the periphery of the detector and other utilities are placed along the sidewalls of the cavern. Figure 1.22 shows a block diagram of the front-end electronics and the data acquisition system. (Note: The optical link depicted in this figure is 800Mbits/s but recent tests have shown good transmission performance of the link operating at 1.6Gbit/s. This speed has picked for the final version and the number of TX circuits in the FE readout module will be reduced to two).

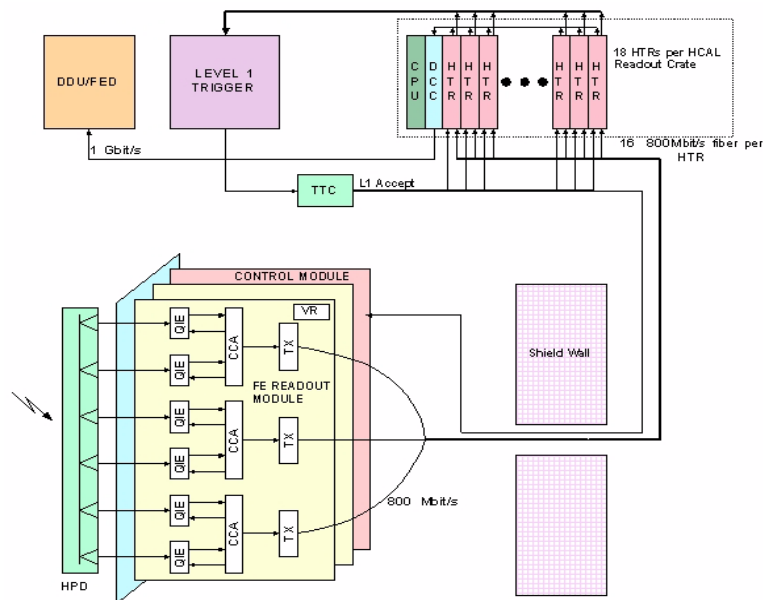


Figure 1.22: FEE and DAQ system layout.

1.7.2.3 Front-end electronics

The front-end electronics system comprises those components located on the detector in close proximity to the calorimeter photo-detectors. These components provide the functions of analog signal conditioning, digitization, synchronization/control and data transmission. Performance and reliability risks associated with placing the digitizer portion of the readout electronics directly on the calorimeter, where routine service is problematic, have been evaluated and incorporated into the requirements for reliability.

A functional block diagram of the system is shown in figure 1.23. Analogue signal conditioning is done using a multi-range current splitter and gated integrator, the QIE (Q for charge, I for integrator, and E for range encoding) ASIC [24]. The last version designed for CMS HCAL incorporates an input difference amplifier and a non-linear 5 bit flash ADC. The outputs of this ASIC are 2 bits of range information and a 5 bit signal corresponding to the FADC outputs. This result corresponds to a 7 bit pseudo floating-point format with 2 bits of range (or exponent) and 5 bits of charge (or mantissa). A separated digital ASIC, denominated CCA, is needed to

control and synchronise the QIE channels with the accelerator radio frequency time structure. Parallel digitized information is serialised using another especially designed ASIC, denominated GOL [25].

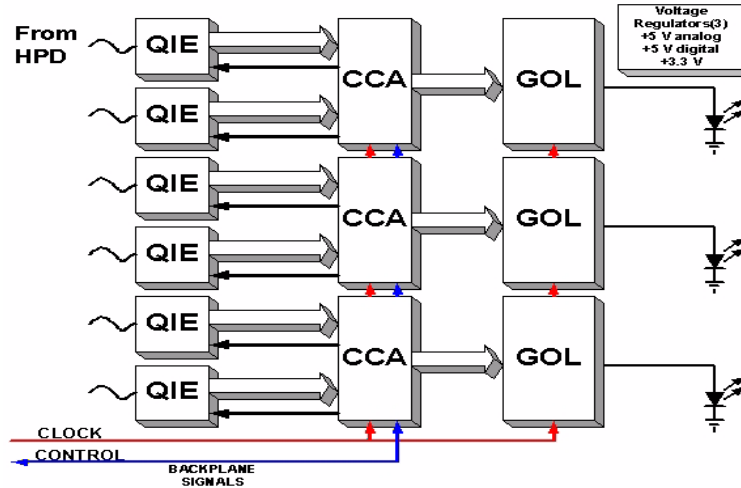


Figure 1.23: Block diagram of the front-end card.

1.7.2.4 Analogue signal conditioning

In the central region (Barrel/ End-Caps), the calorimeter detection elements are scintillators readout with wavelength shifting plastic fibres and the photo-detectors are hybrid photodiodes (HPD). The shape of the light pulse produced is an initial step followed by an exponential decay corresponding to the fluorescence characteristics of the combined scintillator-waveshifter system. This time constant, using a single exponential approximation, has been measured to be 11.3 ns. Thus the expectation is that 89.1% of the light signal occurs in the 25 ns, 9.9% occurs in the next 25ns interval, and 1.0% occurs in the third 25 ns interval on average. The signal is stretched further, when the 5 to 10 ns impulse response of the photo-detector. Differences in optical path lengths of the elements of a tower are taken into account and convolved with the light signal; 68% is in the first interval, 29% in the second, and 3% in the third on average. Finally, statistical fluctuations on these average values are significant, especially for the case of low levels where only tens of photoelectrons are involved.

Since the signals from at least two following beams crossing after the one of interest must be added to obtain the true value, the current produced by the photo-detector must be integrated and digitized over each 25ns interval separately. This is the case when there is pile up of signals from adjacent crossing as estimating the baseline shift requires charge integral results for several early crossing. Therefore, the central systems require a gated integrator that is reset every crossing, has a precise aperture

as close to 25 ns as practical, and suffers negligible charge loss at each 25 ns boundary.

In the forward region, the calorimeter detection elements are quartz fibres directly viewed, and the photo-detectors are photo-multiplier tubes (PMT). The signal produced is due to Cerenkov light from relativistic shower particles, so that it is very fast. Test beam results with small, fast phototubes indicate that the entire signal can easily be made to occur in less than 25 ns. Pile up of signal from adjacent crossing thus does not occur, and the pedestal (or the baseline) depends only on the amount of out-of-time background.

Given that the signal duration is smaller than the bunch-crossing interval, a gated integrator which is reset each crossing is also appropriated for the forward calorimeter. The requirement on aperture precision is modest, 10% is adequate, and the issue of charge loss at the 25ns boundaries is not relevant to the principal measurement.

1.7.2.5 Dynamic range

The main compartments of the barrel and end cap calorimeters, HB and HE, are required to respond reliably to minimum ionising particles in order to contribute to the muon trigger and for off-line identification of muons. This situation determines the details of the low end of the dynamic range. At the high end, studies have shown that the largest energy deposition expected in a central or endcap calorimeter main compartment over 10 years of operation at full luminosity is of the order of half the beam energy, or 3.5TeV. Actual jet energies could be higher, but the energy in a jet is spread over several towers spatially and is shared between the electromagnetic and hadronic depth segmentations. In terms of photoelectrons, these requirements correspond to a dynamic range of 1 to 35000 or 15 bits.

The outer compartments of the central and end cap calorimeters, HOB and HOE, are required to be sensitive to minimum ionizing particles. However, the highest energies seen are significantly lower than those in the main compartments due to the depth at which these layers are located. The physics dynamic range necessary is from minimum ionizing to a rate 1TeV occurrence. When the photoelectron yield and the low-end granularity considerations are taken into account, the requirement is for a 16000 to 1 dynamic range or 14 bits.

For the forward calorimeter, the single photoelectron signal is extremely important as it corresponds to more than a GeV of energy. Cerenkov light, even when directly viewed, is quit weak in intensity. Test beam studies show that the calibration for the main compartment is approximately 0.4 photoelectrons per GeV. Allowing the upper end to extend to the full beam energy gives a dynamic range of 1 to 3000 photoelectrons, or slightly less than 12 bits. Providing an extra factor of 4

granularity for single photoelectron performance then gives an overall dynamic range requirement between 13 and 14 bits.

1.7.3 FEE Components

1.7.3.1 Overview

The requirements for the front-end electronics detailed above call for a low noise, high frequency, wide dynamic range digitiser system. In particular the combination of 4500e⁻ rms noise, 1 fC least count (1fC/LSB¹), 40 MHz clock frequency, and 16 bits dynamic range is unique to the LHC conditions. The LHC case, impose additional special requirements on reliability tolerance, magnetic field immunity, cross-talk and capabilities for DC current measurements.

The front-end electronics design is based on an improved version of the analogue processing QIE ASIC development. As shown in figures 1.22 and 1.23, the building blocks of each FEE module are the analog + digitiser ASIC chip, a control ASIC and a serializer /diode driver. Due to the extreme space constraints present in the barrel and end cap regions, a modular 6 channels format has been selected as indicated in figure 1.23. Each component is described in the following subsection, putting more emphasis on the analog section of the QIE. 2 channels detail of the FEE board is depicted in figure 1.24.

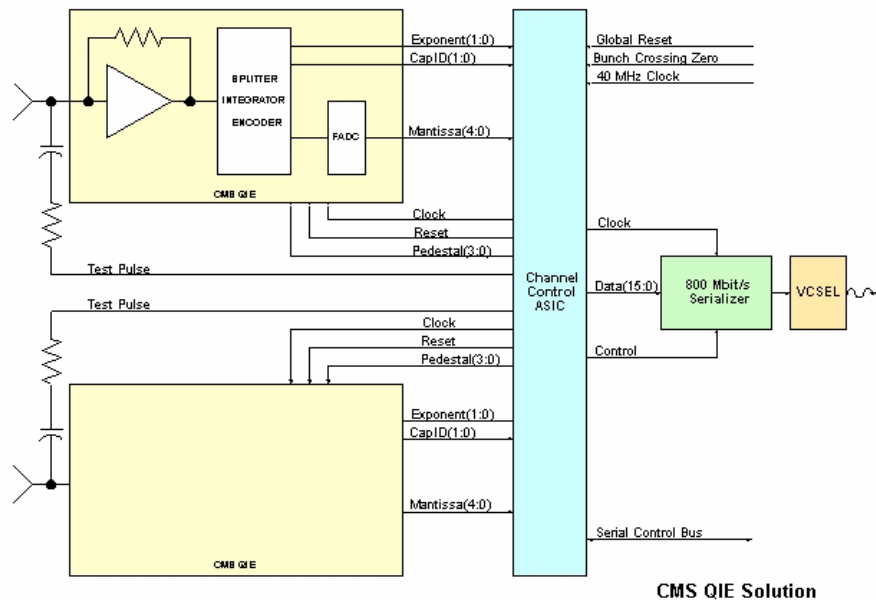


Figure 1.24: FEE channel block diagram.

1 LSB=Less significant bit

1.7.3.2 Analogue conditioning and digitising ASIC-QIE

The QIE is a multi-range device, the input current is simultaneously integrated on all the ranges, and comparators are used to select the lowest range that is not full scale. The outputs are voltages representing the integrated charge plus a two-bit gray code indicating the range. Operations are time multiplexed and pipelined to allow signals to settle and to make the reset interval the same as the integration interval. Latency is 100ns as the pipeline is four clock cycles deep.

The QIE contains multiple sets of eight capacitors of a uniform value. Attached to this structure is a current splitter. Matched transistors in common base configuration and connected in parallel will share the current driven through them equally. This property is exploited in the QIE design to apportion a fixed fraction of the input current to a given capacitor in the array. Each capacitor receives a fraction of the current of its lower range neighbor. For example, if the splitting were simply by powers of two, the capacitor of range n would receive $1/2^n$ of the input current.

The basic circuitry inside the QIE is repeated by four to allow the pipeline operations of a) integration, b) settling and holding, c) Analog to Digital conversion and d) resetting. This means when one set of capacitors integrates the input current for one beam crossing interval; others are holding a voltage proportional to the integrated charge in the previous clock cycle, other set is being read-out by the FADC while the fourth group is being reset. Due to chip has 4 sets of internal capacitors, they have to be calibrated to improve the exactitude of the charge measurement. These capacitors are calibrated before operation and their values are stored in a look-up table resident in the counting room. The QIE identifies the set of capacitors using during the integration by two bits called 'Cap ID' (Figure 1.24).

Summary of QIE requirements

- 40MHz operation.
- 4 stage pipelined device (25nsec per stage)
 - Charge collection
 - Settling
 - Readout (A to D conversion)
 - Reset
- Inverting and Non-inverting inputs. The inverting configuration is used at Barrel and End-caps FEE, where the photo-detectors are hybrid photo detectors (HPDs). The non-inverting configuration is used at very forward FEE, where the photo-detectors are photo-multipliers.
- The front-end amplifier has two inputs. Both currents are integrated and the result is subtracted before the digital conversion. Equivalent to a 'Differential amplifier'

- Impedance of both input terminals 50 ohms or 92 ohms.
- Internal non-linear Flash ADC
- FADC Differential Non-Linearity < .05 LSBs
- Outputs: 5 bits mantissa, 2 bits range exponent and 2 bits Cap ID
- 16 bits dynamic range
- Charge sensitivity: Barrel / End-cap version (HPD photo-detector) = 1 fC/LSB
- Calibration mode = 2000 electrons or 0.32 fC/LSB
- Very Forward Cal. version (Photo-multiplier) = 2.7 fC/LSB
- base thermal noise: 4500 electrons rms (Barrel / End-cap version).
- Systematic errors small enough to measure a few least count source current
- Charge loss at sample boundaries less than 2%
- Cross-talk less than 2%

1.7.3.3 Channel control ASCI (CCA)

The CCA provides the following functions:

- The processing and synchronization of data from two QIEs (Figure 1.24).
- The provision of phase-adjusted QIE clocking signals to run the QIE charge integrator and Flash ADC.
- Checking of the accuracy of the Capacitor IDs, the Cap Ids from different QIEs should be in synchronism.
- The ability to force the QIE to use a given range.
- The ability to set Pedestal DAC values.
- The ability to issue a test pulse trigger.
- The provision of event synchronization checks. A crossing counter will be implemented and checked for accuracy with every beam turn marker.
- The ability to send a know pattern to the serial optic link.
- The ability to 'reset' the QIE at a known and determined time.
- The ability to send and report on any detected errors at a known and determined time.

1.7.3.4 Data links

The CMS trigger system needs information about every crossing. The data will be sent 100-150 meters from the detector to the trigger system using either a 1.6 Gbit/s or a 800Kbit/s optical serial link. An ASIC serializer and laser driver, denominated GOL, is used to achieve the parallel to series conversion and transmission. This chip

has been designed at CERN and will be used for perform this function by different CMS sub-detectors and also other LHC experiments. The principal characteristics of this device are:

- Synchronous operation (constant latency)
- Transmission speed
 - Fast: 1.6 Gbps, 32 bit data input @ 40MHz.
 - Slow: 0.8 Gbps, 16 bit data input @ 40 MHz.
- Two encoding schemes
 - G- Link
 - Fibre channel (8B/10B)
- Interfaces for control and status registers
 - I2C
 - JTAG

1.7.3.5 Linear Rad-Tolerant Voltage Regulators

Each 6 channel board requires 3 power supplies, +5V, +3.3V and +2.5V. The two first voltages are regulated using specially designed Rad-tolerant low-drop voltage regulators. This design achieves an output/input differential mode filtering of more than 40dB at a frequency of 1MHz. The +2.5V bias is generated from the +3.3V bias line using discrete transistors and operational amplifiers.

1.7.4 Front-end Electronics Readout Boxes (RBX).

In the case of the barrel and end caps units, the front-end electronics is close to the HPD photo-detector and both are resident into readout boxes (RBX). For the very forward calorimeter, the electronics is resident into 3U crate separated about 4 m from the photo multiplier tubes.

1.7.4.1 Channel distribution per RBX

- Barrel Hadron (HB):
 - 18 + 18 RBXs installed in the detector.
 - 4 HPDs per box, 12 boards per box.
 - 72 channels per box, 3 boards per HPD.
- End Cap Hadron(HE):

- 18 + 18 RBXs installed in the detector.
- 4 HPDs per box, 12 boards per box.
- 72 channels per box, 3 boards per HPD.
- Outer Barrel/End Cap (HO) :
 - Wheel 0:
 - a. 12 RBXs installed in the detector.
 - b. 3 HPDs per box, 9 boards per box.
 - c. 54 channels per box, 3 boards per HPD.
 - Wheels +1/-1:
 - a. 6 + 6 RBXs installed in the detector.
 - b. 4 HPDs per box, 12 boards per box.
 - c. 72 channels per box, 3 boards per HPD.
 - Wheels +2/-2: 6 + 6 RBXs installed in the detector:
 - a. 4 HPDs per box, 12 boards per box.
 - b. 72 channels per box, 3 boards per HPD.
- Very Forward Calorimeter:
 - 1242 + 1242 channels.
 - Boxes hold up to 30 PMTs.

1.7.4.2 RBX layout

All the equipment installed into and around the detector must be thermally neutral. It forces to design a water-cooled system around the RBX to absorb the heat generated by the FEE. A specially designed aluminum frame with water-cooling pipes is used to hold the FEE boards, photo detectors and the auxiliary optical system.

RBXs hold 4 read-out units. Each unit contains 3 FE boards connected to the multi-anode HPD and an optical decoder (ODU) where fibres coming from the scintillators are coupled to the HPDs. This read-out unit is an 'optical processor' in the sense that light coming from the scintillators is electronically processed, digitised and optically transmitted to the counting room. Figure 1.25 shows an overview of the connection of the HPD with both the FEE board and the ODU. Each unit is powered through an internal back-plane that also distributes 40 MHz clock to

the units, provides a path for RBX bus (serial communication bus) and temperature monitors.

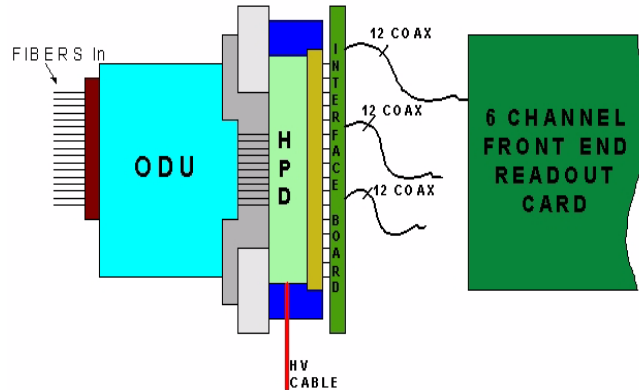


Figure 1.25: Overview of the read-out module.

For the very forward HCAL, the FE boards are housed into standard 3U crates and two coaxial cables per channel connect the QIE inputs to the photo-multipliers (PMTs). This distance is about 4 m. Power and clock is distributed to each FE board using a back-plane.

1.7.4.3 Power requirements per RBX

Each 6 channel board requires +6.5V and +4.5V as primary voltages [26]. As it was presented above, these voltages are adjusted at board level by linear regulators to +5V, +3.3V and +2.5V. The currents required by each board are 0.55A for the +6.5V supply and 0.77A for +4.5V supply.

Including some safety margin, the total design currents per RBX are the following:

	+ 6.5 V	+ 4.5 V
Barrel	6.77 A	14.6 A
End Caps	9.42 A	18.5 A
Outer Hadron	5.18 A	12.24 A
W+1	6.77 A	14.6 A
W+2	6.77 A	14.6 A

Table 1.4 Power consumption.

1.8 PS distribution system of CMS detector

1.8.1 Introduction

The DC low-voltage (LV) and the DC high voltage (HV) distribution system in CMS are based on a primary 400Hz AC distribution system [27]. Figure 1.26 shows the schematic of the power supply distribution of CMS detector. The 400Hz AC system is proposed as primary power source to distribute power to all CMS sub-detectors. It is composed by independent motor-generator sets for each sub-detector that converts the 50Hz AC mains to a 400Hz three-phase 400V system. The AC power system will distribute high voltage between the surface level and the counting room or the periphery of the detector.

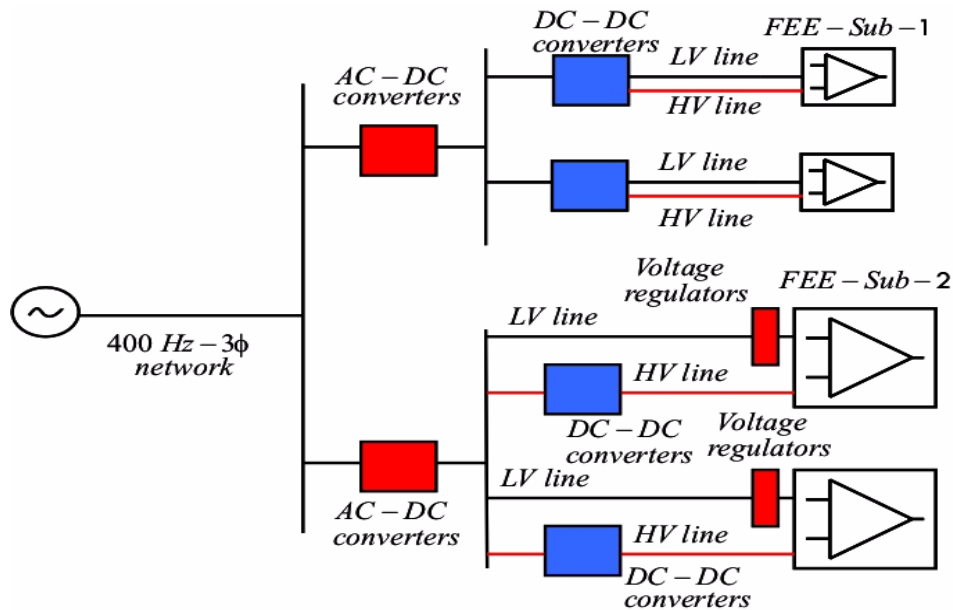


Figure 1.26: PS distribution block diagram of the CMS system

AC/DC converters located at both the periphery of the detector and the counting room rectify the three phase of the 400Hz system and generate a primary DC voltage of 48V for some sub-detectors and around 8V-15V for other sub-detectors. For some sub-systems using the extra DC low voltage, AC/DC converter are located in the periphery of the detector and the low voltage is distributed to the FEE units, where on board LV regulators set the final voltage required by the detector electronics. Other sub-systems needs the DC voltage (48 V) from the rectifiers to supply intermediate DC-DC converters. Each rectifier supplies several DC-DC converters located in the periphery of the detector or in the counting room. Switching regulators convert the 48V to appropriated low voltages that are locally

distributed to the detector read-outs. Locating the DC-DC converters in the hostile environment near the detector is a disadvantage due to the presence of magnetic field and radiation [28][29], so custom power supplies are required. Additionally, the AC/DC units located at the periphery of the detector have to operate under magnetic field and neutron radiation. The transformer has to operate under magnetic field and to avoid its saturation, it has to be over-designed. Special attention should be paid to evaluate the quality of the magnetic material, the magnitude of the external field that the transformer can tolerate without reaching the saturation region during operation and the impact in the system of the transformer's inrush current during start-up.

In general, the subsystems generate the DC High Voltage (HV) using as primary system either the 400Hz AC distribution or the 48-V DC. High Voltage power supplies are, in general, located in remote areas away from the detector due to high energy particle radiation can induce on these systems catastrophic failures. Long cables (80-120 meters) will distribute HV to the sensor devices at the front-end electronics.

Modularity of power supplies (high and low voltage) is the primary requirement. It will facilitate replacement of damaged units during short-period scheduled access to the cavern providing a reduction in the time that a part of the sub-detector is down. The LV cables between the converters and the FEE units are designed to avoid large voltage drop across them, which means the cross-section is over designed for such a current. These lines do not need current protection supplemental to that built-in into the switching power supplies. Under any plausible fault condition, the maximum current that the power supply delivers is lower than the rated current capability of the wires. The voltage drop estimated for those conductors is about 0.8/1V. Custom DC-DC converters are designed to operate under neutron radiation and magnetic fields. All the magnetic devices included in these units are over designed tolerate the external DC magnetic field. Electronic component, in particular switching power devices, are selected to operate reliably under the high-energy neutron radiation. Switching converters are noisier than linear power supplies. Specifications for ripple and EMC will be very tight because of the low noise required by front-end electronics.

As summary, the power distribution for the CMS detector has two distinctive regions: the 400Hz distribution and the DC distribution for the front-end electronics. The 400Hz distribution area is a conventional AC three-phase distribution. The appropriated design can be done following the standards and norms regulating this type of systems. The DC area is characterized by systems with extra low voltages-high current and high voltage (600V-10KV)-very low currents. Special attention must be put in its design regarding to grounding and safety.

1.9 Summary

The CMS calorimeter is a very exotic electro-technical environment. Millions of low-cost measurement channels process very low-level detector signals within a harsh environment (high magnetic field and particle radiation). CMS detector identifies particle interactions and measures their energy using sensitive detection devices such as silicon and pixel detectors, optical devices, wire chambers, etc. The electrical signal detected by the sensors is amplified and processed by the front-end electronics (FEE), which communicates, via optical link, with the acquisition system located 120 meters away from the detector.

The detector is organized in five different sub-systems that are located in different layers. Each of them has a different objective and different signal and power levels. Also, they are independently powered. These sub-systems are Tracker, ECAL, HCAL, Muon chambers and super conducting solenoid. The FEE is the most sensitive part of the detector. It is designed to detect and process signals in the range of a few fC and digitize them at a rate of 40 MHz. The FEE is characterized by a large dynamic range. In general, after digitizing the signal, the electronics read-out serializes it and via an optical link transmits all the information to the acquisition system.

The front-end electronics into the detector can be considered as an isolated system with only a galvanic connection to the exterior through the low voltage and high voltage power supply system. The CMS detector is primary powered by a 400 Hz distribution system. These network supplies 3-phase power to the counting room or to the periphery of the detector. At that location AC-DC converters transform the AC power to DC power required by on LV voltage regulators or intermediate PS units. These PS units supply the final voltage required by the FEE and detector to work. The CMS detector needs around 6500 power supplies units in order to work.

1.10 References

- [1] Evans, L.R, "*LHC status and plans*", Proc. IEEE Particle Accelerator Conference, 1997, Vol 1, pp 61 - 65, May 1997.
- [2] CMS collaboration, "*CMS technical proposal*", (CERN / LHCC 94-38 LHCC / P1, 1994).
- [3] ATLAS collaboration, "*ATLAS technical proposal*", (CERN / LHCC 94-43 LHCC / P2, 1994).
- [4] LHCb collaboration, "*LHCb technical proposal*", (CERN / LHCC 98 004 LHCC / P4, 1998).

- [5] ALICE collaboration, "*ALICE technical proposal*", (CERN / LHCC 95-71 LHCC / P3, 1995)
- [6] CMS collaboration, "*The Tracker project-Technical design report*", (CERN / LHCC 98-06, 1998)
- [7] Gigi Rolandi, "*LHCC Annual Review CMS Tracker*", Slides for Annual review meeting, October 2002.
- [8] M. Raymond, M. French, J. Fulcher, G. Hall, L. Jones, K. Kloukinas, L-K Lim, G. Marseguerra, P. Moreira, Q. Morrissey, A. Neviani, E. Noah, "*The APV25 0.25 μm CMOS readout chip for the CMS Tracker*", Proc. IEEE Nuclear Science Conference, Lyon, France, pp 9/113 - 9/118, October 2000.
- [9] J. Troska, G. Cervelli, F. Faccio, K. Gill, R. Grabit, A.M. Sandvik, F. Vasey, A. Zanet, "*Optical readout and control systems for the CMS Tracker*", Proc. IEEE Nuclear Science Symposium Conference Record 2002, Vol 1, pp 233 - 237, November 2002.
- [10] Giuliano Parrini, "*PS Tracker status*", Slides for CMS electronic week, May 2003
- [11] R. D'Alessandro, G. Parrini, "*General guidelines for the tracker power supply system*", Private communication.
- [12] R. Hammarstrom, "*Mutual wire inductance in MSC prototype*", Private communication.
- [13] CMS collaboration, "*The Electromagnetic Calorimeter project-Technical design report*", (CERN / LHCC 97-33, 1997).
- [14] F. Nessi-Tedaldi, "*The CMS ECAL project. Overview and status report*", IEEE Transactions on Nuclear Science, Vol 46, N- 3, pp 410 - 413, June 1999.
- [15] J. Nash, "*ECAL Electronics - System review and overview*", Slides for the ESR, October 2003.
- [16] P.Sharp, B. Iliev, I. Nanov, S. Stoenchev, S. Dhawan, B. Betev, W. Luster mann and M. Pestalozzi, "*CMS ECAL Low Voltage*", Proc. 9th Workshop on Electronics for LHC experiments, LECC 2003, Amsterdam, pp 353-357, October 2003.
- [17] Paul Aspell, "*Conception et mise au point de l'electronique frontale du detecteur de pied de gerbe de l'experience CMS*", Thesis, July 2001.
- [18] CMS collaboration, "*The Muon project-Technical design report*", (CERN / LHCC 97-32, 1997).
- [19] CMS collaboration, "*The Magnet project-Technical design report*", (CERN / LHCC 97-10, 1997).

- [20] A. Herve, "*The CMS detector magnet*", IEEE Transactions on Applied Superconductivity, Vol 10, N- 1, pp 389 - 394, March 2000.
- [21] CMS collaboration, "*The Hadron Calorimeter project-Technical design report*" (CERN / LHCC 97-33, 1997).
- [22] T. Shaw et. al., "*Front End Readout Electronics for the CMS Hadron Calorimeter*", Proc. IEEE Nuclear Science Conference 2002, Viginia, USA, Vol 1, pp 194-197, November 2002.
- [23] T. Shaw et. al., "*Electro-optical interfaces for CMS hadron calorimetry*", Proc. IEEE Nuclear Science Symposium 1998, Vol 1, pp 514 - 519, November 1998.
- [24] R.J. Yarema, G.W. Foster, J. Hoff, M. Sarraj, T. Zimmerman, "*A fast, wide range charge integrator and encoder ASIC for photomultiplier tubes*" Proc. IEEE Nuclear Science Symposium and Medical Imaging Conference 1992, Vol 1, pp 381-383 October 1992.
- [25] P. Moreira et. al., "*A radiation tolerant gigabit serializer for LHC data transmission*", Proc. 7th Workshop on Electronics for LHC experiments, LECC 2001, Stockholm, Sweden, pp 145-149, September 2001.
- [26] C. Rivetta et. al., "*Design considerations of low voltage DC power distribution for CMS sub-detectors*", Proc. 6th Workshop on Electronics for LHC experiments, LECC 2000, Cracow, Poland , pp 388-392, September 2000.
- [27] F. Arteché, C. Rivetta, F. Szoncsó, "*A common 400 Hz power supply distribution system for CMS Front-end electronics*", Proc. 8th Workshop on Electronics for LHC experiments, LECC 2002 , Colmar, France, pp 203-208 September 2002.
- [28] F.Faccio, "*Radiation effects in the electronics for CMS-Tutorial*", <http://cmsdoc.cern.ch/~faccio/tutorial.pdf>.
- [29] C. Rivetta, B. Allongue, G. Berger, F. Faccio, W. Hajdas, "*Single event burnout in DC-DC converters for the LHC experiments*", Proc. 6th European Conference on Single event burnout in DC-DC converters for the LHC experiments, pp 315-322 September 2001.

Chapter 2

Grounding & Shielding

Safety, system protection and performance are the three main reasons to earth a system. Not all electronic equipment needs to be connected to earth to work, satellites are an example. Sometimes wrong grounding configurations, oriented to satisfy the special power and performance requirements of electronic loading equipment, can compromise safety rules generating dangerous situations for personnel and equipment. Personnel safety, equipment safety and performance grounding issues have to be analyzed together. In any case, safety rules must not be violated. All these concepts as well as the relations between ground issues need to be clarified before passing on to a higher level in the control of the electromagnetic emissions of the system. Along the present chapter, concepts like safety grounding, signal or ground reference plane as well as grounding topologies to achieve electric safety and good performance of the system, are presented. The characteristics of shield structures, shielded power cables as well as their connections to ground are also presented. Finally in the last section, some recommendations to design the CMS detector grounding are included. The grounding design of the detector constitutes the first of several steps to be followed for the detector integration under a electromagnetic compatibility plan.

2.1 Grounding generalities

As described in [1] [2] and [3], proper grounding techniques are necessary for safety, equipment operation and performance. The integrity of both the facility grounding and the proper equipment operation depends on the proper bonding of the grounding electrode system, proper system grounding of service equipment and separately derived sources and proper equipment grounding for operational frequencies (DC or AC-mains) as well as higher frequencies. It is recommended that the grounding design and installation be compliant to all applicable codes and standards [4][5]. The grounding is not designed as an active component of the power supply (PS) distribution system, hence this path must be free of any operational current.

Metal parts of equipment enclosures, racks, raceways and equipment grounding conductors susceptible of being energized by electrical currents (due to circuit faults, electrostatic discharge, and lightning), must be effectively grounded for reasons of personnel safety, fire hazard reduction, equipment protection and equipment performance [6][7]. Grounding these metallic objects facilitates the operation of over-current protective devices during ground faults and permits return current from electromagnetic interference filters and surge protective devices, connecting line to ground or line to chassis, to flow in proper fashion. All metallic conduits and raceways in areas containing electronic load equipment have to be carefully bonded to form an electrically continuous conductor.

All mechanical equipment in the electronic equipment areas should be carefully bonded for an electrical safety and for noise current control. Such equipment should be grounded or bonded to local building steel using direct or higher frequency grounding and bonding means. When located in the same area as the electronic load equipment, mechanical equipment should be bonded at multiple points to the same ground references as the electronic load equipment. Heating, ventilation, air conditioning, process cooling equipment, related metal piping and electrical conduits are recommended to be bonded to the same ground reference serving the electronic load equipment.

Once the grounding complies with the safety rules, the ground connections have to be improved to obtain a good performance of the system. It is important to keep in mind that for operational reasons one should imagine that at low frequencies the ground system is a kind of low resistive divider in which all noise currents usually flows everywhere. However at high frequency the ground impedances start to increase mainly due to the inductive effect, flowing the noise only through the lowest impedance path. Therefore, the ground connections should be tackled in two steps. The first step is oriented to low frequency currents where it is important to avoid ground loops because once these currents are established they can flow everywhere, decreasing the performance of the system. The second step is focused on the noise at high frequency, where one could imagine that everything in the system is connected (through real or parasitic impedances) designing the ground path and connections in an specific way that gives a low impedance path to HF noise currents and thus avoiding the flow of these currents through sensitive parts of the system.

2.2 Grounding for fault and personnel protection.

2.2.1 System grounding or earthing

System grounding or earthing involves the ground connection of power services and separately derived systems. They include generator, transformers, uninterruptible power systems (UPS). The system earthing is the intentional connection of a circuit conductor (typically the neutral on a three phase, four wire system - Protective earth (PE)) to earth. The purpose of the system grounding [3] is for electrical safety of personnel and equipment as well as fire safety reasons. Safety is basically governed by the electrical codes and standards as adopted by government agencies and commercial entities. System grounding also impacts the performance of electronic load equipment for reasons related to the control of the common-mode noise and fault currents, however the personnel and the equipment protection is the primary task of the grounding as it is described in [8].

The grounding of power systems is, from a safety standpoint, oriented to limit the potential difference between grounded objects, to provide a good operation of over-current protective devices in case of ground fault, to stabilize the phase voltages with reference to ground and to limit transient voltages due to lightning and load switching.

There are two basic requirements for grounding power services and separately derived systems or sources (transformer, generators, UPSs, etc.). The first requirement is to bond the neutral or secondary grounded circuit conductor to the equipment grounding terminal or bus. For power services entrances, the incoming neutral conductor is connected to the equipment grounds bus in the switchboard by means of the main bonding jumper. For separately derived sources, the neutral must be bonded to the equipment grounding terminal or bus. The second requirement is that the equipment grounding terminal or bus must be connected to the nearest effective grounded electrode by means of the grounding electrode conductor. To illustrate the grounding connection of a separately derived source, figure 2.1 shows the grounding connection for an isolation transformer. If no effective grounded electrode or building steel is available, then the separately derived source should be connected to the service entrance grounding point via a grounding electrode conductor installed in the most direct and shortest path practicable. In the case that metal interior piping is present near the separately derived source, a supplemental grounding electrode conductor should also be installed from the equipment grounding terminal or bus of the separately derived source to the metal interior water piping.

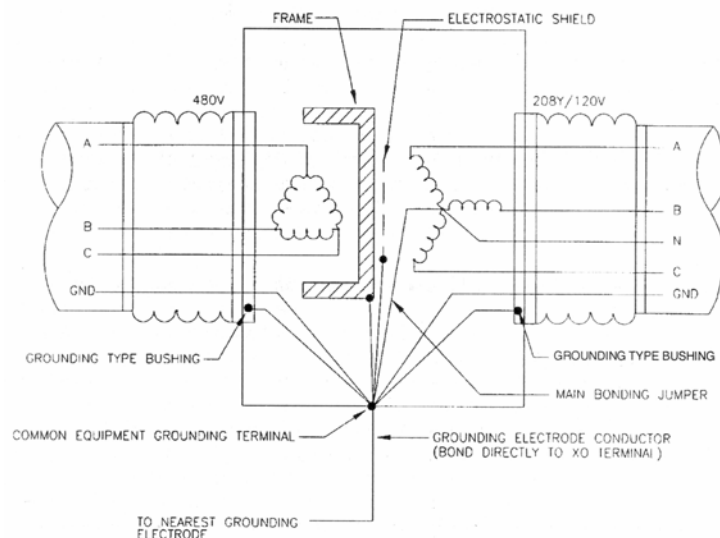


Figure 2.1: Isolation transformer grounding layout.

From a performance standpoint, solidly grounded power systems are recommended practice to ensure the existence of effective conductive paths for the return current of filters and surge protective devices connected line to ground or line to chassis. These filters and surge protective devices may be an integral part of the electronic load equipment or may be separately mounted devices located in the building electrical distribution system. It is recommended in the design to aim at the lowest reasonable impedance between the load equipment containing a filter or surge protective device and the associated power system source. Low-inductance wiring methods should also be used.

2.2.2 Equipment grounding

As described in [9][10][11] and [12], electrical or electronic circuits do not need to be earthed in order to work. Satellites, spacecraft and mobil phones, all work properly without earthing. The earthing or system grounding is a requirement necessary for safety. Electrical safety concerns all electrical design work. Safety requirements cannot be compromised to satisfy the special power and grounding requirements of electronic loading equipment. One should always try "*to make the system design safe and then try to make it work*". This ground philosophy is widely explained in [7], [13] and [14].

The term "equipment grounding" refers to the connection to power system ground of all non-current carrying metallic parts of a power system that may come into accidental contact with circuit phase and neutral conductors. These metallic parts include raceways, conduits, equipment grounding conductors, equipment

enclosure and racks. All these items are ultimately grounded together at the grounding electrode of the power service or a separately derived system. Equipment grounding is required for both personnel safety and power systems protection. From a personnel safety point of view, properly grounded system components minimize potential differences that may exist between various system components under transient and fault conditions. From a system protection standpoint, properly grounded system components provide a low impedance path for ground fault currents and promote the timely operation of over-current protective devices in case of ground faults.

There are two different grounding configurations associated with the connections of the equipment to the PE point; the standard ground configuration and the insulated ground configuration.

- For the standard equipment grounding configuration, a supplementary ground conductor provides an additional low impedance ground path in parallel with the metallic conduit or raceway from the equipment to the power system.
- For the isolated grounded configuration, the electronic or electrical load is not connected to the metallic enclosure and this metallic enclosure is earthed through an independent conductor to the start point of the safety ground. The insulated equipment grounding conductors run with the other circuit conductors feeding electronic load equipment. In an isolated ground configuration, the additional equipment grounding conductor provides the sole grounding path from the electronic or electrical load equipment to the power system or separated derived system.

In either case, the insulated equipment grounding conductor should run in the same raceway or conduit as the phase and neutral conductors. Grounding configurations provide equalization of potentials between grounded objects at the operative frequency. As the frequency increases, other grounding means must be considered to cover the high frequency range.

Robust design of the electronic load equipment for immunity to disturbances on the grounding circuit is a good method to get a good grounding [15]. Particularly for distributed computing and telecommunication electronic loads, using optical signaling interfaces reduces the sensitivity to disturbances on the ground circuit. As it is implemented in the CMS detector, the processed data from the detector is transmitted out of the detector via optical devices, and the slow control signals are isolated from the detector via opto couplers.

2.2.2.1 Standard equipment grounding

The standard equipment ground configuration [13][14][16] uses one equipment grounding conductor (PE or G), in green color, running with the phase and neutral

2.2. Grounding for fault and personnel protection.

receptacle (IGR) only to the equipment grounding terminal or bus of the power system source or separately derived system. This equipment grounding conductor extends radially downstream to the chassis of the electronic load equipment without contacting any grounded metal surfaces such as metal conduits and race ways, panel boards, and outlet boxes for receptacles. This configuration is shown in figure 2.3.

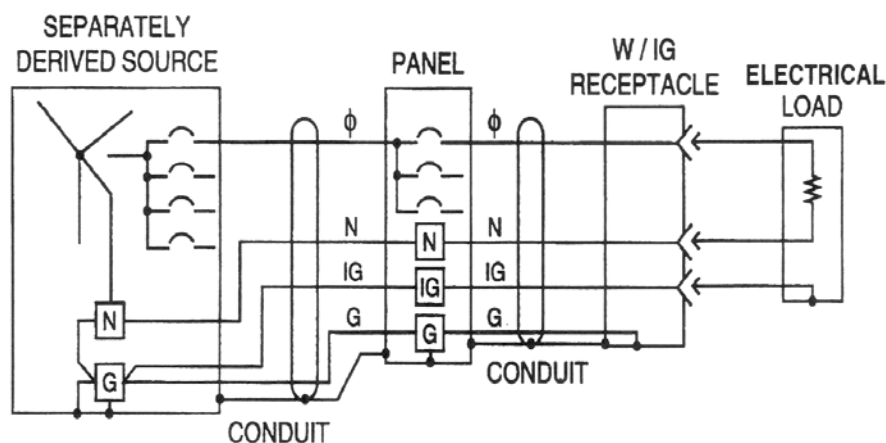


Figure 2.3: Isolated ground configuration.

The isolated equipment grounding conductors are sized according to the table of standards for equipment grounding conductors and are properly connected and bonded to the metal enclosure at load level as explained in the standard equipment grounding. This type of equipment grounding configuration is only intended to be used for reducing the common mode (CM) electrical noise on the electronic load equipment circuit as described in [13] and [17].

This type of configuration may produce better or worse noise conditions than when a standard equipment grounding configuration is used to serve electronic load equipment. Noise effects will be somewhat proportional to the overall length of the circuit [17]. Under power system fault conditions, the potential difference between the electronic load equipment and grounded objects may be sufficient to cause a safety hazard or to disrupt the electronic load equipment performance.

The isolated grounded configuration is only directly applicable to metal-enclosed wiring means and has no useful purpose with nonmetallic wiring systems. Non-metallic wiring systems are at least partially constructed as if they are isolated grounding types, since no metal conduit or raceway is involved in the wiring path or is bonded to the equipment grounding conductor of the circuit. In any case, the non-metallic wiring system does not provide electromagnetic shielding for the enclosed circuit conductors and should not be used.

The application of the isolated ground configuration may provide beneficial effects to circuits supplying electronic load equipment that do not otherwise connect to grounded objects. However, if the electronic equipment contains other connections to grounded objects as in the standard ground configuration, the performance of the isolated grounding configuration decreases. These connections to ground may be either intentional or unintentional. Typical examples of these connections are interconnections of various equipment through grounded shields of data cables and bonding of equipment chassis to grounded metal equipment racks.

2.3 High frequency grounding configuration

The grounding configurations described above provides the necessary connections to ensure the overall electrical safety of the system. When two or more components of an interconnected system are installed in an area where there is a physical space between them and across their separation data input/output cables and inter-unit power circuit cables (DC, AC or both) are routed, there exist indirect bounding problems ranging from DC to several tens of MHz or higher that can compromise the system performance. A reasonable grounding system has to be designed, without compromising electrical safety, by defining a ground reference structure over a broad range of frequencies. For separated equipment or units is necessary to place all of them on a single sheet of metal in the form of a signal reference plane and then to use direct grounding or bonding techniques to connect the entire perimeter of the base of the unit to signal reference structures (SRS). These reference structures can be built as reference planes (RP) or grid structures (GS). Linear brazing or welding around the perimeter of the unit's base is one method for grounding to the structures. However, such direct connections are not often practical, and the next best approach is to use multiple indirect bonding straps of minimized length to connect individually the plane to each unit locally.

The SRS is not intended to be dielectrically or galvanically insulated or isolated from the safety grounding conductor (PE) system that is part of the fault/personnel protection grounding system. The principal purposes of the SRS are:

- To enhance the reliability of signal transfer between interconnected items of equipment by reducing inter-unit common electrical noise over a broad band of frequency.
- To prevent damage to inter-unit signal circuits by providing a low-inductance, and hence, effective ground reference for all of the externally installed AC and DC power, telecommunications, or other signal level, line to ground/chassis connected equipment that may be used with the associated equipment.
- To prevent or minimize damage to inter-unit signal circuits and equipment power supplies when a power system ground fault event occurs.

2.3. High frequency grounding configuration

The need of an SRS is minimal when all of the inter unit signal and telecommunication circuits are interfaced to the associated electronic equipment via optically or isolations transformer coupled means. It is used in CMS detector, where these interfaces have good common mode voltage breakdown characteristics.

However, the need for an SRS may easily rise to that of a requirement in the event any of the following three conditions are given:

- When the logic AC-DC power supplies used in the associated electronic equipment are installed with one of the terminals connected to the equipment's metal frame/enclosure. This is typical and recommended practice in the equipment industries.
- When the signal-level circuits and logic AC-DC power supply common terminals are dielectrically insulated or galvanically isolated from the equipment ground against recommended practice, and are instead connected to an insulated ground terminal that is intended for connection to an externally installed signal ground reference circuit.
- When there are actual performance problems occurring with the equipment, which can be assigned to common mode electrical noise or similar common mode interference related to the equipment's existing grounding system, whatever its design, or the signal-level

Improved HF grounding for data signaling cables between (non-contiguous) areas can typically be accomplished by reducing the open loop area enclosed by the cable and its grounded surroundings. This is typically accomplished via the use of metal conduit or electrically continuous, solid-bottom, metal cable tray, wire-way, or similar forms of signal transport ground-plane constructions.

The main advantages of the SRS are:

- Low-impedance return path for RF noise currents
- Containment of EM (noise) fields between their source (cable, etc.,) and the plane
- Increased filtering effectiveness of contained EM fields
- Shielding of adjacent equipment

An SRS may be typically constructed using one the following methods (in decreasing order of effectiveness), which are well described in [16]:

- Solid covering of sheet metal (RP).
- Grid of cooper straps (GS).
- Grid of cooper and aluminium wire (GS)
- Rised flooring substructure (GS).

Hybrid forms of SRS employing mixtures of signal reference grid and signal reference planes for varied construction and improved overall performance are also

useful. They are used where the benefits of each type of SRS are needed for the collective support of a variety of interconnected electronic load equipment that is susceptible to CM noise current.

The use of RP may be recommended for some applications where the subject system operates at a higher frequency than the typical GS signal design cut-off frequency. Although the RP does not offer a zero impedance path across its surface, it does offer several orders of magnitude of improvement over any signal or ground of large-cross section wires that might be used for bonding between units. The general equation for determining the impedance between two points on a plane is:

$$Z_{gp} = (R_{DC} + j \cdot Z_{RF}) \cdot \left[1 + \tan \frac{2 \cdot \pi \cdot d}{\lambda} \right] \quad (2.1)$$

where R_{DC} is the DC resistance of the ground plane using the Ω/m^2 , Z_{RF} is the impedance of the ground plane in Ω/m^2 . and d the distance between two points.

Accordingly, the impedance between two points on a ground plane should be approximately equal to the ohms per square value of the material of which it is composed and of the length such that the distance d is short compared with wave length λ of the highest frequency of interest in the design. Finally, the ground plane must be at least as wide as d. Based on this concept, it may be seen that the impedance value between points across dimensions d is constant at DC level and gradually rises as the applied frequency of the current is risen. Finally, isotropic rise in impedance may be expected at the first resonant point encountering 0.25λ on the plane and at each succeeding odd-order multiples 0.5λ of the first resonant point generally approaching the expected impedance along the projection of Z_N . This is shown in figure 2.4. The most favorable area of operation for the ground plane is in the range where $1 < 1/20 \cdot \lambda$ at the highest frequency of concern.

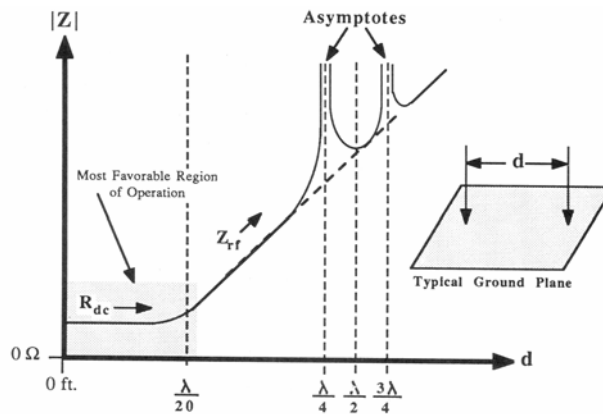


Figure 2.4: Frequency response of a ground plane.

Often the solid form of a ground plane cannot be obtained and a mesh or grid form must be a substitute for it. GS may be thought of as a plane in which holes, whose dimensions have been kept below a critical value, have been placed in a repeating pattern. In general only grounding grids using squared cells are recommended for use for HF currents. One of the most important issues related to grounding grids operating in the HF area, as opposed to DC and AC power frequency areas, is the need for minimizing the reactance in the path of the grounding grid instead of the resistance.

2.3.1 Multipoint and single point grounding connections

There exist different grounding configurations according to the connection of the different components or units to a signal reference system. Although they are well explained in [14] and [16], some details of the most important configurations, the single point and the multipoint connections are now presented. The determination to use single-point grounding or multipoint grounding typically depends on the frequency range of interest. Analog circuits with signal frequencies up to 300 kHz may be candidates for single-point grounding. Analogue/Digital circuits with signal frequencies in the MHz range should use multipoint grounding.

2.3.1.1 Single point

As it is shown in figure 2.5, the single point grounding is the easiest configuration of grounding. It is very useful in small systems. Nevertheless, if the real configuration of the single point grounding is analyzed (figure 2.6), it is the most undesirable ground system from the EMC point of view. Firstly, because of the big inductance that the ground path presents, the ground loops and the stray capacitance associated with the system. Secondly, because of the unreasonable large amount of wire necessary.

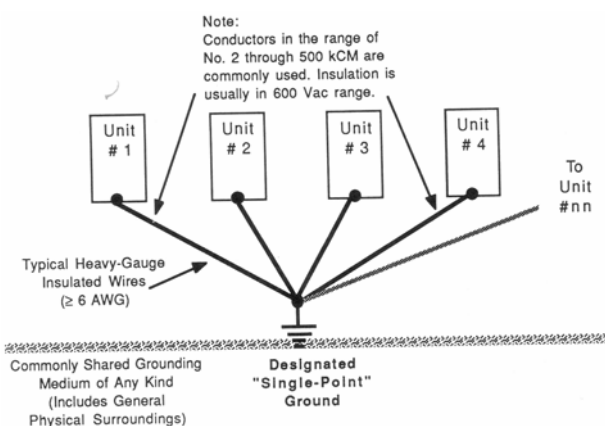


Figure 2.5: Single point grounding configuration.

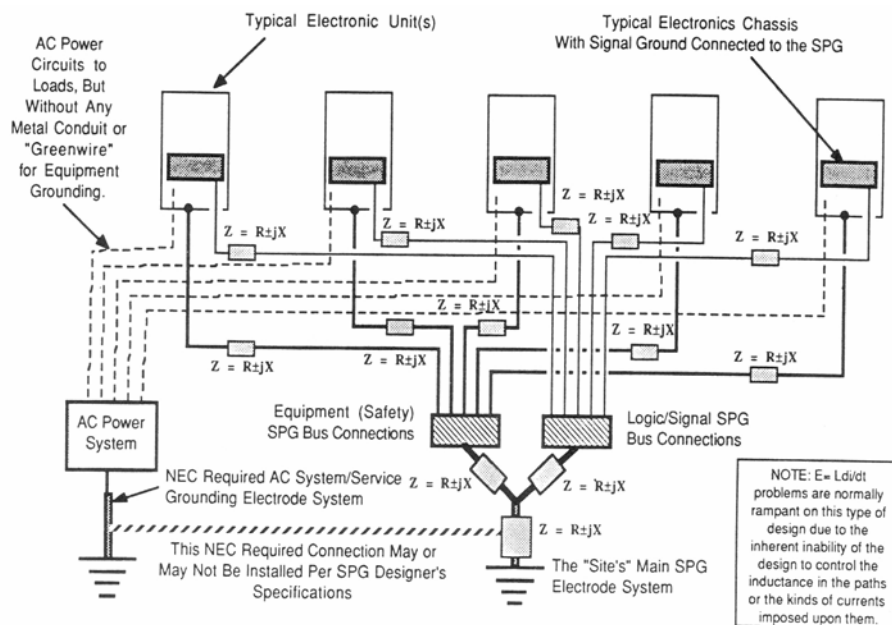


Figure 2.6: Real single point ground configuration.

Single point grounding cannot be easily implemented in SRS since these structures depend on a multiplicity of connections. Single-point grounding is usually implemented with a physical bus or bulkhead form of construction, where all conductors are connected prior to entering or leaving the signal reference grid area. A potential violation is to have a single-point ground area where one additional grounding connection occurs at a remote point within the electronic load equipment that is normally designed to be grounded only at one point. Such a connection may be intentional or unintentional. This configuration would provide a well defined and concentrated current path through the electronic load equipment, which could cause performance problems or component damage. More details about this kind of designs are shown in [19].

2.3.1.2 Multipoint

The recommended practice for signal reference systems (SRS) is multipoint grounding. Multipoint grounding requires that all metallic objects crossing or intersecting the signal reference system are effectively bonded to it. This type of grounding is shown in figure 2.7

2.3. High frequency grounding configuration

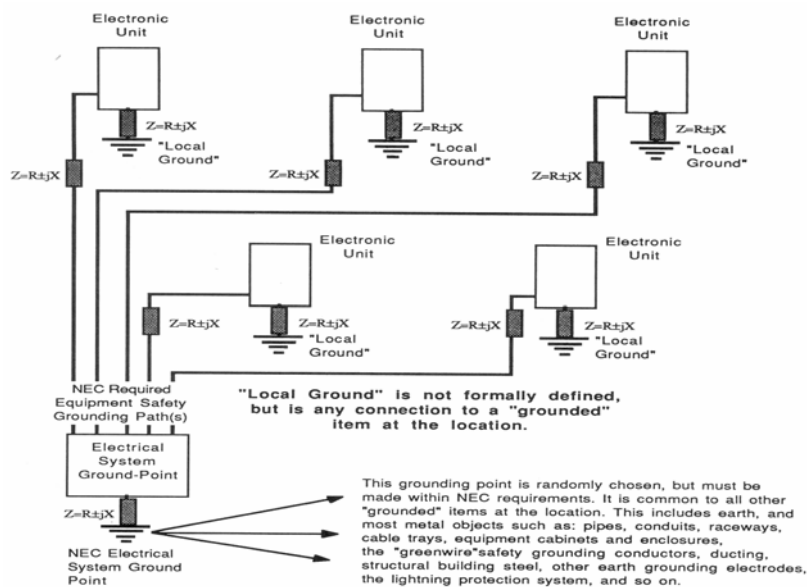


Figure 2.7: Multi point ground configuration.

Multipoint grounding to the SRS minimizes the possibility for all types of electrical currents flowing in the signal reference grid to be unwanted onto a few conductors of the signal reference system (this controls near-field conditions and potential difference as well). Based on this type of grounding, it is strongly recommended to separate at the origin the ground (reference or return) of analog signals, digital signals, power supplies and racks and afterwards connect them in a specific way that minimizes the differential of potential between different grounds. This is valid at system or board level. More details can be found in [16] and [18].

2.3.2 Bonding and straps

All equipment, especially electronic load equipment, should be connected to the signal reference system through a low-inductance path. The connections can be made at both the facility and equipment level by means of indirect bonds or direct bonds. The indirect bond is the connection in that a wire, strap or bus bar is used to interconnect the items or units together, whereas in the direct case, the bonding connection is made by direct connection using screws or solder joints. Indirect bonding is discussed in this section.

The purpose of bonding two items is to equalize potential between the items and to ensure that a minimum of potential can be developed between them over a broad frequency range, typically from DC to several tens of MHz and beyond. To achieve this goal, the design of bonding strap must be one providing low impedance across the desired frequency range for AC and very low resistance for DC. There is always

resistance in the metallic path and for high frequency currents the impedance increases due to skin effect and inductive effects.

Bonding path installed on the site and intended for use at or near the power main frequency, such as for ground fault currents, need not consider much more than the resistance of the material being used together with its heating and fusing characteristics. Thus simple wire resistance and capacity tables are normally adequate for the determination of the path's performance with regard to the sizing and minimizing of ground fault voltage drop across the bonding path. However for longer ground fault path lengths, wire impedance tables that account for the slightly increased impedance due to skin effect and reactance at the power fundamental frequency must be used. When unwanted AC signals are present in the grounding / bonding path, things are somewhat different. In these cases the need to minimize the potential developed across the bonding path under high frequency (HF) voltage and current conditions of all kinds is of major importance. This need entails the consideration of the path impedances and with the reactance of the bonding path being of greatest importance.

In general the total impedance of a bonding conductor is given by:

$$Z = R_{DC-AC} + j \cdot \omega \cdot L \quad (2.2)$$

The most important term of the above equation is the inductance L. The magnitude of the inductance L is calculated based on the concept of 'partial inductance'. The partial inductance assumes that a current flowing through a segment of unitary length defines a virtual loop, where the opposite segment is at infinity. Based on figure 2.8, the partial inductance $L_{p_{ij}}$ is the ratio of the magnetic flux penetrating the surface between segment i and the infinity and the current j that produces it.

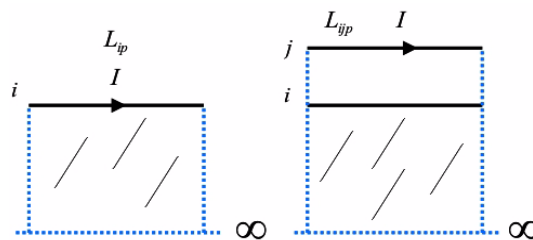


Figure 2.8: Partial self and mutual inductance loops.

This definition is used to represent the eventual loop interaction without the prior knowledge of the current loop. Based on this definition it is possible to calculate partial self and mutual inductance. The total or loop inductance is equivalent to the sum of the partial self-inductance and mutual inductances of the segments, as shows equation 2.3.

2.3. High frequency grounding configuration

$$L = \sum_{j=1}^N \pm L_{pij} \quad (2.3)$$

where the loop contains a total of N segments in which the loop has been divided. Each segment supports a current I_j , and the sign of each term corresponds to the relative orientation of the currents assigned to segments j . A detailed definition and analysis about partial and total inductance can be found in [12][20][21][22] and [23].

Based in the definition above mentioned, it is possible to calculate the partial inductance of a single round bounding.

$$L_{\mu H} = 0.002 \cdot l \cdot \left(\ln\left(\frac{4 \cdot l}{d}\right) - 0.75 \right) \quad (2.4)$$

where l is the length in centimeters and d is the diameter of the wire also in centimeters. Basically the value of this inductance depends on the length and the diameter of the bounding, increasing the diameter of round conductors has a limited effect on the HF impedance presented by the strap. On the other hand, if a rectangular bonding strap is considered as a flat-strap, the following equation applies:

$$L_{\mu H} = 0.002 \cdot l \cdot \left(\left(\ln\left(\frac{2 \cdot l}{b+c}\right) \right) + 0.5 + 0.2235 \cdot \frac{b+c}{l} \right) \quad (2.5)$$

where l is the length in centimeters, b is the width of the wire in centimeters and c is the thickness of the strap. The length to width ratio of a strap may be significantly altered to benefit a bonding path's performance, whereas altering the diameter of a round wire cannot produce useful improvements. Basically, it is much better to do the ground connections with flat-straps than with round conductors. It is also well known that the inductance increases by winding a conductor into a coil or similar form where the magnetic lines of force along the conductor may be concentrated causing an interaction among them. Thus, it must be expected that the best performance is achieved on a bonding path or with only a minimum and gentle bends in the winding conductor. Loops and sharp angles must be avoided unless an inductance is deliberately being created at the point of path discontinuity.

Bounding straps may self-resonate or may resonate with the stray or parasitic capacitance between the equipment and ground. The bonding strap exhibits high impedance near resonance and at resonance it looks much like an open circuit. Hence operation on this area must be avoided. The variation of the impedance with the frequency and the equivalent circuit of the strap are shown in figure 2.9.

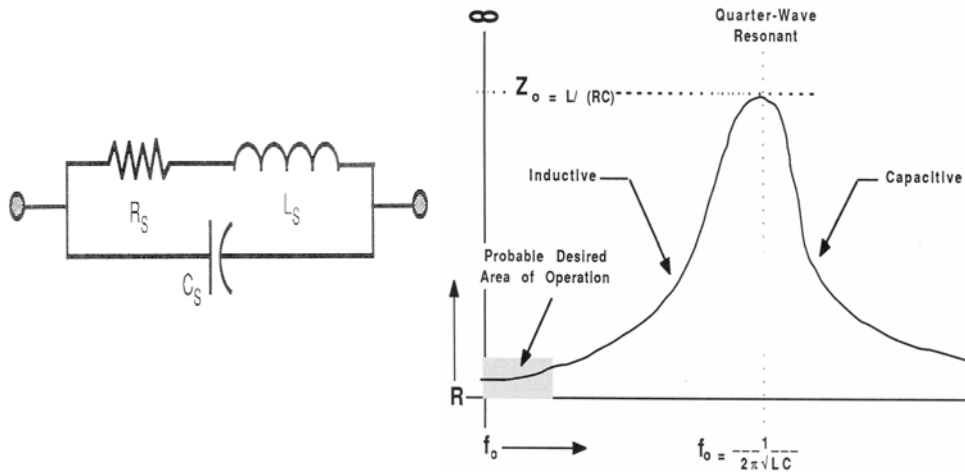


Figure 2.9: Strap's equivalent circuit and frequency response impedance.

Radiation to or from a bonding strap is not to be overlooked as a possible problem. However this is a problem only at and very near the actual point of parallel resonance in the strap. Typically any radiator, that is kept to $1 < 1/20 \cdot \lambda$, will not act as a good radiator or receptor. As expected this consideration can also pose major design limitations on the overall length of bonding straps or any conductor used as a ground connection.

Minimizing the impedance between the items being bonded is always important. The use of a single bonding strap between items may make this difficult to accomplish. If multiple, parallel straps are used, the impedance may be reduced between items according to:

$$L_T = \frac{1}{1/L_1 + 1/L_2 \dots + 1/L_n} \tag{2.6}$$

Resistance (AC and DC) and inductance are affected in much the same way.

However in the case of the inductance, unless the mutual inductance is also kept to a minimum between parallel straps, they will not act as independent inductances in parallel, the mutual inductance in that case must be considered also. Spacing must therefore be maintained between straps for at least the length of the longest strap employed if this problem wants to be avoided. A detailed analysis of this concept is shown in [16]. Grounding straps should be as short as possible to minimize inductive reactance in the path. The use of at least two bonds widely spaced apart on the same item of equipment is recommended to further reduce the reactance of the grounding path. These straps should be of different length such that they will have different self-resonant frequencies. The straps should never be folded or coiled, nor bent into curves. Even in equipment, lineups where the equipment is

bonded together, the recommended practice is to bond each enclosure to the signal reference grid with its own strap or two if it becomes easier. Flat foil strips, which are relatively wide in relation to the length, are the recommended practice. Connections to the equipment frame or a supplied grounding terminal are critical. Paint or other surface contact inhibitors should be removed before bonding straps are directly attached to metal enclosures or cabinet surfaces. Subsequently, the connections should be properly treated to inhibit rust, corrosion and moisture.

2.3.3 Signal reference structure for non-continuous area

The signal reference grid or signal reference plane is appropriate for a single two dimensional area and nearby contiguous areas, but is impractical and not as effective between widely separated areas or buildings, as it is the case of the CMS complex. Recommended practice is to augment the circuits with surge protective devices. Other methods (e.g. optical isolators or suitable wide band common mode current filters) can also provide increased noise and surge immunity for the interconnected telecommunication, data, and signal circuits.

2.4 Shielding

2.4.1 Introduction

The objective of electromagnetic, electric and magnetic shielding is to provide a significant reduction or elimination of incident fields that can affect sensitive circuits as well as to prevent the emission of components of the system from radiating outside the boundaries limited by the shield. The basic approach is to interpose between the field source and the circuit a barrier of conducting or magnetic material.

Shielding effectiveness can be defined as the reduction in magnetic, electric or electromagnetic field magnitude caused by the shield. The effectiveness of a shield depends on the shield material as well as the characteristics of the incident field (far or near field), which is defined by the distance between the source and the victim. So, it is found that techniques for shielding depend on the type of source; whether the source is a magnetic field, electric field or electromagnetic field source. The shielding effectiveness (S) in dB, can basically be calculated as the sum of three components, namely, reflection loss (R), absorption loss (A) and a correction factor (B) used in special cases to consider multiple reflections in the shield.

$$S = A + R + B \quad (2.7)$$

Each component has a different expression and value depending on whether the incident wave is magnetic, electric or electromagnetic field. Although analyzed in detail in [12][24][25][26] some issues are presented in this section. The presence of holes and joints can decrease the effectiveness of a shield and its analysis is well detailed in [12] and [25]. The present study does not provide further analysis on the subject though it should always be taken into account during the design phase. Other important point analyzed in this section is the shielding of cables. Special attention is paid to the connection of the shield at either one or two ends of a cable and the implications that these connections have in the performance of the system.

2.4.2 Electromagnetic field shielding

Although any radiated wave is an electromagnetic wave, the term electromagnetic wave is generally used to describe a far-field, plane wave, where the ratio between the electric field and the magnetic field is defined by the characteristic impedance of the free space ($Z_0=377 \Omega$). When an electromagnetic wave passes through a medium, two phenomena, known as absorption and reflection losses, are present. In the former, induced currents generate ohmic loss, heating the material, and producing an exponential attenuation of the amplitude in the direction of the wave propagation [24]. In the latter, when a field arrives at an interface between two media, part of the field can be reflected, introducing new losses. Basically the total loss is a combination of these two losses. The multiple reflection correction term is normally not considered for this type of waves as the reflection loss is high and the correction term is small.

Assuming the electromagnetic wave propagates perpendicular to the shield surface, the absorption and reflection losses (in dB) can be calculated as:

$$A = 131.4 \cdot t \cdot \sqrt{f \cdot \mu_r \cdot \sigma_r} \quad (2.8)$$

$$R = 168 - \left(10 \cdot \log \frac{\mu_r \cdot f}{\sigma_r} \right) \quad (2.9)$$

where t is the thickness of the shield in m., f the frequency, μ_r the relative permeability and σ_r the conductivity. This equation is in close relation to the skin depth of the material. The reflection losses decrease with the frequency, whereas the absorption losses increase due to the skin effect. Based on these equations, it is possible to state that the reflection loss is the primary contributor to the shielding effectiveness at low frequencies. However, at higher frequencies the absorption loss is the primary contributor to the shielding effectiveness at high frequencies.

2.4.3 Electric field shielding

In the near-field, the relation between magnetic field and electric field is not determined by its characteristic impedance in free space (377Ω). The basic mechanisms of shielding observed for far-field sources are valid for near-field sources, but the type of source is critical for determining the shielding methodology to apply. For sources dominated by high voltages the predominant near-field is characterized by an electrical field, whereas for sources with high currents the dominant near-field is a magnetic field.

Basically, electric shielding consists of conductive barriers, metal enclosures, metal conduits or cable coverings around circuits. The spatial electric shield acts as a capacitive voltage divider between the field source and the circuit. As it was defined before, for a field propagating perpendicular to the shield surface, the effectiveness of the shield against an electric field is defined by the absorption and reflection losses, in which the absorption term is unaffected by the source, being equal to the equation 2.8. However, the reflection loss factor depends on the source and in the case of an electric field can be approximated by:

$$R = 322 - \left(10 \cdot \log \frac{\sigma_r}{\mu_r \cdot f^3 \cdot r^2} \right) \quad (2.10)$$

where r is the distance between the source and the shield. When the distance is undetermined, the equation showed for the far-field reflection could be used instead, as electric near-field reflection losses are always lower than, or equal to, the far-field reflection losses, hence introducing a certain safety margin. Based on those equations, conclusions for fields with dominant electric component are very similar to those attained for electromagnetic fields. The reflection loss is predominant at low frequencies, while absorption loss is predominant at higher frequencies.

2.4.4 Magnetic field shielding

In the case the magnetic component of the near-field is dominant, and the wave propagates perpendicular to the shield surface, the absorption losses are the same as those for far-field, defined by equation 2.8. However, the reflection losses are different and can be approximated as:

$$R = 14.57 - \left(10 \cdot \log \frac{\sigma_r \cdot f \cdot r^2}{\mu_r} \right) \quad (2.11)$$

Based on this equation, the reflection loss decreases for decreasing frequencies, and is lower than the reflection loss for the plane wave reflection. So, reflection losses

are usually negligible for lower frequencies and absorption losses are small for low frequencies too. This fact forces the use of different shielding techniques against low frequency magnetic fields [27][28][29].

Basically, there exist two different ways for shielding against low frequency magnetic fields [12][24].

- Deviation of the magnetic flux with high permeability material.
- The shorted tuned method, which consists in the generation of opposing fluxes that cancel the magnetic field in the area of interest.

To deviate the magnetic flux, it is recommended the use of magnetic material instead of conductor material because it increases the absorption losses, hence improving the attenuation of the magnetic field (as it is the primary shielding mechanism at low frequency against magnetic fields). However, when a magnetic material is considered as material shield, two properties of this material, which introduce some limitations, have to be taken account:

- The permeability of a magnetic material decreases by increasing the frequency.
- The permeability of a magnetic material decreases by increasing the magnetic field strength.

The former depends only on the material, the latter depends on the material and the section of the magnetic circuit. For example mu-metal material has a permeability of over 10000 from DC up to 1 kHz, however at 20 kHz the permeability is not larger than cold-rolled steel. The working conditions of the shield is an important point as it has a serious impact in the selection of the shielding material.

As a summary a magnetic material such as steel or mu-metal makes a better magnetic field shield at low frequencies than does a good conductor such as aluminium or copper. However at high frequencies, good conductors provide better magnetic shielding. For non-magnetic material the shield effectiveness increases with the frequency, therefore, it is recommended to calculate the attenuation for the lowest frequency of interest. On the other hand, for magnetic materials the shield effectiveness may reduce due to the decrease of the permeability with the frequency.

2.4.5 Cable shielding

In the present section the main characteristics of a shielded cable as well as the implications of the shield connections in the performance of the system are presented. The main goal of a shield is to avoid perturbing fields to penetrate into the internal conductors or perturbing currents in the central conductors to radiate. The type of shield material and the shield connections have a direct influence in the performance of the shield.

2.4. Shielding

A shield is made of non magnetic materials, which as it has been shown in the previous section, has very bad properties to attenuate magnetic fields, and specially low frequency magnetic fields. A shield should never be considered as a good shield against magnetic fields unless a current is allowed to circulate through it, which can create an opposite field that tends to cancel the perturbing field. These currents can only circulate if both sides of the shield are connected.

When a shield is not connected to ground or is connected only in one side, the shield attenuates only the electric component of the incident field. In this configuration, the shield can be considered as a capacitive voltage divider as it is shown in figure 2.10. Connecting the shield to ground is required to define the capacitive voltage divider. The shield side closest to the electronic system should be grounded in this case.

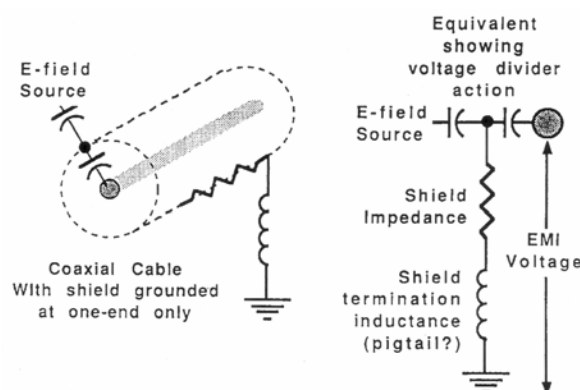


Figure 2.10: *Shield connection.*

This type of connection has been devised in order to prevent conductive "ground loops" from being established, which would cause unwanted current to flow in a shield grounded at more than one place, e.g at each end. This implementation only avoids ground loops when dealing with low frequency signals. At higher frequencies, the parasitic components capacitance between the cable's shield and the surrounding areas allows flowing currents through the shield. Additionally, the efficiency of the cable shield working as an antenna (receptor or transmitter) starts to play an important role in the emission, propagation and reception of the noise in the system. When a cable's shield is grounded at one end only the opposing end of the shield is under grounded and it can represent a fire and shock hazard if the cable's shield becomes energized. Reasons for being energized could be; AC power system ground faults, accidental contact of the shield at some point along its length with a conductor of another system or higher voltage, lightning, etc.

When EMI protection of the signal from near-field with strong magnetic field component is required, it is necessary to ground the cable's shield at both ends. It allows flowing a shield current induced by the near field magnetic component. This

shield current generates a magnetic field opposite to the perturbing magnetic field, attenuating its effect on the central conductors of the shielded cable. This effect does not have any adverse effects on the cable shield attenuation to electric field components.

The attenuation to electric field and magnetic fields is quantified in shielded cables by two characteristic parameters as the transfer admittance and the transfer impedance, respectively. The transfer impedance of a shield is defined as the ratio between the voltage per unit length generated by the circuit formed by the shield and the conductors inside the shield and the shield current. The transfer impedance gives the open-circuit voltage developed between the internal conductors and the shield for one ampere of shield current, in a cable of 1 meter long [25]. On the other hand, the transfer admittance of a shield is defined as the ratio between the current per unit length in the conductors inside the shield and the voltage between the shields and the external structure. The transfer admittance gives the short-circuit current induced in the internal conductors (when the internal conductors are shorted to shield) for one volt between the shield and the external structure, in a cable of 1 meter long [25]. Both the surface transfer impedance and the surface transfer admittance are characteristic parameters of shielded cables and are studied more in detail in chapter 4.

Cable shields grounded at both ends can carry unwanted shield currents due to potential difference between the two grounded ends of the shield. In general, these currents will be related to the power system's fundamental and harmonic frequencies. DC and low frequency currents in the shield, as described above, can be eliminated or significantly attenuated by placing a blocking device between the shield and its ground connection point at one end. For example, a series-connected, back-to-back arranged stack of rectifier diodes or capacitors can be used. When high frequency capacitors are used at one end of the shield, the capacitor blocks the low frequency currents but allows high frequency current to flow through the shield to increase the shield attenuation to magnetic fields at high frequency. Back-to-back diodes or surge diodes can be used when the connection between the shield and the ground point has to be established if the potential between these two structures is higher than the voltage drop of the semiconductor devices [14].

The cable's shield also offers a return path to common currents flowing through the central conductors. The return path is particularly important in shielded power cables to return the common mode currents generated at the output terminals of switching power supplies. If a regular cable without shield is used to connect these power supplies to the load, common mode current will establish between the conductors and the signal reference system (SRS), existing a large radiation loop for these currents. In order to be effective, shields must be grounded via low-impedance paths at the frequencies of interest. Long shields need to be grounded at multiple locations along their length [12][16][17]. To be effective, shields should be grounded using especial connectors that bonds the total

periphery of the shield to the chassis or frame where the shield has to be continued. 'Pig tail' connection of the shield to the chassis reduces the attenuation of the shield at high frequencies.

2.5 CMS grounding

In this section only some of the characteristics and rules for the CMS detector grounding are presented. The goal of the chapter is not to provide a receipt to define the detector grounding, but give some direct rules to orient the design. These rules are not fixed and depend on the personal knowledge of the designer and grounding philosophy chosen by the detector. This is one of the reasons why the grounding policy must be done by only one or two persons. Assigning this responsibility to one or more persons per sub-detector can lead to different grounding topologies, which may direct to catastrophic consequences during the integration of the detector. Three major rules have to be considered as basic for designing the system grounding and these are:

- Grounding is not required for correct operation of the system.
- No current returns should use reference/safety ground.
- Shielding should divert pick-up currents from FEE.

The detector integration based on the electromagnetic compatibility (EMC) of the different sub-systems has several stages and the grounding design is only one of them. The grounding design of the system constitutes only the first EMC issue in order to achieve electrical safety and good performance for the complete detector. The other issues, as sub-system emission and susceptibility, are oriented to control the interference among electronic units. It is an enormous error to think that a good grounding solves all the problems related to electromagnetic interferences.

Starting with the design of the grounding system to comply with the electrical safety, the CMS detector must follow the CERN electrical safety rules based on European standards. They can be achieved following these steps:

- Connection to ground of all exposed metallic structures and parts.
- Avoid current returns through the ground structure of the complete detector during normal operation.
- During faults, the ground path should be able to carry safely the fault current.

This current path not only has to have the ampacity necessary to carry the fault current but also this path has to present an impedance low enough to activate all the over-current protections properly included in the system to prevent fire during faults.

The main grounding structure of the detector is the own metallic structure of the detector together with the concrete reinforcement structure at ground level. This is the ground reference system of the detector (SRS). All safety and protective grounds have to be connected to these structures. Both are shown in figure 1.3 in green color.

At CMS detector we can distinguish two different areas, where the grounding design can follow different strategies. Those areas are the 'DC-area' around the detector itself and the '400Hz distribution area'. The first area includes very low voltage units, in the range of 2.5V to 10V with current capabilities up to 100A, and high voltage units ranging between 600V and 10KV with very tinny current capability. The '400Hz distribution area' is composed by the three phase 400V power distribution system with a possible installed apparent power of 500-750VA.

As it was described briefly in chapter 1, the '*DC-area*' is composed by all the front-end electronics (FEE) of the sub-detectors. They can be arranged in millions of channels where the sensitive detector is close integrated to the front-end amplifier and signal processor or can be composed by amplifiers that process tinny signals coming from chambers distributed in a vast area of the detector (muon system). In both cases, the metallic structures, boxes or frames containing the electronics and the detection devices have to be connected to the metallic structure of the detector or SRS. The general practice is to use the metallic frame or box as shield or screen for the sensitive electronics, forcing to connect internally the common point of the electronics to the box or frame. Then, when the FEE is considered as a load, each unit has one of the power terminals connected to the metallic box or frame, which is different to the scheme represented in figures 2.2 and 2.3. Additionally, due to the voltage levels and current capabilities associated to the equipment in this area, an independent conductor for PE is not included and each FEE is directly grounded to the SRS. This topology is similar to the multi-point grounding connection depicted in figure 2.7, but the PE o green cable is not included.

Power supplies (PS) for the FEE system, in general, are located outside of the detector, in the CMS case, they will be placed in two areas, one around 20-40 mts away from the FEE and the other about 100-120 m. To avoid the return current from the FEE uses as path the SRS structure of the detector, the outputs of the power supplies are generally floating respect to their frame or case. This frame or case has to be grounded locally to the SRS. This topology is possible in the case of low voltage distributions due to the extreme low voltage involved ($V < 45V$). For high voltage power supplies, the output terminals are not completely floating as the low voltage PS and usually resistors or back to back diodes are connected between the common terminal and the PS case. This topology assumes that all the power supplies include a transformer with screen that separates electrically the input terminals from the output terminal, which is in general observed for all practical applications.

Considering the system at the input terminals of the power supplies as individual loads, each one is now in close agreement with the diagram depicted in figures. 2.2 and 2.3. The AC or DC distribution system at this side is perfectly defined by standards [25] and no violations of safety rules are allowed. In the '400Hz distribution area', the PEs run in parallel with the power cables and they are connected together at the secondary star of power distribution transformer. This is shown in figure 2.11, where the proposed grounding topology of the HCAL sub-detector along the power supply is shown.

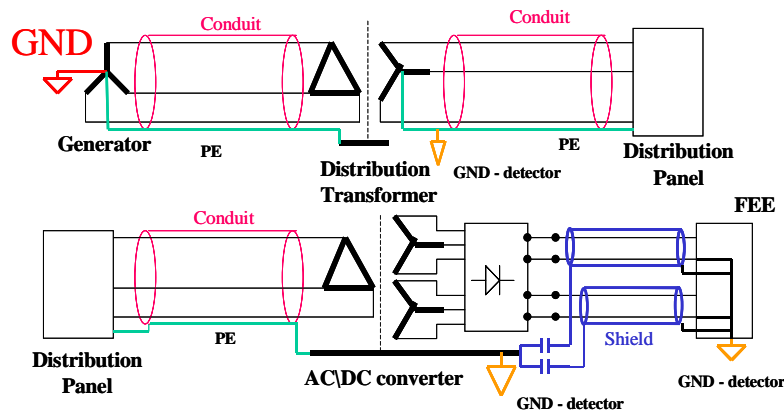


Figure 2.11: HCAL grounding scheme.

The isolation transformer included in the distribution isolates in common mode, the different parts of the system at low frequencies, while this isolation is degraded at high frequency due to the parasitic components of the transformer. The use of this transformer is still not clear, as the system will be isolated from the AC mains (the system will use a set of motor-generator to power the detector or static converters with transformers). The final selection will depend on the definition of the final configuration for the 400 Hz distribution system. The transformer in the AC-DC converter is included to reduce the voltage (400V) distribution to extra low voltage (48V or 10V). These transformers must be able to work into a magnetic field and also isolate the AC-LV area from the DC-extra low voltage area. These transformers should include electrostatic screen, which will improve the rejection of low frequency common mode currents coming from the AC line. The transformer metallic structures and the screen have to be connected to ground.

That overview of the grounding system for CMS basically covers the first two points described above about electric safety. The current capability of all the fault current paths for the '400Hz distribution area' is well described in standards [14][30]. When the design is extended to the 'DC part', special care must be observed in the analysis of the fault path, particularly, its current capability and impedance. When one of the input terminals on the FEE is energized during a fault, the current will flow back to the source using the SRS path. This path is established

through the connection between the FEE and the metallic case holding it. This point is critical due to the front-end electronics in general uses the frame or case as screening. From safety point of view, this connection is better at the input power terminal to avoid that the fault current uses as path the FEE where the fault current capability is probably not enough. From performance point of view, it is convenient to connect the FEE to the screen as close as possible to the sensitive amplifier or detector to reduce the parasitic currents coupled to the amplifier. A trade-off between performance and safety occurs in the selection of the connection point between the FEE and the metallic case, prevailing the design based on electrical safety.

The brief description of grounding design based on electrical safety considers a low frequency range, covering from DC to a few KHz. Grounding can affect the performance of the equipment installed and it is necessary to evaluate its impact considering the high frequency behavior of the system. As it was described in chapter 1, data signals from the FEE installed into the detector are transmitted to the counting room via optical links. Slow control signals are electrically isolated via opto couplers. The signal transmission via optical links simplifies considerably the grounding configuration and allows focusing the grounding issues of the detector to the power distribution system. This configuration allows considering the only mechanism of interference among FEE units installed into the detector is conduction and radiation through the power cables.

The electronic load equipment installed on the detector is multipoint grounded to the signal reference structure. Basically, reference terminal or common points of the digital and analog electronics are connected at a convenient point at the board level to optimize performance. Electronics, hardware and power parts are grounded separately at module level and then connected together at a single point, which represents the main ground per sub-detector. As it was pointed before these connection is a trade-off between safety and performance.

The noise generated by the PS units can be galvanically coupled to the FEE. This noise is more severe in switched mode power supplies due the high frequency switching of semiconductor devices. This noise has to be filtered by EMI filters included at the input and output of the power supplies. Additionally, EMI filters can be included at the input terminals of the FEE. Although, CM currents can flow through the power cables, the return path for these currents will be the SRS if no shield is used in the cable, increasing the capability of the cables to radiate. Shields reduce the radiation area for these currents and reduce the noise current flowing through the ground of the detector.

The shield of power cables are connected to one end at low frequency (FEE side) and to both ends at high frequency. This can be achieved grounding the shield to the PS side through a capacitor. Cable's shields connected at both side at high frequency adds screening to the conductor from external electromagnetic fields, avoiding the

induced current to flow through the sensitive parts of the front-end electronics. All auxiliary equipment as cooling system, etc. should be bonded to the signal reference system. The equipment should be isolated from the FEE to avoid antenna behavior.

Each piece of electronic equipment has to be connected to the SRS. The bonding connections should be as short as possible with no sharp folds or bends. Flexible and multiple straps are preferred instead of round conductors. The main goal of these connections is to decrease as much as possible the ground connection impedance as well as to increase the resonant frequency of the strap. As a result, the performance of the FEE is not affected. As example of strap effects, the ground connection between the read-out box (RBX) to a reference copper plane has been studied. The HCAL-RBX is connected during the FEE immunity test via a strap as it is shown in figure 2.12 and the inductance measured. Results are shown in table 2.1

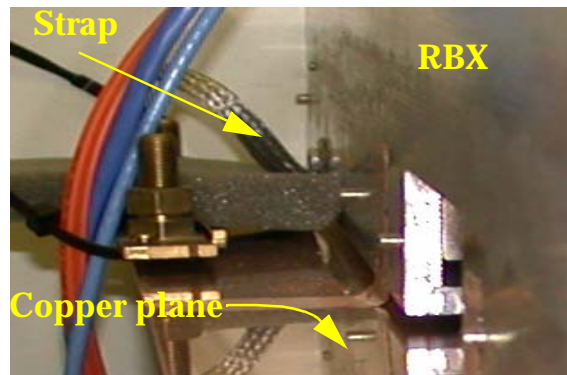


Figure 2.12: RBX - SRS (copper plane) single strap connection

	$mA - Strap$	$mV - Strap$	L
At 5 MHz	3.384	22.4	0.209 μH
At 5 MHz	1.298	8.40	0.205 μH
At 10 MHz	0.987	12.2	0.165 μH
At 10 MHz	1.196	13.90	0.187 μH
Average			0.191 μH

Table 2.1 Strap's inductance of RBX prototype.

The ground connection presents two resonant frequencies at 18.5 MHz and at 21.7 MHz, associated with the strap inductance and the parasitic capacitance between the RBX to copper plane. Based on equation of figure 2.9 values for stray

capacitances associated to the strap and to the RBX are estimated. These values correspond to 380 pF and 275 pF. The problem associated to the strap resonance frequency may be easily solved by decreasing the length of the straps and adding more connections to send the resonance frequency beyond the frequency of interest of the FEE. Also these straps or ground connections should be connected to opposing corners of the equipment and to the nearest, but separate points, on the signal reference grids. This is shown in figure 2.13.

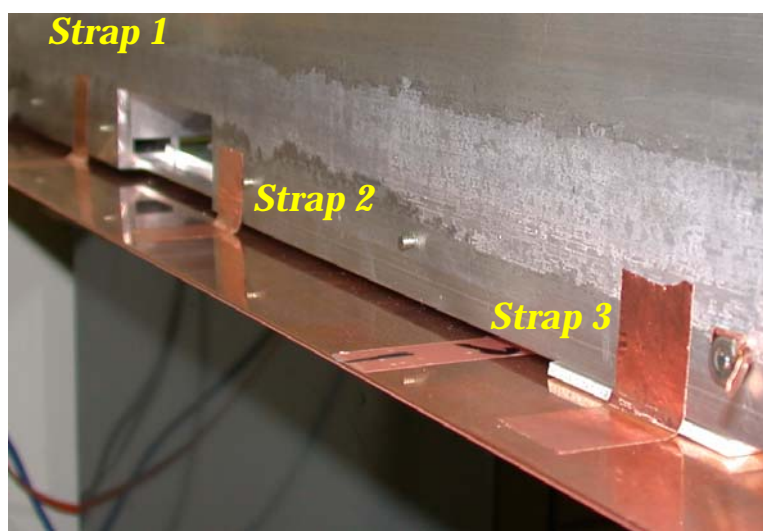


Figure 2.13: RBX - SRS (copper plane) multiple strap connection.

2.6 Summary

Grounding is necessary for safety, protection and performance reasons. It is based on standards and no violation of safety rules can be done to improve the performance of the electronics. The metal parts of equipment, enclosures and racks, which are susceptible to be energized by electrical currents must be grounded for personnel safety reasons and equipment protection. No operational currents must flow in this ground (structures and cable). The ground conductor or protective earth must run in parallel with the phase and neutral conductors.

There are mainly two different ways of grounding the electronic equipment, they are: the isolated ground and the standard ground. The main difference between both grounding configurations is that in the isolated ground configuration, the metallic parts holding the load are grounded independently from the rest of the metallic parts of the system, whereas in the standard ground, the metallic box holding the load is directly connected to the general structure of the ground system. The standard ground configuration only needs a simple cable as ground conductor, which is called protected earth. However, the other configuration needs one

additional cable, which must fulfill with the typical requirements of the ground conductors, and is used to ground independently some areas of the system.

In cases when two or more components of an interconnected system are installed in an area where there is a physical space between them and across their separation data input/output cables and inter-unit power circuit cables (DC, AC or both) are routed, there are indirect bounding problems ranging from DC to several tens of MHz or higher that can compromise the system performance. To make compatible the grounding with the system performance, electronic components are locally grounded to ground planes or grids known as signal reference surfaces. The main advantage of these structures is to provide a low impedance path for the RF noise current and to contain electromagnetic fields between their source and the plane. The connection layout to the equipment to the reference structures can be made in different ways but the two most important ones are: the single point ground connection and multi-point ground connection. The former use only one point where the components of the system can be grounded. For large systems, this connection is not recommended due to the large amount of cables needed, the large magnitude of the impedances associated with the ground connection and the poor CM rejection due to the parasitic components associated with the system. In the multi-point ground connection each component is grounded at two points; one at load level and other at the safety ground point. This configuration allows a much better control of the noise of the system. Attention should be paid to the generation of low frequency ground loops, which could deteriorate the system performance. The connection of the components of the system to the ground is made by straps. These straps must be as short as possible to minimize inductive reactance of the path. The use of at least two bond straps widely separated on the same equipment is suggested to reduce the reactance of grounding path. These straps should have different lengths.

Shielding of different components of the detectors is necessary to attenuate the electromagnetic, electric or magnetic field that can couple into the system causing performance deterioration or malfunction. The nature of the incident field as well as the frequency of interest is of primary importance to select the shielding method. As an example, magnetic materials are used to attenuate magnetic fields, whereas conductor materials are recommended to attenuate electric and electromagnetic fields.

The selection of shielded cables as well as the connection of the shield to the equipment is very important. The cables's shields are made of conducting materials, so they only can be used to attenuate electric or electromagnetic fields. The attenuation of magnetic fields only can be performed if a current flows through the shield, implying the connection of the shield to ground at both ends.

CMS detector can be separated in two different parts, the AC-400 Hz distribution area and the DC distribution area. For grounding purposes, the former is a standard

ground system used in power distribution in which the 'protective earth' wire runs in parallel with the system. The DC distribution area is characterized by equipment powered by extra low voltage/high current and high voltage/very low current. The ground system is a sub-class of the standard configuration where there is not a 'protective earth' wire running in parallel with the power distribution cables. The detector structure is used as signal reference surface and the front-end equipment is locally grounded to this structure using straps. In this area it is necessary to take special care about the grounding because it is not standard topology. Ground connections have to be established to provide, in this order, personnel safety, equipment safety (prevent fire hazard) and optimal system performance

2.7 References

[1] F. Szonsco, "*Earthing of High Energy Physics Detector systems*", CERN internal document - Pre-print, 2002.

[2] F.Szonsco, "*Assessment of EMC Parameters of LHC Front End Electronics*", Proc. 5th Workshop on Electronics for LHC experiments, LEB 1999, Snowmass, Colorado, USA, pp 20-24, September 1999.

[3] P. Van der Laan, M. Van Houten, A. Van Deursen, "*A grounding philosophy*", Proc. IEEE Symposium on Electromagnetic compatibility, CD-ROM Symposia Records 1955-1995.

[4] "*European Standards*", 93/68/CEE - (73/23/CEE), Ed. 1993

[5] "*CERN code C1-Electrical Code*", Ed. 1990

[6] William T. Rhoades, "*Congruence of low voltage power main transient designs*", Proc. IEEE National Symposium on Electromagnetic compatibility, Denver, USA, pp 285-293, May 1989

[7] Edward C. Cantwell, "*Effective grounding- The key to personnel and proper equipment operation*", Proc. IEEE Symposium on Electromagnetic compatibility, pp 194-199, 1980.

[8] A. Chouvelon, W Weingarten, "*Grounding as seen by TIS*", TIS-GS/TM/98-01, CERN-1998.

[9] Stanley A. Erickson, "*Spacecraft electromagnetic environment prediction*", Proc. IEEE Symposium on Electromagnetic compatibility, pp 106-115, 1978.

[10] Jasper J. Goedbloed, "*Electromagnetic compatibility*", ISBN-0-13-249293-8, 1990

[11] Tim Williams, "*EMC for product designers, Paraninfo*", ISBN-0-12-55710-0, 1997.

- [12] Clayton R. Paul, *"Introduction to Electromagnetic Compatibility"*, NY, Wiley Interscience, ISBN-0-471-54927-4, 1992.
- [13] *"IEC 61000-5-2 Electromagnetic compatibility -Part 5: Installation and mitigation guidelines - Section 2: Earthing and cabling"*, Ed. 1997.
- [14] *"IEEE-Std 1100- Recommended designs/installations practices - Chapter 8"*, Ed. 1999
- [15] Jhon D. M. Osburn, Donald R. J. White, *"Grounding a recommendation for the future"*, Proc. IEEE Symposium on Electromagnetic compatibility, pp 158-159, 1987.
- [16] Reinaldo Perez, *"Handbook of Electromagnetic Compatibility"*, Academic press, ISBN-0-12-55710-0, 1995.
- [17] Warren H. Lewis, *"The use and abuse of insulated / isolated grounding"*, IEEE Transactions on industry applications, Vol 25, N-26, pp 1093-1101, Nov./Dec. 1989.
- [18] Henry M. Hoffart, *"Single point grounding and multiple reference grounding"*, Proc. IEEE Symposium on Electromagnetic compatibility, CD-ROM Symposia Records 1955-1995.
- [19] G.M. Kunkel, *"Practical and theoretical aspects of single point grounding"*, Proc. IEEE Symposium on Electromagnetic compatibility, 1987-CD ROM Symposia Records 1955-1995.
- [20] T. Hubing, T. Van Doren and J. Drewniak, *"Identifying and quantifying printed circuit inductance"*, Proc. IEEE Symposium on Electromagnetic compatibility, pp 205-208, 1994.
- [21] X-D Cai, G.I. Costache, *"Numerical extraction of partial inductance of package reference (power/ground) plane"*, Proc. IEEE Symposium on Electromagnetic compatibility, pp 12-15, 1995.
- [22] Albert Ruehli, Clayton Paul and Jan Garrett, *"Inductance Calculations using Partial Inductances and Macromodels"*, Proc. IEEE Symposium on Electromagnetic compatibility, pp 23-26, 1995.
- [23] F.W. Grover, *"Inductance Calculations: Working Formulas and Tables"*, Dover Publications Inc., 1973.
- [24] Henry Ott, *"Noise reductions techniques in electronics systems"*, New York, NY: Wiley, 1988, ISBN - 0-471-85068-3.
- [25] Edward F. Vance, *"Coupling to shield cables"*, 1987, ISBN - 0-89874-949-2
- [26] R. Schulz, V.C. Plantz and D.R. Brush, *"Shielding Theory and Practice"*, IEEE Transactions on EMC, Vol 30, N-3, pp. 187-201, August 1988.

[27] L. Hasselgren and J. Luomi, "*Geometrical Aspects of magnetic shielding at extremely low frequencies*", IEEE Transactions on Electromagnetic Compatibility, Vol. 37, N-3, pp 409-419, August 1995.

[28] C. Taylor, C. Harrison and N. Younan, "*On predicting the Effectiveness of magnetic Shields at low frequencies*", Proc. IEEE International Symposium on Electromagnetic Compatibility, pp 176 - 178, August 1993.

[29] A. Ishiyama and H. Hirooka, "*Magnetic Shielding for MRI superconducting magnets*", IEEE Transactions on Magnetics, Vol. 27, N- 2, pp.1692-1695, March 1991

[30] Thomas M. Gruz, "*Design considerations for powering 415 Hz computer systems*", IEEE Transactions on industry applications, Vol 25 N-6 pp 1102-1109, Nov./Dec. 1989.

Chapter 3

Conducted noise

CMS has proposed a 400Hz AC distribution system to power up the front-end electronics installed into the detector. This system generates a set of 400V three-phase voltage at the ground level of the CMS building and distributes it from that level up to the periphery of the detector in the cavern or counting room. Each sub-detector has proposed different low-voltage (LV) units based on this primary distribution at 400Hz. Some of them will use simple three-phase transformer and rectifier units with inductive-capacitive output filters. The transformer and rectifier are located in the periphery of the detector and they have to operate reliably under neutron radiation and fringe magnetic fields. In this sub-system, the final LV regulation is achieved using linear low voltage regulators located near the front-end electronics. Other sub-detectors have proposed to use LV units based on AC/DC converters and DC-DC converters as post-regulators. In this equipment, the 400Hz distribution is converted to an intermediate 48VDC distribution and DC-DC converters perform the final step-down conversion to the required low voltages. DC-DC converters will be placed around the detector where the environment conditions are similar to the one described above. A simplified scheme of the distribution system for the CMS detector is shown in figure 3.1.

All switching converters generate and emit high frequency noise. The noise generated by DC-DC converters depends strongly on the topology of the converter, layout design, parasitic components, etc. Emissions are mainly coupled to the sensitive front end electronics (FEE) by conduction or radiation via the cables connected to them. To reduce the conducted noise, additional filtering is necessary at the input and the output of the converters. These filters have to attenuate noise components that range from the switching frequency of the converter up to 30-50 MHz.

Filters can interact adversely with the converter at low frequencies, resulting in severe performance degradation or even instability. This problem is originated by the negative input impedance that DC-DC converters present when they operate with tight close-loop regulation of the output voltage. This negative impedance interacts with the input filter, input distribution cables, and other converters

connected to the same distribution bus, giving place to instabilities or deterioration of the dynamic performance. Input EMI filters have to be properly selected to avoid this problem and also to provide the adequate attenuation in a wide range of frequency.

The 400Hz distribution system is fully loaded by AC/DC converters. These non-linear loads generate harmonic currents in the distribution system that interact with the distribution system impedance and produce distortion in the sine wave voltage. Harmonics are prejudicial as they over-heat equipment, affect the voltage quality of the distribution, radiate noise, excite power distribution resonance, induce malfunction of sensitive equipment, etc.

All the noise sources described and their location in the distribution system are shown in figure 3.1. This chapter addresses the analysis of the conducted noise generated by DC-DC converters and the filter design to mitigate the noise emission. In addition, the generation of current harmonics and their effects in the 400Hz distribution system is briefly studied.

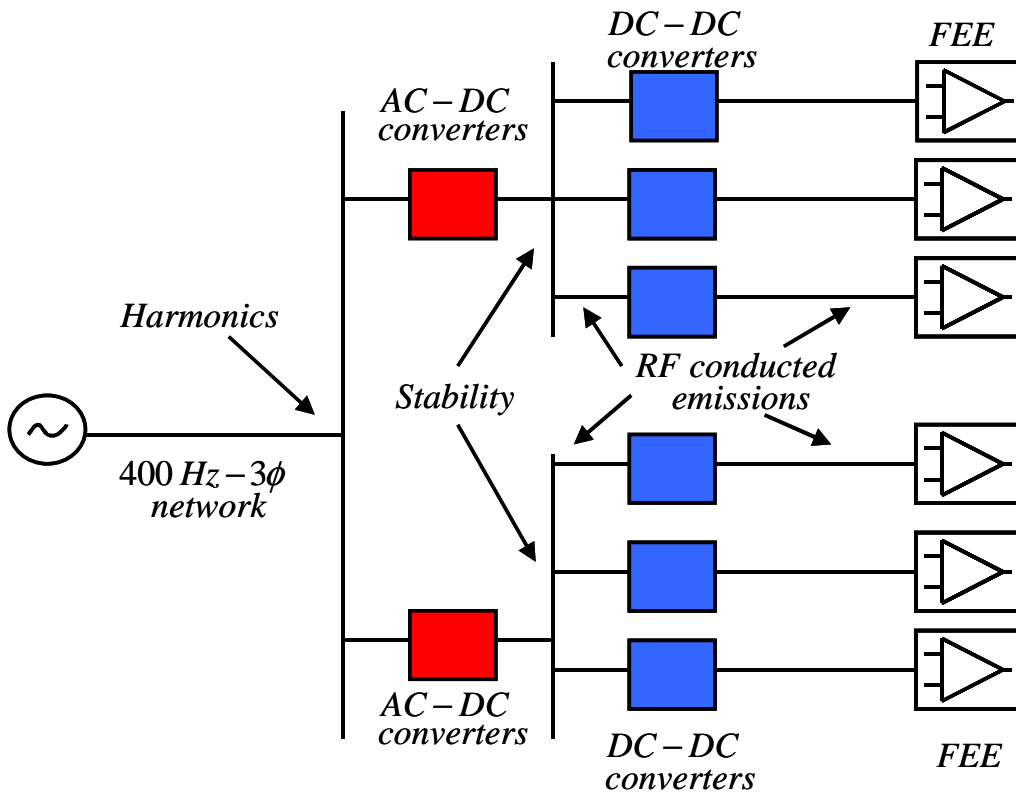


Figure 3.1: Power distribution layout

3.1 RF conducted noise

DC power distribution has been used by aerospace and telecommunication industries [1][2]. This topology distributes a high voltage (HV) and converts it to a low voltage (LV) either locally or near the electronic equipment. CMS and Atlas detectors [3][4] have proposed similar topologies to power-up the front-end electronics. In such proposals, the primary 50Hz or 400Hz AC mains is rectified away from the detector and DC high voltage (200V or 48 V) is distributed to the periphery of the detector. At that location, DC-DC converters transform with high efficiency the HV into the LV required by the FEE. Those converters are located between 20-40 meters from the front-end electronics due to the intense magnetic field that exists inside the detector.

For the CMS experiment, converters must operate reliably under high-energy neutron radiation and fringe magnetic fields. DC-DC converters must also present high efficiency, isolate galvanically the input and output, and couple a low amount of noise to the surrounding electronic equipment. Switching power converters intrinsically generate a noise level that, in general, is not compatible with the sensitive electronics used in high energy physics (HEP) experiments. Input and output filters are necessary to attenuate the level of noise coupled by radiation and conduction through the cables.

Regulation of electromagnetic interference (EMI) began in early days of electronics. Today, there exists a vast collection of standards [5][6] covering equipment used in industry, military applications, commerce and residence. In Europe, the limits of high frequency noise are specified either by generic standards (EN50081-1 for residential, commercial, and light industry, EN50081-2 for industrial environment) or by standards for specific product families (EN55014 for household appliances, EN55022 for information technology equipment, or EN55011 for radio-frequency equipment) for industrial, medical and scientific applications. In USA, the Federal Communication Commission (FCC) issues EMC standards, with different limits for class A and class B devices. Both FCC standards are defined for digital equipment marketed for use in commerce, industry or business environments (class A) and a residential environment (class B). Typically, European standards for conducted high frequency emissions are specified in the frequency range from 150KHz to 30MHz, and in the United States from 450KHz to 30MHz. The allowed conduction emission levels are between 46 dBuV and 79 dBuV. These limits are imposed to the input of the equipment under test and the compliance is verified inserting a line impedance stabilization network (LISN) between the AC mains and the power cord. The measured values correspond to the voltage level registered across any input wire terminated at the source with a 50 ohms impedance to ground (LISN termination).

Old Military standards for conducted emissions (MIL-STD-461 CE-03) differ from the other standards. It does not use the LISN¹, it directly measures the emission

current using a current probe. Also it specifies that conducted emissions have to be measured on other cables in addition to the power cord. The range of frequencies covered is between 14 kHz and 50 MHz and the emission level are between 86 $dB\mu A$ and 20 $dB\mu A$. To compare these standard we should normalized the measurement to $dB\mu A$ or $dB\mu V$ assuming a normalized impedance of 50 ohms. Figure 3.2 depicts the three standards normalized in $dB\mu V$.

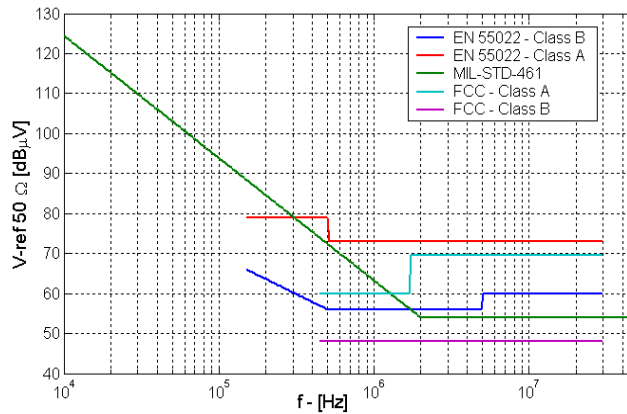


Figure 3.2: Conducted emission level fixed by EU, FCC and MIL standards

3.2 Switching mode power supplies

Large amount of conducted noise, in the detector, is created by the switching mode power supplies (SMPS) installed either in the control room or on the periphery of the detector. SMPSs generate high frequency noise due to the switching action. There is an important effort to reduce the volume of the power converters keeping constant their efficiency. This improvement is achieved by increasing the switching frequency of the converter and using soft-switching commutation. Although a big effort is put in the converter design to reduce the noise emission, the levels achieved still are not compatible directly with the levels required by HEP detectors.

The conducted noise studies are carried out using VICOR power converters. These switching power units are Zero Current Switching (ZCS) Forward Quasi-Resonant converters (QRC) with secondary-side resonance operating in half-wave mode. Figure 3.3 shows a simplified electrical diagram of the VICOR DC-DC converters used during this test. This topology is a forward converter switching at zero current. During each cycle, a fix amount of energy is transferred between the input to the output of the converter. The output voltage is regulated by a closed loop, adjusting the switching frequency of the converter, according to external conditions

1 New Military standards use a LISN

as input voltage, output current. The high efficiency of DC-DC converters operating with ZCS allows operation with relatively high frequencies (up to 1 MHz).

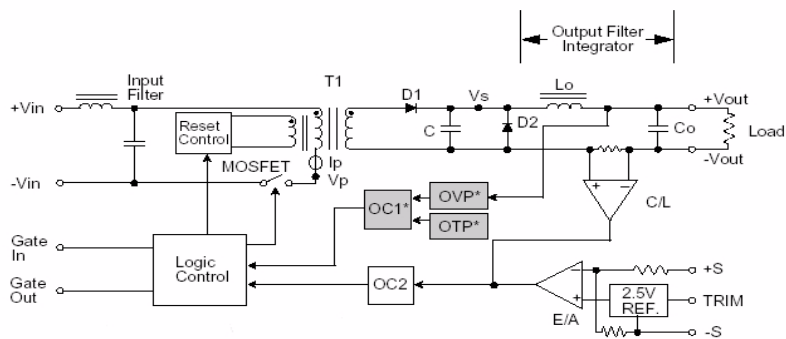


Figure 3.3: VICOR DC-DC converter scheme.

As conclusion, the main characteristics of ZCS QRC converters are:

- Reduced switching losses.
- Increased power density, since the size and weight of the magnetic components is decreased by increasing the operating frequency.
- Reduced Electromagnetic Interference (EMI) due to ZCS.
- High reliability.
- Fast transient response

3.2.1 Conducted RF emission of SMPS

The input and output currents in SMPS contain not only the DC components that contribute to the real power transfer, but also contain a large amount of harmonic components of the switching frequency. These harmonic components are the electromagnetic interference conducted out from the power supply through the input and output cables [8][9].

Both the input and the output terminals of the switching power supply can be considered as a two terminal (positive, negative terminals) port with a common return (chassis or case), where the terminal current can be decomposed into two modes:

- Differential mode (DM)
- Common mode (CM)

Figure 3.4 shows both common and differential modes of propagation. These modes are related with the terminal currents as:

$$\hat{I}_+ - \hat{I}_- = \hat{I}_{DM} \quad (3.1)$$

$$\hat{I}_+ + \hat{I}_- = \hat{I}_{CM} \quad (3.2)$$

where I_+ and I_- are the current at positive and negative terminals, respectively.

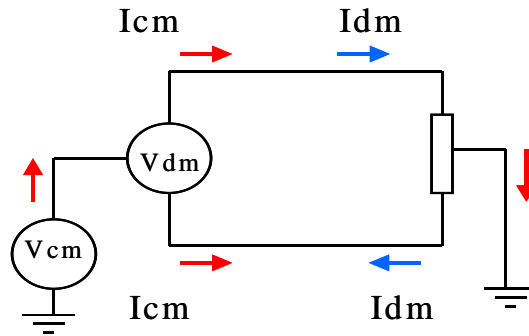


Figure 3.4 CM and DM noise propagation

The propagation of the differential mode EMI takes place between conductor pairs, which form a conventional return circuit (e.g. negative/positive conductors, line phase/neutral conductors). The DM EMI is the direct result of the fundamental operation of the switching converter. The DM is caused by the voltage induced across the equivalent series inductance and resistance of input and output filter capacitors at high di/dt . Selecting the adequate capacitors with low series inductance and series resistance, it is possible to decrease the DM emissions.

The propagation of the common mode EMI takes place between a group of conductors and either ground or another group of conductors. The path for the CM EMI often includes parasitic capacitive or inductive coupling. The origin of the CM EMI is either magnetic or electric. EMI is electrically generated when a circuit with large dv/dt has a significant parasitic capacitance to ground. Magnetically generated CM EMI appears when a circuit loop with large di/dt in it has significant mutual coupling to a group of nearby conductors.

The CM noise is difficult to cancel. Signals with high dv/dt coupled through the parasitic capacitances between the switching devices and the heat sink and between primary and secondary windings of the transformer induce common-mode currents. These currents flow through the wires at the input and output of the converter interfering with the neighborhood due to conducted and radiated noise. In switching power converters, the same fundamental mechanism that is responsible for conducted EMI can also generate radiated EMI. Metal cases around the converter tend to attenuate the internal high frequency electromagnetic fields.

Input and output cables or improperly grounded apparatus can still lead to substantial radiation.

3.2.2 Conducted noise measurements

In the HEP community there has not been a systematic approach in defining the emission levels of EMI signals [7]. Some experiments have chosen to purchase equipment that comply with either European or American standards, but there does not exist any quantitative limit in the emission level of power distribution and signal cables routed inside the detectors. CMS is trying to define limits for emission of the electronic equipment to be installed in the experiment. These limits are established basing on a combination of emission and immunity tests, thus it is necessary to define a complementary test for both applications. For that purpose, the values selected to measure the emission of the PS units are noise currents, as these parameters will be used to identify the immunity of the FEE. This normalized test measures the input and output emissions with a current probe and a spectrum analyzer. The current measured at the positive terminal is referred to 50 ohms to compare with any of the standardize levels.

The test layout is very important to ensure the validity of this test. The test layout should represent the worst case in terms of current emissions, but following as similar as possible the final topology of the PS system. For that purpose the DC-DC converters are connected to the load and primary source in such way that creates a very low impedance path for the CM and DM currents, resulting the measured noise currents with this test equal or bigger than the final ones presented in the experiment. The selection of this topology introduces a safety margin in the measurements. Also, this layout is very useful for the evaluation of the EMI filters because the performance of a filter with very low impedance loads is smaller than 50 or 150 ohms loads. Therefore, these tests introduce a new safety margin when the PS units are tested with filters.

3.2.2.1 Experimental set-up

To measure the input and output noise of the VICOR DC-DC converters, a set-up was implemented consisting of a primary power supply, the unit under test and a load. An electric diagram of such a set-up is depicted in figure 3.5. A power supply unit DELTA - SM3000 is used as primary source and the load is a resistive one. The DC-DC power converter V300B12C250A3 operated at 200V input voltage, 7.5V output voltage and 7.5A output current. The currents are measured by a current probe (EMCO-Model 91550)¹ and a spectrum analyzer (HP 8594E) in peak mode.

¹ See appendix C - Transfer impedance curve.

Two currents are recorded at the input and output terminals, the common mode current and the current flowing through the positive terminal. Shielded cables connect the power converter unit to the primary power supply and the load to include a return path to the CM currents [8]. Common mode filter capacitors are added between the converter's terminals and the case and also at the input of the primary power supply.

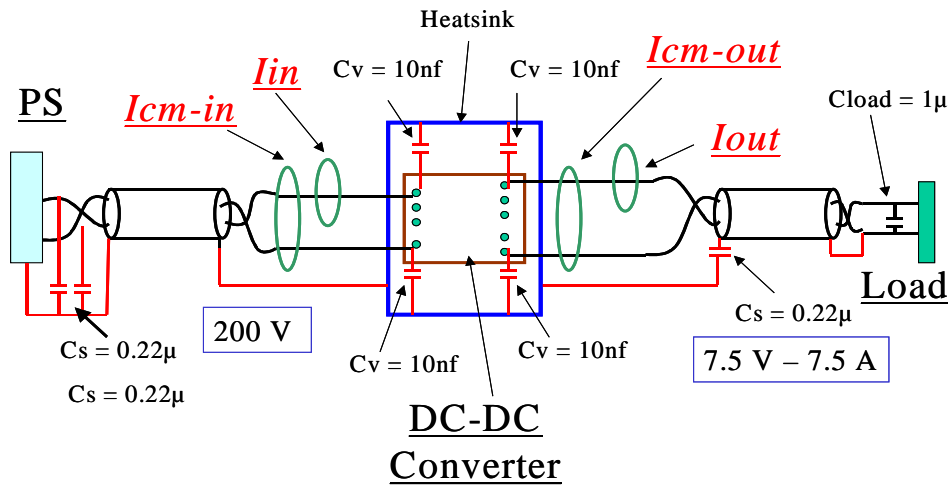


Figure 3.5: Conducted emission test layout

All the measures are performed with the spectrum analyzer in two steps, one covering a frequency range between 10kHz and 5MHz using a bandwidth of 1 kHz to obtain a good resolution and the other covering the range between 5 MHz and 30 MHz with a bandwidth of 30kHz. This bandwidth is adequate to obtain a good resolution reducing the time of measurement. As an example, figure 3.6 shows the current spectrum measured directly at the input of the DC-DC converter.

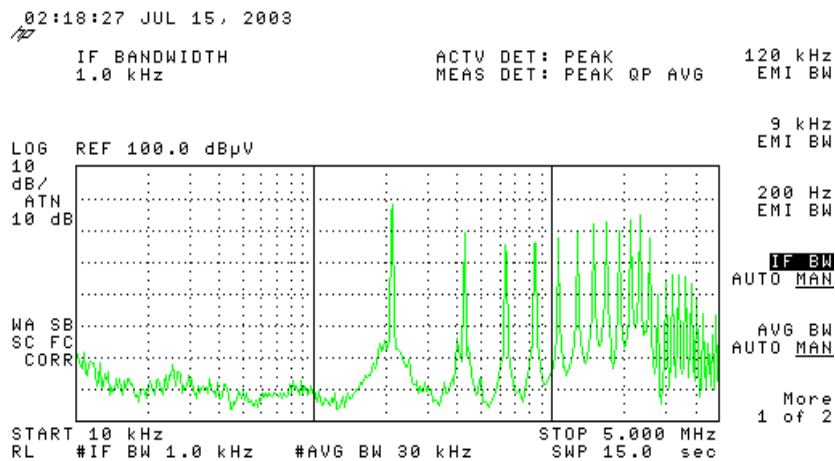


Figure 3.6: Noise in the positive lead

3.2. Switching mode power supplies

For data analysis, the acquired values are converted to $dB\mu V$ after correcting the measured current by the transfer impedance curve of the current probe (Z_t). All the currents are converted to voltage using $50\ \Omega$ as normalized impedance to compare its magnitude with the voltage magnitude defined by standards. The data collected is measured with the spectrum analyzer is *peak mode*, while the standards define the emission levels in *quasi peak mode*, given similar results for stationary loads. The transformation from current to voltage follows the equations. 3.3-3.5.

$$I(dB\mu A)_{dmcm} = V(dB\mu V)_{dmcm} - Z_t \quad (3.3)$$

$$I(\mu A)_{dmcm} = 10^{\left(\frac{I(dB\mu A)_{dmcm}}{20}\right)} \quad (3.4)$$

$$V_{ref(50\Omega)}(dB\mu V)_{dmcm} = 20 \cdot \log\left(\frac{I(\mu A)_{dmcm} \cdot 50}{1(\mu V)}\right) \quad (3.5)$$

Figure 3.7 shows the noise floor at the input and the output of the DC-DC converter when the unit is switched off. Under this conditions the DELTA PS unit is at 150 V and 0 A.

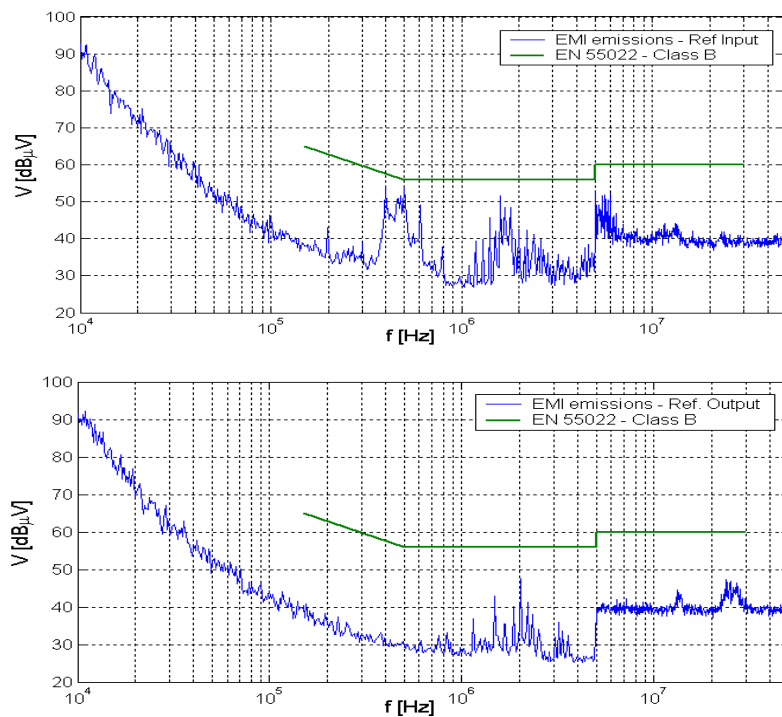


Figure 3.7: Input and output noise floor

3.2.2.2 Measurement results

Figures. 3.8 and 3.9 show the measured current noise at the positive input terminal and the input common mode current noise, respectively, for the Vicor converter V300B12C250AL operating at $V_{in}=200V$, $V_{out} = 7.5V$ and $I_{out} = 7.5A$.

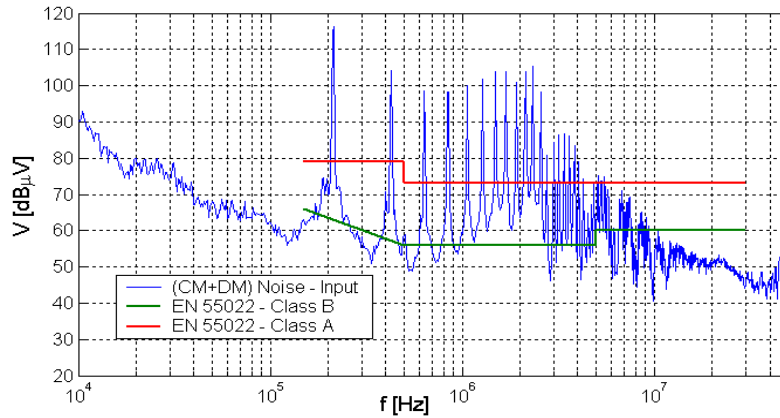


Figure 3.8: Input noise, positive terminal current.

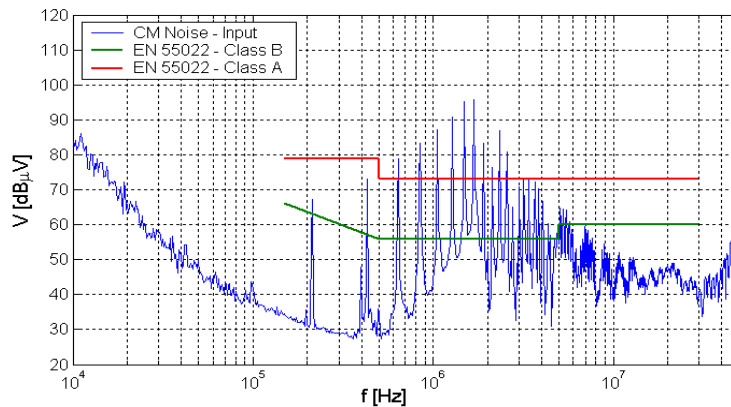


Figure 3.9: Input noise, CM current.

The filter has to attenuate the CM and DM mode components of the current to comply with the noise specifications. The filter has to be characterized and designed considering that both CM and DM currents are present at the input of the filter, then it is important to analyze the CM and DM contents of the input current [5][6]. The common mode component is directly measured and its magnitude is comparable with the total current measured at the positive terminal in the frequency range between 10 kHz and 50 MHz. In this frequency range, the input current is mainly

composed by DM and CM currents and a filter with good attenuation for both modes is necessary. At low frequency (up to 1 MHz.), the differential mode components are dominant and the external filter has to present strong attenuation for the DM mode. It is interesting to point-out that if a simple DM filter is used to attenuate the noise spectrum depicted in figure 3.8, the result, after filtering, will be similar to the noise spectrum depicted in figure 3.9. The common mode components remain unaffected and the system does not comply with the standard.

Figures 3.10 and 3.11 show the current noise of the positive lead and the common mode current at the output of the VICOR converter.

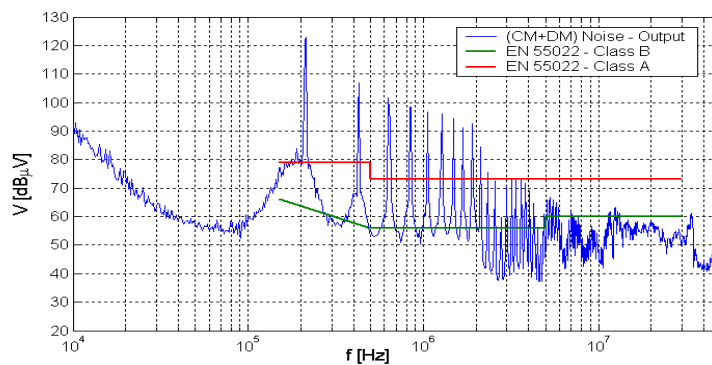


Figure 3.10: Output noise, positive terminal current.

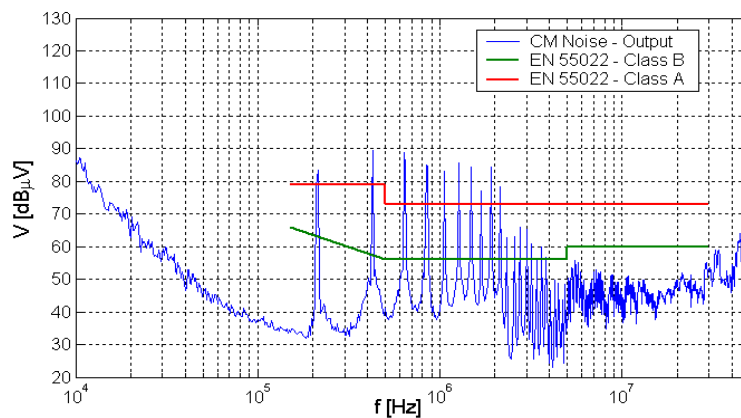


Figure 3.11: Output noise, CM current.

At the output of the DC-DC converter, the noise spectrum is slightly different to the one at the input. The CM and DM emissions are very similar, and the contribution of the CM is higher than the emission at the input. This is something expected, as

the manufacturers pay more attention to the input as it is this area that is specified by the standards.

3.3 Filter selection

Additional filtering is necessary at the input and output of the converter to reduce the conducted noise to values lower than the levels specified by the standards. Filters have to provide attenuation in a wide range of frequencies covering from the switching frequency up to 30-50 MHz. To fulfill these requirements, cascades of selective low-pass filters are used.

The power converter includes two internal filters, one at the input and the other at the output as depicted in figure 3.3. These filters contribute to the DM noise attenuation but based on previous measurements, the conducted noise in both ports of the converter does not comply with the standards. To further attenuate both the input and output conducted noise, high frequency (HF) filters are added to both ports of the converter. This HF filter is in cascade with the internal filter included with the converter and it is mainly designed to attenuate both DM and CM noise components in high frequency. The complete filter at the input can interact adversely with the converter at low frequency, resulting in severe performance degradation or even instability of the system. A brief review about this problem is presented in section 3.4.

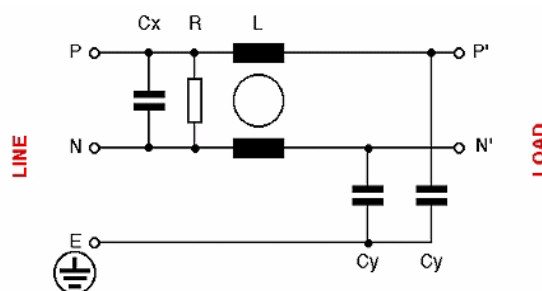


Figure 3.12: Single phase filter - EMI structure

The typical structure of the HF filter added to the input and output ports of the converter is depicted in figure 3.12. This filter attenuates both CM and DM noise components. The CM components are attenuated by the common mode choke (L) and C_y capacitors, while the DM components are attenuated by the C_x capacitors and the parasitic leakage inductance of the CM choke. The filter shown in figure 3.12 is a commercial unit used also in AC applications. In this case, the C_y capacitors are connected to the safety conductor and its capacitance is limited by safety requirements in order to avoid AC high leakage currents through the safety

conductor. In our application, external capacitors are added in parallel with C_y and C_x to achieve the attenuation required.

Manufacturers specify the insertion loss of these HF filters for DM and CM components covering a frequency range up to 30MHz. This information allows understanding the effect in the attenuation of the parasitic elements in each component [5].

3.3.1 Non ideal behavior of components.

Typical circuit components used in the design of passive EMI filters are discussed in this section. Basically, the mathematical model of the components, including the non-ideal behavior, is presented. The parasitic capacitance, resistance and inductance as well as the variation of the permeability and magnetic losses of the magnetic material are taken into account due to their influence in the filter attenuation.

3.3.1.1 Resistor

The ratio between the voltage and current in frequency domain of a resistor has a magnitude equal to the resistance value and a phase angle equal to 0. However at high frequency, the parasitic inductance and capacitance change considerably the ideal behavior of the resistors. The model of a resistor valid in a wide frequency range is depicted in figure 3.13.a, while the frequency response of the magnitude of this component is shown in figure 3.13.b. for a carbon resistance of $1.05\text{ k}\Omega$. At low frequency, the magnitude of the impedance is coincident with the resistance magnitude but at high frequency the parasitic components are dominant in the frequency behavior.

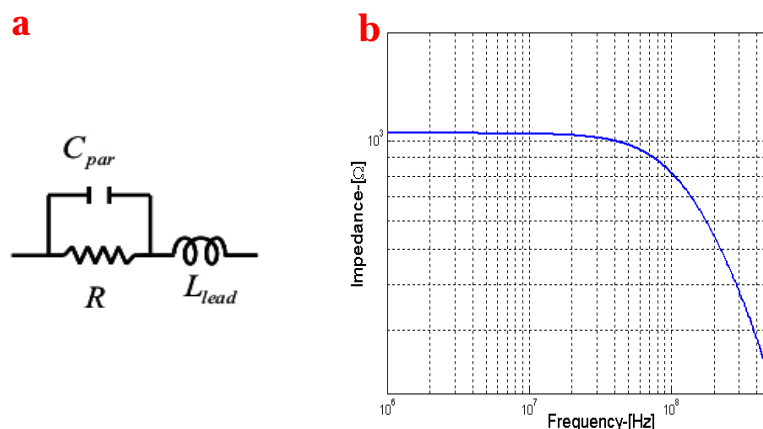


Figure 3.13: HF resistance model

3.3.1.2 Capacitors

There are numerous type of capacitors according to the dielectric used. Dielectrics generally used are: ceramics, polyester, tantalum, Aluminum oxide, etc. The ratio between the voltage and current in frequency domain of a ideal capacitor presents a magnitude which decreases with the frequency at 20 dB per decade and the phase is constant and equal to 90 degrees for all frequencies. However the parasitic components associated with the capacitor produce important modifications in the capacitor performance.

The capacitor can be considered as a pair parallel plates separated by a dielectric material and characterized by a capacitance C . The losses in the dielectric can be represented as a parallel resistance R_{diel} . Generally this value is relative high. The resistance of the plate is represented by a series resistor R_s . Leads attached to the capacitor have an inductance and a capacitance represented by C_{lead} and L_{lead} . These components depend on the configuration of the leads. In general, R_{diel} is large enough that can be neglected and C_{lead} is negligible respect to the intrinsic capacitance C . Thus, the equivalent circuit for the capacitor valid in a wide frequency range consists of the series combination of the intrinsic capacitor C , the lead inductor L_{lead} , and the series resistor R_s . This model is shown in figure 3.14a, while figure 3.14b shows the frequency response of this component for a ceramic capacitor resistance of 470 pf .

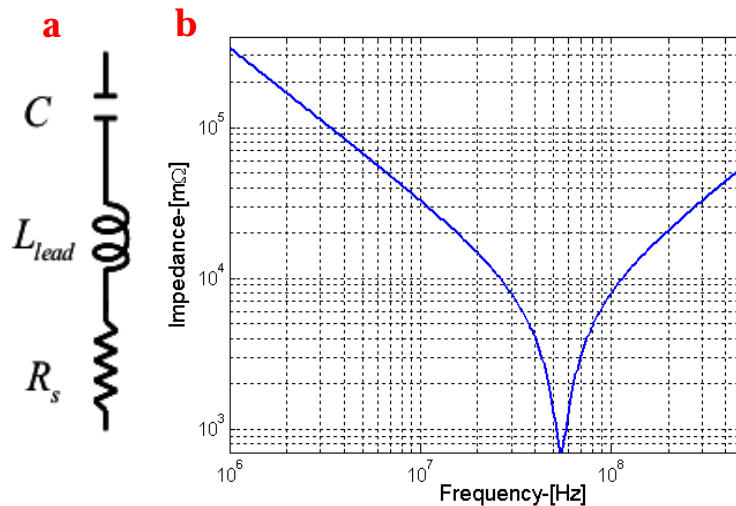


Figure 3.14: HF capacitance model

Based on this model, the magnitude of the capacitor’s impedance decreases inversely proportional with the frequency until the frequency equals to the self-resonant frequency of the capacitor.

$$f_o = \frac{1}{2 \cdot \pi \cdot \sqrt{L_{lead} \cdot C}} \quad (3.6)$$

This self-resonant frequency varies depending on the construction of the capacitor. It can range from a few kHz for aluminum oxide electrolytic capacitors to several MHz for surface mount ceramic capacitors.

3.3.1.3 Inductors

The ratio between the voltage and current in frequency domain of an ideal inductor is defined by a magnitude that increases with the frequency at 20 dB per decade and a phase that is constant and equal to -90 degrees for all frequencies. However, the parasitic components [11][12] associated with the inductor modify this ideal behavior mainly at high frequencies. For filter applications in DC-DC converters, the inductor has to carry DC currents and also to be compact. Ferromagnetic cores with small air-gap are used to fulfill both requirements.

The ferromagnetic core makes the magnitude of the inductor dependent of the DC current. In an air-gapped devices properly designed, the core saturation reduces the intrinsic inductance only at high currents. In addition, the core introduces magnetic losses [13] that can be modeled by a non-linear dissipative element in parallel with the inductor, that takes into account the loss variation with the frequency. The series resistance of the coil and the magnitude of the inductance change due the skin effect with the frequency. The parasitic inter-winding capacitance reduces the impedance presented by the inductor at high frequencies. A simple model for the inductor is shown in figure 3.15a, which consists of the combination of the intrinsic inductance L , the parasitic capacitance C_{par} , the series resistance R_{ser} and a parallel resistor R_{par} to model the losses in the magnetic core. Figure 3.15b shows the frequency response of this component, where all the components are assumed frequency independent.

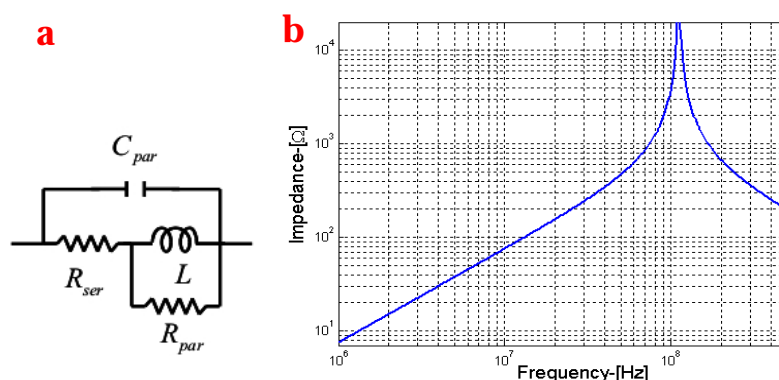


Figure 3.15: HF inductor model

3.3.1.4 Common mode chokes

This component, similar to a high frequency transformer, consists of a pair of coils wound around a ferromagnetic core in such a way that presents a high impedance for CM currents and low impedance for DM currents. Figure 3.16 shows the circuit and impedances for both modes of propagation of an ideal choke.

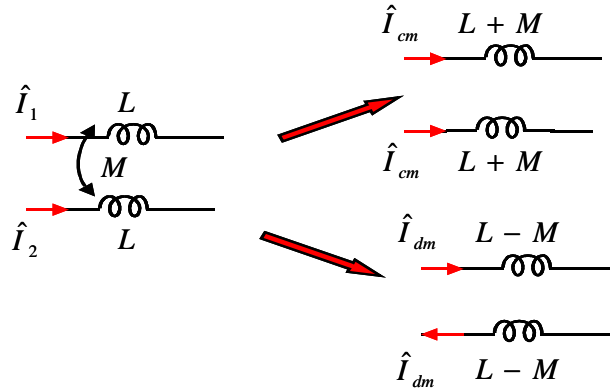


Figure 3.16: CM choke equivalent impedances

If the current is decomposed in both common and differential mode, the impedance for each mode is:

$$Z_{CM} = j\omega(L + M) \quad (3.7)$$

$$Z_{DM} = j\omega(L - M) \quad (3.8)$$

where L and M are the self and mutual inductance of the choke.

The parasitic components associated with the choke limit the attenuation to CM currents introduced by this component in a circuit. The two main parasitic components are:

- Inter-windings and inter-layer capacitances
- Core losses due to Eddy-currents and magnetic hysteresis.

Inter-winding and inter-layer capacitances reduce the effective Z_{cm} at high frequency because this parasitic effect manifests as a capacitor in parallel with Z_{cm} . The core losses appears as a dissipative element also in parallel with Z_{cm} . The effect in the circuit of this dissipative element depends on the core magnetic material [14], the operation frequency and the input-output voltage across the choke. Several papers in the literature [15]-[19] have reported different models of the CM choke. The model chosen for the present analysis is described in [20] and it is shown in figure 3.17. In this model, Lk_{ck} represents the choke's leakage

inductance or L_{dm} , the $C_{in_{ck}}$ the inter-coil capacitances, $C_{w_{ck}}$ the inter-winding capacitance, R_{ck} the winding resistance and $R_{c_{ck}}$ represents the core losses, which depends on the magnetic material, the frequency and the input-output voltage.

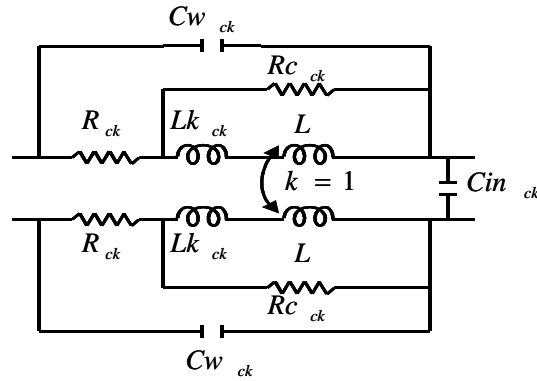


Figure 3.17: CM choke equivalent circuit.

3.3.2 Insertion loss

EMI filter manufacturers characterize the attenuation of the filter by the insertion loss (IL). In a filter, the insertion loss [21] is defined by the ratio between the power consumed by the load in a reference circuit before and after the filter is inserted into the circuit. The IL is expressed as:

$$IL = 10 \cdot \log\left(\frac{P_1}{P_2}\right) = 20 \cdot \log\left(\frac{V_1}{V_2}\right) \quad (3.9)$$

where P_1 and P_2 correspond to the power dissipated by the load and V_1 and V_2 are the voltages across the load before and after the filter is inserted, respectively, as it is shown in figure 3.18.

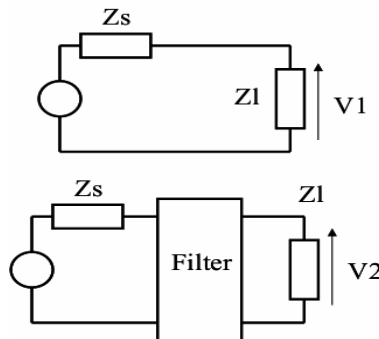


Figure 3.18: Insertion loss circuit

The IL depends on the terminal impedances, and therefore cannot be stated independently of these impedances. Most of the manufacturers give the insertion loss of the filter as function of the frequency referred to 50 ohms, because this is the normalized impedance value for emission tests (LISN impedance). However in real applications, this impedance does represent neither the load nor the source impedance for the filter. The value of the source/load impedances for the filter can vary from a few ohms up to a few thousands of ohms. To correct this problem some manufacturers give the insertion loss curves of the filter measured in accordance to CISPR 17 [22]. The standard defines two test conditions, one using normalized 50 ohm impedances as source/load impedances and the other condition using an source impedance of 0.1 ohms and a load impedance of 100 ohms and vice versa.

3.3.3 Filter characterization

Two commercial HF filters (Schaffner FN 2010-1 and FN 2010-20) have been used in the present analysis. Filters have been modeled including the components with the associated parasitic elements. The component parameters haven been calculated based on the insertion loss curves provided by the manufacturer. The filter layout, including the parasitic elements in each component, is shown in figure 3.19.

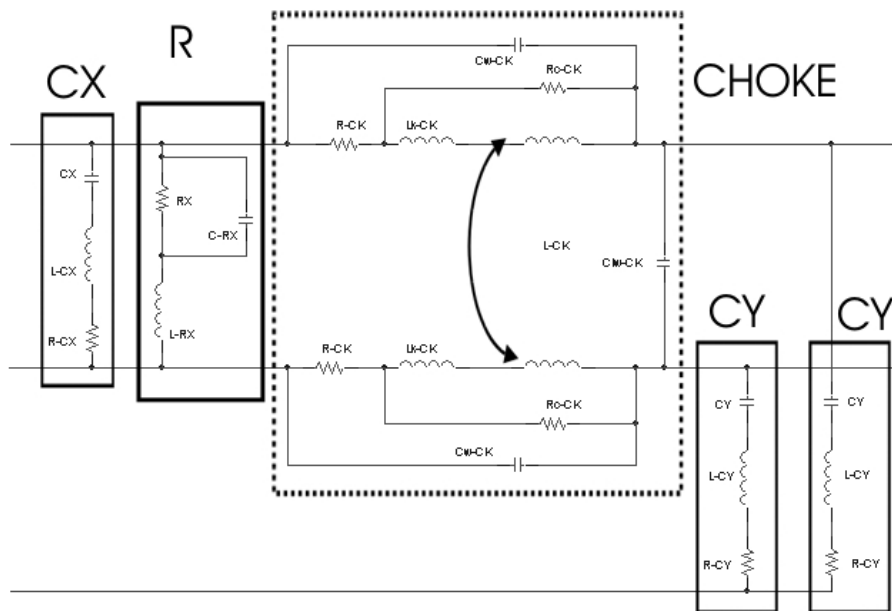


Figure 3.19: Parasitic components of the filter

The component parameters are shown in table 3.1. These parameters have been validated calculating the CM and DM insertion loss of the filter using MATLAB simulation. In this analysis, the skin effect¹ and the variation of the magnetic losses

3.3. Filter selection

in the core with the frequency are considered. The skin effect model follows the development described in appendix A, while the core loss variation with the frequency is modeled defining two different constant resistance values for the DM and CM circuits. Figures 3.20 and 3.21 show the IL of the filters given by the manufacturer, referred to 50/50 Ω , and the simulated results for the input and the output filters, respectively. There are small differences at high frequency, but acceptable for the present analysis.

	FN2010 - 1	FN2010 - 20
CX	0.104 μF	95 nF
L-CX	350 nH	13 nH
R-CX	0.085 Ω	0.022 Ω
CY	4.7 nF	4.7 nF
L-CY	9 nH	13.2 nH
R-CY	0.8 Ω	0.05 Ω
R	1 $M\Omega$	1 $M\Omega$
L-R	10 nH	10 nH
C-R	1.2 pF	1.2 pF
L_{ck}	12.5 mH	0.6 mH
Lk_{ck}	50 μH	1.05 μH
R_{ck}	$0.6 \cdot \left(1 + \sqrt{\frac{f}{10 \times 10^3}}\right) \Omega$	$0.08 \cdot \left(1 + \sqrt{\frac{f}{5 \times 10^3}}\right) \Omega$
$R_{C_{ck}}$	CM -135 $k\Omega$ DM -2 $k\Omega$	2 $k\Omega$
$C_{in_{ck}}$	6.5 pF	0.1 pF
$C_{w_{ck}}$	1.5 pF	4.5 pF

Table 3.1 Components parameters of FN2010 - 1 and FN2010 - 20 filters

3. Conducted noise

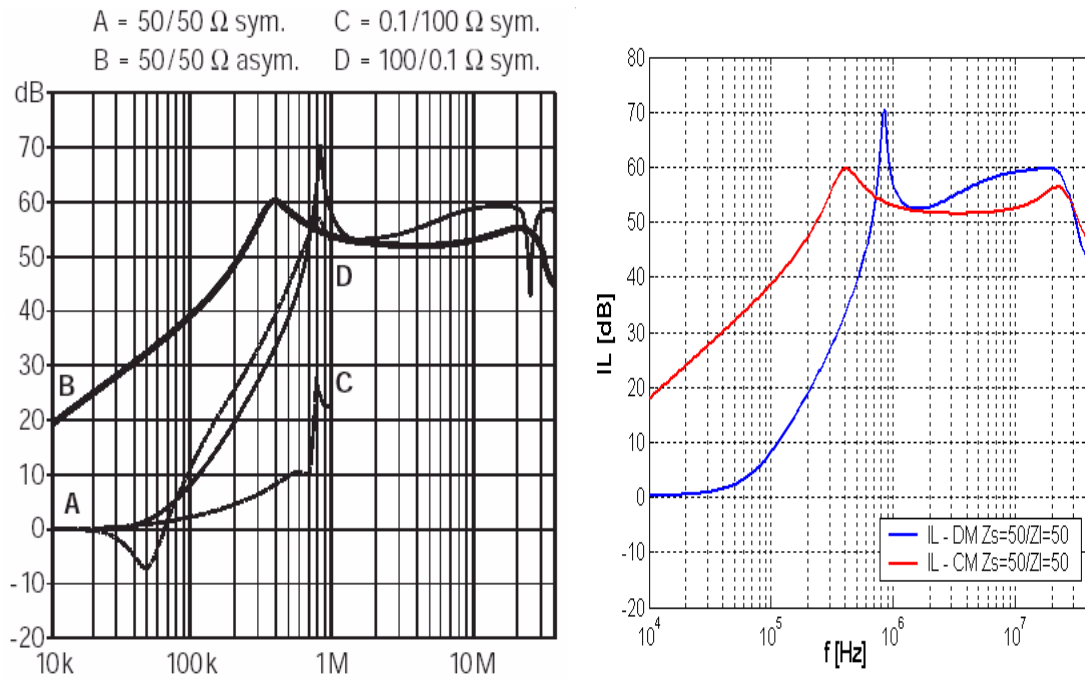


Figure 3.20: Insertion Losses - FN 2010 - 1- Measured and simulated results.
 (50/50sym=IL-DM-Sym; 50/50asym=IL-CM-Asym)

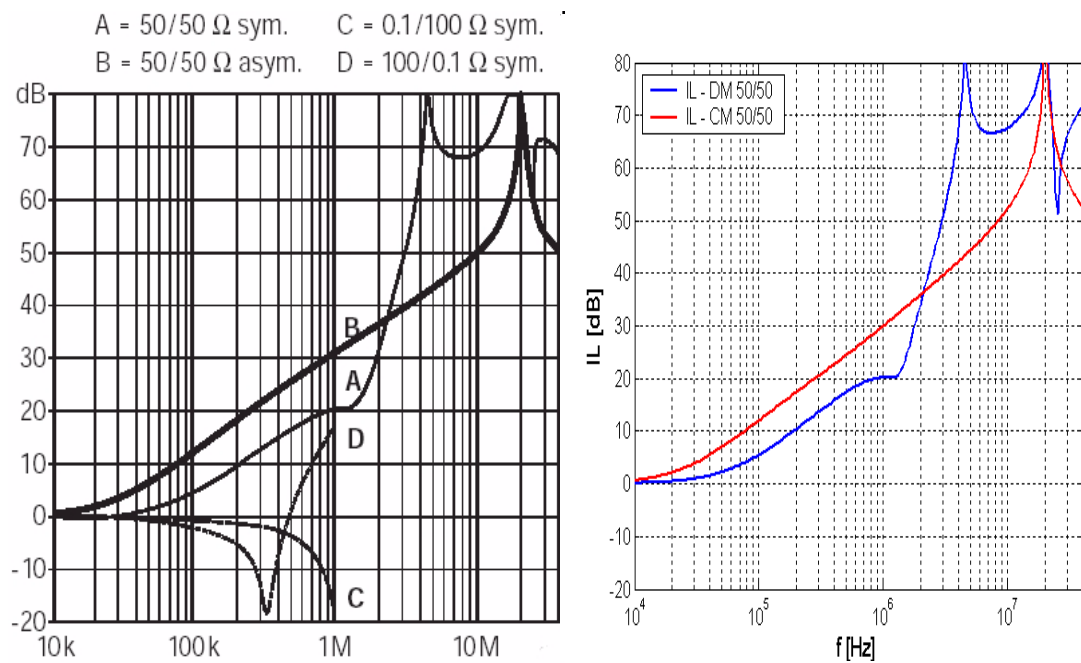


Figure 3.21: Insertion Losses - FN 2010 - 20- Measured and simulated results.
 (50/50sym=IL-DM-Sym; 50/50asym=IL-CM-Asym)

3.3.4 Filter performance

The methodology followed in the selection of both input and output filters consists on measuring the conducted noise generated by the power converter at both the input and output terminals and estimating the filter attenuation required to satisfy some standard. Assuming the system has to comply with the European standard level EN-55022 at both the input and the output ports, the filter attenuation required can be estimated from figures 3.8 and 3.10. For the input port, it is necessary an insertion loss greater than 40dB at low frequencies for DM and noise reductions greater than 30dB in the high frequency range for both DM and CM components. For the output, it is necessary attenuations greater than 45dB at low frequencies for DM and noise reductions greater than 30dB in the high frequency range for both DM and CM components.

Filter manufacturers specify the insertion loss (IL) of HF filters for DM and CM components covering a frequency range up to 30MHz. This insertion loss generally is referred to a load and a source impedances of 50 ohms, which generally is quite far from realistic values. In real applications, the impedance presented to the HF filter by the converter and the line can have values between a few ohms and thousands ohms, which result in different filter attenuations. Additionally, the reactive components of the filter can resonate with the source and the load impedances. Some manufacturers specify the DM insertion loss referred to load/source impedances of 0.1/100 Ω and 100/0.1 Ω using the standard CISPR17 [23], however this curves do not provide enough information to do the optimal selection of the filter for the DC-DC converters.

The main problem to synthesize the HF filter is the lack of knowledge of the source and load impedances connected to the filter terminals. These impedances define partially, the insertion loss of the HF filter. To calculate the magnitude of the filter components that achieve the IL required, the worst filter performance is studied by changing the magnitude of load/source impedances in a practical range. The load/source impedances are assumed resistive given an uncertainty due to possible resonances between the filter impedances and the load/source impedances, respectively. Based on this study, it is possible to define the filter attenuation closer to the real conditions. Once the filter IL for the worst condition is calculated, the conducted emission at the input and output of the DC-DC converter with HF filter are estimated.

The HF filter design is performed following the decomposition of the filter in a differential mode sub-circuit and a common mode sub-circuit. In order to estimate the noise current magnitude after the filter is added to the converter, the measured currents without filter have to be decomposed in DM and CM. This decomposition is straight-forward when a LISN is used to measure the noise current. In our case that currents are measured directly with a current probe, the common mode current is directly measured and the differential mode current is estimated based on the

terminal current and the common mode current. The magnitude of the current is recorded by the spectrum analyzer, resulting unknown the phase between the CM and the terminal current. To estimate the DM current, the worst case is considered by assuming that the DM current has a phase shift of 180 degrees respect to CM current. Then, the DM current magnitude is calculated as the sum of both the positive terminal current and CM current magnitudes. Having both the CM and the DM current magnitude without filter, the current after filtering is estimated by dividing the current magnitude by the insertion loss magnitude. Once the CM and DM output current are estimated, the terminal current is calculated by adding them, assuming the worst case that both current components are in phase. During this decomposition the background noise shown in figure 3.7 is considered as a non-correlated noise with the current measured. Its effect in the estimation is included at the output adding its magnitude in quadrature to the estimated current.

3.3.4.1 Output filter performance

Figure 3.22 depicts the layout of the complete filter, showing the components that define source impedance, Z_S , and the load impedance, Z_L , presented by the converter and the external circuit to the HF filter.

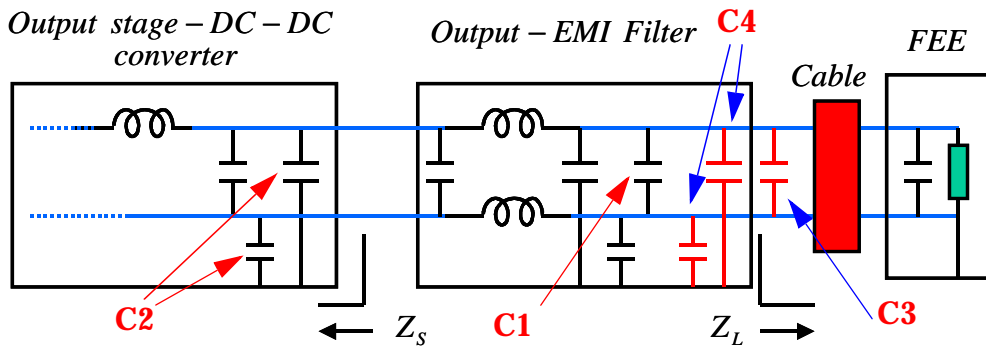


Figure 3.22: Output filter connections.

The source impedance is defined by the output capacitors of the DC-DC converter and the CM capacitors included between the output terminals and the case. In DM, this impedance is low up to high frequency where the influence of the parasitic inductance of the layout becomes important. It is possible to assume this impedance can range from $m\Omega$ in low frequency up to tenths of ohms in high frequency. For the CM topology, the internal impedance of the converter is generally high, being the source impedance mainly defined by the CM capacitor C2 (10 nF) and the components of the output circuit layout. In general, it can be assumed that this impedance is lower than 50 ohms above 200 kHz.

3.3. Filter selection

The load impedance of the filter in DM is defined by the cable that connects the filter to the load and the input capacitors of the FEE. This impedance is generally low at low frequency increasing with the frequency due to the inductive effect of cable.

The HF output filter is implemented using the commercial part FN2010-20 adding the polyester capacitor C1 of $0.33 \mu F$ to achieve the required attenuation. In this analysis, the parasitic components of this capacitor ($L_c=8 \text{ nH}$, $R_c=0.01 \Omega$) have been included. This filter can achieve a DM-IL greater than 30dB in high frequency for a set of sources and loads.

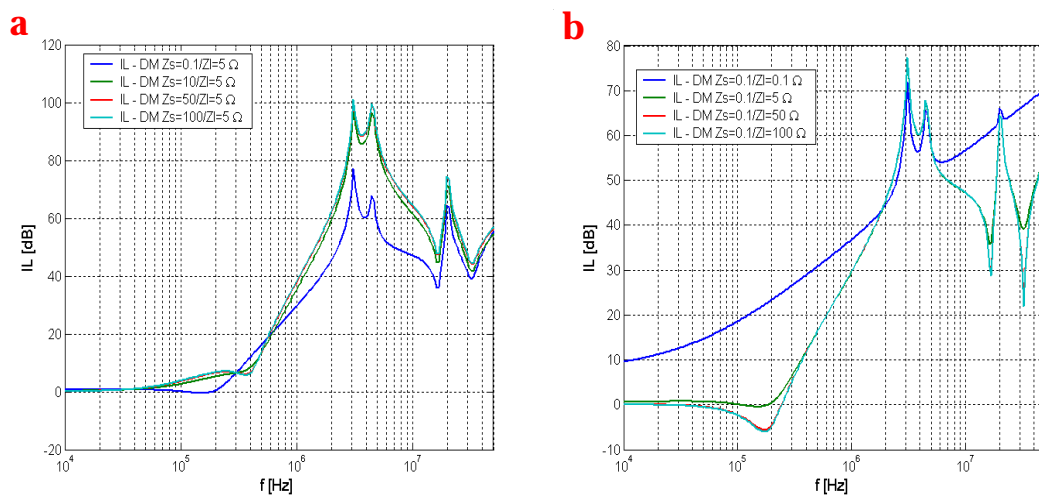


Figure 3.23: Insertion loss for the HF output filter in differential mode a) IL variation for different Z_S , b) IL variation for different Z_L

Figure. 3.23 shows the IL of the output filter in differential mode. Part a) depicts the IL for a fix load impedance $Z_L = 5 \Omega$ and for different values of the source impedance 0.1, 10, 50 and 100 Ω . The plot shows that the filter attenuation is not very sensitive to source impedance variations for a given load impedance. A source impedance change by a factor 1000 produces a maximum variation of the IL of about 22-24 dB (factor 20). Part b) shows the filter attenuation is not influenced by variations of the load impedance when it changes in the range between 5 and 100 Ω . For lower values of the load impedance the IL increases. From figure 3.23, it is possible to conclude that the worst case corresponds to the condition $Z_S = 0.1 \Omega$ and $Z_L = 100 \Omega$. This insertion loss is used to estimate the noise current attenuation in DM introduced by the complete filter, which seems to be enough to achieve the require attenuation at high frequency.

For the CM noise, a similar procedure was followed assuming that the CM source impedance can change between 1 Ω and 50 Ω and the CM load impedance between 5 Ω and 150 Ω . Figure 3.24 shows the CM insertion loss for that set of

impedances. From this figure, it is possible to conclude that the worst case frequency where the common mode starts to be important, corresponds to the combination $Z_S = 50\Omega$ and $Z_L = 5\Omega$. This attenuation is used to estimate the noise current reduction introduced in CM by the HF filter.

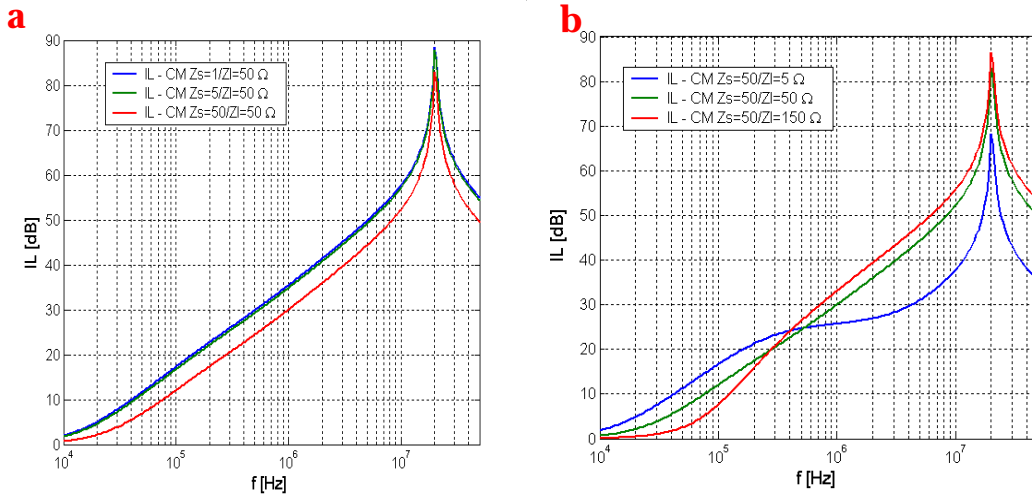


Figure 3.24: Insertion loss for the HF output filter in common mode. a) IL variation for different Z_S , b) IL variation for different Z_L .

Based on the worst case CM-IL, the CM noise at the output of the converter with HF filter is estimated. Figure 3.25 shows the estimated values of CM output current noise for the DC-DC converter with the HF filter, while figure 3.26 depicts the measured CM output noise current for the converter including the same HF filter.

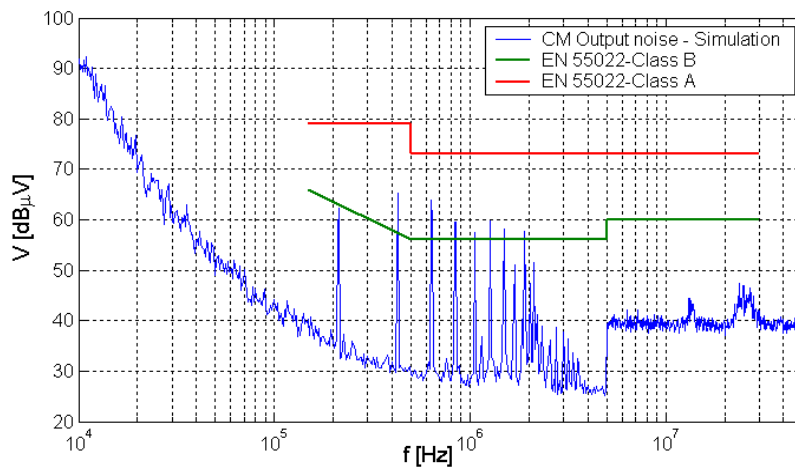


Figure 3.25: CM output current conducted emissions of Vicor converter with HF filter. Simulated values.

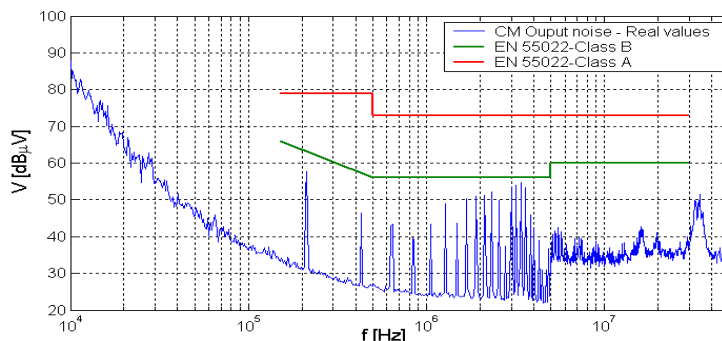


Figure 3.26: CM output current conducted emissions of Vicor converter with HF filter Measured values.

The estimated and the measured noise current values have a similar spectrum. There are two clear differences between both plots. The first difference is in the second, third and fourth harmonics. Measurements (figure 3.26) shows the performance of the real filter (figure 3.25) is better in that frequency range than the IL calculated for different load/source impedances. The origin of this difference can be found in the different characteristics of load and source impedances between the real and the simulated circuits. Resistive load and source impedances are used in the simulation model. However for the real circuit, the load and source characteristics are either inductive or capacitive. They change with frequency producing a dynamic variation of the filter performance with the frequency. The selection of the constant resistor magnitude for the load and source represents the worst case, allowing to limit the uncertainties created by the impedance variation with the frequency. The second difference is found in the frequency range between 2.5 and 5 MHz. For this frequency range, the measured values are higher than the estimated ones. The origin of these differences is due the measurement set up. The circuit layout can affect the performance of the filters to CM noise due to the long cables that connects the ground of the DC-DC and ground of the filter. This can be easily observed adding an inductance in the ground path in the simulation model, which produces a drop in the IL-CM of the filter.

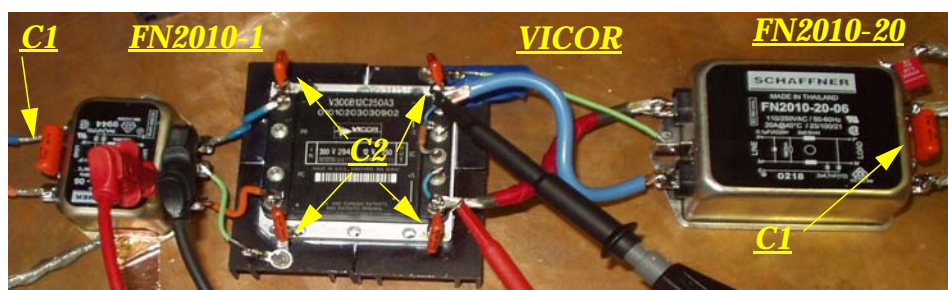


Figure 3.27: RF conducted test layout for VICOR converter.

As it is shown in figure 3.27, long cables are necessary to perform current measurements between the DC-DC converter and filter. For the final version, the layout can be improved by placing all the units on a ground plane, which decreases the impedance of the grounds paths and connections improving the performance of the filter.

To estimate the total noise at the output of the converter after the HF filter is added, from figures 3.23 and 3.24, it is possible to conclude the worst case attenuation corresponds to the combination $Z_S = 50\Omega$ and $Z_L = 5\Omega$ for the CM-IL and $Z_S = 0.1\Omega$ and $Z_L = 100\Omega$ for the DM-IL. Based on the DM-IL and the CM-IL worst cases, the noise at the output of the converter is estimated. Figure 3.28 and 3.29 show the estimated and real output noise current for the VICOR converter with HF filter.

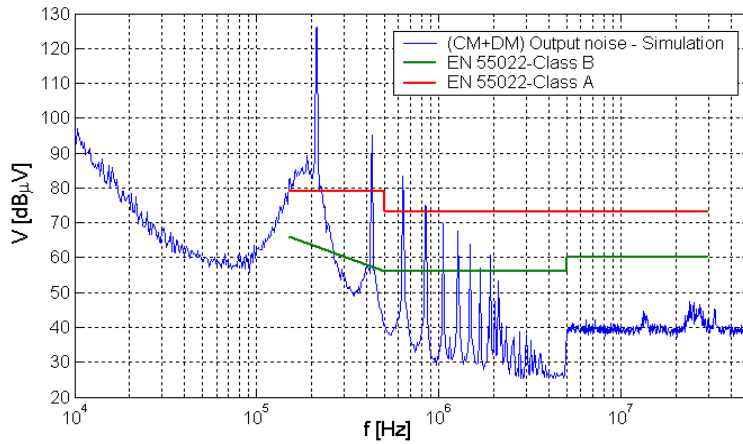


Figure 3.28: Output current conducted emissions of Vicor converter with HF filter. *Simulated values.*

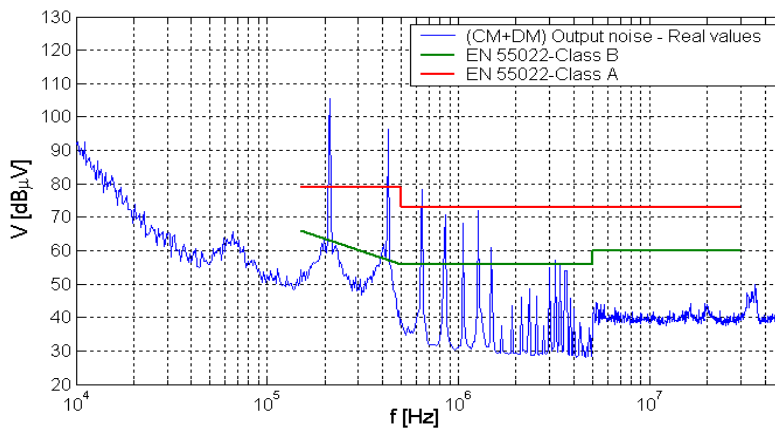


Figure 3.29: Output current conducted emissions of Vicor converter with HF filter. *Measured values.*

3.3. Filter selection

It is possible to observe a close agreement between the estimated and the measured noise current values. Again, the estimated values are higher than the measured ones, giving a safety margin during the selection process of the filter. Also, there is only a significative difference between both plots in the frequency range between 2.5 and 5 MHz, as analyzed in figures. 3.27 and 3.26.

Based on the simulated results at low frequency the attenuation is not enough to comply with the EN 55022-Class A. To improve the IL at low frequency, two differential mode capacitors in parallel (C3) are added to the HF filter output. ceramic SMPS-MLC¹ capacitors of 82 μF are selected to achieve enough attenuation (45 dB) at low frequency for different load/source conditions. These capacitors are characterized by a very low parasitic series resistance, being very important to improve the filter performance at low frequency. In simulations, the parasitic components of the capacitor ($L_c=2.4 \text{ nH}$, $R_c=0.0025 \Omega$) have been included.

The DM-IL for the new filter are re-calculated for different input and output impedances. Figure 3.30 shows the insertion loss of the previous HF filter with the extra capacitor (C3) in differential mode. Part a) depicts the IL for a constant load, while the source impedance is changed. The DM-ILs are quite invariant with the source impedance variation. A similar characteristic presents the DM-IL when the load impedance changes, as depicted in fig. 3.30 part b).

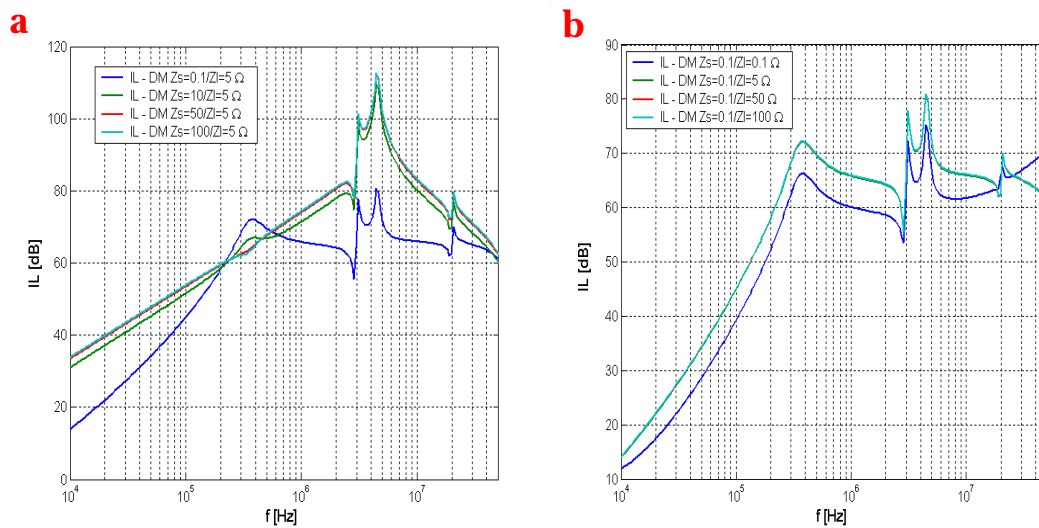


Figure 3.30: Insertion loss for the HF output filter in differential mode with the addition of the capacitor C3. a) IL variation for different Z_S , b) IL variation for different Z_L

From these plots, it is possible to observe that the DM-IL worst case corresponds to a low source and a low load impedance. The DM insertion loss for $Z_S = 0.1 \Omega$ and

¹ Capacitor from AVX company

$Z_L = 0.1\Omega$ is used to estimate the DM noise current attenuation introduced by the complete filter. The capacitor C3 added to the output does not affect the CM emissions, which based on the simulated results depicted in figure 3.25 are still slightly high. To attenuate the CM emission in the frequency range between 200 kHz and 2 MHz, two polyester capacitors (C4) of 40 nF are include between the filter terminals and ground. These capacitors are shown in figure 3.22. The CM-IL of the HF output filter with the capacitors C3 and C4 is shown in figure 3.31 for different load and source impedances. In this simulation, the parasitic components of the capacitor C4 ($L_c=2.4$ nH , $R_c=0.050$ Ω) have been included.

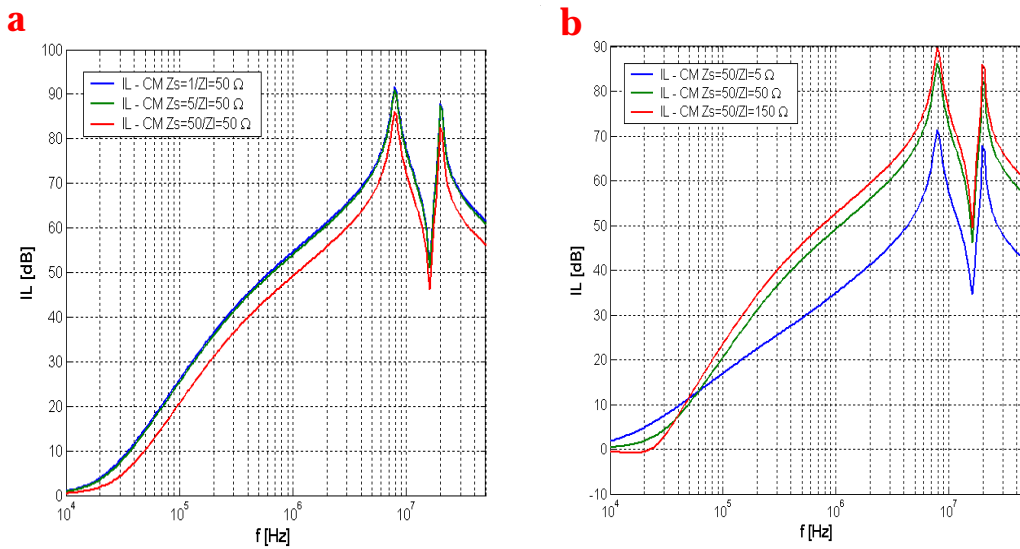


Figure 3.31: Insertion loss for the HF output filter in common mode with the addition of the capacitor C4. a) IL variation for different Z_S , b) IL variation for different Z_L .

The filter CM-IL with the CM capacitors C4 is, in general, quite invariant to source and load impedances except for the case of large source impedances and small load impedances. Based on the CM-IL, the worst case corresponds to $Z_S = 50\Omega$ and $Z_L = 5\Omega$. If we compare the IL depicted in figure 3.31 with the IL shown in figure 3.24 corresponding to the HF filter without the CM capacitor C4, it is possible to note that CM-IL curves are practically identical at low frequency. At this frequency, the main element defining the CM attenuation is the CM choke, that in our case is the same in both cases. If a higher attenuation is required at low frequency, it is necessary to select another filter with larger series inductance.

Based on the DM-IL defined for $Z_S = 0.1\Omega$ and $Z_L = 0.1\Omega$ and the CM-IL set by $Z_S = 50\Omega$ and $Z_L = 5\Omega$, the terminal noise current is estimated. Figure 3.32 shows the estimated noise current.

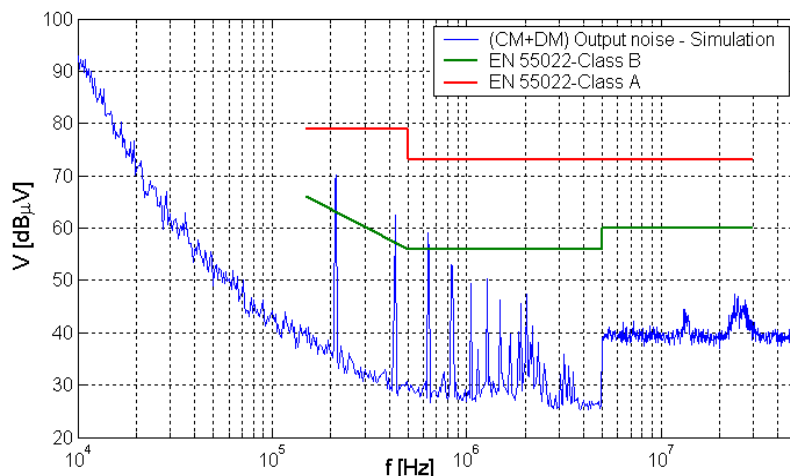


Figure 3.32: (CM+DM) output conducted emissions of Vicor converter with filter plus extra capacitors C3 and C4. Simulated values

3.3.4.2 Input filter performance

Following a procedure similar to the output filter design, the HF input filter is designed to comply with the EN 55022-Class A standard. Figure 3.33 shows the electrical scheme of the DC-DC converter, the HF filter and the load.

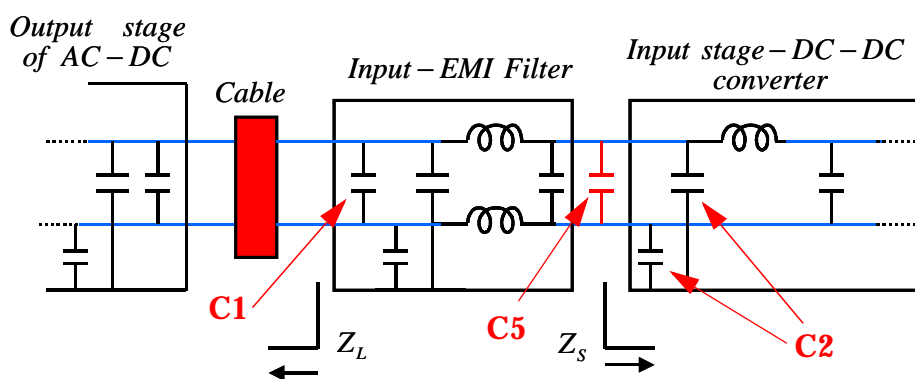


Figure 3.33: Input filter connections

The source impedance for the DM topology is defined by the input stage of the DC-DC converter, which basically depends on the internal inductance and CM capacitors (C2) added to the input terminals of the Vicor converter. The magnitude of the internal inductance is $60 \mu H$ and the CM capacitance is 10 nF , giving a resonance frequency for the DM filter of 300 kHz . Above this frequency, the source impedance is mainly defined by the CM capacitors and the layout of the input

circuit. If the resonance between the internal inductor and the CM capacitors is damped, the source impedance for the DM topology can be assumed lower than 200 ohms for a frequency range that extends up to 50MHz. For the CM topology, the internal impedance of the converter is generally high, being the source impedance mainly defined by the CM capacitors C2 and the parasitic components of the input circuit layout. In general, it can be assumed that this impedance is lower than 50 ohms above 200 kHz.

The load impedance of the filter in DM is defined by the short cable that connects the filter to the primary power supply and the output capacitors of the power supply. This impedance is generally low. In case of CM, these load impedance are mainly defined by the capacitor of $0.22\mu F$ that connects the shield to the negative output of the primary voltage as it is shown in figure 3.5.

The HF input filter is implemented using the commercial part FN2010-1 with the additional capacitor C1 of $0.33\mu F$ to achieve the required attenuation at high frequency. In this analysis, the parasitic components of the capacitor ($L_c=8\text{ nH}$, $R_c=0.006\ \Omega$) have been included. This filter itself can achieve a DM-IL greater than 40dB in high frequency for a set of source and load impedances.

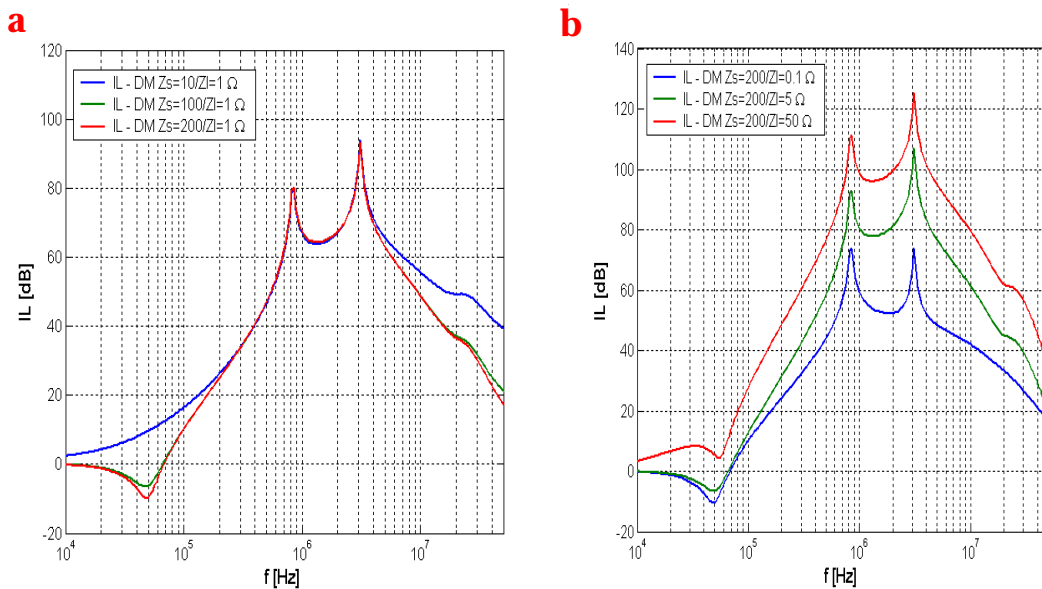


Figure 3.34: Insertion loss for the HF input filter in differential mode. a) IL variation for different Z_S , b) IL variation for different Z_L .

Figure 3.34 shows the insertion loss of the HF filter in differential mode. Part a) depicts the IL for a constant load $Z_L = 1\ \Omega$, while the source impedance is changed from 10 ohms to 200 ohms. This plot shows a relative independence of the IL respect to the magnitude of the source impedance. Part b) depicts the IL for different load impedances, while the source impedance is kept constant at $Z_S = 200\ \Omega$. This plot

3.3. Filter selection

shows the filter attenuation is sensitive to load variations, but the IL is not generally lower than 40dB at medium frequency. From figure 3.34, it is possible to conclude that the worst case corresponds to the condition $Z_s = 200$ ohms and $Z_l = 0.1$ ohms. The insertion loss depicted in these plots is used to estimate the noise current attenuation in DM introduced by the complete filter. These plots show the attenuation required at high frequency is achieved for the set of loads and sources considered but the IL is not sufficient at low frequency.

For the CM noise, a similar procedure is used, considering that the CM source impedance changes between 1-50 ohms and the CM load impedance between 5-150 ohms. Figure 3.35 shows the CM insertion loss for that set of impedances. From this figure, it is possible to conclude the worst case in the frequency where the common mode starts to be important, corresponds to the combination $Z_s = 50\Omega$ and $Z_L = 5\Omega$. This attenuation is used to estimate the noise current reduction introduced in CM by the HF filter.

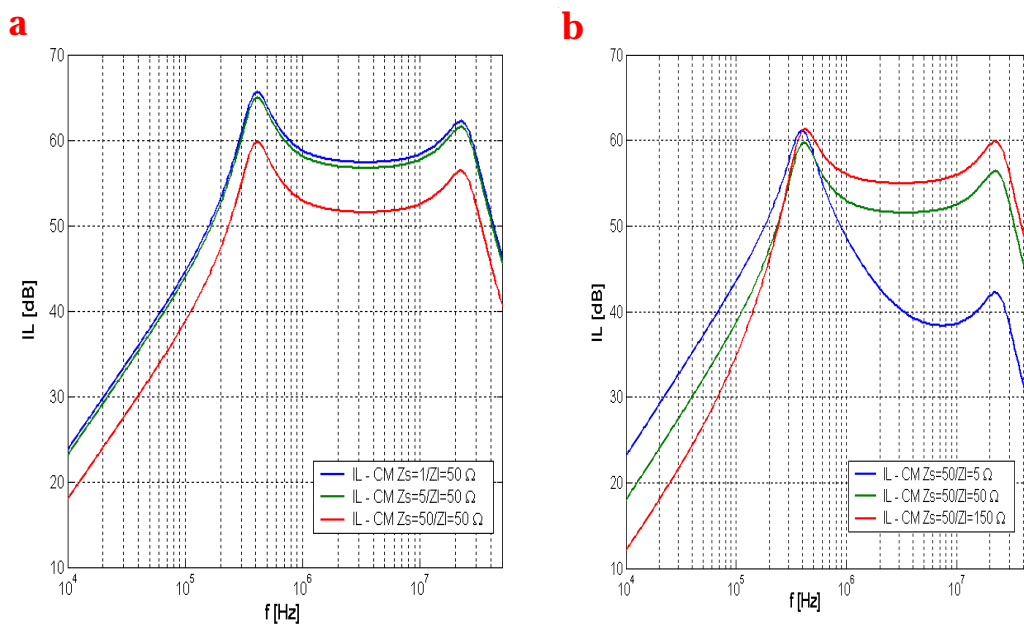


Figure 3.35: Insertion loss for the HF input filter in common mode. a) IL variation for different Z_s , b) IL variation for different Z_L .

Based on the worst case IL for differential mode and common mode, the noise at the input of the converter is estimated. Figure 3.36 shows the estimated input current noise for the Vicor converter adding the HF filter with the capacitor C1. Figure 3.37 depicts the measured input current noise for the converter including the same HF filter.

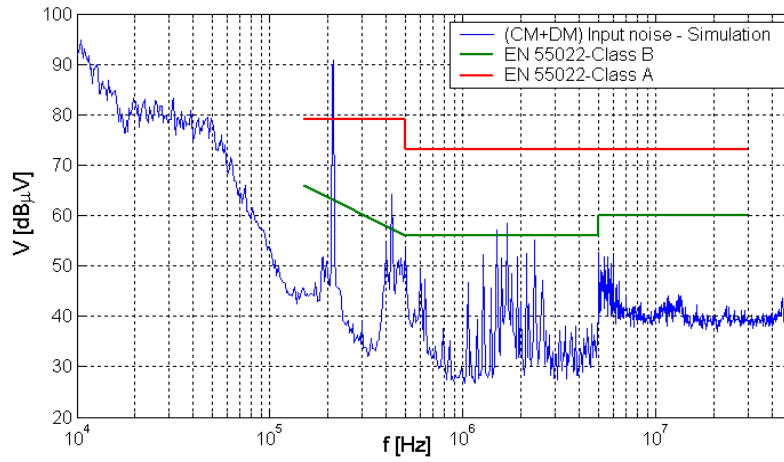


Figure 3.36: *Input current conducted emissions of Vicor converter with HF filter
Simulated values.*

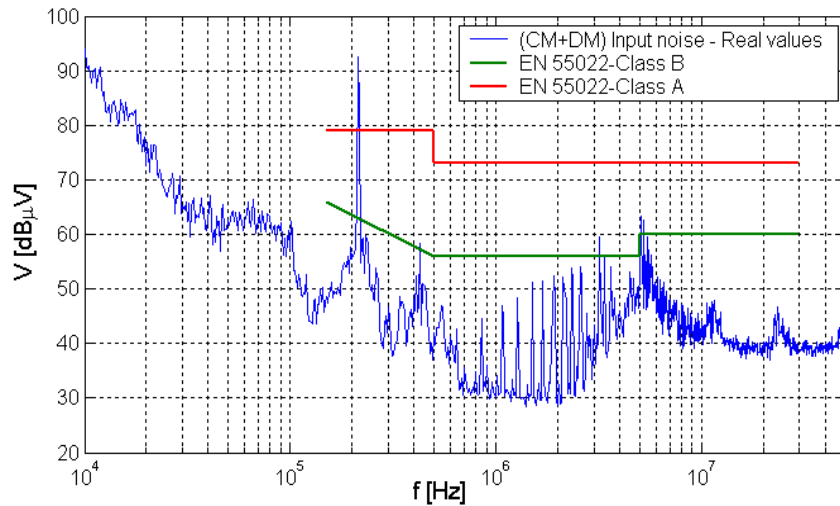


Figure 3.37: *Input current conducted emissions of Vicor converter with HF filter
Measured values.*

It is possible to observe a close agreement between the estimated and the measured noise current values. Basically, the estimated values are higher than the measured ones, giving a safety margin during the selection process of the filter. There is only a significant difference between both plots in the frequency range between 2.5 and 5 Mhz. For this frequency range, the measured values are higher than the estimated ones. The origin of this difference is the measurement set up as it has been detailed in the previous section 3.3.4.1

3.3. Filter selection

As it was predicted above, the attenuation is not enough to comply with the EN 55022-Class A at low frequency. A differential mode capacitor C5 has to be included in the HF filter to improve the filter performance to comply with the standards class A. A capacitor of $5 \mu F$ between input terminals of the HF filter provides 40dB of IL at low frequency for different load/source conditions. The DM-IL of the new filter are calculated again for different input and output impedances. In this simulation, the parasitic components of the capacitor ($L_c=2.4 \text{ nH}$, $R_c=0.150 \Omega$) have been included. Figure 3.38 shows the insertion loss of the previous HF filter with the extra capacitor (C5) in differential mode. Part a) depicts the IL for a constant load, while the source impedance is changed. The DM-IL, are quite invariant with the source impedance variation. However, the DM-IL results are quite sensitive to load variations. Part b) depicts the IL for different load impedances, while the source impedance is kept constant. The worst condition IL is used to estimate the noise current attenuation in DM introduced by the complete filter.

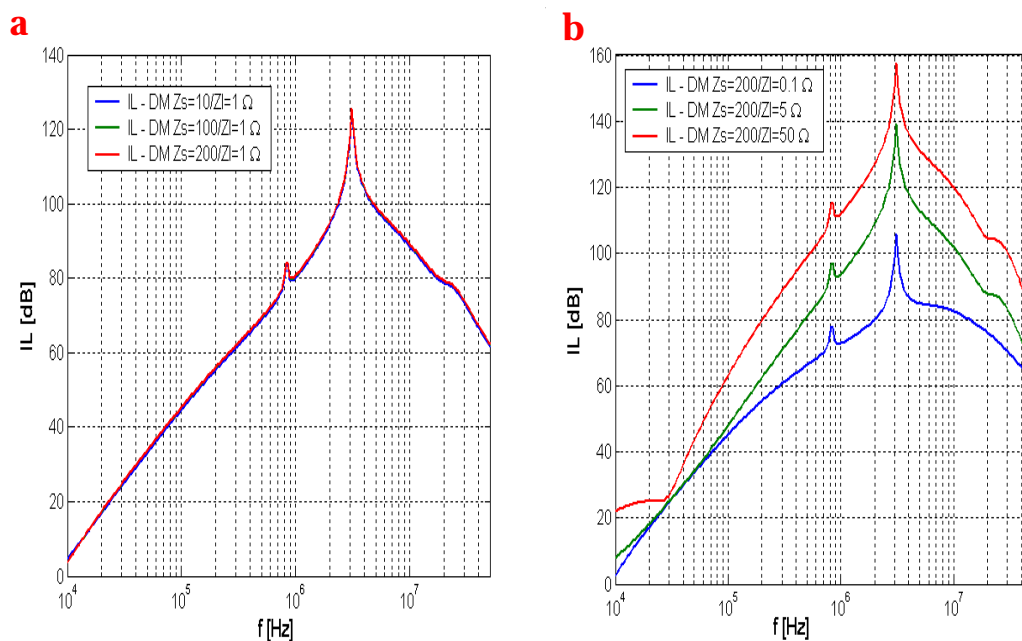


Figure 3.38: Insertion loss for the HF input filter in differential mode with the addition of the capacitor C5. a) IL variation for different Z_S , b) IL variation for different Z_L

The capacitor C5 does not produce any variation in the CM-IL of the HF filter with the capacitor C1, being the CM-IL exactly the same to the ones shown in figure 3.35. Again, based on the worst case IL for differential mode and common mode, the noise at the input of the converter is estimated. Figure 3.39 shows the estimated input current noise for the DC-DC converter including the new HF filter.

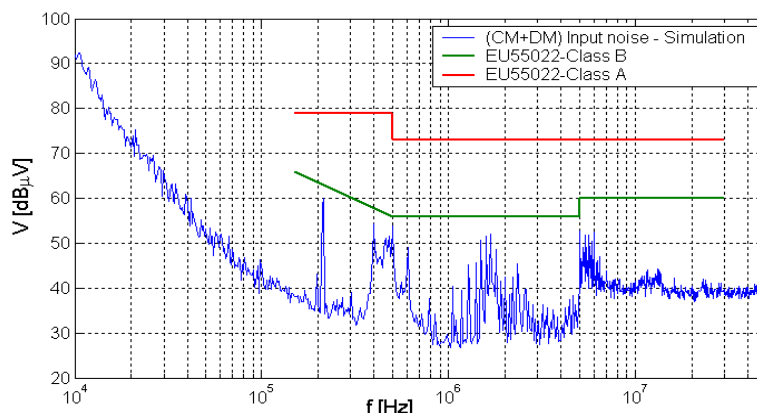


Figure 3.39: *Input current conducted emissions of Vicor converter with HF filter plus C3 Simulated values.*

The level selected for the present analysis correspond to the limits at the mains terminal of the most common specific European standards EN 55011 and 55022. The final level selection for the emission test will be based on the FEE immunity test, which will be presented in future sections. In case of selection of a different level defined by other standards like military, FCC or a new one defined by HEP, the design methodology does not change. Only the limit levels will be changed.

3.4 Stability problems with SMPS - Negative input impedance

DC-DC switching converters with tight output voltage regulation operate as a constant power load. The instantaneous value of the input impedance is positive but the incremental or dynamic impedance is negative. Due to this negative input impedance characteristic interaction among switching converters and another part of the system connected to the same distribution bus may result in system instability [24][25][26].

To analyze the behavior of the converter and the interaction with the rest of the system a reduced model of the system is necessary. The reduced model has to represent the behavior of the system at low frequency in the range between DC and frequencies near the bandwidth of the power converter. In this frequency range, the power converter behaves at the input as a constant power load in cascade with the input filter. The rest of the system can be modeled as follows: the distribution line can be approximated by a lumped inductance in series with a resistor and the HF filter can be reduced to the DM capacitors.

3.4. Stability problems with SMPS - Negative input impedance

To present a qualitative behavior of the converter at the input terminals, let us consider first the simple equivalent circuit depicted in figure 3.40. It represents a VICOR converter connected to a primary source with short leads. Using as state variables, the inductor current i_l and the capacitor voltage V_c , the state equation is:

$$C \cdot \frac{dV_c}{dt} = i_l - \frac{P_c}{V_c} \quad (3.10)$$

$$L \cdot \frac{di_l}{dt} = E - (i_l \cdot r_l) - V_c \quad (3.11)$$

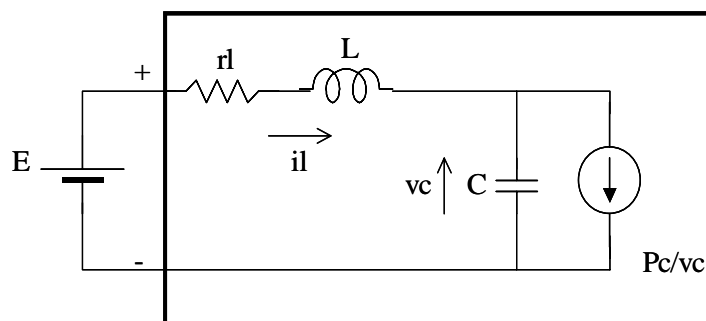


Figure 3.40: Model at the input terminals of the DC-DC converter.

This equation has two real valued equilibrium points if the condition shown in equation 3.12 is verified.

$$r_l < \frac{E^2}{4 \cdot P_c} \quad (3.12)$$

One of the equilibrium points is the operation point of the converter and the other is defined for low voltage and high current, which in general, is unstable. In order to force the converter's operation around of the equilibrium point, converters either include limits into the dynamic range of the control circuit or disable the operation of the power transistor for low values of the input voltage. VICOR converters disable the unit if the input voltage magnitude is outside of a voltage band around the equilibrium point (e.g. $V_{nom}=300V$, $V_{in}=180-375V$). In this case, the converter can still be modeled by equations 3.10 and 3.11 but including the condition, $P_c \neq 0$ if V_c is between 180V and 375V, and $P_c = 0$ if V_c is outside of this region. Figure 3.41 shows the phase portrait of equation 3.10 and 3.11, including the last condition for different initial conditions. Trajectories converge to the equilibrium point SS1 assuming it is stable. The stability of this point is defined by the condition:

$$r_l > \frac{P_c \cdot L}{C \cdot V_c} \quad (3.13)$$

where V_c is the capacitor voltage at equilibrium.

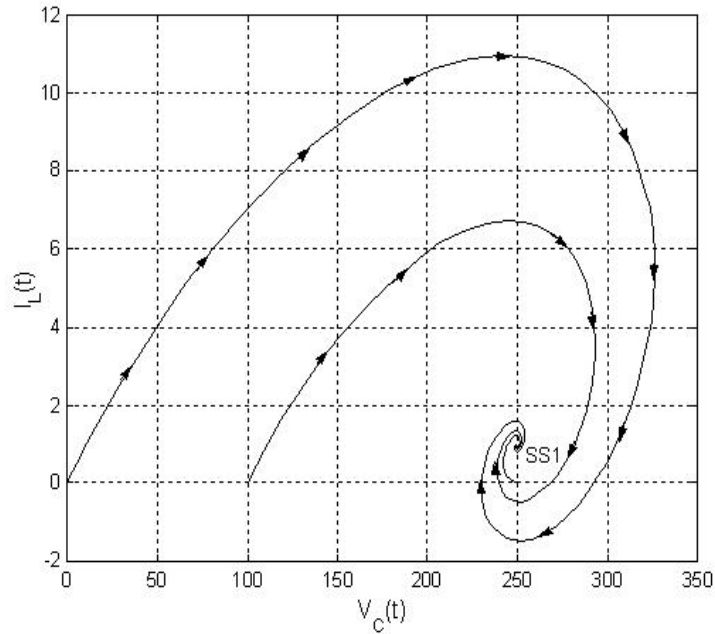


Figure 3.41: Phase portrait of the DC-DC converter input filter

As conclusion from this brief analysis, to analyse the stability of the system, the converter model can be simplified by a linearized model around the equilibrium point (small-signal analysis). The region of convergence can be estimated analytically or by simulation using a non-linear model of the converter. The linearized model of the converter at input terminal is characterized by a negative resistance of magnitude $r_n = -\frac{E}{i_l}$, where the E is the DC input voltage and i_l is the DC input current. This current depends of the load of the power converter and r_n can take different values according to the operating conditions.

Let us consider now a generic DC power distribution system composed by one AC/DC converter, a distribution line of 120 meters and N converter units connected to the end-point, as it is depicted in figure 3.42. Each DC-DC converter unit is composed by 2 DC-DC converters, connected in parallel at the input. Only one input HF filter is used per unit. The values of the components are shown in table 3.2

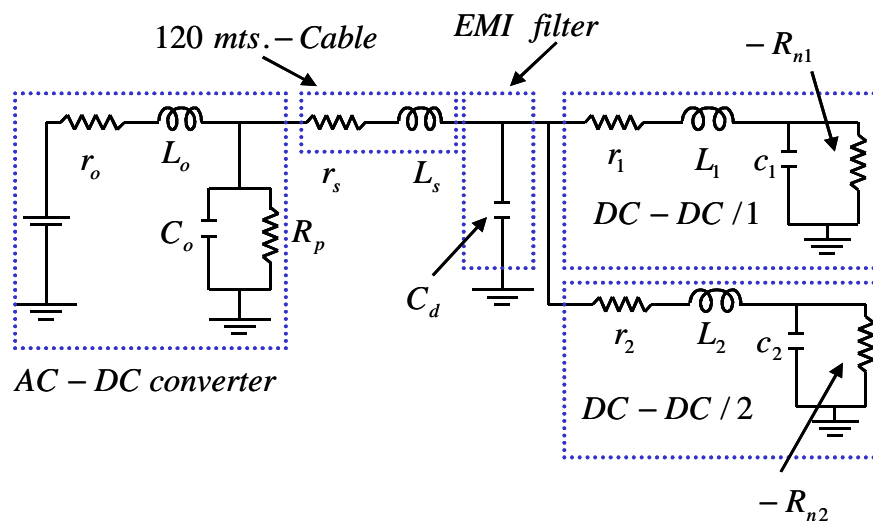


Figure 3.42: Generic DC power distribution system layout.

DC-DC / 1	DC-DC / 2	Cable	EMI filter	AC-DC unit
$L_1 = 60\mu H$	$L_2 = 100\mu H$	$L_s = 75\mu H$	$C_d = 5\mu f$	$L_o = 10mH$
$C_1 = 350nf$	$C_2 = 350nf$	$r_s = 0.4\Omega$		$C_o = 4000\mu f$
$r_1 = 4\Omega$	$r_2 = 4\Omega$			$r_o = 0.1\Omega$
$-R_{n1} = 246\Omega$	$-R_{n2} = 213\Omega$			$r_p = 1000\Omega$

Table 3.2 Parameters of generic DC power distribution system.

At the distribution bus, the system can be represented by a simplified block diagram, as shown in figure 3.43. The source sub-system contains the impedance of the AC mains, the AC/DC converter and the LV distribution cable. The load sub-system is composed by N DC-DC converter units. The source sub-system is stable when it is loaded by a resistor. Each DC-DC converter unit is stable if it is connected directly to a power supply.

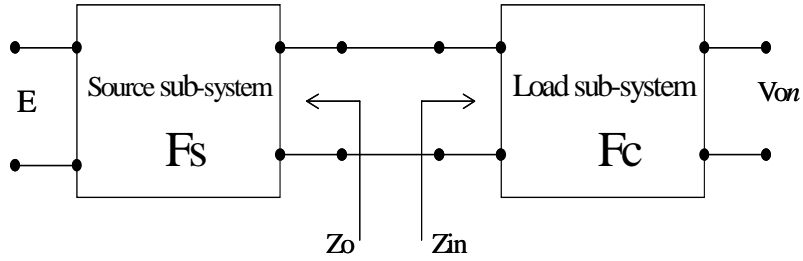


Figure 3.43: System block diagram.

Assuming the source sub-system has an input/output transference F_s and each DC-DC converter a transference F_c , the overall transference is given by.

$$\frac{V_{on}}{E} = \frac{F_s \cdot F_c}{1 + \frac{Z_o}{Z_{in}}} = \frac{F_s \cdot F_c}{1 + T_m} \quad (3.14)$$

where Z_o is the output impedance of the source sub-system and Z_{in} is the input impedance of the load sub-system. Due to both F_c and F_s are stable transference functions. The stability of the system is defined by the term $(1 + T_m)^{-1}$ that represents the loading effect between the source and load sub-systems.

If $|Z_{in}| \gg |Z_o|$ for all frequencies, the loading effect is negligible. This condition can be difficult to achieve in all the frequency range. This rule prevents any noticeable interaction between source and load sub-systems and may be overly conservative. If $|Z_o|$ is larger than $|Z_{in}|$ a considerable loading effect exists. It does not necessarily imply a stability problem. In this case, either the Nyquist criterion or Bode based analysis can be applied to the gain (T_m) to determine the system stability [2][27][28][29][30].

Figure 3.44 shows, in the upper plot, the Bode plot of the output impedance of the source sub-system and the input impedance of the load sub-system for different capacitance C_d (figure 3.42). This capacitance is included to improve the LF noise filtering and improve the stability in the high frequency region (around point B). In that area, figure 3.44 shows that T_m is equal to one and the phase is near 180° . Plots in figure 3.44 depict the load impedance for only one DC-DC converter unit connected to the bus. With an increasing number of converters connected to the bus, the input impedance Z_{in} decreases, and the stability of the system becomes critical at low frequency (point A). At this frequency, there exists interaction between the AC/DC converter filter and the negative impedance of the DC-DC converters. In this case, to improve the stability margin, it is necessary to increase the damping of the AC/DC converter.

3.4. Stability problems with SMPS - Negative input impedance

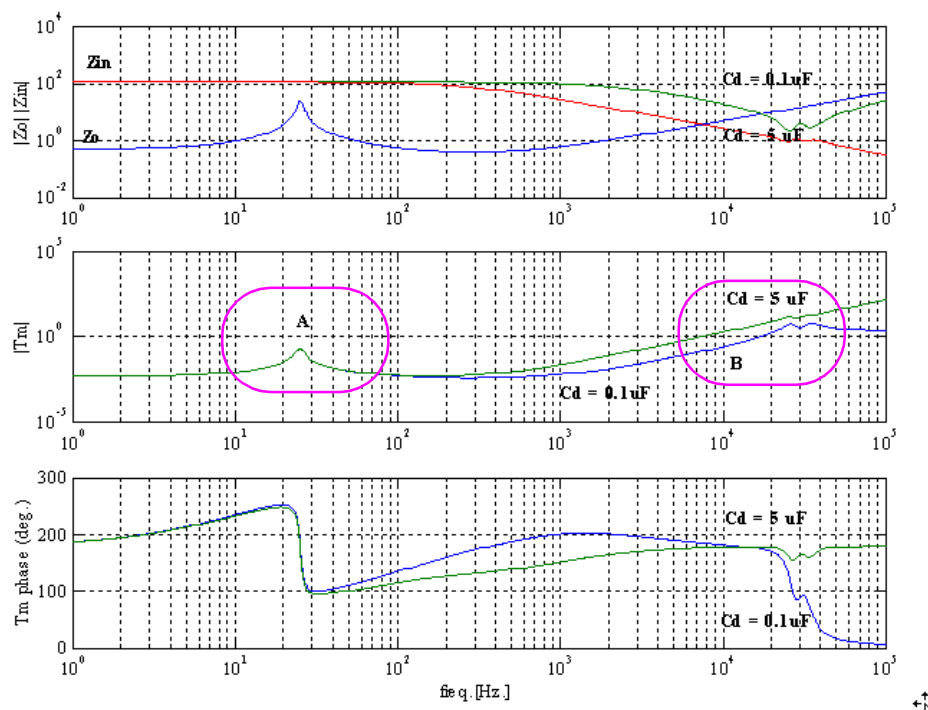


Figure 3.44: Bode plots of T_m , Z_o and Z_{in} .

In summary the influence of the damping resistor, DM filter capacitor and number of DC-DC units connected to the same bus bar are limited for stability reasons and thus it is necessary to achieve a compromise between these limitations. Table 3.3 summarizes for the presented example presented the limitations of the number of units with respect to the damping resistance and EMI filter capacitor.

Maximum number of DC-DC units		EMI filter capacitor (Cd)- μf	
		0.1	5
Damping Resistance (Rp)- Ω	30	3	7
	1000	3	5

Table 3.3 Stability summary - Maximum number of DC-DC units

3.5 Harmonics

A 400Hz AC system will be used as primary system to distribute power to the front-end electronics at CMS. The topology is based on motor-generators (M-G) that convert the 50Hz AC mains into a three phase 400Hz, 400V system that is distributed to the detector. There are three set of M-Gs that are connected in parallel to create the 400 Hz primary source. A back up M-G unit will be installed and will be used as replacement of the original M-G in case of failure of any unit or during maintenance. The proposed distribution system is depicted in figure 3.45. The motor-generator set will be installed at the surface level of the detector building. The power is transmitted to the counting room where it is separated in different networks which supply power to specific areas of the periphery of the detector. At that location, AC-DC converters transform the AC power to the DC-LV power needed by the DC-DC converters and the LV regulators feeding the front-end electronics.

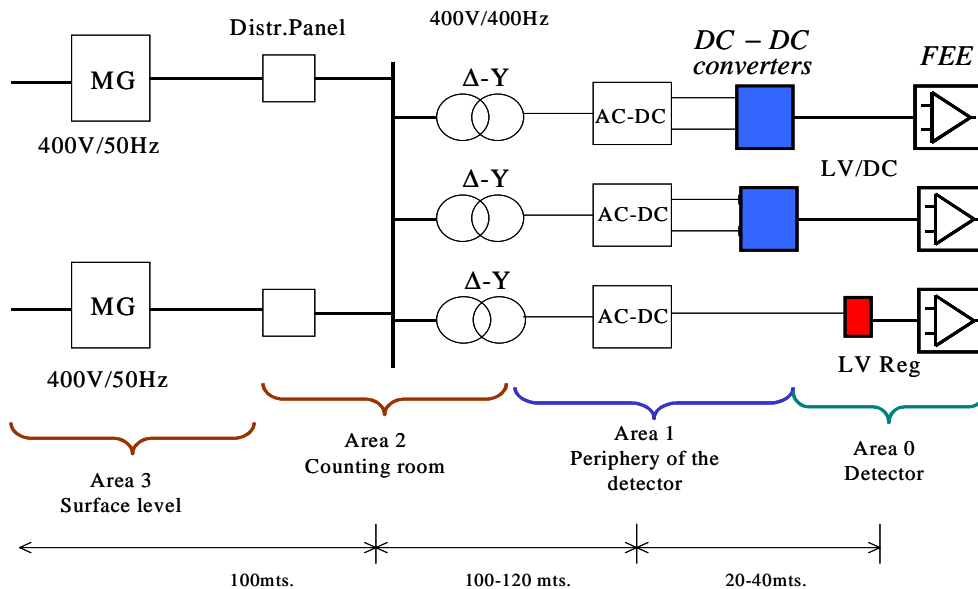


Figure 3.45: 400Hz power supply distribution block diagram

The AC-DC converters are the total loads connected to the 400Hz distribution system and they are highly non-linear. They generate harmonic currents that interact with the distribution system impedance and produce distortion in the sine wave voltage. Harmonic are prejudicial because they over-heat equipment, radiate noise, excite power distribution resonance if there exists, induce malfunction of sensitive equipment, etc. Operating at 400Hz, the harmonics extend in a range of frequencies higher than 50 Hz harmonics, inducing more problems [31]. In this

sense, harmonic standards for 400Hz systems are more strict than standards limiting harmonics in 50/60Hz systems.

Power generators and static converters generating a sine wave produce harmonic voltages as a product of the conversion. Commercial generators specify a total harmonic distortion (THD) less than 4%, individual frequency voltage harmonics less than 3% and total deviation less than 3%, while static converters can produce an output sine wave with a THD better than 3% for all the load range. In both cases, the quality of the output waveform is very high.

It will be ideal to compensate harmonics at the point where they are generated, but in-situ compensation is not economic and it is more practical to force the loads to reduce the number of harmonics injected to the distribution system. The definition of harmonic indices and limits are characterized by [31];

- The values given by the harmonic indices should be physically meaningful and strongly correlated to the severity of the harmonic effects.
- It should be possible to determine by measurements whether or not the limits of the harmonics indices are met.
- Harmonic indices should be simple and practical so that they can be widely used with ease.

Harmonic effects differ substantially depending on the characteristics of the equipment affected. Therefore, the severity of the harmonic effects imposed on all types of equipment cannot be perfectly correlated to a few, simple indices. Recommended harmonic indices are: Individual and total voltage distortion, individual and total current distortion and depth of total notch area and distortion of bus voltage distorted by commutation notches.

The IEEE Std 519-1992 [32] describes the recommended practice to define harmonic limits for individual consumers at 50/60Hz. This standard defines the limits for individual loads based on the load size, load diversity, etc. The objectives of the harmonic current limits are to limit the maximum individual frequency voltage harmonic to 3% of the fundamental and the voltage THD to 5%. Current limits based only on voltage distortion are not complete because it assumes the unlimited ability of the generator and distribution system to absorb harmonic currents [33]. This standard defines the absolute harmonic current limits using similar criteria than above. For dedicated systems, as CMS, it limits the individual harmonic current for low order harmonics to 4%.

To estimate the effect of the load harmonic current, different configurations of three phase rectifiers coupled with a step-down transformer are used. For the first estimation, the transformer is assumed ideal and the effect of the switching overlapping of the rectifiers are neglected. Three phase rectifiers coupled by transformers have the advantage of using the winding connection at both the primary and secondary to cancel harmonics.

The topology of a three-phase full-bridge rectifier with a Delta/Wye transformer is depicted in figure 3.46. Line-line and line neutral voltages and ideal line current waveforms are shown in figure 3.47 for this converter. The harmonic current levels and the voltage drop of those harmonic currents in the distribution lines are depicted in figure 3.46. This analysis was carried out assuming a distribution line with a size wire AWG#7 with a length of 100mts. At the end of the line, 15 power converters are connected.

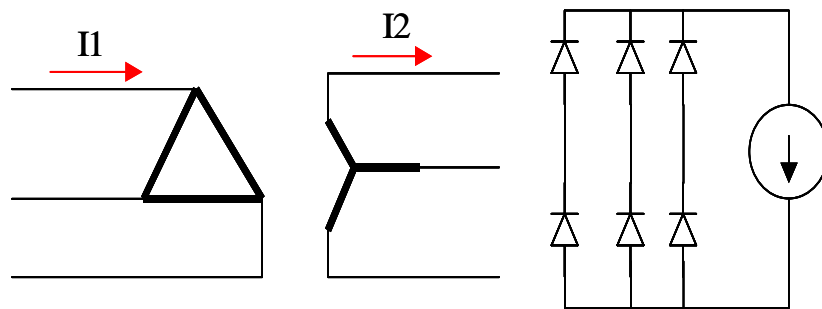


Figure 3.46: Electric scheme of the AC/DC converter

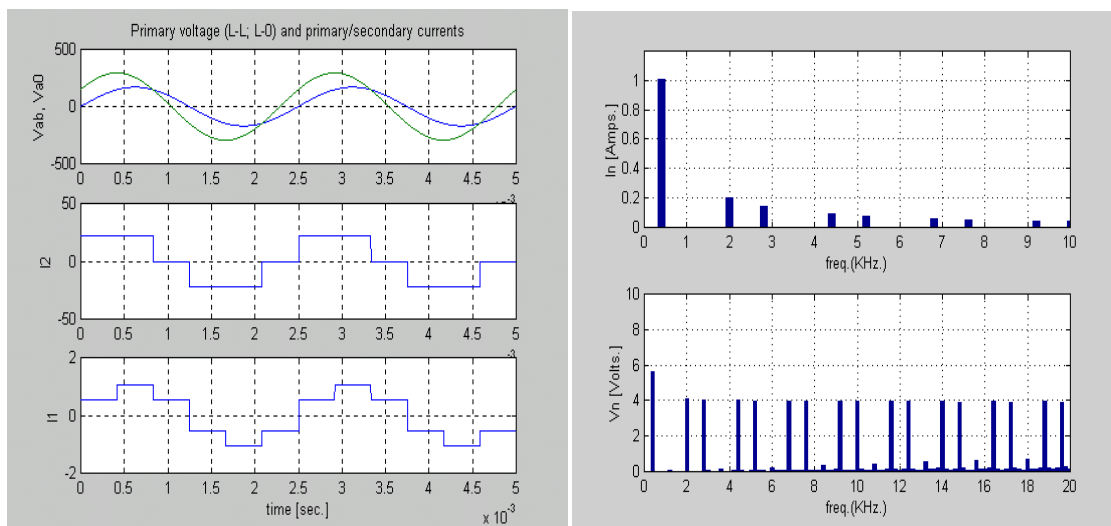


Figure 3.47: a) Primary and secondary phase current and voltage. b) Spectrum of the rectifier input current, Spectrum of the voltage drop in the distribution lines

From figure 3.47, the individual frequency voltage harmonic is about 2.3% that is close to the limit defined by the IEEE-Std 519. The individual frequency current limit defined by the same standard is 4% of the fundamental for harmonic orders lower than 11, and the converter analyzed has the 5th harmonic component equal to 20% of the fundamental while the 7th harmonic component is 14.3%. If some of the

limits presented here are going to be used in the 400Hz distribution, particular care must be taken to reduce the harmonic content produced by the load using filtering or harmonic cancellation.

3.6 Summary

The CMS LV distribution system is composed by switching power supplies and AC-DC converters that generates conducted electromagnetic emissions and harmonics in the distribution cables. All switching converters generate high frequency conducted noise, which depends strongly on the topology and parasitic components of the converter. The measurement of this noise current is very important to evaluate the performance of the power supplies. Standards generally use a LISN to perform these measurements. This device presents a constant impedance of 50 ohms to the noise sources in certain frequency range. However, in the real system, DC-DC converters are connected directly to the load or primary power source using cables and the impedance presented by the system to the input or output of the converter varies from a hundreds of mohms to hundreds of ohms. This configurations may generate higher conducted emission than the configurations loaded with 50 ohms. For that purpose, noise emissions are measured based on a topology closer to the real one where the converter load is low impedance.

The conducted emission can affect the performance of the FEE, being necessary the use of EMI filters to attenuate these emissions to acceptable levels required to FEE. Commercial filters are used to attenuate these emissions. The filter performance is defined by the insertion loss of the filter. The IL depends strongly on the impedances to which they are connected, this impedances can change with the frequency or resonate with the filter reducing the filter performance. The differential mode-IL is more sensitive to impedance variations than the common mode-IL, being necessary to select the adequate load and source impedance of the filter that allows to estimate the filter performance with enough safety margin.

Input filters interact adversely with DC-DC converters and the distribution system at low frequency, resulting in severe performance degradation or even instability. This problem is originated by the negative input impedance that DC-DC converters present when they operate with tight close-loop regulation of the output voltage. These instability limits the number of DC-DC converters connected to the same AC-DC box. It can be controlled establishing a compromise between damping, differential mode capacitor and number of units connected to the same bus.

The 400Hz power distribution system of CMS is fully loaded by non-linear loads. These non-linear loads generate harmonic currents in the distribution system that disturbs the voltage generated by the motor-generators sets. The harmonics can be

cancelled forcing to the loads to reduce the number of harmonics injected to the distribution system.

3.7 References

[1] P.Lindman, L. Thorsell, "*Applying Distributed Power Modules in Telecom Systems*", IEEE Transactions on Power Electronics, Vol 11, N-2, pp 365-373, March 1996.

[2] B. Cho, F. Lee, "*Modeling and Analysis of Spacecraft Power Systems*", IEEE Transactions on Power Electronics, Vol 3, N-1, pp 44-54, January 1988.

[3] J. Kierstead, H. Takai, "*Switching Power Supply Technology for ATLAS Lar Calorimeter*", Proc. 6th Workshop on Electronics for LHC experiments, pp 380-382, September 2000.

[4] B. Allongue et al., "*Design Consideration of low Voltage DC Power Distribution*", Proc. 6th Workshop on Electronics for LHC experiments, pp 388-392, September 2000.

[5] C.R. Paul, "*Introduction to Electromagnetic Compatibility*" NY: Wiley-Interscience, 1992, ISBN-0-471-54927-4

[6] T. Williams, "*EMC for Product Designers*", 1997, ISBN-0-7506-2466-3

[7] F.Szoncso, "*EMC in High Energy Physics*", Proc. 5th Workshop on Electronics for LHC Experiments, LEB 99, pp 20-24, September 1999

[8] F. Arteché, C. Rivetta, F. Szoncso, "*Effects of CM and DM noise propagation in LV distribution cables*", Proc. 9th Workshop on Electronics for LHC experiments, LECC2003, pp 380-385, Amsterdam, October 2003

[9] M. Vilathgamuwa, J. Deng, K.J. Tseng, "*EMI suppression with switching frequency modulated DC-DC converters*" Industry Applications Magazine-IEEE, Vol. 5, Issue 6, pp 27 -33, December 1999

[10] D. M. Mitchell, "*Power line filter design considerations for DC-DC converters*", Industry Applications Magazine-IEEE, Vol. 5, Issue 6, pp 16 -26, December 1999

[11] Marian K. Kazimierzczuk, Giuseppe Sancineto, Gabriele Grandi, Ugo Reggiani and Antonio Massarini, "*High-Frequency small signal model of ferrite core inductors*" IEEE Transactions on Magnetics, Vol. 35, N-5, pp 4185-4191, September 1999

[12] W.D. Kimmel, "*Wide frequency impedance modeling of EMI ferrites*", Proc IEEE International Symposium on Electromagnetic Compatibility, 1994, Chicago, IL, USA, pp 221 -223, August 1994

- [13] Christopher Olivier, "A new core loss model" Switching power magazine, pp 28-30, Spring 2002.
- [14] M.J. Nave, "On modeling the common mode inductor", Proc. IEEE 1991 International Symposium on Electromagnetic Compatibility, 1991, Cherry Hill, NJ, USA, pp 452-457, August 1991.
- [15] F. Amemiya, K. Takagi, N. Kuwabara, S. Hamada, Y. Iwamoto, "Developing a common-mode choke coil with high-permeability core used high-speed telecommunications port for UTP cable", Proc. 2002 IEEE International Symposium on Electromagnetic Compatibility Vol. 1, N-5, pp 314-319. September 2002.
- [16] P. F. Okyere, "A novel physically-based Pspice compatible model for common mode chokes", Proc. of International Symposium on Electromagnetic Compatibility, Tokyo, Japan, pp.33-36, May 1999.
- [17] Robert West , "Common mode inductors for EMI filter require careful attention to core material selection", PCIM magazine, July 1995.
- [18] P. F. Okyere, L. Heinemann, "Computer-aided analysis and reduction of conducted EMI in switched-mode power converter", Proc. Applied Power Electronics Conference and Exposition, APEC '98, Anaheim, CA, USA, Vol. 2, pp 924-928, 1998.
- [19] Michael Tao Zhang, "Electrical, thermal and EMI design of high density, low profile power supplies", Dissertation, ETD-173510281975580, Virginia Polytechnic institute, February 1997.
- [20] D. Dallas, "Gain Confidence In Network Designs By Simulating The LAN Magnetics", Electronic Design Magazine, Vol. 48, N- 2, pp 121-128 March 2000.
- [21] Feng Zhang, "Investigation of electromagnetic interface of PWM motor drives in automotive electrical systems", LEES Technical report TR-99-004, Massachusetts Institute of Technology (MIT), December 1999.
- [22] Keith Armstrong, "Choosing and using filters", EMC & Compliance Journal, <http://www.compliance-club.com/>
- [23] Keith Armstrong, "Design Techniques part 3 - Filters and surge protection devices", EMC & Compliance Journal , <http://www.compliance-club.com/>.
- [24] Liu Jinjun, T.G. Wilson, T.G.; Zhao Qun, Dong Wei, F.C. Lee, "Large-signal model of a downstream Dc/DC converter for analysis and design of front-end PFC rectifier using computer simulation", Proc. IEEE Applied Power Electronics Conference and Exposition APEC 2003, Vol 2, pp 1002 - 1007, February 2003.

- [25] B. Allonge, F. Arteche, C. Rivetta, F. Szoncsó, "*EMI Filter Design and Stability Assessment of DC Voltage Distribution based on Switching Converters*", Proc. 7th Workshop on Electronics for LHC experiments, LECC 2001. Stockholm, pp 353-357, September 2001.
- [26] A. Ciccolella, T. Blancquaert, J. Verniolle, "*Power inter-face characterization between the Russian module and the ESA automated transfer vehicle*", Proc. Sixth European Space Power Conference, May 2002.
- [27] C. Wildrick et.al., "*A method of defining the load impedance specification for a Stable Distributed Power System*", IEEE Transactions on Power Electronics, Vol.10, N-3, pp 280-285. May 1995
- [28] Choi, B. Cho, B, "*Intermediate Line Filter Design to Meet Both Impedance Compatibility and EMI Specifications*", IEEE Transactions on Power Electronics, Vol.10, N-5, pp 583-588, September 1995.
- [29] L.R. Lewis, B.H. Cho, F.C. Lee, B.A. Carpenter, "*Modeling, analysis and design of distributed power systems*", Proc. Annual IEEE Power Electronics Specialists Conference PESC '89 Record., Vol 1, pp 152 - 159, June 1989.
- [30] M. Florez-Lizarraga, A. Witulski, "*Input filter Design for multiple-module DC power systems*", IEEE Transactions on Power Electronics, Vol.11, N-3, pp 472-479, May 1996.
- [31] T. Gruz, "*Design Considerations for Powering 415-Hz Computer Systems*", IEEE Trans. on Industry Applications, Vol. 25, N-6, 1989.
- [32] IEEE-Std 519-1992, "*IEEE Recommended practice for Harmonic Control in Electrical Power Systems*", Ed 1992.
- [33] T. Gruz, "*Uncertainties in Compliance with Harmonic Current Distortion Limits in Electric Power Systems*", IEEE Transactions on Industry Applications, Vol. 27, N-4, 1991.

Chapter 4

Noise Propagation

Power supply units for the CMS detector will be placed in two areas, the periphery of the detector, distant about 20-40 meters from the front-end electronics and the counting room located about 100-120 meters away from the FEE. The front-end electronics and the power supply units are connected through long power cables that propagate the output noise from the power supplies to the detector.

The understanding of the effect of long shielded power cables in the noise propagation and its interaction with the FEE becomes an important issue to define FEE immunity levels and the conducted noise emission levels required for the power supplies. In addition, near and far electromagnetic fields induce currents in the cable shields that interfere with the system if those currents are coupled to the conductors feeding the FEE. This coupling depends on the surface transfer impedance and surface transfer admittance of the shielded cable, which define the quality and cost of the cable.

In this chapter, the analysis of the conducted noise propagation through long cables and its effect in the system are presented. The balance among cable parameters, filters, and ground connection defines the effect on the FEE performance of common mode (CM) and differential mode (DM) noise generated by the power supplies. The influence of these parameters is studied using numerical simulation based on multi-conductor transmission line models whose parameters are extracted from real multi-conductor samples. The CM and DM propagation as well as the cross-conversion between CM and DM conducted emissions are addressed in this study.

4.1 Introduction to Multi-conductor Transmission lines (MTL)

The traditional model of a multi-conductor transmission line is a distributed parameter, multi conductor transmission line equation. There are a set of $(n+1)$

partial differential equations representing a line consisting of n conductors and a reference conductor for the line voltages. The line is considered to be a uniform line in that the $(n+1)$ conductors are parallel to each other and the z -axis of a rectangular coordinate system as it is shown in figure 4.1

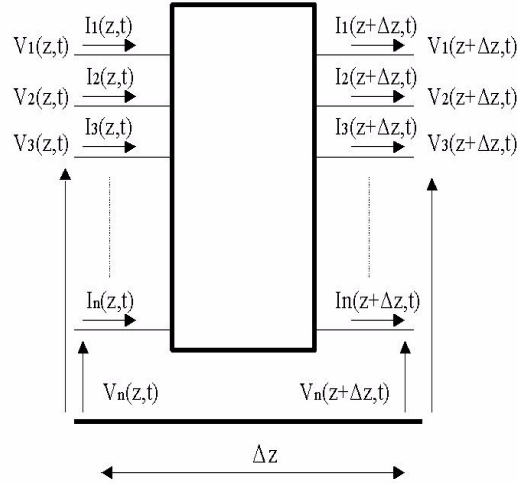


Figure 4.1: MTL model.

Based on the previous picture, the system can be modeled by the set of partial differential equations:

$$\frac{\partial}{\partial z} V(z, t) = -R \cdot I(z, t) - L \cdot \frac{\partial}{\partial t} I(z, t) \quad (4.1)$$

$$\frac{\partial}{\partial z} I(z, t) = -G \cdot V(z, t) - C \cdot \frac{\partial}{\partial t} V(z, t) \quad (4.2)$$

Where $I(z,t)$ and $V(z,t)$ are vectors representing the current and the voltage respect to the reference conductor, respectively, L, C, R, G are the per unit length inductance, capacitance, resistance and conductance $N \times N$ matrices representing the characteristic properties of the line and z is the position along the transmission line. This model assumes transverse electromagnetic (TEM) waves as the propagation mode. It allows a cable to be represented by per-unit parameters, which are relatively easy to measure or calculate given the geometry of the cable.

A detailed analysis of MTL is presented in [1]-[4]. In the present chapter only the basic concepts used to analyze the cables are defined. For the case of a generic multi-conductor cable, figure 4.2 shows a scheme of an infinitesimally length dz , where the parameters per-unit length have been identified. For the case of shielded cables, the shield has been considered as the reference conductor.

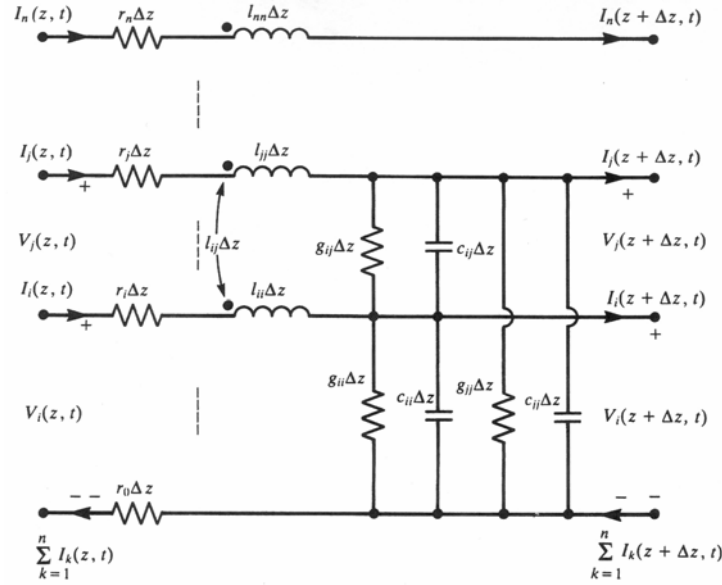


Figure 4.2: Distributed MTL model

4.2 Definitions of per-unit length parameters

Based on the TEM model of the transmission line, L,C,R,G parameters can be calculated as static field solution in the transversal plane for perfect line conductors. The definitions of these matrices are given in the following paragraphs.

4.2.1 Per unit length inductance matrix

The per-unit length inductance matrix L, relates the current flowing in each conductor with the flux linking the circuits formed by the conductors.

$$\phi = L \cdot I \quad (4.3)$$

The diagonal elements represent the self-inductance, that are defined as the ratio between the flux linking the loop formed by the i-th conductor and reference and the current flowing through the i-th conductor.

$$l_{ii} = \frac{\phi_i}{I_i} \Big|_{I_1 = \dots = I_{i-1} = I_{i+1} = \dots = I_n = 0} \quad (4.4)$$

The mutual inductances l_{ij} are defined as the ratio between the flux linking the loop formed by the i-th conductor and reference and the current flowing through the j-th conductor.

$$l_{ij} = \frac{\Phi_i}{I_j} \Big|_{I_1 = \dots = I_{j-1} = I_{j+1} = \dots = I_n = 0} \quad (4.5)$$

$$L = \begin{bmatrix} l_{11} & l_{12} & \dots & l_{1n} \\ l_{21} & l_{22} & \dots & l_{2n} \\ \dots & \dots & \dots & \dots \\ l_{n1} & l_{n2} & \dots & l_{nn} \end{bmatrix} \quad (4.6)$$

The definition of the i-th circuit is critically important in obtaining the correct value and the sign of these elements. The i-th circuit is the surface between the reference conductor and the i-th conductor (which is of arbitrary shape but is uniform along the line). The magnetic flux per-unit-length penetrating this surface is defined as being in the clockwise direction around the i-th conductor when looking in the direction of increasing z. In other words, the flux direction, Ψ_i , through surface s_i , has the direction of the magnetic flux that would be generated by the current of the i-th conductor. This is shown in figure 4.3.

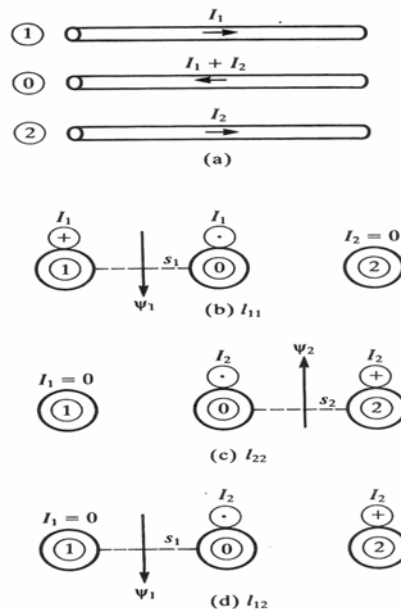


Figure 4.3: Flux circuits for the estimation of the per-unit length inductances for a ribbon cable structure of three conductors.

4.2.2 Per unit length capacitance matrix

The per-unit length capacitance matrix, C , relates the line voltage with the total charge in each conductor.

$$Q = C \cdot V \quad (4.7)$$

The coefficients of the matrix C are the electrostatic induction coefficients.

$$C = \begin{bmatrix} \Sigma(C_{1k}) & -C_{12} & \dots & -C_{1n} \\ -C_{21} & \Sigma(C_{2k}) & \dots & -C_{2n} \\ \dots & \dots & \dots & \dots \\ -C_{n1} & -C_{n2} & \dots & \Sigma(C_{nk}) \end{bmatrix} \quad (4.8)$$

The diagonal terms represent the self -electrostatic induction coefficients,

$$Q_i = V_i \cdot B_{ii} = V_i \cdot \sum_{k=1}^n C_{ik} \quad (4.9)$$

where $V_j = 0$ for all $j \neq i$

These coefficients define a relation between the charges stored in the i -th conductor with the voltage applied to the i -th conductor when the rest of conductors are connected to the reference. Each self-induction coefficient is equal the sum of self and mutual capacitances defined by the conductor.

The off-diagonal terms are the mutual-electrostatic induction coefficients and defined as:

$$Q_i = B_{ij} \cdot V_j = -C_{ij} \cdot V_j \quad (4.10)$$

where $V_i = 0$ for all $i \neq j$

This represents the charge stored in the i -th conductor when a unit voltage is applied to the j -th conductor with all other conductors connected to the reference.

The elements of the C matrix are frequently referred to as the electrostatic induction coefficients. However, these coefficients are not equal to the self and mutual capacitance among the conductors and the term "electrostatic induction coefficients" might be confusing. The self and mutual capacitance coefficients are shown in figure 4.4.

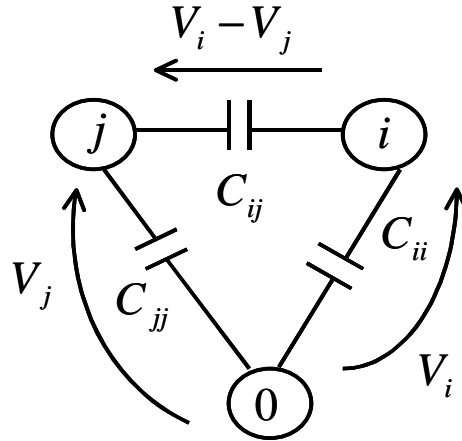


Figure 4.4: Circuits of the definition of the per-unit length capacitance coefficients: self terms and mutual terms.

A simple form to obtain the electrostatic inductance coefficients is by definition of the potential matrix P .

$$V = P \cdot Q \quad (4.11)$$

The entries in P are referred to as the coefficients of potential. Once the entries in $[P]$ are obtained, the electrostatic induction coefficients are obtained taking the inverse of $[P]$ ($[C] = [P]^{-1}$).

$$p_{ii} = \frac{V_i}{q_i} \Big|_{q_1 = \dots = q_{i-1} = q_{i+1} = \dots = q_n = 0} \quad (4.12)$$

$$l_{ij} = \frac{V_i}{I_j} \Big|_{q_1 = \dots = q_{j-1} = q_{j+1} = \dots = q_n = 0} \quad (4.13)$$

This method is usually used in finite element programs to calculate the capacitance matrix based on the geometry and material properties of the transmission line. In the section *Measurement Procedure*¹, a measurement method to determine both the self and mutual-capacitances and the electrostatic induction coefficients is presented.

¹ See section 4.3

4.2.3 Per unit length resistance matrix

The per-unit length resistance matrix, R , relates the current flowing in each conductor to the line voltage drop

$$R = \begin{bmatrix} R_1 + R_o & R_o & \dots & R_o \\ R_o & R_2 + R_o & \dots & R_o \\ \dots & \dots & \dots & \dots \\ R_o & R_o & \dots & R_n + R_o \end{bmatrix} \quad (4.14)$$

The diagonal elements of the matrix correspond to the sum of the per unit length resistance of the i -th conductor and the resistance of the reference conductor. The off diagonal of the matrix correspond only to the per-unit length resistance of the reference conductor.

4.2.4 Per unit length conductance matrix

The per unit length conductance matrix G , relates all the line voltages to the total transverse conduction current passing between the conductors.

$$I_t = G \cdot V \quad (4.15)$$

$$G = \begin{bmatrix} \Sigma(g_{1k}) & -g_{12} & \dots & -g_{1n} \\ -g_{21} & \Sigma(g_{2k}) & \dots & -g_{2n} \\ \dots & \dots & \dots & \dots \\ -g_{n1} & -g_{n2} & \dots & \Sigma(g_{nk}) \end{bmatrix} \quad (4.16)$$

The diagonal elements of the conductance matrix correspond to the sum of self-conductance and mutual-conductance of conductor i , while the off diagonal elements of the matrix corresponds to the negative value of the coefficient mutual conductance between i -th and j -th conductor.

To determine the entry in G in the i -th row and j -th column we could enforce a voltage between the j -th conductor and the reference conductor, with all other conductor voltages set to zero and determine the transverse current, I_{ji} , flowing between the i -th conductor and reference conductor, as it is shown in figure 4.5

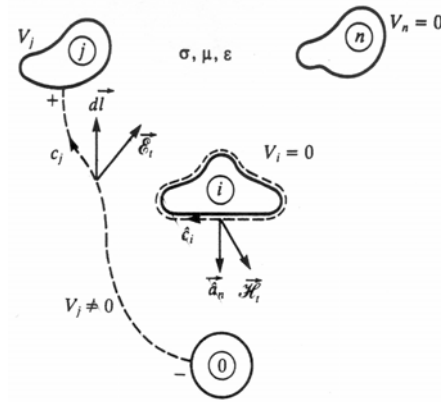


Figure 4.5: Circuits of the definition of the per-unit length conductance coefficients.

Denoting each of the entries in G as G_{ij} we have:

$$G_{ij} = \frac{I_{ii}}{V_j} \Big|_{V_{q1} = \dots = V_{i-1} = V_{i+1} = \dots = V_n = 0} \quad (4.17)$$

In general the values of this matrix are very small in the range of frequencies of our interest and G-matrix can be considered as a null matrix. For this reason these values have not been measured.

4.3 Parameters measurement procedure

All per unit values defined above can be measured or calculated based on the geometry and material properties. In the present study some of them are calculated based on [4] and some of them are measured using an LRC meter covering a frequency range between 1 kHz and 5 MHz. Some of these parameters are frequency dependent due to skin¹ effect in the conductors and proximity effects. The measurement procedure is presented and results from HCAL power cable and Tracker power cable are used as an example of these measurement procedure.

4.3.1 Inductance

Let us consider a tracker power cable as a multi-conductor cable with three conductors and a reference line (for the HCAL power cable this is actually a two conductor cable). In both cases, the shield of the cable is considered as the reference

¹ A detailed analysis of this effect is presented in appendix A.

4.3. Parameters measurement procedure

conductor. The aim of the measurement procedure is to calculate the 6 values (3 for HCAL) of the multi-conductor theory inductance matrix, which is symmetrical. The self-inductance (L_{11}, L_{22}, L_{33}) and mutual-inductance between conductors (L_{12}, L_{13}, L_{23}) are measured to complete the inductance matrix.

The dependence of the cable inductance with the frequency and the cable resonances force the use of cables with different length to carry out the measure of the cable inductance in the whole frequency range. Short cables are used to perform the measurement of the inductance at high frequency to avoid the resonance of cable and to have completely developed the skin effect. However long cables are used to measure the inductance at low frequency, where the skin effect is not still developed. At low frequency, the cable length has to be compatible with minimum impedance and precision that the instrument can measure.

The values of the self-inductance of the cable have been measured with the following configuration. The line to be measured and the shield are short-circuited. All remaining lines are left in an open circuit configuration. Figure 4.6 shows the layout to measure the inductance L_{ii} . The measured value is the inductance between the i -th and reference conductor.

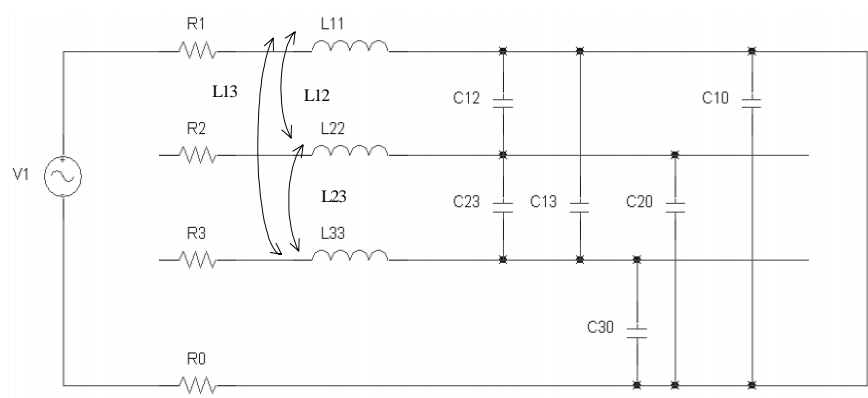


Figure 4.6: Cable connection to calculate the Self inductance of line 2.5V of Tracker power cable (MSC).

The values of each mutual inductance of cable can be measured with the following configuration shown in figure 4.7. The lines, whose mutual inductance will be measured, should be connected together and all remaining lines and the reference are left in an open circuit configuration.

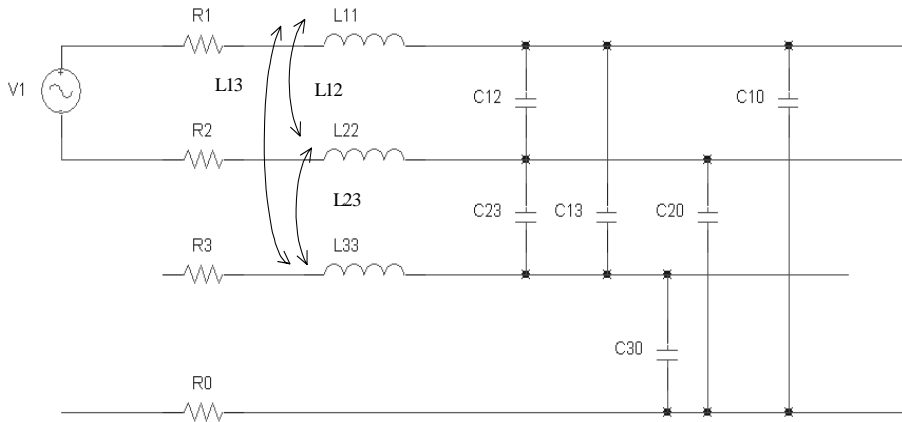


Figure 4.7: Cable connection to calculate the Mutual inductance of line 1 and 2 for Tracker power cable (MSC).

$$L_{ij} = \frac{L_{ii} + L_{jj} - M_{ij}}{2} \quad (4.18)$$

Where the M_{ij} is the value measured with the LRC meter. The same procedure is used to obtain the rest of the values of the matrix. The measured values for both cable samples are shown in figure 4.8 and 4.9.

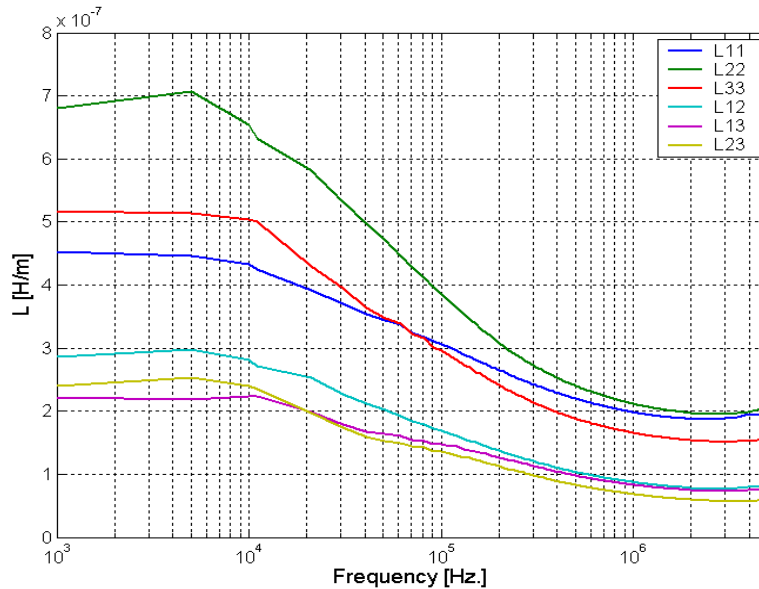


Figure 4.8: Measured values of per-unit length inductance matrix for Tracker power cable (MSC).

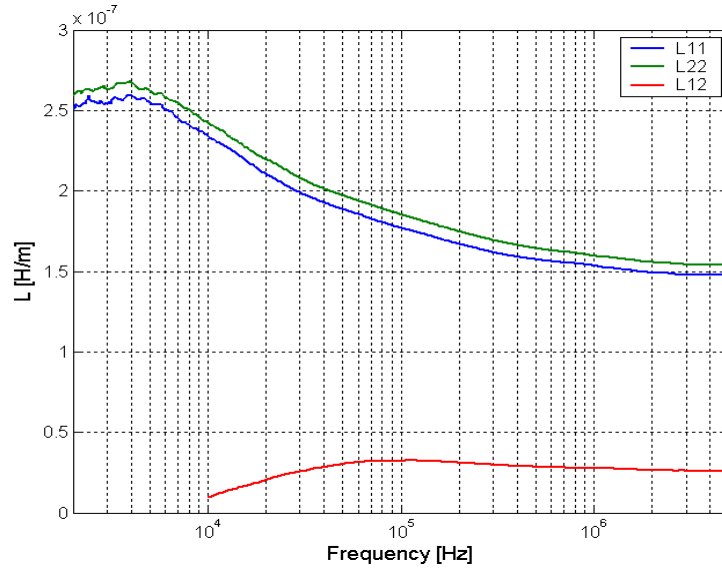


Figure 4.9: Measured values of per-unit length inductance matrix for the HCAL power cable.

From the above picture it is possible to see that the inductance values are dependent of the frequency due to skin effect. The total per unit length inductance of a transmission line is the sum of the external and internal inductance. The external inductance is frequency independent and depends mainly of the external configuration of the cable. However, the internal inductance is approximately constant (for a single wire is equal to 50 nH/m) only in the low frequency range, up to a frequency where the conductor radius is on the order of skin depth. Above this frequency the conductor internal inductance decreases with an order of \sqrt{f} or 10 dB per decade. Thus the total inductance at low frequencies is equal to:

$$l = l_i + l_e \quad (4.19)$$

At high frequencies the internal inductance can be neglected and the total inductance can be approximated by:

$$l \approx l_e \quad (4.20)$$

4.3.2 Capacitance

Let us consider the three-conductor cable of the tracker power cable (Two-conductors for HCAL) and a reference line. The self and mutual -capacitance are defined as depicted in figure 4.10.

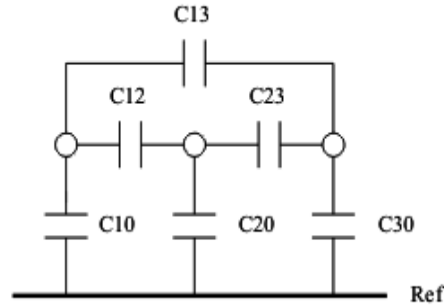


Figure 4.10: Self and mutual capacitance of Tracker power cable (MSC).

To identify the capacitances shown in figure 4.10 one performs a series of measurements, that are the dual with respect to the ones performed to obtain the inductances. This technique is well described in [5] and [6], hence in this section only two particular cases are analyzed. Let us denote Cm_{ij} as the measured value, that is, the capacitance between the i -th and j -th conductors following the connections indicated in figure 4.11.

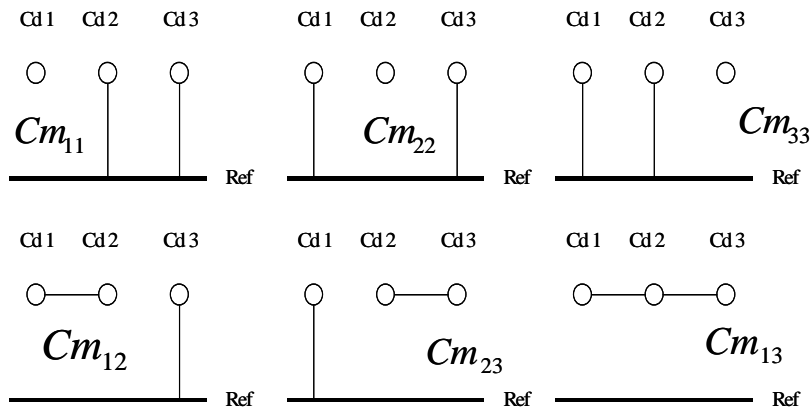


Figure 4.11: Cable connection to calculate the capacitance matrix values of Tracker power cable (MSC).

The lines in this figure indicate a short-circuit connection between the conductor and ground or between the conductors. The definition of Cm_{ij} and C_{ij} involves symmetry relations and we need to establish $\frac{(n^2 - n)}{2} + n$ relations instead of n^2 (6 unknowns values for the tracker instead of 9, and 3 unknowns instead of 4 for the HCAL power cable).

4.3. Parameters measurement procedure

Based on the definition given in figures 4.10 and 4.11, it is possible to establish the following relations.

$$Cm_{11} = C_{10} + C_{12} + C_{13} \quad (4.21)$$

$$Cm_{12} = C_{10} + C_{13} + C_{22} + C_{23} \quad (4.22)$$

$$Cm_{13} = C_{10} + C_{20} + C_{30} \quad (4.23)$$

$$Cm_{22} = C_{12} + C_{22} + C_{23} \quad (4.24)$$

$$Cm_{23} = C_{12} + C_{22} + C_{33} + C_{13} \quad (4.25)$$

$$Cm_{33} = C_{13} + C_{23} + C_{33} \quad (4.26)$$

To identify the capacitance coefficients and the electrostatic induction coefficients based on the measurement of the equivalent capacitances Cm_{ij} , three different vectors are defined by:

$$Cm = [Cm_{11}, Cm_{12}, Cm_{13}, Cm_{22}, Cm_{23}, Cm_{33}]^t \text{ - Measured vector} \quad (4.27)$$

$$C_p = [C_{10}, C_{12}, C_{13}, C_{20}, C_{23}, C_{30}]^t \text{ - Self / Mutual capacitance vector} \quad (4.28)$$

$$C = [B_{11}, B_{12}, B_{13}, B_{22}, B_{23}, B_{33}]^t \text{ - Electrostatic induction coefficient}^1 \text{ vector} \quad (4.29)$$

Based on equation 4.8 and 4.21 to 4.25, the vectors are related by the following equations.

$$C = D^{-1} \cdot H^{-1} \cdot Cm \quad ; \quad C_p = H^{-1} \cdot Cm \quad (4.30)$$

Where the definitions of H and D^{-1} are:

$$H = \begin{bmatrix} 1 & 1 & 1 & 0 & 0 & 0 \\ 1 & 0 & 1 & 1 & 1 & 0 \\ 1 & 0 & 0 & 1 & 0 & 1 \\ 0 & 1 & 0 & 1 & 1 & 0 \\ 0 & 1 & 1 & 1 & 0 & 1 \\ 0 & 0 & 1 & 0 & 1 & 1 \end{bmatrix} \quad D^{-1} = \begin{bmatrix} 1 & 1 & 1 & 0 & 0 & 0 \\ 0 & -1 & 0 & 0 & 0 & 0 \\ 0 & 0 & -1 & 0 & 0 & 0 \\ 0 & 1 & 0 & 1 & 1 & 0 \\ 0 & 0 & 0 & 0 & -1 & 0 \\ 0 & 0 & 1 & 0 & 1 & 1 \end{bmatrix} \quad (4.31)$$

1 Multi conductor theory capacitance matrix coefficients are defined by equation 4.8

The measured values are shown in figure 4.12 for tracker (MSC) and 4.13 for the HCAL power cable. As it can be observed from the plots, the magnitude of the capacitance is not as strongly frequency dependent [7] as the inductance.

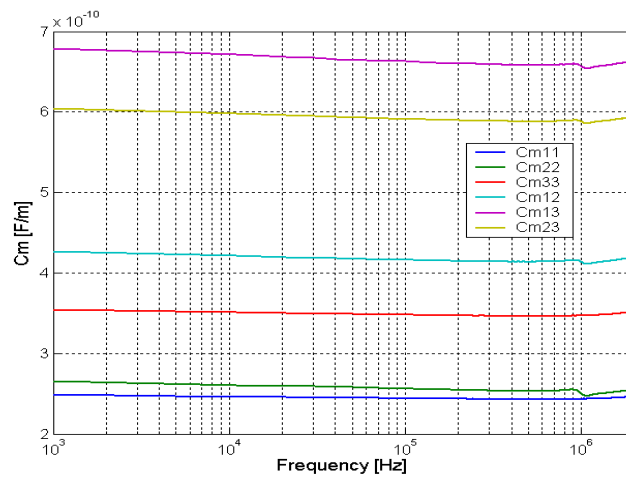


Figure 4.12: Measured values of per-unit length C_m -vector for the Tracker power cable (MSC).

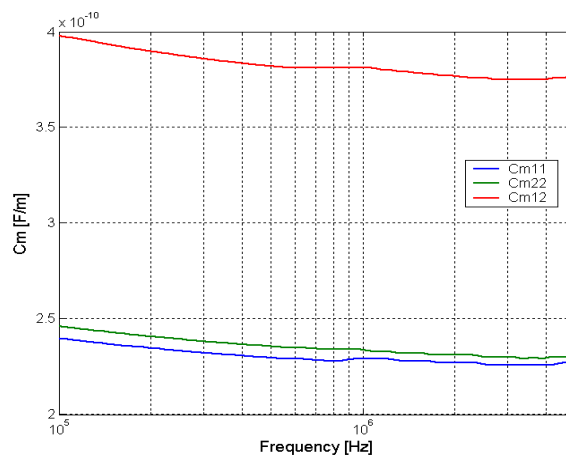


Figure 4.13: Measured values of per-unit length C_m -vector for the HCAL power cable

4.3.3 Resistance

The goal of this measurement is to calculate the 4 values of the multi-conductor theory resistance matrix for the tracker (3 values for HCAL power cable). The resistance of each conductor (R_1, R_2, R_3) and the resistance of the shield (R_0) are needed to complete the resistance matrix. These values were measured at the same

4.3. Parameters measurement procedure

time as the inductance was measured with the LRC meter. The measured values are $(R_{11}, R_{22}, R_{33}, R_{12}, R_{23}, R_{13})$. The values of the diagonal can be obtained directly and the value of R_0 is easily calculated by solving an equation system. From the conductor and shield resistance values, the resistance matrix (equation 4.14) can be calculated. Figure 4.14 and 4.15 show the values of the resistance per unit length as a function of the frequency for Tracker power cable and HCAL power cable.

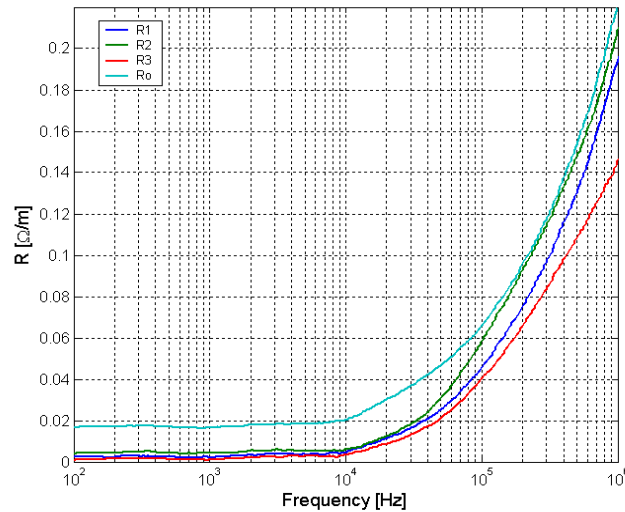


Figure 4.14: Measured values of per-unit length resistance for the Tracker power cable (MSC).

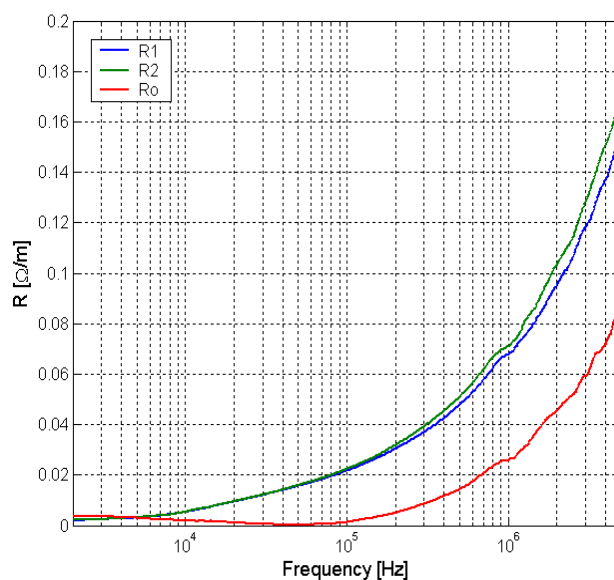


Figure 4.15: Measured values of per-unit length resistance for the HCAL power cable.

4.4 Frequency domain solution of MTL systems.

Transmission lines are distributed parameter systems. If the electrical dimensions of a structure are small in comparison with the wavelength of the signal considered, the line can be modeled as a lumped-parameter system. The independent variables for a distributed parameter system are the spatial dimension, x , y , z , and time. In the case of a lumped parameter system, the quantities of interest are lumped rather than distributed throughout the space so that they depend only on time. Lumped parameters systems are characterized by ordinary differential equations (ODE), whereas distributed-parameters systems, such as transmission lines, are characterized by partial differential equations.

$$\frac{\partial}{\partial z}V(z, t) = -R \cdot I(z, t) - L \cdot \frac{\partial}{\partial t}I(z, t) \quad (4.32)$$

$$\frac{\partial}{\partial z}I(z, t) = -G \cdot V(z, t) - C \cdot \frac{\partial}{\partial t}V(z, t) \quad (4.33)$$

As the frequency domain solution is considered, the use of phasor quantities removes the time dependence. In the case of transmission lines the only spatial parameter is the line axis, z , along the transmission line and, in frequency-domain, the partial differential equations become ordinary differential equations with independent variable z and complex value coefficients. This simplification is summarized in equations 4.34-4.35.

$$\frac{d}{dz}\hat{V}(z) = -\hat{Z} \cdot \hat{I}(z) \quad (4.34)$$

$$\frac{d}{dz}\hat{I}(z) = -\hat{Y} \cdot \hat{V}(z) \quad (4.35)$$

Assuming $G=0$, the impedance and admittance per unit length are defined by:

$$\hat{Z} = R + j \cdot \omega \cdot L \quad (4.36)$$

$$\hat{Y} = j \cdot \omega \cdot C \quad (4.37)$$

where $\hat{V}(z)$ and $\hat{I}(z)$ are phasors defined as $\hat{V}(z) = V(z) \cdot e^{j \cdot \omega \cdot t}$, where $j = \sqrt{-1}$, $\omega = 2 \cdot \pi \cdot f$ and L, R, C are the parameter matrices defined in the previous sections.

Equations 4.34 and 4.35 may be presented in a more compact form.

$$\frac{d}{dz}\hat{X}(z) = \hat{A} \cdot \hat{X}(z) \quad (4.38)$$

$$\text{Where } \hat{X}(z) = \begin{bmatrix} \hat{V}(z) \\ \hat{I}(z) \end{bmatrix} \text{ and } \hat{A}(z) = \begin{bmatrix} 0 & -\hat{Z} \\ -\hat{Y} & 0 \end{bmatrix} \quad (4.39)$$

Thus, it is possible to make a direct analogy between the sinusoidal steady state transmission-lines equation and those of general lumped-parameter system represented by an ODE, by viewing the spatial parameter, z , in the distributed-parameter system phasor equations as the equivalent of time, t , in the lumped-parameter system governing equations.

Based on this analogy, which is well explained in [3] [4], the general solution for the lines voltages and currents is:

$$\begin{bmatrix} \hat{V}(L) \\ \hat{I}(L) \end{bmatrix} = \begin{bmatrix} \hat{\Phi}_{11}(L) & \hat{\Phi}_{12}(L) \\ \hat{\Phi}_{21}(L) & \hat{\Phi}_{22}(L) \end{bmatrix} \cdot \begin{bmatrix} \hat{V}(0) \\ \hat{I}(0) \end{bmatrix} \quad (4.40)$$

Where 0 represents the beginning of the line and L the end point of the transmission line.

The matrix $\hat{\Phi}(L)$ is the NxN state-transition matrix and it has several properties as:

$$\hat{\Phi}(0) = I_{2n} , \quad (4.41)$$

where I_{2n} is the unit NxN matrix.

$$\hat{\Phi}^{-1}(L) = \hat{\Phi}(L) \quad (4.42)$$

$$\hat{\Phi}(L) = I_{2n} + \frac{L}{1!} \cdot \hat{A} + \frac{L^2}{2!} \cdot \hat{A}^2 + \dots \quad (4.43)$$

So the essential task in solving the MTL equations is to determinate the chain parameter matrix $\Phi(L)$. This is generally done by the modal method. The idea is to define the characteristic mode, which propagates in the multi-conductor line. In this case, there will be different natural propagations modes and also different characteristic impedances. These characteristics modes are calculated transforming the propagation equations into an uncoupled model, which can be easily solved. This transformation is achieved by obtaining the second order differential equations of 4.34 and 4.35:

$$\frac{d}{dz} \left(\frac{d}{dz} \hat{V}(z) \right) = -\hat{Z} \cdot \frac{d}{dz} \hat{I}(z) \quad (4.44)$$

$$\frac{d}{dz} \left(\frac{d}{dz} \hat{I}(z) \right) = -\hat{Y} \cdot \frac{d}{dz} \hat{V}(z) \quad (4.45)$$

Then, the first derivatives of current and voltage of equations 4.44 and 4.45 are substituted by the values of equation 4.34 and 4.35, which leads to:

$$\frac{d^2}{dz^2} \hat{V}(z) = \hat{Z} \cdot \hat{Y} \cdot \hat{V}(z) \quad (4.46)$$

$$\frac{d^2}{dz^2} \hat{I}(z) = \hat{Y} \cdot \hat{Z} \cdot \hat{I}(z) \quad (4.47)$$

It is possible to find a similarity transformation \hat{T}_v and \hat{T}_i , which simultaneously diagonalize the per-unit length parameter matrices, \hat{Z} , \hat{Y} , $\hat{Z} \cdot \hat{Y}$ and $\hat{Y} \cdot \hat{Z}$. The transformation essentially changes a n-coupled, first order differential equation set to an n-uncoupled differential equation set. This similarity transformation preserves the eigen-values of the original matrices, which are known as the propagation constants.

The matrices that achieve such transformation are:

\hat{T}_v - is the matrix whose columns are the complex eigen-vectors of $\hat{Z} \cdot \hat{Y}$.

\hat{T}_i - is the matrix whose columns are the complex eigen-vectors of $\hat{Y} \cdot \hat{Z}$.

These matrices have the following property:

$$\hat{T}_i^t = \hat{T}_v^{-1} \quad (4.48)$$

Applying the transformation, the equations of the modal system are obtained (Eq.4.49 and 4.50):

$$\frac{d^2}{dz^2} \hat{V}_m(z) = \hat{T}_v^{-1} \cdot \hat{Z} \cdot \hat{Y} \cdot \hat{T}_v \cdot \hat{V}_m(z) \quad (4.49)$$

$$\frac{d^2}{dz^2} \hat{I}_m(z) = \hat{T}_i^{-1} \cdot \hat{Y} \cdot \hat{Z} \cdot \hat{T}_i \cdot \hat{I}_m(z)$$

$$\frac{d^2}{dz^2} \hat{V}_m(z) = \hat{\gamma}^2 \cdot \hat{V}_m(z) \quad (4.50)$$

$$\frac{d^2}{dz^2} \hat{I}_m(z) = \hat{\gamma}^2 \cdot \hat{I}_m(z)$$

$$\hat{\gamma}^2 = \begin{bmatrix} \hat{\gamma}_1^2 & 0 & \dots & 0 \\ 0 & \hat{\gamma}_2^2 & \dots & 0 \\ \dots & \dots & \dots & \dots \\ 0 & 0 & \dots & \hat{\gamma}_n^2 \end{bmatrix} \quad (4.51)$$

where $\hat{V}_m(z) = \hat{T}_v^{-1} \cdot \hat{V}(z)$ and the $\hat{I}_m(z) = \hat{T}_i^{-1} \cdot \hat{I}(z)$. Each value of the diagonal corresponds to the propagation constant of the i -th mode. $\hat{\gamma}$ is the matrix containing the complex eigen-values of, $\hat{Z} \cdot \hat{Y}$ and $\hat{Y} \cdot \hat{Z}$.

The general solutions of these uncoupled equations are:

$$\hat{I}_m(z) = e^{-\hat{\gamma}z} \cdot \hat{I}_m^+ - e^{\hat{\gamma}z} \cdot \hat{I}_m^- \quad (4.52)$$

$$\hat{V}_m(z) = e^{-\hat{\gamma}z} \cdot \hat{V}_m^+ + e^{\hat{\gamma}z} \cdot \hat{V}_m^- \quad (4.53)$$

$$\text{where } e^{\pm \hat{\gamma}z} = \begin{bmatrix} e^{\pm(\hat{\gamma}_1 \cdot z)} & 0 & \dots & 0 \\ 0 & e^{\pm(\hat{\gamma}_2 \cdot z)} & \dots & 0 \\ \dots & \dots & \dots & \dots \\ 0 & 0 & \dots & e^{\pm(\hat{\gamma}_n \cdot z)} \end{bmatrix} \quad (4.54)$$

The actual voltages and currents can be obtained by multiplying this result by the transformation:

$$\hat{V}(z) = (\hat{T}^{-1})^t \cdot (e^{-\hat{\gamma}z} \cdot \hat{V}_m^+ + e^{\hat{\gamma}z} \cdot \hat{V}_m^-) \quad (4.55)$$

$$\hat{I}(z) = \hat{T} \cdot (e^{-\hat{\gamma}z} \cdot \hat{I}_m^+ - e^{\hat{\gamma}z} \cdot \hat{I}_m^-) \quad (4.56)$$

$$\hat{T} = \hat{T}_i \quad (4.57)$$

Evaluating previous equations, 4.55 and 4.56, at both ends of the lines ($z = 0$ and $z = L$) and substituting the results into equation 4.40, the components of the chain parameter matrix may be evaluated.

$$\hat{\Phi}_{11}(L) = \frac{1}{2} \cdot \hat{Y}^{-1} \cdot \hat{T} \cdot (e^{\hat{\gamma}L} + e^{-\hat{\gamma}L}) \cdot \hat{T}^{-1} \cdot \hat{Y} \quad (4.58)$$

$$\hat{\Phi}_{12}(L) = -\frac{1}{2} \cdot \hat{Y}^{-1} \cdot \hat{T} \cdot \hat{\gamma} \cdot (e^{\hat{\gamma}L} - e^{-\hat{\gamma}L}) \cdot \hat{T}^{-1} \quad (4.59)$$

$$\hat{\Phi}_{21}(L) = -\frac{1}{2} \cdot \hat{T} \cdot (e^{\hat{\gamma}L} - e^{-\hat{\gamma}L}) \cdot \hat{\gamma}^{-1} \cdot \hat{T}^{-1} \cdot \hat{Y} \quad (4.60)$$

$$\hat{\Phi}_{22}(L) = \frac{1}{2} \cdot \hat{T} \cdot (e^{\hat{\gamma}L} + e^{-\hat{\gamma}L}) \cdot \hat{T}^{-1} \quad (4.61)$$

At each frequency the matrix elements $\hat{\Phi}_{ij}(L)$ are constant and confirm the properties shown in equation 4.41, 4.42 and 4.43.

4.4.1 Solution of MTL incorporating the terminal conditions.

The chain parameter matrix given in 4.38 relates the phasor voltage at $z=0$ and at $z=L$, but does not explicitly determine these voltages and currents. Essentially, $2n$ relations are needed to explicitly determinate the terminal voltages and currents from the chain parameter matrix relation. These relations are provided by the terminal constraints. The aim of this section is to incorporate these terminal constraints to explicitly determine the terminal voltages and currents and complete this important last step in the solution.

There are many ways of relating the voltages and currents at the terminals of an n port network. If the network is linear, this relationship will be a linear combination of the port voltages and currents. One obvious way is to generalize the Thevenin equivalent representation of a 1 port as:

$$\hat{V}(0) = \hat{V}_S + \hat{Z}_S \cdot \hat{I}(0) \quad (4.62)$$

$$\hat{V}(L) = \hat{V}_L + \hat{Z}_L \cdot \hat{I}(L) \quad (4.63)$$

The $N \times 1$ vectors \hat{V}_S and \hat{V}_L contain the effects of the independent voltage and current in the termination networks at $z=0$ and $z=L$, respectively. The $N \times N$ matrices, \hat{Z}_S and \hat{Z}_L contain the effects of the impedances and controlled sources in the terminal networks at $z=0$ and $z=L$, respectively.

In general, the impedance matrices \hat{Z}_S or \hat{Z}_L , have diagonal and off diagonal components. However, there may be terminal-network configurations where these impedances matrices are diagonal and the only coupling occurs along the MTL.

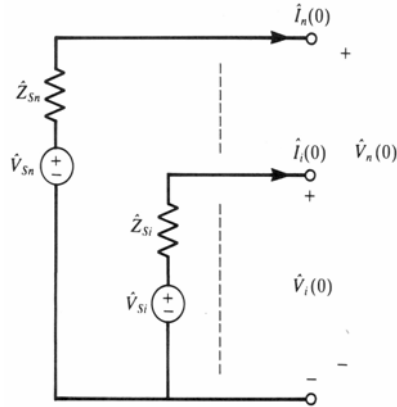


Figure 4.16: The Generalized Thevenin representation at source level

Figure 4.16, shows such a case where in each line at $z=0$ is terminated directly to the chosen reference conductor with an impedance and a voltage source. In this case the matrices become:

$$\hat{V}_S = \begin{bmatrix} \hat{V}_{S_1} \\ \hat{V}_{S_2} \\ \dots \\ \hat{V}_{S_n} \end{bmatrix} \quad \hat{Z}_S = \begin{bmatrix} \hat{Z}_{S_1} & 0 & \dots & 0 \\ 0 & \hat{Z}_{S_2} & \dots & 0 \\ 0 & 0 & \dots & 0 \\ 0 & 0 & \dots & \hat{Z}_{S_n} \end{bmatrix} \quad (4.64)$$

$$\hat{V}_L = \begin{bmatrix} \hat{V}_{L_1} \\ \hat{V}_{L_2} \\ \dots \\ \hat{V}_{L_n} \end{bmatrix} \quad \hat{Z}_L = \begin{bmatrix} \hat{Z}_{L_1} & 0 & \dots & 0 \\ 0 & \hat{Z}_{L_2} & \dots & 0 \\ 0 & 0 & \dots & 0 \\ 0 & 0 & \dots & \hat{Z}_{L_n} \end{bmatrix} \quad (4.65)$$

The generalized Thevenin equivalent characterizations in equation 4.62 and 4.63 are substituted into the chain parameter matrix characterization given in 4.40, to solve the MTL equations with the terminal conditions.

$$\hat{V}(L) = \hat{\Phi}_{11}(L) \cdot \hat{V}(0) + \hat{\Phi}_{12}(L) \cdot \hat{I}(0) \quad (4.66)$$

$$\hat{I}(L) = \hat{\Phi}_{21}(L) \cdot \hat{V}(0) + \hat{\Phi}_{22}(L) \cdot \hat{I}(0) \quad (4.67)$$

To yield

$$(\hat{\Phi}_{12} - \hat{Z}_S \cdot \hat{\Phi}_{11} - \hat{Z}_L \cdot \hat{\Phi}_{22} + \hat{Z}_L \cdot \hat{\Phi}_{21} \cdot \hat{Z}_S) \cdot \hat{I}(0) = \hat{V}_L - ((\hat{\Phi}_{11} - (\hat{Z}_L \cdot \hat{\Phi}_{21}))) \cdot \hat{V}_S \quad (4.68)$$

$$\hat{I}(L) = \hat{\Phi}_{21} \cdot \hat{V}_S + ((\hat{\Phi}_{22} - (\hat{\Phi}_{21} \cdot \hat{Z}_S)) \cdot \hat{I}(0)) \quad (4.69)$$

Equation 4.68 is a set of n equations that defines the current at z=0 as function of the external voltages. Once these equations are solved, the n terminal currents at z=L, $\hat{I}(L)$, can be obtained from 4.69. The n terminal voltages, $\hat{V}(L)$ and $\hat{V}(0)$ can be obtained from equation 4.62 and 4.63.

All of the equations presented above were incorporated in a MATLAB program to study the signal propagation in power cables and also to analyze the susceptibility of some connections of the HCAL-FEE. Other commercial software oriented to solve electrical circuits as Pspice, Saber, etc. incorporate models to analyze transmission lines. However the necessity of incorporating the skin effects, shields currents and external fields perturbations, which will be analyzed later, forced us to work directly with the equations in MATLAB¹.

There are many more studies and equivalent circuits that could incorporate the terminal conditions to the MTL equations such as Norton equivalent circuit and a mixed representation of both Thevenin and Norton circuits. These representations were not used in the present study and thus they are not explained here in detail. A detailed bibliography of these configurations is shown in [2][4].

4.5 Noise propagation in cables

4.5.1 Introduction

The effects that electrically-long power cables have on the noise propagation have been addressed recently in the literature [8][9][10]. Some of those studies are focused on predicting the effects introduced on the measurement of the conductive noise, based on the EU standard, when the equipment under test is connected to the normalized impedance using a long cable. In the present analysis, the shielded twisted power cable of the HCAL sub-system has been chosen to study the effect of noise propagation in long power cables. In this part of the analysis, it is assumed that no current flows through the cable shield. The study is focused on the input/output transfer functions of a 15 mts. shielded twisted power cable for different load conditions. The topology of the circuit under study is shown in figure 4.17.

¹ Program validation in appendix A

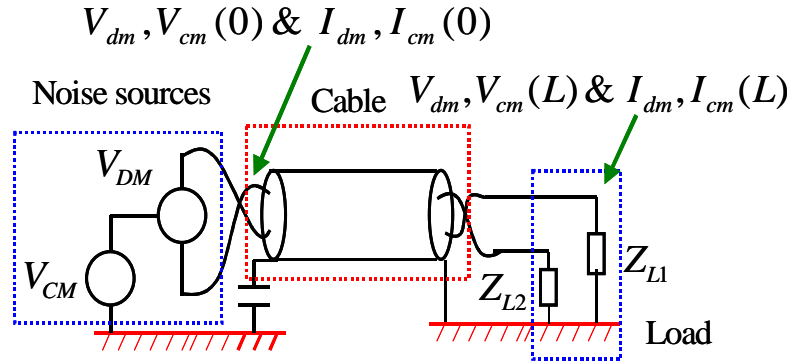


Figure 4.17: Circuit layout for the noise propagation analysis.

The per unit length parameter matrices for this cable are taken from the measurements of the HCAL power cable presented in section 4.3. The chosen values are measured at 1-MHz. The values of the inductance and capacitance per unit length matrix are:

$$L = \begin{bmatrix} 0.1479 & 0.0260 \\ 0.0260 & 0.1540 \end{bmatrix} \times 10^{-6} \frac{H}{m} \quad (4.70)$$

$$C = \begin{bmatrix} 0.2292 & -0.0412 \\ -0.0412 & 0.2339 \end{bmatrix} \times 10^{-9} \frac{F}{m} \quad (4.71)$$

The cable model includes the skin effect in the central conductors and in the shield. According to the skin effect modelization presented in [4], the frequency dependence of the resistance of a conductor may be approximated as:

$$R(f) = R_{DC} + R_{DC} \cdot \left(\sqrt{\frac{f}{f_o}} \right) \quad (4.72)$$

The value of f_o is the frequency where the skin depth is half of the conductor radius. This approximation has a deviation at the transition frequency but for the required frequency domain analysis, the error is minimized. The value of the resistance for the HCAL power cable matrix is found to be:

$$R = \begin{bmatrix} 0.0017 \cdot \left(1 + \sqrt{\frac{f}{5400}}\right) + 0.0035 \cdot \left(1 + \sqrt{\frac{f}{160000}}\right) & \left(0.0035 \cdot \left(1 + \sqrt{\frac{f}{160000}}\right)\right) \\ \left(0.0035 \cdot \left(1 + \sqrt{\frac{f}{160000}}\right)\right) & 0.0018 \cdot \left(1 + \sqrt{\frac{f}{5400}}\right) + 0.0035 \cdot \left(1 + \sqrt{\frac{f}{160000}}\right) \end{bmatrix} \frac{\Omega}{m} \quad (4.73)$$

Four load configurations have been chosen to study their influence in the noise propagation:

- a) ($Z_{L1} = Z_{L2} = Z_c$)
- b) ($Z_{L1} = Z_{L2} = 150\Omega$)
- c) $Z_{L1} = 150\Omega$ $Z_{L2} = 0\Omega$
- d) $Z_{L1} = 150\Omega | C = 1\mu f$ $Z_{L2} = 0\Omega$

For the first configuration, the load impedances are equal to the characteristic impedance of the cable. For the analysis of the CM noise propagation, they are set equal to $Z_{c-cm} = 30.4\Omega$ and for the DM noise propagation, they are equal to $Z_{c-dm} = 21.4\Omega$. This case is unpractical for power distribution and it is included in the study as reference. For the second one, a balanced impedance of 150Ω is selected as load. This case is chosen because 150Ω is used as the normalized impedance for studies in CM propagation in cables. Finally the last two configurations represent unbalanced loads. In this condition, one of the lines is directly connected to ground and the other is loaded with a resistor larger than the characteristic impedance of the cable. The case d) includes a capacitor in parallel with the 150Ω resistor to simulate the effect of an input filter at the load-end.

The terminal configurations of the CM and DM circuit presented are characterized as a generalized Thevenin equivalent as in (4.62 and 4.63) where:

$$Z_L = \begin{bmatrix} Z_{L1} & 0 \\ 0 & Z_{L2} \end{bmatrix} \Omega, \quad V_L = \begin{bmatrix} 0 \\ 0 \end{bmatrix} V \quad \text{Load level (Both configurations)} \quad (4.74)$$

$$Z_S = \begin{bmatrix} 0 & 0 \\ 0 & 0 \end{bmatrix} \Omega, \quad V_{S_{CM}} = \begin{bmatrix} 1 \\ 1 \end{bmatrix} V \quad \text{and} \quad V_{S_{DM}} = \begin{bmatrix} 1 \\ -1 \end{bmatrix} V \quad \text{Source level} \quad (4.75)$$

This study is conducted decomposing the voltage and current for each conductor, at each position, in two orthogonal components. For currents, the common and differential mode are defined as:

$$I_{cm}(z) = \frac{I_1(z) + I_2(z)}{2} \quad (4.76)$$

$$I_{dm}(z) = \frac{I_1(z) - I_2(z)}{2} \quad (4.77)$$

where $I_1(z)$ and $I_2(z)$ are the current flowing through conductor 1 and 2 respectively at the z position in the cable. Similar definition is used for voltages.

4.5.2 Common mode noise effects

To study the propagation of the common mode signals, based on the circuit depicted in figure 4.18, the CM current transfer function is defined as:

$$T_{cm_I} = \frac{I_{cm}(L)}{I_{cm}(0)} \quad (4.78)$$

where $I_{cm}(0)$ and $I_{cm}(L)$ are the CM current at the sending-end and receiving-end of the cable. Figure 4.18 shows the simulated results of the CM current transfer function for the four load configurations.

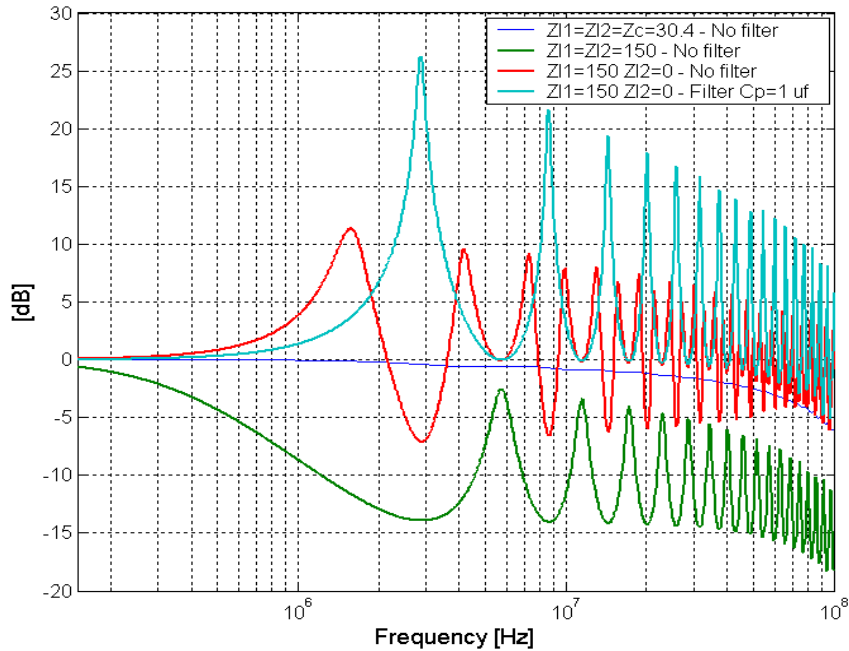


Figure 4.18: CM current transfer function - Simulated values.

For load resistors equal to the CM characteristic impedance of cable, the behavior is similar to a low-pass filter where the attenuation is defined by the series resistance of the conductors. When the load is not matched, cable resonances are leading in the propagation of noise along the cable. For the balanced case and high impedance load, resonances are present, however the CM current is attenuated when it propagates along the cable. On the other hand, when the load impedance is

balanced and lower than the characteristic impedance, the cable starts amplifying the CM currents at the resonance frequencies. Unbalanced load displays similar results to the balanced load condition. In the case d), where a filter capacitor is added to an unbalanced load, both loads are connected to ground through low impedances, the CM currents can be amplified up to 26 dB (20 times) at certain frequencies. This situation might happen if a RF capacitor is placed at the load in order to filter the noise of the line. This capacitor at high frequency presents very low impedance to ground at the end of the line. This effect is important to take into account because the CM current flowing through the cables defines mainly the radiated emission of the cables.

The common mode voltage at the load-end is defined by the CM current and the load impedance. For case d) the CM voltage at the load is effectively attenuated by the load impedance while for the other cases, the CM voltage at the load is similar or larger than the CM mode voltage applied at the sending-end. To show this behaviour, the CM voltage transfer function, is defined as and plotted in figure 4.19.

$$T_{cm_V} = \frac{V_{cm}(L)}{V_{cm}(0)} \quad (4.79)$$

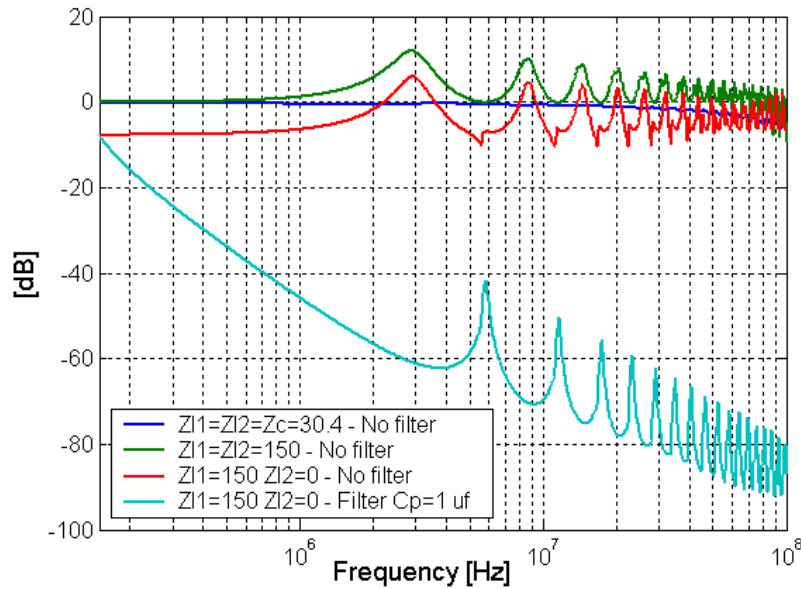


Figure 4.19: CM voltage transfer function - Simulated values.

Another important aspect in this analysis is the CM to DM conversion. This conversion is due to the load unbalance and also to the intrinsic minor unbalance of the cable. Figure 4.20 shows the CM to DM current transfer function for the four configurations. This transfer function is defined as:

$$T_{cm - dm_I} = \frac{Idm(L)}{Icm(0)} \quad (4.80)$$

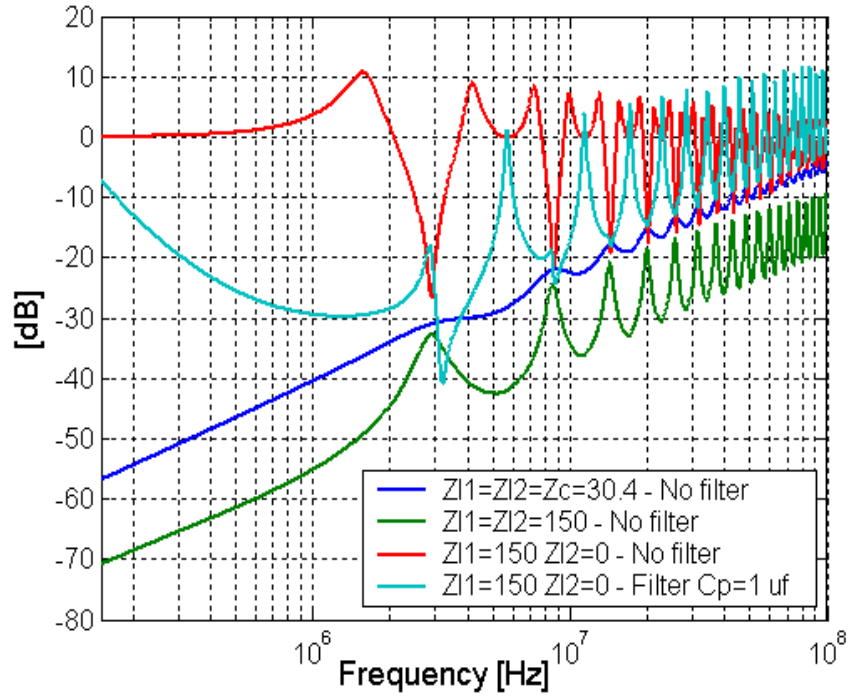


Figure 4.20: CM to DM current transfer function - Simulated values.

For balanced loads (cases a) and b)), the CM to DM conversion exists due to the unbalances in the cable parameters, which are dominated by the mismatch of the cable inductance. From figure 4.20, it is possible to observe that this effect is important only at very high frequencies. For the case of unbalanced loads, the conversion is determined by the load and at some resonant frequencies the conversion mode can have a gain of 10 dB or more.

Figure 4.21 shows the CM to DM voltage transfer function for the four configurations. This transfer function is defined as:

$$T_{cm - dm_V} = \frac{Vdm(L)}{Vcm(0)} \quad (4.81)$$

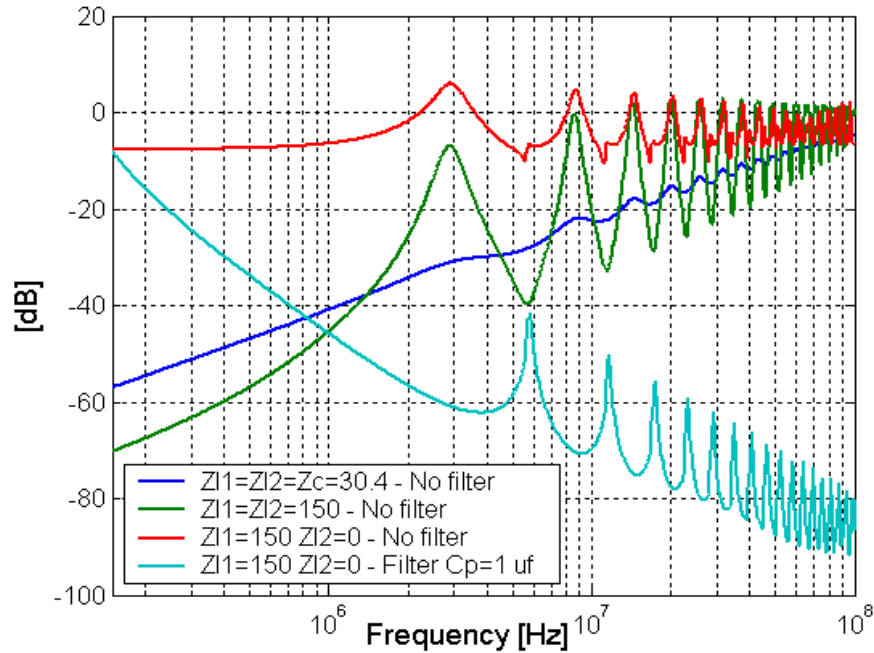


Figure 4.21: CM to DM voltage transfer function - Simulated values.

This analysis is used to get a better understanding of the effect of unbalances of the input power circuit of the FEE. The worst case is found when the system is unbalanced at load level, $Z_{L1} = 150\Omega$ - $Z_{L2} = 0\Omega$ -(in red). For the balanced-load case the dominant effect is the unbalance of the cable, which is basically defined by the inductance of cable in the frequency range of analysis.

4.5.3 Differential mode noise effects

The DM current and DM current transfer functions of the circuit are defined as:

$$T_{dm_I} = \frac{I_{dm}(L)}{I_{dm}(0)} \quad (4.82)$$

Figure 4.22 shows the DM current transfer function for the four load configurations mentioned before.

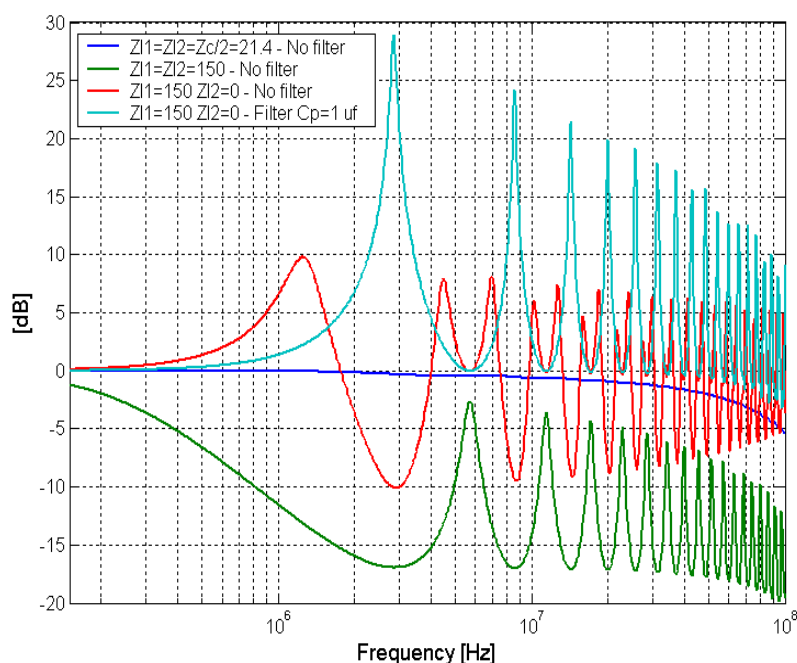


Figure 4.22: *DM current transfer function - Simulated values.*

Again, the resonant frequencies are only attenuated for values equal to the DM characteristic impedance of cable $Z_{L1} = Z_{L2} = 21.4\Omega$, being amplified for low impedances values. These results are very similar to the ones for the CM current transfer function. However, their implications are not as important as in the CM currents because the DM current ability to radiate is much lower than the CM currents and also the FEE is more sensitive to CM perturbations flowing through the power cables than DM perturbations [11].

Plots 4.23, 4.24 and 4.25 show the DM voltage, DM to CM current and DM to CM voltage transfer functions. The curves are very similar to the ones presented in the CM analysis with only small differences in amplitude and resonant frequencies. Basically both configurations are the same with the only difference being the impedances of both CM and DM circuits.

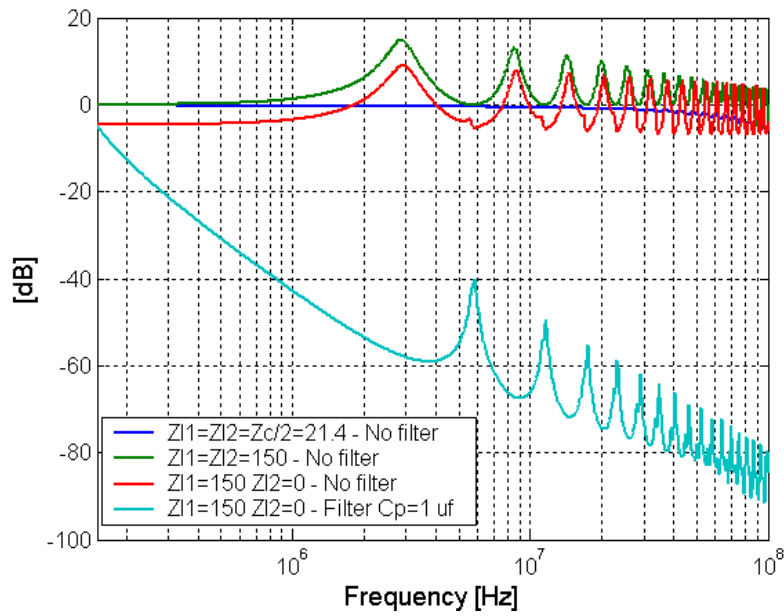


Figure 4.23: DM voltage transfer function - Simulated values.

It is important to remark that the transfer functions (current and voltage) of CM to DM and DM to CM conversion are very similar, confirming the close relation between both modes.

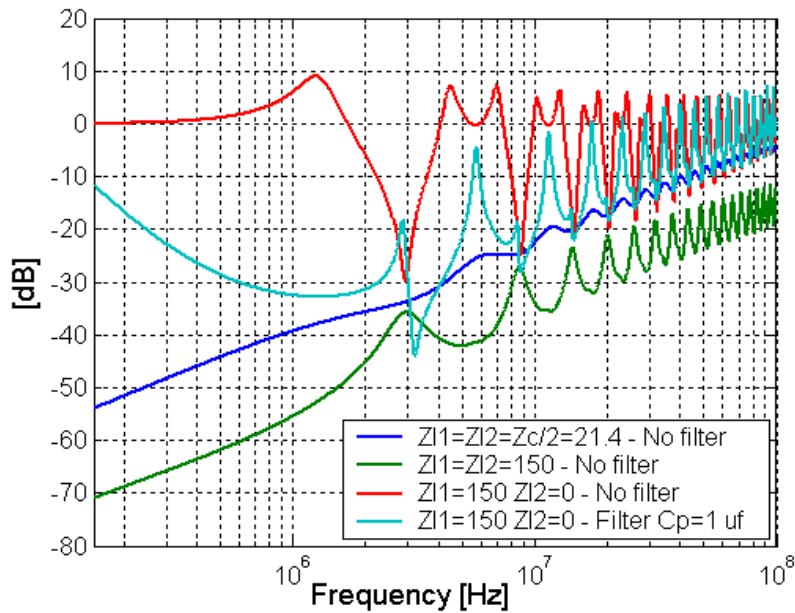


Figure 4.24: DM to CM current transfer function - Simulated values.

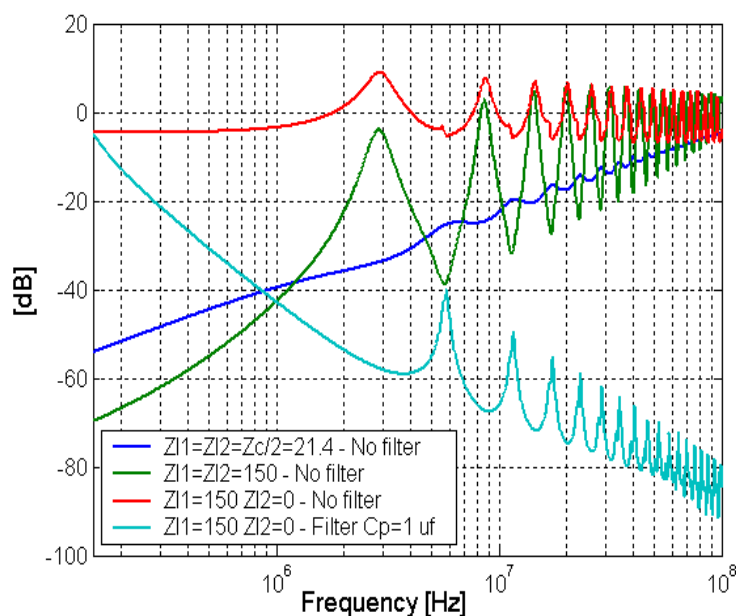


Figure 4.25: DM to CM voltage transfer function - Simulated values.

4.5.4 Summary of noise propagation

The study presented above considers different impedances at the load-end of the cable to demonstrate that both CM/DM currents and voltages can be amplified by the cable resonance when they propagate from the sending-end to the receiving-end. The only case where resonances do not exist is when the load impedance matches the characteristic impedance of the cable, being for power distribution completely unpractical.

High impedance, balanced loads attenuate the CM and DM currents transmitted through the cable, but the CM and DM voltage across the load terminals is amplified. On the other hand, low impedance and balanced loads amplify the CM and DM currents at the resonance frequencies.

In high-energy physics applications, generally, the return plane of the FEE is connected to ground to minimize the voltage variations across the parasitic capacitances between the shielding box and the sensitive inputs of the amplifiers or to provide a return to faults currents¹. This connection implies in general, that the return power cable is connected to ground. From this study it is shown that for unbalanced loads, both the CM and DM mode signal are amplified at the resonant frequencies of the cable. In particular, when a capacitor filter is included across the

¹ See chapter 2

load terminals, the CM and DM currents flowing through the cable are amplified, but the DM and CM voltage across the load terminals are effectively attenuated. This configuration reduces the noise current coupled to the resistive part of the load by-passing those currents through the capacitor. This behavior explains a typical EMC-based design rule, which is to put the by-pass filter capacitor of the input power filter as close as possible to the entrance point of the power cable [3]. This filter limits both the DM and CM voltage at the input but amplifies both the CM and DM currents flowing through the cables. If the filter is placed close to the sensitive electronics into the screened box or cabinet, the power cable running inside the box, from the entrance point to the filter, radiates and could interfere with the FEE.

The current levels produced by the amplification of the CM and DM currents for the case of unbalanced loads with capacitor filter can generate unwanted electromagnetic radiation from the cable. The radiation efficiency of a cable is proportional to the loop area of the current path. For differential mode currents, the effective area is minimum if the both conductors, active and return, are adjacent to each other or are twisted. For CM currents, the return path is not always perfectly defined. In the present analysis, it is assumed the CM current return through the internal part of the shield and, in this case, the effective area is ideally zero. If the cable has no shield, the return path is not completely defined by the cable itself but it is also defined by the position of the cable with respect to the reference structure and hence the effective radiation area can be large. It is critical for cables without shielding to have reduced levels of CM current to avoid unwanted electromagnetic radiation.

4.5.5 CM and DM mode noise propagation in HCAL power supply distribution system

4.5.5.1 Introduction

In the previous sections, the effect that the cable and the load have on the conducted noise propagation has been presented. In this section, the noise propagation induced by power supplies (PS) and the noise generated by ground currents are studied for the power supply distribution of the HCAL sub-system. In this sub-system, the nominal low voltages at the FEE input power are 6.5V and 4.5V and internal linear regulators convert those values to 5V, 3.3V and 2.5V. Shielded twisted-pair cables, whose length is between 15 and 20 meters, connect the power supply units and the FEE.

In this analysis, the model is composed by three blocks: the PS unit and EMI filter, the cable and the FEE, as it is depicted in figure 4.26.

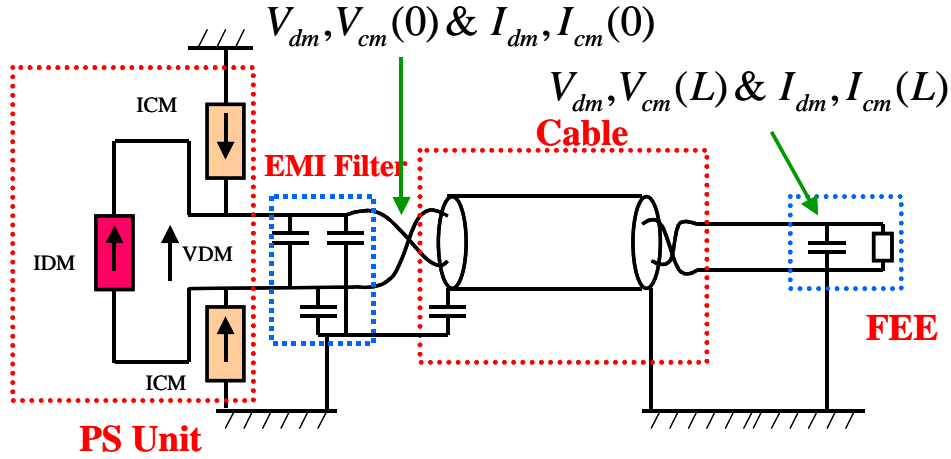


Figure 4.26: HCAL power supply distribution layout

The PS unit and EMI filter are represented by the combination of two current generators (CM and DM) and output capacitors. These sources represent the emissions generated by a DC-DC converter. The EMI filter is represented by three capacitors, one DM capacitor of 1 μF and two CM capacitors of 5 nF. Power supplies are connected to the FEE through a 15 meter-long cable¹ (external diameter of 12 mm), placed 10 mm above a metallic tray. The FEE input power is represented by a reduced model composed by a set of real capacitors of 1 μF , with parasitic resistance is equal to 0.2 Ω , in parallel with a 1 M Ω resistance.

4.5.5.2 Common mode noise propagation

The terminal configurations of the CM circuit are characterized by a generalized Thevenin equivalent as in (4.62 and 4.63) where:

$$Z_S = \begin{bmatrix} \frac{Z_{cm1} \cdot (Z_{cm2} + Z_{dm})}{Z_{cm1} + Z_{cm2} + Z_{dm}} & \frac{Z_{cm1} \cdot Z_{cm2}}{Z_{cm1} + Z_{cm2} + Z_{dm}} \\ \frac{Z_{cm1} \cdot Z_{cm2}}{Z_{cm1} + Z_{cm2} + Z_{dm}} & \frac{Z_{cm2} \cdot (Z_{cm1} + Z_{dm})}{Z_{cm1} + Z_{cm2} + Z_{dm}} \end{bmatrix} \Omega \quad (4.83)$$

The values of $Z_{cm1} = \frac{1}{j \cdot \omega \cdot C_{cm}}$, $Z_{cm2} = \frac{1}{j \cdot \omega \cdot C_{cm}}$ and $Z_{dm} = \frac{1}{j \cdot \omega \cdot C_{dm}}$ correspond to the impedance of the output filter of the power supply.

¹ The per-unit length matrices of the cable are presented in equations 4.70 and 4.71.

$$V_S = \begin{bmatrix} V_{S1} \\ V_{S2} \end{bmatrix} = \begin{bmatrix} \frac{(Z_{cm2} + Z_{dm})}{Z_{cm1} + Z_{cm2} + Z_{dm}} \frac{Z_{cm1}}{Z_{cm1} + Z_{cm2} + Z_{dm}} & \\ \frac{Z_{cm2}}{Z_{cm1} + Z_{cm2} + Z_{dm}} \frac{(Z_{cm1} + Z_{dm})}{Z_{cm1} + Z_{cm2} + Z_{dm}} & \end{bmatrix} \cdot \begin{bmatrix} I_{cm1} \cdot Z_{cm1} \\ I_{cm2} \cdot Z_{cm2} \end{bmatrix} \text{Volts} \quad (4.84)$$

Where the $I_{cm1} = 1$ and $I_{cm2} = 1$.

$$Z_L = \begin{bmatrix} Z_{L1} & 0 \\ 0 & Z_{L2} \end{bmatrix} \Omega, \quad V_L = \begin{bmatrix} 0 \\ 0 \end{bmatrix} \text{V Load level} \quad (4.85)$$

Where $Z_{L2} = 0\Omega$ $Z_{L1} = 150\Omega || C = 1\mu f + 0.2\Omega$.

Figure 4.27 shows the CM current and voltage transfer function of the system between the output of the filter and at the input of the FEE.

$$TF_{cm-I} = \frac{I_{cm}(L)}{I_{cm}(0)} \quad \text{and} \quad TF_{cm-V} = \frac{V_{cm}(L)}{V_{cm}(0)} \quad (4.86)$$

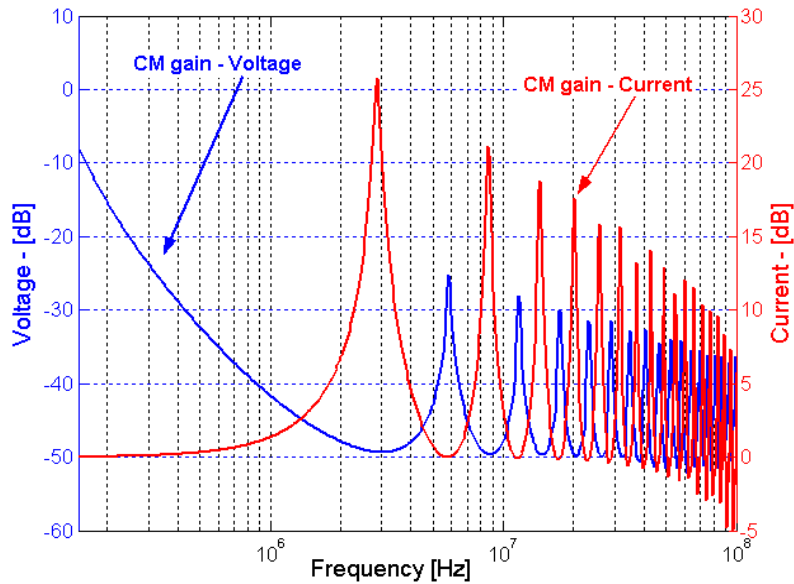


Figure 4.27: CM current and voltage transfer function of HCAL power supply distribution system - Simulated values.

The low impedance presented by the FEE at high frequency, amplifies the CM currents at the resonance frequencies but effectively attenuates the CM voltage at the input terminals. Based on these results, a combination of three factors is necessary to take into account during the design to reject the direct effect of CM currents generated by power supplies. First, a low level of CM emission at the output of the power supply should be specified. Second, a power cable with screen should be used to limit the radiation of the long cable and finally an appropriate CM filter has to be included at the input of the FEE. The location of this filter is very critical, the best position is as close as possible to the entrance of the power cable into the shielding cabinet or box.

It is important to analyze the cross-effect from CM to DM because the front-end electronics is more sensitive to CM perturbations coming through the power cables than DM perturbations. The CM-DM transfer functions are defined as.

$$TF_{cm-dmI} = \frac{I_{dm}(L)}{I_{cm}(0)} \quad \text{and} \quad TF_{cm-dmV} = \frac{V_{dm}(L)}{V_{cm}(0)} \quad (4.87)$$

Figure 4.28 shows the transfer function for both modes of propagation.

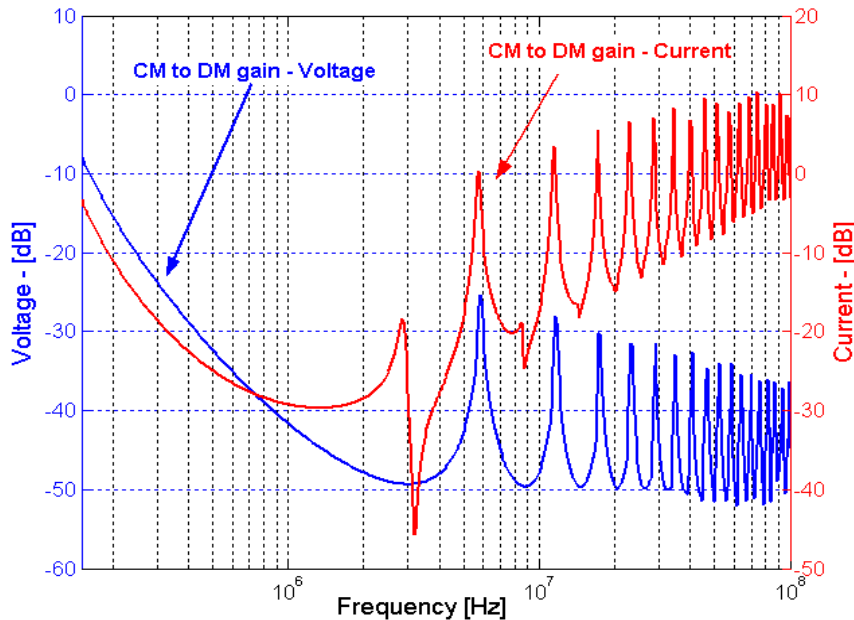


Figure 4.28: CM to DM conversion current and voltage transfer function of HCAL power supply distribution system - Simulated values.

The current transfer function increases with the frequency. This effect is generated by the unbalance of the cable impedance at high frequency. On the other hand the

voltage TF decreases with the frequency because the input filter of the FEE presents very low impedance, reducing the noise voltage at the input terminals

4.5.6 Differential mode noise propagation

The terminal configurations of the DM circuit presented are characterized by a generalized Thevenin equivalent, the same as that found in 4.62 and 4.63:

$$Z_S = \begin{bmatrix} \frac{Z_{cm1} \cdot (Z_{cm2} + Z_{dm})}{Z_{cm1} + Z_{cm2} + Z_{dm}} & \frac{Z_{cm1} \cdot Z_{cm2}}{Z_{cm1} + Z_{cm2} + Z_{dm}} \\ \frac{Z_{cm1} \cdot Z_{cm2}}{Z_{cm1} + Z_{cm2} + Z_{dm}} & \frac{Z_{cm2} \cdot (Z_{cm1} + Z_{dm})}{Z_{cm1} + Z_{cm2} + Z_{dm}} \end{bmatrix} \Omega \quad (4.88)$$

The values of Z_{cm1} , Z_{cm2} and Z_{dm1} correspond to the CM and DM filter capacitor impedance placed at the output of the power supply. In the present study the CM capacitor of this filter is equal to 5 nF and the differential capacitor is equal to 1 μF.

$$V_S = \begin{bmatrix} V_{S1} \\ V_{S2} \end{bmatrix} = \begin{bmatrix} \frac{(Z_{cm2} + Z_{dm})}{Z_{cm1} + Z_{cm2} + Z_{dm}} & \frac{Z_{cm1}}{Z_{cm1} + Z_{cm2} + Z_{dm}} \\ \frac{Z_{cm2}}{Z_{cm1} + Z_{cm2} + Z_{dm}} & \frac{(Z_{cm1} + Z_{dm})}{Z_{cm1} + Z_{cm2} + Z_{dm}} \end{bmatrix} \cdot \begin{bmatrix} I_{cm1} \cdot Z_{cm1} \\ I_{cm2} \cdot Z_{cm2} \end{bmatrix} \text{Volts} \quad (4.89)$$

Where the $I_{cm1} = 1$ and $I_{cm2} = -1$.

$$Z_L = \begin{bmatrix} Z_{L1} & 0 \\ 0 & Z_{L2} \end{bmatrix} \Omega, \quad V_L = \begin{bmatrix} 0 \\ 0 \end{bmatrix} \text{V Load level} \quad (4.90)$$

Where $Z_{L2} = 0\Omega$ $Z_{L1} = 150\Omega || C = 1\mu F + 0.2\Omega$.

Figure 4.29 shows the DM current and voltage transfer function of the system between the output of the power supply and the input of the FEE.

$$TF_{dmI} = \frac{I_{dm}(L)}{I_{dm}(0)} \text{ and } TF_{dmV} = \frac{V_{dm}(L)}{V_{dm}(0)} \quad (4.91)$$

Figure 4.30 shows the value of the DM to CM conversion transfer function generated in the circuit. It represents the ratio between DM (current and voltage) at the input of the cable and CM (current and voltage) at the end of cable.

4.5. Noise propagation in cables

$$TF_{dm-cmI} = \frac{I_{cm}(L)}{I_{dm}(0)} \quad \text{and} \quad TF_{dm-cmV} = \frac{V_{cm}(L)}{V_{dm}(0)} \quad (4.92)$$

The values are very similar to the CM ones because the impedances of the circuit for both modes are practically the same. These slight differences produce small changes in magnitude and resonant frequencies of the transfer functions.

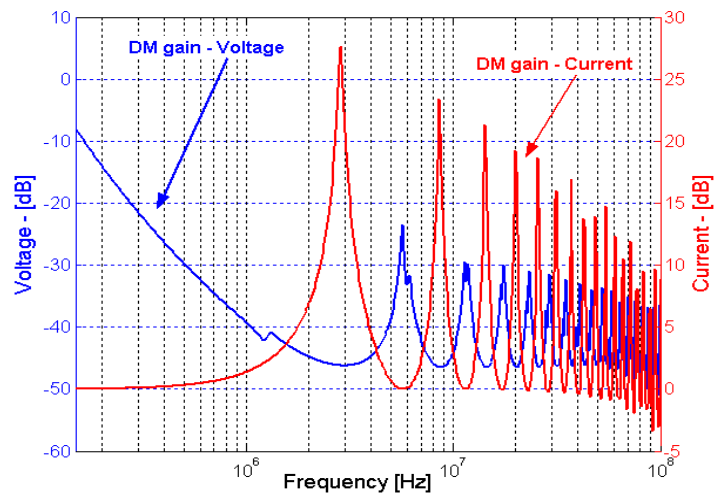


Figure 4.29: DM current and voltage transfer function of HCAL power supply distribution system - Simulated values.

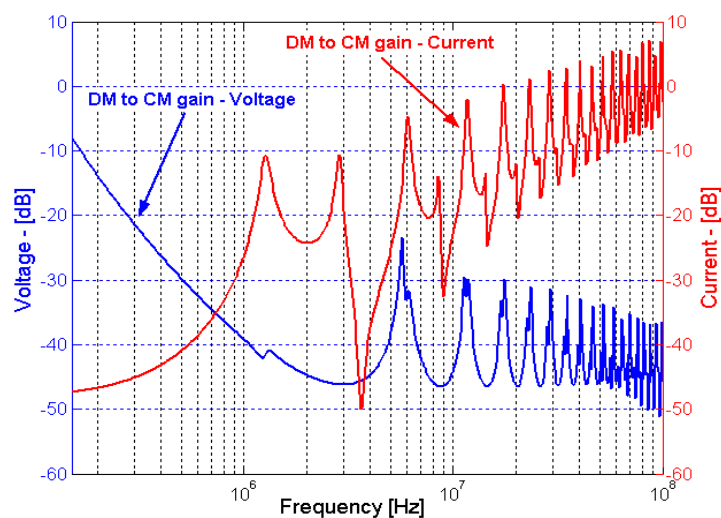


Figure 4.30: DM to CM conversion current and voltage transfer function of HCAL power supply distribution system - Simulated values.

4.6 Shield models

4.6.1 Surface transfer impedance and admittance

The model presented in section 4.1¹ does not include the coupling effect in the central conductors of currents flowing through the shield. The equivalent circuit of figure 4.31 represents this coupling mechanism based on the MTL theory for a sector of line of infinitesimal length [12]. The circuit consists of the inner system representing the central conductor of the coaxial cable and the braided shield as reference conductor. The outer system (shield- metallic tray) is considered as a transmission line, where the metallic tray is the reference of the outer system and the shield is the conductor.

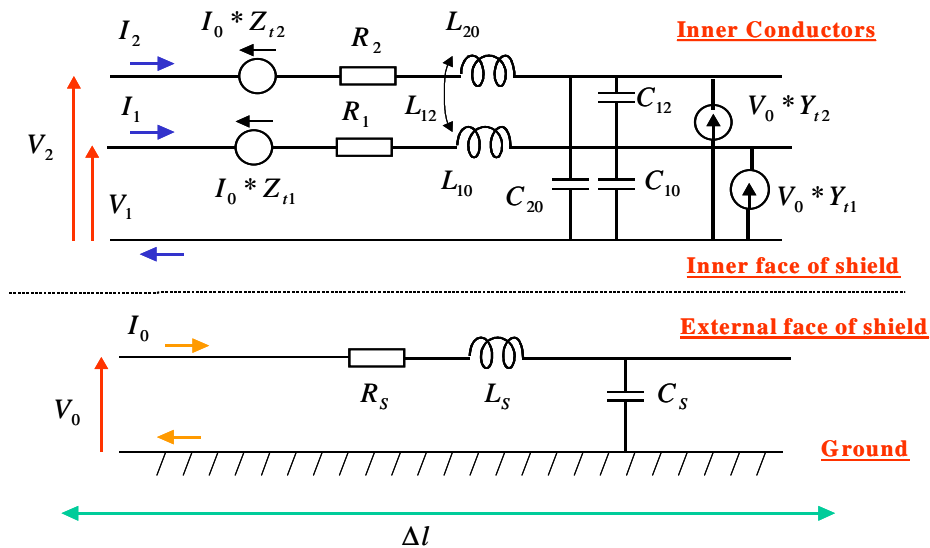


Figure 4.31: Distributed MTL model for shielded twisted pair cable.

The voltage and the current sources at each inner conductor represent the interaction between both inner and outer systems. Z_t and Y_t represent the surface transfer impedance and the surface transfer admittance. The transfer impedance of a shield Z_{Ti} is defined as the ratio between the voltage per unit length generated by the circuit formed by the shield and the conductors inside the shield and the shield current. The transfer impedance gives the open-circuit voltage developed between the internal conductors and the shield for one ampere of shield current, in a cable 1-meter long. On the other hand, the transfer admittance of a shield Y_{Ti} is defined as the ratio between the current per unit length in the conductors inside the

¹ See figure 4.2

shield and the voltage between the shields and the external structure. The transfer admittance gives the short-circuit current induced in the internal conductors (when the internal conductors are shorted to shield) for one volt between the shield and the external structure, in a cable of 1 meter long. Both surface transfer impedance and admittance are characteristic parameters of the shielded cables.

The transfer impedance depends on three parameters Z_d , M_h and M_b as defined by equation [13] -[17].

$$Z_t = Z_d(\omega) + j \cdot \omega \cdot (M_h \pm M_b) \quad (4.93)$$

$Z_d(\omega)$ - The diffusion coupling component is due to skin effect in the shield. It is predominant at low frequencies.

$$Z_d(\omega) = \frac{1}{2 \cdot \pi \cdot a \cdot \sigma \cdot T} \cdot \frac{(1+j) \cdot T/\delta}{\sinh(1+j) \cdot T/\delta} \quad (4.94)$$

where a is the radius of the shield, T is its wall thickness, σ is the conductivity of the shield, permeability δ is the skin depth in the shield given by:

$$\delta = \frac{1}{\sqrt{\pi \cdot f \cdot \sigma \cdot \mu}} \quad (4.95)$$

M_h - The aperture coupling component is defined as the coupling through the holes of the shield. It plays an important role in the value of the transfer impedance at high frequencies.

M_b -The braid inductance component is defined as the coupling between the external and internal layer of the shield.

Figure 4.32 shows the variation in frequency of the surface transfer impedance of the HCAL power cable.

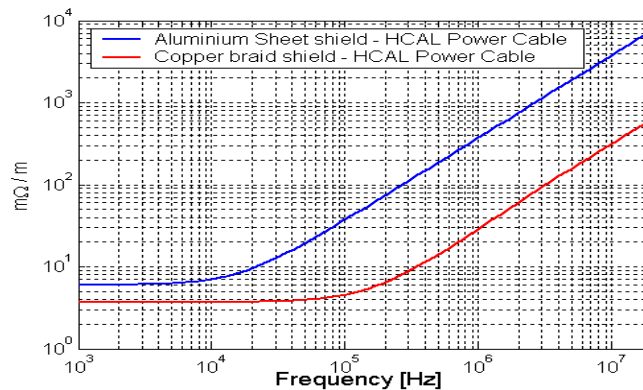


Figure 4.32: Transfer impedance of Aluminium and copper shielded HCAL power cable.

4.6.2 Solution for the cable including the shield in the frequency domain

The mathematical model defined by equation 4.1 and 4.2 is complemented with the generators $V_{Sh}(z, t) = Z_t \cdot I_0(z, t)$ and $I_{Sh}(z, t) = Y_t \cdot U_0(z, t)$ to include the effect of the surface transfer impedance and admittance in the inner conductors, as it is shown in figure 4.31 and equations below [4].

$$\frac{\partial}{\partial z} V(z, t) = -R \cdot I(z, t) - L \cdot \frac{\partial}{\partial t} I(z, t) + Z_t \cdot I_0(z, t) \quad (4.96)$$

$$\frac{\partial}{\partial z} I(z, t) = -G \cdot V(z, t) - C \cdot \frac{\partial}{\partial t} V(z, t) + Y_t \cdot U_0(z, t) \quad (4.97)$$

The solution of the complete equation system starts with the solution of the outer system, which is approximated by a transmission line model. The external system is solved following the procedure described in section 4.4, and the distributed voltage $\hat{V}_0(z)$ and current $\hat{I}_0(z)$ at every location z of the outer system (shield - ambient) are calculated using the equation 4.55 and 4.56.

These voltages and currents are used to calculate the magnitude of the additional generators defined in equation 4.96 and 4.97. Defining $\hat{V}_{Sh}(z) = \hat{I}_0(z) \cdot Z_t$ and $\hat{I}_{Sh}(z) = \hat{V}_0(z) \cdot Y_t$, these equations, can be re-written in state-variable form as a coupled set of first order ordinary differential equations given by:

$$\frac{d}{dt} \begin{bmatrix} \hat{V}(z) \\ \hat{I}(z) \end{bmatrix} = \begin{bmatrix} 0 & -\hat{Z} \\ -\hat{Y} & 0 \end{bmatrix} \cdot \begin{bmatrix} \hat{V}(z) \\ \hat{I}(z) \end{bmatrix} + \begin{bmatrix} \hat{V}_{Sh}(z) \\ \hat{I}_{Sh}(z) \end{bmatrix} \quad (4.98)$$

The solution to the phasor MTL equation 4.98 can be obtained by the analogy to the state-variable equations for lumped systems show in equation 4.38. Therefore, the solution to the phasor MTL equations becomes, by the directly analogy:

$$\hat{X}(z) = \hat{\Phi}(z - z_o) \cdot \hat{X}(z_o) + \int_{z_o}^z \hat{\Phi}(z - \tau) \cdot \begin{bmatrix} \hat{V}_{Sh}(\tau) \\ \hat{I}_{Sh}(\tau) \end{bmatrix} \cdot d\tau \quad (4.99)$$

where $\hat{X}(z) = \begin{bmatrix} \hat{V}(z) \\ \hat{I}(z) \end{bmatrix}$ and the chain parameter matrix, $\hat{\Phi}(z)$ was previously defined by equation. 4.38. It can be observed that the shield effect adds a convolution term to the usual chain parameter relation. The solution at $z=L$ of equation 4.99 is:

$$\begin{bmatrix} \hat{V}(L) \\ \hat{I}(L) \end{bmatrix} = \begin{bmatrix} \hat{\Phi}_{11}(L) & \hat{\Phi}_{12}(L) \\ \hat{\Phi}_{21}(L) & \hat{\Phi}_{22}(L) \end{bmatrix} \cdot \begin{bmatrix} \hat{V}(0) \\ \hat{I}(0) \end{bmatrix} + \begin{bmatrix} \hat{V}_{ShT}(L) \\ \hat{I}_{ShT}(L) \end{bmatrix} \quad (4.100)$$

where the total source voltages $\hat{V}_{ShT_i}(L)$ and currents $\hat{I}_{ShT_i}(L)$ are calculated according to the equation:

$$\hat{V}_{ShT}(L) = \int_0^L [\hat{\Phi}_{11}(L-\tau) \cdot \hat{V}_{Sh}(\tau) + \hat{\Phi}_{12}(L-\tau) \cdot \hat{I}_{Sh}(\tau)] d\tau \quad (4.101)$$

$$\hat{I}_{ShT}(L) = \int_0^L [\hat{\Phi}_{21}(L-\tau) \cdot \hat{V}_{Sh}(\tau) + \hat{\Phi}_{22}(L-\tau) \cdot \hat{I}_{Sh}(\tau)] d\tau \quad (4.102)$$

Based on these equations, the equivalent circuit of the lines - shields system can be viewed as an unexcited line in series with equivalent sources $\hat{V}_{ShT_i}(L)$ and $\hat{I}_{ShT_i}(L)$, located at $z = L$ as it is shown in figure 4.33.

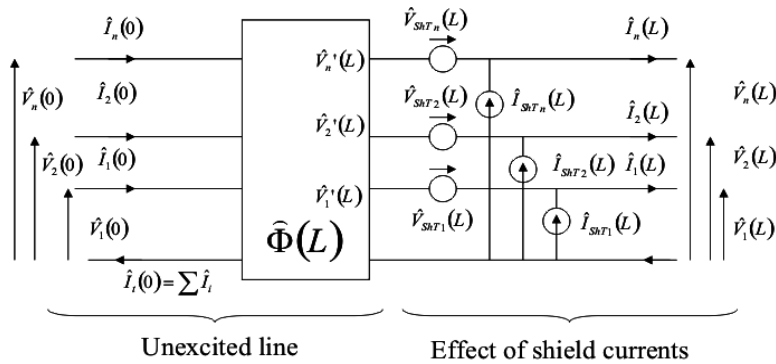


Figure 4.33: Representation of MTL of a shielded cable having lumped sources that represents the effects of shield currents and voltages

Now that the general solution of the phasor MTL equations has been obtained in terms of the chain parameter matrix and the surface transfer impedance and surface transfer admittance forcing functions, the terminal conditions to arrive to an explicit solution for the phasor line voltages and currents are incorporated.

Based on figure 4.33, the voltages and currents at the right end of the unexcited line are denoted as $\hat{V}'(L)$ and $\hat{I}'(L)$. These are related to the actual desired voltages and currents, $\hat{V}(L)$ and $\hat{I}(L)$ as:

$$\hat{V}'(L) = \hat{V}(L) - \hat{V}_{ShT}(L) \quad (4.103)$$

$$\hat{I}'(L) = \hat{I}(L) - \hat{I}_{ShT}(L) \quad (4.104)$$

In this way it is possible to incorporate the shield effects in the solution by replacing $\hat{V}(L)$ and $\hat{I}(L)$ in the equations¹ for the terminal responses without shield effects given in the section 4.4.1 with $\hat{V}(L) - \hat{V}_{ShT}(L)$ and $\hat{I}(L) - \hat{I}_{ShT}(L)$. When the general solution given in 4.100 in terms of the chain parameter matrix with sources is reformulated in the form of the chain parameter relation without shield effects, it gives:

$$\begin{bmatrix} \hat{V}(L) - \hat{V}_{ShT}(L) \\ \hat{I}(L) - \hat{I}_{ShT}(L) \end{bmatrix} = \begin{bmatrix} \hat{\Phi}_{11}(L) & \hat{\Phi}_{12}(L) \\ \hat{\Phi}_{21}(L) & \hat{\Phi}_{22}(L) \end{bmatrix} \cdot \begin{bmatrix} \hat{V}(0) \\ \hat{I}(0) \end{bmatrix} \quad (4.105)$$

Considering the terminal conditions written in the form of generalized Thevenin equivalent:

$$\hat{V}(0) = \hat{V}_S + \hat{Z}_S \cdot \hat{I}(0) \quad (4.106)$$

$$\hat{V}(L) = \hat{V}_L + \hat{Z}_L \cdot \hat{I}(L) \quad (4.107)$$

Substituting into equation 4.104 and 4.103 gives:

$$\begin{aligned} & [\hat{\Phi}_{11} \cdot \hat{Z}_S + \hat{Z}_L \cdot \hat{\Phi}_{22} - \hat{\Phi}_{12} - (\hat{Z}_L \cdot \hat{\Phi}_{21} \cdot \hat{Z}_S)] \cdot \hat{I}(0) = \\ & [\hat{\Phi}_{11} - \hat{Z}_L \cdot \hat{\Phi}_{21}] \cdot \hat{V}_S - \hat{V}_L + [\hat{V}_{ShT}(L) - (\hat{Z}_L \cdot \hat{V}_{ShT}(L))] \end{aligned} \quad (4.108)$$

$$\hat{I}(L) = \hat{I}_{ShT}(L) + \hat{\Phi}_{21} \cdot \hat{V}_S + ((\hat{\Phi}_{22} - (\hat{\Phi}_{21} \cdot \hat{Z}_S)) \cdot \hat{I}(0)) \quad (4.109)$$

From these values and equation 4.106 and 4.107 the voltages at both ends of the lines can be obtained.

All of these equations are implemented in a MATLAB program to analyze the susceptibility of the HCAL power cable to shield currents. The validation of the model presented in this section and a more detailed analysis is shown in appendix A.

¹ Equations 4.66 and 4.67

4.6.3 Susceptibility of HCAL power cable to shield currents

4.6.3.1 Introduction

In this section, the influence of the cable's shield quality in the coupling and propagation of the noise induced by shield currents in the HCAL power distribution system is presented. These currents are originated by near and far electromagnetic fields and by voltage differences at the connection points of the cable's shield. Figure 4.34 shows a schematic of the circuit under study. Two kinds of shields, aluminum sheet and copper braid have been analyzed. Their surface transfer impedance has been depicted in figure 4.32.

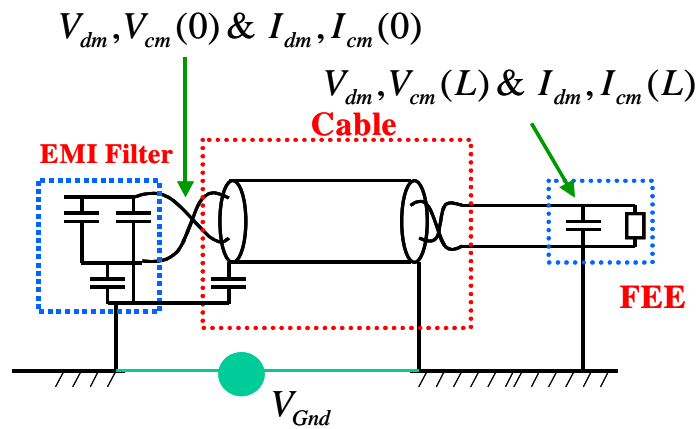


Figure 4.34: HCAL power supply system layout for shield currents analysis.

The example presented corresponds to a 15 meter long power cable (external radius 6 mm) placed 10 mm above a metallic tray, while a voltage difference is applied between the two ground connections of the shield at the detector and the power supply. This cable connects the FEE and the power supply, which are represented in the presented model by their input and output filters, respectively.

The circuit is split in two parts, inner and outer system. The outer system represents the external circuit that the cable's shield forms with the metallic tray. This circuit is approximated as a transmission line, where the metallic tray is the reference of the outer system and the shield of the conductor. The circuit transmission line parameters are calculated using the expression of the inductance and capacitance for a 6 mm external radius cable placed 10 mm above the reference tray, which are presented in detail in [4]:

$$L_{Sh} = \frac{\mu}{2 \cdot \pi} \cdot \operatorname{acosh}\left(\frac{h}{r}\right) = 0.22 \frac{\mu H}{m} \quad (4.110)$$

$$C_{Sh} = \frac{2 \cdot \pi \cdot \epsilon}{\text{acosh}\left(\frac{h}{r}\right)} = 50.5 \frac{pF}{m} \quad (4.111)$$

The resistance is measured at DC and to include the skin effect in the model the resistance¹ (copper braid shield) is represented in the frequency domain as:

$$R_{Sh} = \left(0.0035 \cdot \left(1 + \sqrt{\frac{f}{160000}}\right)\right) \quad (4.112)$$

The terminal configurations of the circuit presented are characterized as a generalized Thevenin equivalent as in 4.62 and 4.63, where:

$$Z_S = 0\Omega, \quad V_S = 1V \quad \text{Power supply level} \quad (4.113)$$

$$Z_L = 0\Omega, \quad V_L = 0V \quad \text{Load level} \quad (4.114)$$

The second part of the circuit is the inner system representing the central conductors of shielded cable taking as reference conductor the braided shield. The per unit length parameter matrices for this cable are based on the measurements, which has been presented² in section 4.5.1. The terminal configurations of the circuit presented are characterized as a generalized Thevenin equivalent, where:

$$Z_L = \begin{bmatrix} Z_{L1} & 0 \\ 0 & Z_{L2} \end{bmatrix} \Omega, \quad V_L = \begin{bmatrix} 0 \\ 0 \end{bmatrix} V \quad \text{Load level} \quad (4.115)$$

with $Z_{L2} = 0\Omega$ $Z_{L1} = 150\Omega || C = 1\mu F$.

The equivalent initial configuration of the power supply filter is calculated based on Kenelly's Theorem to simplify the calculation of the source impedance matrix. The final impedance matrix at source level is equal to:

$$Z_S = \begin{bmatrix} \frac{1}{j \cdot \omega \cdot C_a} + \frac{1}{j \cdot \omega \cdot C_c} & \frac{1}{j \cdot \omega \cdot C_c} \\ \frac{1}{j \cdot \omega \cdot C_c} & \frac{1}{j \cdot \omega \cdot C_b} + \frac{1}{j \cdot \omega \cdot C_a} \end{bmatrix} \Omega, \quad \text{and } V_S = \begin{bmatrix} 0 \\ 0 \end{bmatrix} V \quad \text{Source level} \quad (4.116)$$

where $C_a = 2.005\mu F$, $C_b = 2.005\mu F$ and $C_c = 10.025nF$.

1 Aluminum sheet shield - DC resistance of $6 \frac{m\Omega}{m}$ and $f_o \approx 10kHz$

2 Equations 4.70 and 4.71

4.6.3.2 Common mode

Figure 4.35 shows the trans-admittance between the CM current at the input of the load ($z = L$) and the CM voltage applied between both ground connections, defined as:

$$Y_{cm} = \frac{I_{cm}(L)}{V_{Gnd}} \quad (4.117)$$

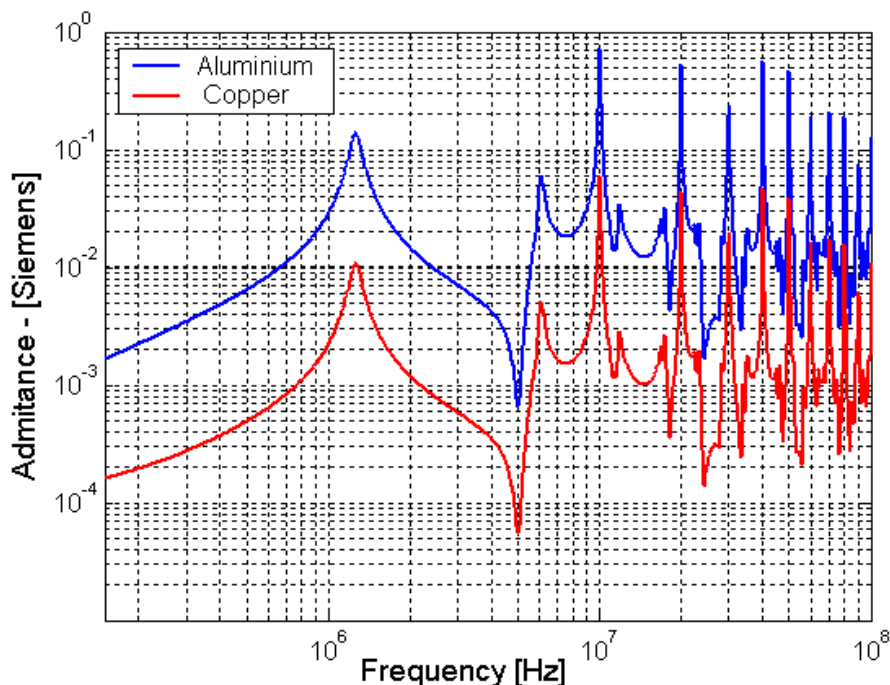


Figure 4.35: CM admittance of shielded (aluminum and copper) HCAL power cable - Simulated values.

When a voltage difference is applied between the ground connections, a current flows through the shield and a CM voltage appears in the central conductors induced by the transfer impedance. At high frequency, the induced CM voltage and resulting CM currents increase due to the increasing characteristic of the surface transfer impedance. Nevertheless, at high frequency the shield current decreases because of the inductive characteristic of the external shield circuit, and additionally, the resonant frequencies of the cable start to play an important role. The most important point of this study is the big difference between both kinds of shields. The aluminum shield has higher admittance values and hence provides lower noise immunity. As a consequence the final selection of the shield will depend on the susceptibility of the FEE to this noise currents. In case the FEE is very

sensitive to noise, it will be necessary to use a very good shielding to improve the noise susceptibility of the system.

Figure 4.36 shows the transfer function between the CM voltage at the input of the load and the CM voltage applied between ground connections. This transfer function is defined as:

$$TF_{cm} = \frac{V_{cm}(L)}{V_{Gnd}} \quad (4.118)$$

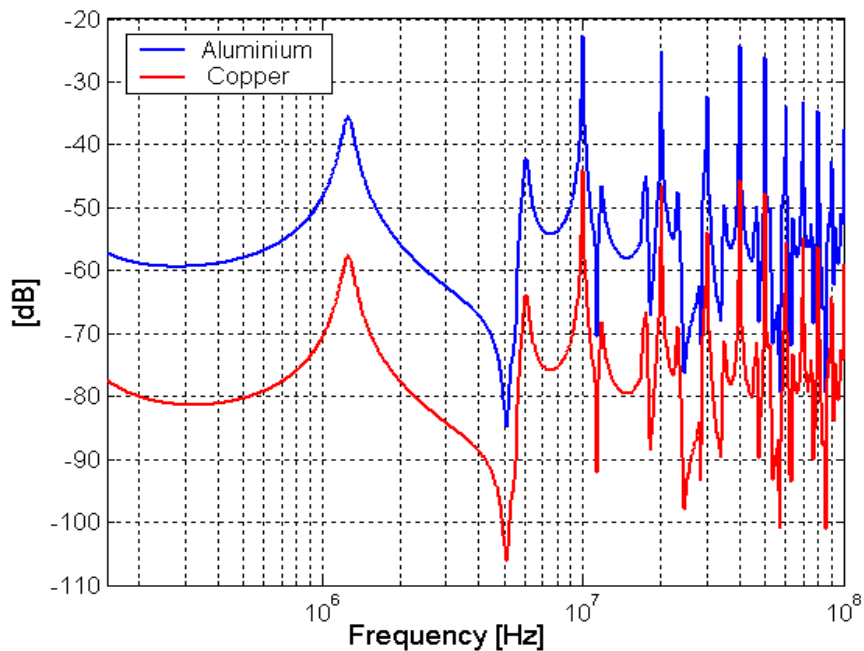


Figure 4.36: CM voltage transfer function of shielded (aluminum and copper) HCAL power cable - Simulated values.

As it is expected there is a difference between both types of cables. In addition the values of the transfer function for both cases do not decrease with the frequency because of the real capacitors at the input of the FEE.

4.6.3.3 Differential mode

Figure 4.37 shows the trans-admittance between the DM current at the input of the load and the CM voltage applied between ground connections, defined as:

$$Y_{dm} = \frac{I_{dm}(L)}{V_{Gnd}} \quad (4.119)$$

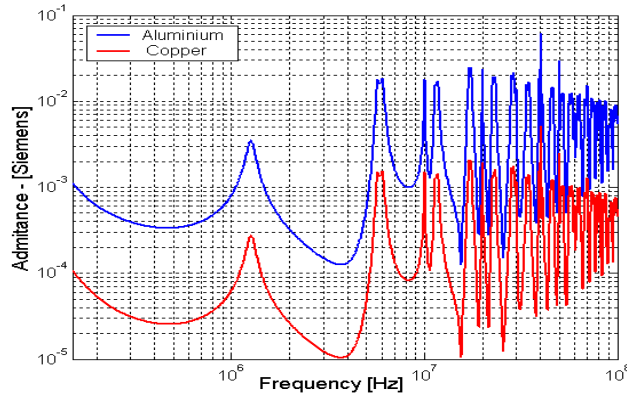


Figure 4.37: DM admittance values of shielded (aluminum and copper) HCAL power cable - Simulated values.

Again, there is an important difference between both types of shields. The value of the admittance increases with frequency. When a current flows through the shield, it induces a CM voltage in the central conductors, giving a similar relation to the CM to DM conversion previously analyzed. This conversion depends on the unbalanced impedance of the system, which at high frequency is caused by the cable inductance imbalances.

Figure 4.38 shows the transfer function between the DM voltage at the input of the load and the CM voltage applied between both grounds.

$$TF_{dm} = \frac{V_{dm}(L)}{V_{Gnd}} \quad (4.120)$$

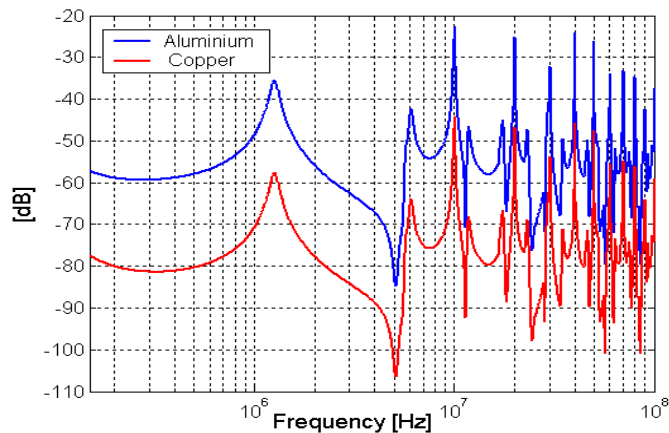


Figure 4.38: DM voltage transfer function of shielded (aluminum and copper) HCAL power cable - Simulated values.

The quality of the shield is very important to define the amount of noise that can be coupled to the central conductors. The value of the transfer function do not decrease at high frequency due to the real capacitor at the input of the FEE.

4.7 Summary

Based on a multi-conductor transmission line model, the important parameters to analyze the behavior of both the tracker multi-service cable and the tracker low impedance cable have been estimated during the first part of this chapter. These measurements show the dependence of both inductance and resistance values with frequency. The measurements are used to parameterize the models defined to study the effects of noise propagation in long cables.

The second part of the chapter addresses the effect of long cables on the noise propagation between the power supply units and the FEE. CM and DM noise currents flowing into the input power terminals of the FEE degrades the noise performance of the sensitive electronics. To avoid that these currents flow into the FEE, CM/DM filters have to be placed at the power entrance. Input filters balance the load presented to the cable at high frequency, which effectively decreases the CM to DM and DM to CM conversion. However, these filters amplify the CM currents flowing through the cable and it can radiate severely. To attenuate this effect, power supplies have to exhibit, at the output, a low level of conducted CM emission and the cables have to present shielding. The quality of the shielded cable and the property of coupling shield currents into the central conductors is defined by the surface transfer impedance. The use of copper braid shields helps to decrease the coupling of noise due to shield currents.

4.8 References

- [1] V.K. Tripathi and J.B. Rettig, "A Spice Model for Multiple Coupled Microstrips and Other Transmission Lines", IEEE Transactions on Microwave Theory and Techniques, Vol 33, pp1513 - 1518, December 1985.
- [2] A. R. Djordjevic, T. K. Sarkar and R. F. Harrington, "Time domain Response of Multi-conductor Transmission Lines", Proc. IEEE PROC-75, N-6, pp. 743-764, June 1987.
- [3] C.R. Paul, "Introduction to Electromagnetic Compatibility" NY: Wiley-Interscience, 1992, ISBN-0-471-54927-4
- [4] C.R. Paul, "Analysis of multi-conductor transmission lines", 1992, ISBN-0-471-02080-X

- [5] Lech Znamirowski, Olgierd A. Palusinski, "*Algorithm for Accurate Capacitance Matrix Measurements of the Multi-conductor Structure for VLSI Interconnections*", Private note.
- [6] Lech Znamirowski, Olgierd A. Palusinski, "*Analysis of error propagation in computing the Maxwell matrix of multi-conductor structure from measurements*", Proc. IEEE Science, Measurement and Technology, Vol 145, pp 117 - 121, May 1998.
- [7] Roger B. Marks, Dylan F. Williams, "*Characteristic impedance determination using propagation constant measurement*", IEEE Microwaves and guided wave letters, Vol 1 N-6, pp 141 - 143, June 1999.
- [8] Sergio A. Pignari, A. Orlandi "*Long-Cable effects on conducted emissions levels*", IEEE Transactions on Electromagnetic Compatibility, Vol 45, N-1, pp 43-54 February 2003.
- [9] S. Canigia, F. Maradei, "*Equivalent circuit models for the analysis of coaxial cables immunity*", Proc. IEEE International Symposium on Electromagnetic Compatibility, pp 881-886, August 2003.
- [10] A. Orlandi, "*Frequency and time domain modeling of the transfer impedance and distributed longitudinal induced voltage by means of a Spice equivalent circuit*", IEEE Transactions on Electromagnetic Compatibility, Vol. 45, N-1, pp 125-129, February 2003.
- [11] F. Arteché, C. Rivetta, F. Szoncsó, "*EMC immunity test results of HCAL FEE*", Proc. 9th Workshop on Electronics for LHC experiments, LECC2003, Amsterdam, pp 358-363, October 2003.
- [12] Lorenz-Jung, Jan Luiken ter Haseborg, "*Evaluation of measured complex transfer admittance for the characterization of shield in-homogeneities of Multi-conductor Cables*", IEEE Transactions on Electromagnetic Compatibility, Vol. 41, N-4, pp 358-363, November 1999.
- [13] Edward F. Vance, "*Coupling to shielded cables*", 1987, ISBN 0-89874-949-2.
- [14] Jasper J. Goedbloed, "*Electromagnetic Compatibility*", 1990, ISBN-0-13-249293-8.
- [15] Tyni M., "*The transfer impedance of coaxial cables with braided outer conductor*", Proc. Nauk, Inst Telekomun Akust. Politech Wroclaw Ser. Konfi, pp 410-419, 1975.
- [16] S.Sali, "*An improved Model for the Transfer Impedance Calculations of Braided Coaxial Cables*", IEEE Transactions on Electromagnetic Compatibility, Vol. 33, N-2, pp 139-143, November 1991.
- [17] R. De Leo, G. Gerri, V. Mariani Primiani, R. Botticelli, "*A simple but effective way for cable shielding measurement*", IEEE Trans. on Electromagnetic Compatibility, Vol. 41, N-3, pp 175-179, August 1999.

Chapter 5

Susceptibility at early design stage

The purpose of this chapter is to present the assessment of the electromagnetic compatibility during the early stage of the electronic design. It is partially based on the models presented in previous chapter. As an example, the connection between the FEE and the photo-detector of the Forward Hadron Calorimeter is studied. This area of the HCAL sub-system has the particularity that the read-out amplifiers are placed 4 meters away from the detector. This characteristic as well as the functional properties of the QIE, which only admits positive currents, creates one of the most delicate connections of the detector, susceptible to very low EMI signal coming from ground currents or external electromagnetic fields. The goal of this chapter is to predict grounding and shielding problems and estimate the effect of the noise interference in the electronic system to achieve a design with high noise immunity.

5.1 Introduction

The FEE of Forward Hadron Calorimeter¹ is composed of about 3000 photo-multipliers (PMT) arranged in boxes housing 24 PMTs each one. Read-out amplifiers are arranged in 6 channel daughter cards located about 4 meters from the PMTs. Photo-detectors are biased using a resistive divider and its gain can be adjusted between 4×10^5 and 5×10^6 . High voltage power supplies are located into the counting room about 120 m. away from the metallic boxes housing the PMTs.

The anode current is amplified and digitized by a special gated charge amplifier. This ASIC chip, denominated Charge Integrator Encoder (QIE)² is a differential current mode amplifier with an input impedance of either 92Ω or 50Ω for the frequency span of 40MHz and the full input current range. The sensitivity of this amplifier is $2.7fC/LSB$ and it integrates the signal during a period of 25nsec. The dynamic range of each input current is asymmetric, positive currents in both inputs

1 See section 1.7

2 See section 1.7.2 and 1.7.3

can be processed up to a maximum charge of 27pC, while negative currents can reach only a few fC. Due to the asymmetric dynamic range, two cables with their own current return have to be used to complete the differential topology. For the present study coaxial cables (50 Ω) have been chosen to connect the PMTs to the amplifiers. The complete circuit for one channel is depicted in figure 5.1

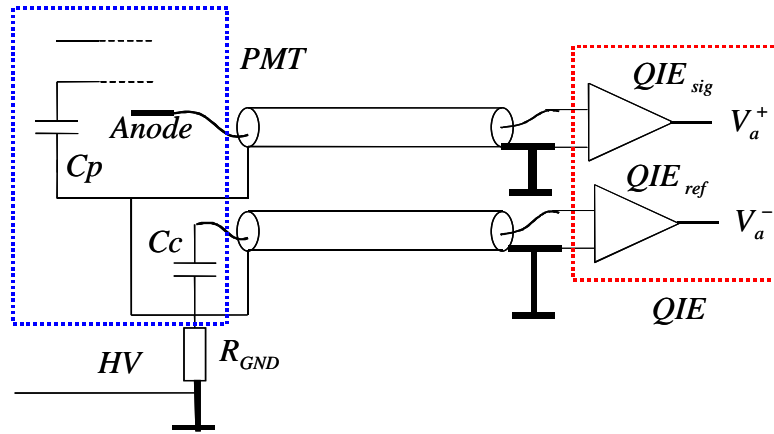


Figure 5.1: Circuit Layout of PMTs - QIE

Amplifiers are grouped in 6 channel cards and more than 10 boards are housed in small crates. All the amplifier cards are locally grounded at the detector ground. The box holding the PMTs is also locally grounded at the detector structure but about 4 mts. from the ground connection of amplifiers. As it is depicted in figure 5.1, each return point of the PMTs is isolated from the ground connection through the resistor R_{GND} .

5.2 Considerations about the noise in the FEE

The noise level defines the minimum signal that the FEE can process. The noise at the FEE is due to the contribution of different sources and perturbations as thermal noise of transistors and resistors, noise picked-up by connections between the sensor devices and the FEE, spurious signals, etc. Taking as a common point the analogue output stage of the QIE to analyse the total noise, it can be written as:

$$n_a(t) = n_{th}(t) + n_{cm}(t) + n_{emi}(t) + \dots \quad (5.1)$$

where $n_{th}(t)$ is the thermal noise contribution, $n_{cm}(t)$ is the noise due to common mode signals, and $n_{emi}(t)$ represent the contribution due to electromagnetic interference (EMI). These three terms are the most important in this analysis.

The thermal noise is characterized by the power spectral density

$$N_{th}^2(\omega) = 2 \cdot [|T_e(\omega)|^2 \cdot e_n^2(\omega) + |T_i(\omega)|^2 \cdot i_n^2(\omega)] \cdot |T_{amp}(\omega)|^2 \quad (5.2)$$

where $e_n^2(\omega)$ and $i_n^2(\omega)$ are the spectral density of the equivalent series and parallel thermal noise generators of the QIE and $T_e(\omega)$ and $T_i(\omega)$ are the transfer function between the voltage or current thermal noise generators and the voltage or current at the input of the QIE.

The additional noise due to common mode signals and EMI can be mathematically represented as voltage spectral density by:

$$N_{cm}(\omega) = T_{cm}(\omega) \cdot T_{amp}(\omega) \cdot V_{cm}(\omega) \quad (5.3)$$

$$N_{emi}(\omega) = [T_{emi_H}(\omega) \cdot H(\omega) + T_{emi_E}(\omega) \cdot E(\omega)] \cdot T_{amp}(\omega) \quad (5.4)$$

where $T_{cm}(\omega)$ is common mode transference, $T_{amp}(\omega)$ QIE transference and $T_{emi_H}(\omega)$, $T_{emi_E}(\omega)$ output voltage to magnetic field and electric field transference, respectively.

The criteria generally used to set the total noise contribution in a design is to define the total noise mainly due to the thermal noise, making any external noise perturbation much lower than the thermal noise. This means:

$$\langle n_a^2 \rangle \cong \langle n_{th}^2 \rangle \quad (5.5)$$

$$\langle (n_{cm} + n_{emi} + \dots)^2 \rangle \rightarrow 0 \quad (5.6)$$

In order to use this criteria for the design it is necessary to know and minimize $\langle n_{th}^2 \rangle$ and to define the factors $T_{cm}(\omega)$, $T_{emi_H}(\omega)$ and $T_{emi_E}(\omega)$ to reduce their contribution in the total noise.

5.3 Thermal noise

The QIE is the key element of the FEE. It amplifies, shapes and digitizes the incoming signal from the optical devices. The QIE presents two inputs, one for the incoming signal and the other for a reference signal. The input currents can flow only into one direction in both QIE input. Both input currents are amplified and integrated by the first stage of the QIE and then subtracted before the analog to digital conversion takes places. The QIE acts as a difference amplifier where the input current is integrated during 25 ns. If we define i_+ and i_- , the QIE input currents, c is the integrator capacitance, and $g(t)$ the impulse response of the

amplifying stage before the integration, the analog signal before the digital conversion can be expressed as:

$$v_a(t) = v_a^+ - v_a^- = \frac{1}{c} \cdot \int_0^\tau g(t) * (i_+(t) - i_-(t)) dt \quad (5.7)$$

Where v_a^+ is the input voltage of the QIE signal, v_a^- is the input voltage of the QIE reference, τ corresponds to the 25 ns. integration interval and '*' denotes the convolution operation. Using the Laplace transform to evaluate the equation 5.7

$$v_a(s) = L(v_a(t)) = \frac{1 - e^{-(s \cdot \tau)}}{s} \cdot \frac{G(s) \cdot (I_+(s) - I_-(s))}{c} = T(s) \cdot (I_+(s) - I_-(s)) \quad (5.8)$$

where $G(s) = L(g(t))$. the magnitude of $T(s)$ can be evaluated in frequency domain by replacing $s = j \cdot \omega = j \cdot 2 \cdot \pi \cdot f$.

The calculate intrinsic thermal noise contribution at the output of the amplifier, each signal path of the QIE amplifier can be modeled by the equivalent circuit depicted in figure 5.2.

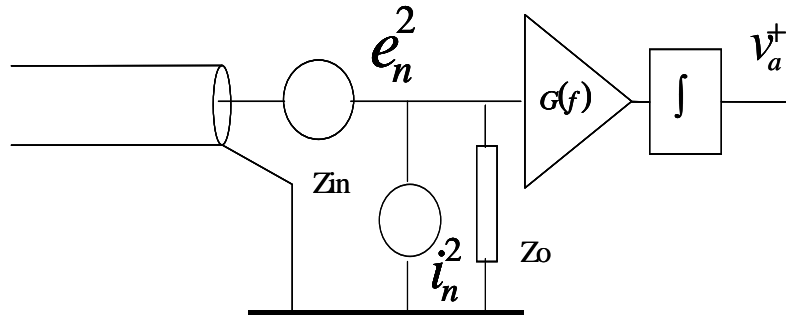


Figure 5.2: Equivalent circuit to calculate the thermal noise

The cable connecting the photo-tube and the QIE is 4 m. long and the characteristic impedance is Z_o . The cable is matched by the input impedance of the amplifier. The opposite end of the cable can be considered open in a first approximation. The amplifier thermal noise is characterized by two independent sources modeling the series equivalent noise and the parallel equivalent noise. It has been assumed that both sources represent white noise characterized by a constant unilateral normalized power spectrum e_n^2 and i_n^2 , respectively.

The impedance presented by the line at the input of the amplifier can be calculated for the case of infinite impedance at the end of cable as:

$$Z_{in} = -j \cdot Z_o \cdot \cot(\beta \cdot L) \quad (5.9)$$

where $\beta = \frac{\omega}{v}$ v : is the phase velocity of the cable and $\omega = 2 \cdot \pi \cdot f$. The input current at any QIE input in frequency domain is:

$$i_i(\omega) = \frac{e_n(\omega)}{(Z_{in} + Z_o)} + \frac{i_n(\omega) \cdot Z_{in}}{(Z_{in} + Z_o)} = [T_e(\omega) \cdot e_n(\omega) + T_i(\omega) \cdot i_n(\omega)] \quad (5.10)$$

The normalized power spectrum at each QIE input is:

$$i_i^2(\omega) = |T_e \omega|^2 \cdot e_n^2 + |T_i \omega|^2 \cdot i_n^2 \quad (5.11)$$

and the normalized power spectrum after the integration assuming the noise contribution at each input statistically independent is:

$$n_{ih}^2(\omega) = 2 \cdot [|T_e(\omega)|^2 \cdot e_n^2(\omega) + |T_i(\omega)|^2 \cdot i_n^2(\omega)] \cdot |T(\omega)|^2 \quad (5.12)$$

The transfer functions can be calculated by:

$$|T_e(\omega)|^2 = \left| \frac{1}{Z_{in} + Z_o} \right|^2 = \frac{1}{(Z_o)^2 \cdot (1 + [\cot(\beta \cdot L)]^2)} = \frac{[\sin(\beta \cdot L)]^2}{|Z_o|^2} \quad (5.13)$$

$$|T_i(\omega)|^2 = \left| \frac{Z_{in}}{Z_{in} + Z_o} \right|^2 = \frac{|Z_{in}|^2}{(Z_o)^2 \cdot (1 + [\cot(\beta \cdot L)]^2)} = [\cos(\beta \cdot L)]^2 \quad (5.14)$$

and

$$|T(\omega)|^2 = \left| G(\omega) \cdot \frac{\tau}{c} \cdot \frac{\sin\left(\frac{\omega \cdot \tau}{2}\right)}{\left(\frac{\omega \cdot \tau}{2}\right)} \right|^2 = \frac{4 \cdot G(\omega)^2}{c^2} \cdot \frac{[\sin\left(\frac{\omega \cdot \tau}{2}\right)]^2}{\omega^2} \quad (5.15)$$

In this development $|Z_{in} + Z_o|^2 = |Z_{in}|^2 + |Z_o|^2$ because we are assuming that Z_o is real and Z_{in} is imaginary, being β also real. Assuming the bandwidth of the amplifying stages is much larger than $f = \frac{1}{\tau}$, it is possible to assume that $G(\omega) = G = cte$. Evaluating the integral, we get:

$$\frac{2 \cdot G^2 \cdot e_n^2}{\pi \cdot c^2 \cdot |Z_o|^2} \int_0^\infty \left(\frac{[\sin\left(\frac{\omega \cdot \tau}{2}\right)]^2}{\omega^2} \cdot [\sin(\beta \cdot L)]^2 \right) d\omega = \left(\begin{array}{l} \frac{G^2 \cdot e_n^2}{c^2 \cdot |Z_o|^2} \cdot \frac{\tau}{4} \quad \text{if } ((\beta \cdot L) \geq \frac{\omega \cdot \tau}{2}) \\ \frac{G^2 \cdot e_n^2}{c^2 \cdot |Z_o|^2} \cdot \frac{L}{2 \cdot v} \quad \text{if } ((\beta \cdot L) < \frac{\omega \cdot \tau}{2}) \end{array} \right) \quad (5.16)$$

$$\frac{2 \cdot G^2 \cdot i_n^2}{\pi \cdot c^2} \int_0^\infty \left(\frac{\left[\sin\left(\frac{\omega \cdot \tau}{2}\right) \right]^2}{\omega^2} \cdot [\cos(\beta \cdot L)]^2 \right) d\omega = \begin{cases} \frac{G^2 \cdot i_n^2}{c^2} \cdot \frac{\tau}{4} & \text{if } ((\beta \cdot L) \geq \frac{\omega \cdot \tau}{2}) \\ \frac{G^2 \cdot i_n^2}{c^2 \cdot |Z_o|^2} \cdot \frac{\tau - L}{2} & \text{if } ((\beta \cdot L) < \frac{\omega \cdot \tau}{2}) \end{cases} \quad (5.17)$$

Then the thermal noise is given by the following expression,

$$\langle n_{th}^2 \rangle = \begin{cases} \frac{G^2}{c^2} \cdot \left(\frac{e_n^2}{|Z_o|^2} + i_n^2 \right) \cdot \frac{\tau}{4} & \text{if } ((\beta \cdot L) \geq \frac{\omega \cdot \tau}{2}) \\ \frac{G^2}{c^2} \cdot \left[\left(\frac{e_n^2}{|Z_o|^2} - i_n^2 \right) \cdot \frac{L}{2 \cdot v} + i_n^2 \cdot \frac{\tau}{2} \right] & \text{if } ((\beta \cdot L) < \frac{\omega \cdot \tau}{2}) \end{cases} \quad (5.18)$$

From these equations it is important to note if $(\beta \cdot L) \geq \frac{\omega \cdot \tau}{2}$, the length of the cable has not any influence on the output power noise, as it is shown in figure 5.3. In addition, the output power noise decreases if the characteristic impedance of cable increases.

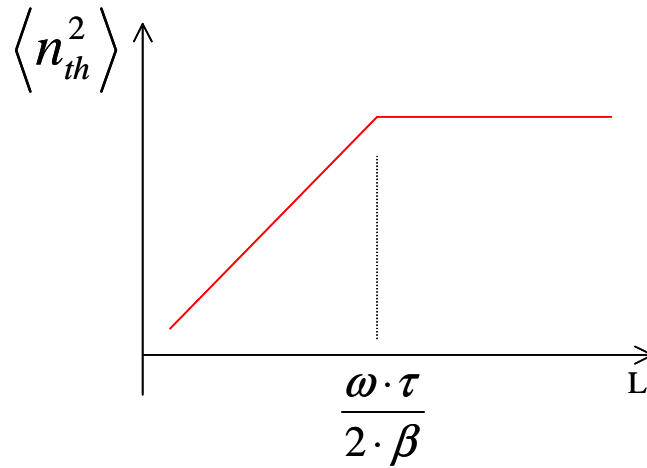


Figure 5.3: Output power noise - $Z_o = cte$ - $G = cte$

Assuming a propagation velocity of cable equal to 66% of the light speed, the critical length results equal to 2.5 meters, which results smaller than the cable length of the circuit under study.

5.4 Susceptibility to CM currents

The common mode rejection of the differential topology has been studied considering the circuit depicted in figure 5.4

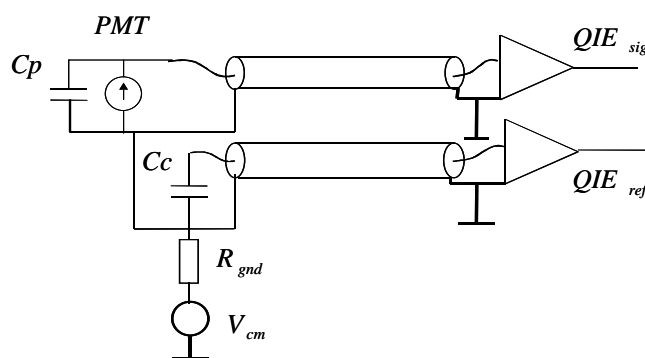


Figure 5.4: Equivalent circuit to analyse the common mode rejection of the system

The effect of unbalances in the circuit are studied considering a mismatch between the parasitic capacitance of the PMT anode, socket and board, C_p and the compensation capacitance C_c . In addition, the relative position of the coaxial cables respect to the reference tray has been considered, assuming the coaxial cables may be placed at different heights respect to the reference. For all those cases, the resistor R_{GND} is changed and used as a parameter to quantify the common mode rejection of the front-end electronics.

The EMI immunity study of this circuit has been carried out following a similar analysis to that presented in chapter 4. The solution of this circuit is based on MTL models [1][2][3] presented in equations 4.96 and 4.97. For that purpose, the circuit is split in two parts [4][5], inner and outer system as it has been shown in section 4.6.1. The outer system represents the external circuit that the cables forms with the metallic tray. This circuit is approximated in this example by a transmission line, where the metallic tray is the reference of the outer system and the shield of the conductors are the transmission lines.

The per unit length parameters¹ of the MTL equations not only can be measured as it has been shown in section 4.3 but they can also be obtained directly from the definition. It can be achieved solving equations 4.3 and 4.7 analytically for simple topologies or using finite element analysis programs² for more complex topologies. The transmission line parameters of the outer part of the presented circuit can be

¹ See equation 4.6, 4.8 and 4.14

² MAXWELL 2D-3D

simplified to the case of 2 wires (shields) above and parallel to an infinite, perfectly conducting plane (metallic tray). The per-unit length inductance, capacitance and resistance matrix equations applied in this example can be found in several books [2][3]. A simple diagram of the circuit used to estimated the per unit length parameters of the circuit is shown in figure 5.5.

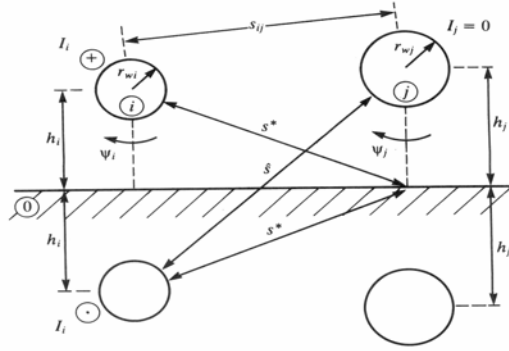


Figure 5.5: Illustration of the calculation of per-unit length inductance of two conductors above a ground plane.

The expression of the inductance and capacitance of two cables placed h mm above the ground is given by:

$$L_{ii} = \frac{\mu}{2 \cdot \pi} \cdot \ln\left(\frac{2 \cdot h}{r_i}\right) \quad (5.19)$$

$$L_{ij} = \frac{\mu}{4 \cdot \pi} \cdot \ln\left(\frac{4 \cdot h_i \cdot h_j}{s_{ij}^2} + 1\right) \quad (5.20)$$

The capacitance matrix is calculated using the fundamental relationship obtained for a homogeneous medium., which in this case is considered the free space.:

$$C = \mu \cdot \varepsilon \cdot L^{-1} \quad (5.21)$$

In this way it has been calculated the inductance and capacitance matrix of a system formed by two coaxial cables (external radius (r) 2mm) placed 7 mm (h=9 mm.) above the ground and with the conductor centers separate a distance of 6 mm are:

$$L = \begin{bmatrix} 0.4394 & 0.2302 \\ 0.2302 & 0.4394 \end{bmatrix} \times 10^{-6} \frac{H}{m} \quad (5.22)$$

$$C = \begin{bmatrix} 34.86 & -18.27 \\ -18.27 & 34.86 \end{bmatrix} \times 10^{-12} \frac{F}{m} \quad (5.23)$$

5.4. Susceptibility to CM currents

The inductance and capacitance matrix of a system formed by two coaxial cables one placed 7 mm above the ground and the other placed 10 mm are:

$$L = \begin{bmatrix} 0.4394 & 0.2360 \\ 0.2360 & 0.4969 \end{bmatrix} \times 10^{-6} \frac{H}{m} \quad (5.24)$$

$$C = \begin{bmatrix} 33.95 & -16.12 \\ -16.12 & 30.02 \end{bmatrix} \times 10^{-12} \frac{f}{m} \quad (5.25)$$

The resistance matrix, which include the shield skin effect¹ (without considering the resistance of the metallic tray) is shown as:

$$R_{Sh} = \begin{bmatrix} \left(0.014 \cdot \left(1 + \sqrt{\frac{f}{250 \times 10^3}}\right)\right) & 0 \\ 0 & \left(0.014 \cdot \left(1 + \sqrt{\frac{f}{250 \times 10^3}}\right)\right) \end{bmatrix} \Omega \quad (5.26)$$

Once the per unit length parameter are calculated, it is necessary to fix the terminal configurations to solved the MTL equation in the frequency domain, following the procedure showed in section 4.6.2, the terminal configurations of the external circuit presented are characterized as a generalized Thevenin² equivalent where:

$$Z_L = \begin{bmatrix} 0 & 0 \\ 0 & 0 \end{bmatrix} \Omega, \quad V_L = \begin{bmatrix} 0 \\ 0 \end{bmatrix} V \text{ Load level} \quad (5.27)$$

$$Z_S = \begin{bmatrix} R_{GND} & R_{GND} \\ R_{GND} & R_{GND} \end{bmatrix} \Omega, \quad V_S = \begin{bmatrix} V_{cm} \\ V_{cm} \end{bmatrix} V \text{ Source level} \quad (5.28)$$

The second part of the circuit consists of the inner system representing the central conductor of coaxial cable taking as reference conductor the braided shield. One of the coaxial cables is used as a signal cable (s) and the other as a reference conductor (r). The per unit length parameter matrix for these cables are based on the measurements of coaxial cable [6]-[9]. The values of the inductance and capacitance per unit length matrix are:

$$L_S = L_R = [0.25] \times 10^{-6} \frac{H}{m} \quad (5.29)$$

¹ See Appendix I

² See equations 4.106 and 4.107.

$$C_S = C_R = [100] \times 10^{-12} \frac{F}{m} \quad (5.30)$$

In the case of the resistance matrix the resistance of the internal conductors have been considered. The shield resistance has not been included in the model as it is much lower than the resistance of internal conductor in all frequency range.

$$R = \left[0.0343 \cdot \left(1 + \sqrt{\frac{f}{110 \times 10^3}} \right) \right] \frac{\Omega}{m} \quad (5.31)$$

The terminal configurations of the internal circuit presented are characterized as a generalized Thevenin equivalent¹:

$$Z_{Ls} = Z_{Lr} = [50] \Omega \quad , \quad V_{Ls} = V_{Lr} = [0] V \text{ Load level} \quad (5.32)$$

$$Z_{Ss} = \left[\frac{1}{j \cdot \omega \cdot Cp} \right] \Omega \quad , \quad Z_{Sr} = \left[\frac{1}{j \cdot \omega \cdot Cc} \right] \Omega \quad V_{Ss} = V_{Sr} = [0] V \text{ Source level} \quad (5.33)$$

The simulated values of surface transfer impedance function² [5][10]-[12] of the coaxial cable [13]-[15] used in the present analysis is shown below in figure 5.6

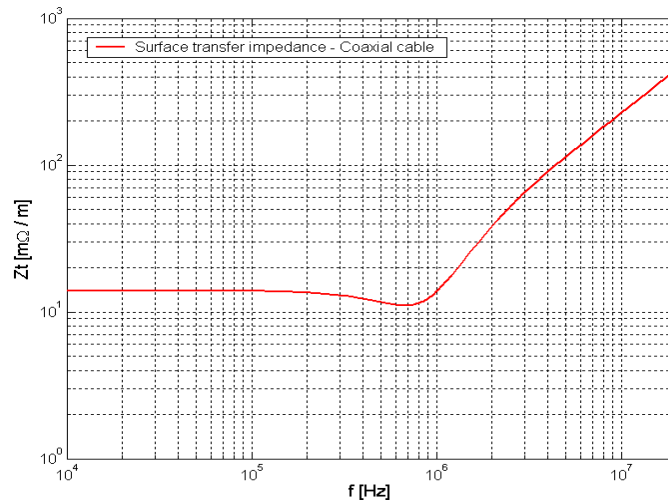


Figure 5.6: Simulated values of the surface transfer impedance function.

1 See equations 4.106 and 4.107

2 See equation 4.93

5.4. Susceptibility to CM currents

The common mode rejection $T_{cm}(f)$ of the complete circuit is defined as:

$$T_{cm}(f) = 20 \times \log\left(\frac{V_a}{V_{cm}}\right) \quad (5.34)$$

This transference function includes the effects of the cable topology and the QIE frequency response. The output voltage V_a is equal to the difference between the output voltages of the individual QIE amplifiers, labeled as QIE sig. and QIE ref. in figure 5.4.

Figure 5.7 depicts the simulated results of the common mode transfer function, for a frequency range between 10kHz and 100 MHz, for different values of R_{GND} (100Ω , $1 k\Omega$, $10 k\Omega$), with the parasitic capacitance C_p different of C_c . As it can be observed, the resistor R_{GND} improves the common mode rejection of the system proportionally to its magnitude. However, around the cable resonance, the effect of the resistor is not very important. The common mode transference presents notches at frequencies 40MHz and 80MHz due to the 25ns. integration interval of the QIE amplifier.

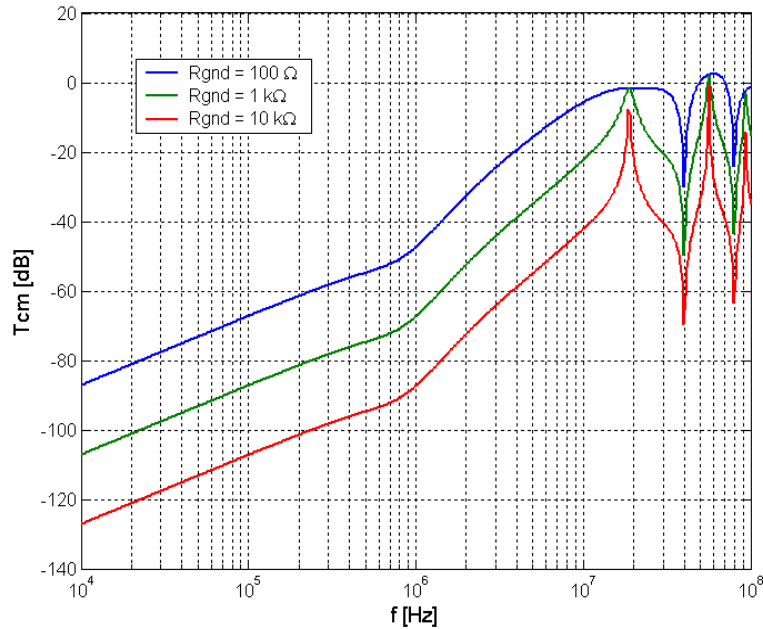


Figure 5.7: Common mode rejection - Unbalanced circuit in capacitance, $C_p=40$ pf, $C_c=30$ pf - $R_{gnd}=100 \Omega$, $1 k\Omega$, $10 k\Omega$ both cables at the same height $h=7$ mm.

Let us analyse now the effect of cable positions, unbalances due to the position of both coaxial cables respect to the metallic tray reduce the capacity of the system to

reject common mode signals. This effect is due to the currents flowing through the shields are not equal coupling different voltages into the central conductors.

In figure 5.8 depicts $T_{cm}(f)$ for two different configurations. In one of them, the system has perfectly balanced capacitances C_p and C_c but the coaxial cables are placed at different heights (7 mm & 10 mm). The other has unbalanced capacitances but both coaxial cables are placed at the same level. In both cases, the magnitude of R_{GND} was fixed to 1 k Ω .

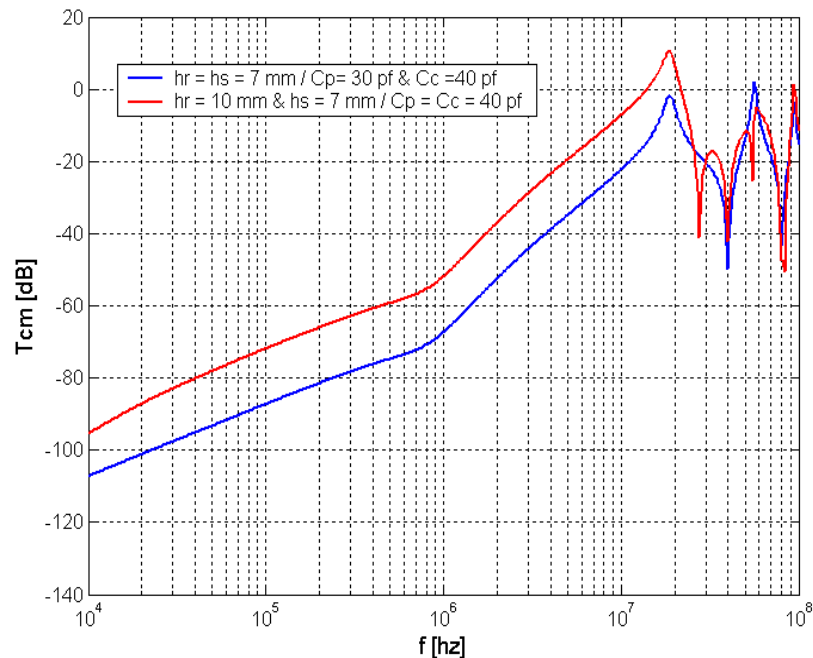


Figure 5.8: Common mode rejection - Comparison between the effect of cable position and the effect of input capacitance unbalanced

5.5 External electromagnetic fields

5.5.1 Introduction

The effect of coupling external electromagnetic fields into a multi-conductor transmission line is also well described in [16]-[18]. The coupling effect in multi-conductor transmission lines was first introduced by Clyton [19] and later extended to multi-conductor lines by Harrison [20]. A short description of the most important aspects is presented here.

5.5. External electromagnetic fields

The effect of the incident field is configured as distributed sources along the line. Incident field effects appear as a set of voltage and current sources. Figure 5.9 shows a generic circuit of an infinitesimally length Δz illuminated by an external electromagnetic field, where the parameters per-unit length have been identified.

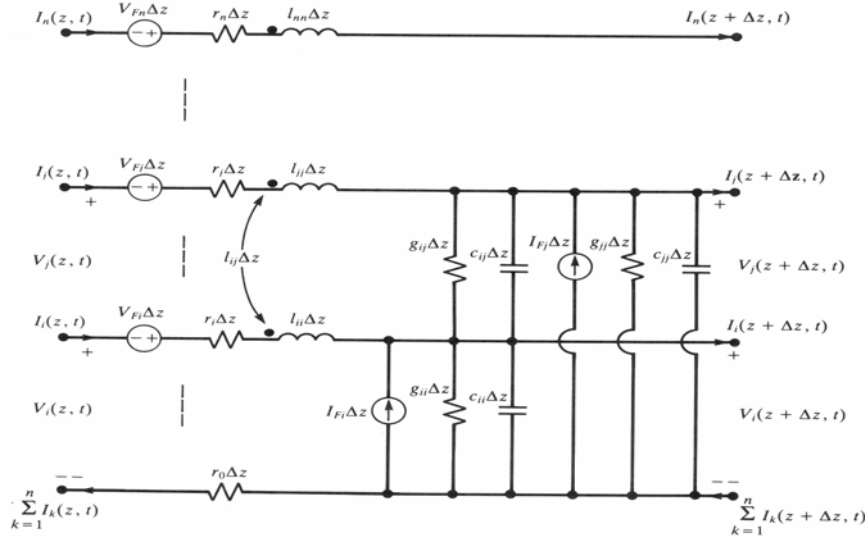


Figure 5.9: Distributed MTL model for external field

The MTL equations including the external electromagnetic field effects are:

$$\frac{\partial}{\partial z} V(z, t) = -R \cdot I(z, t) - L \cdot \frac{\partial}{\partial t} I(z, t) + V_F(z, t) \quad (5.35)$$

$$\frac{\partial}{\partial z} I(z, t) = -G \cdot V(z, t) - C \cdot \frac{\partial}{\partial t} V(z, t) + I_F(z, t) \quad (5.36)$$

where the $N \times 1$ vectors on the right hand side, $V_F(z, t)$ and $I_F(z, t)$, model the effects of the incident fields and are determined by the components of the incident electric and magnetic fields that lie in the transverse plane. They are as well influenced by the geometry of cables respect to the reference. These vectors are given by:

$$\hat{V}_F(z, t) = \frac{\partial}{\partial t} \int_a^{a'} \vec{B}^i \cdot \vec{a}_n dl \quad (5.37)$$

$$\hat{I}_F(z, t) = -G \cdot \begin{bmatrix} \dots \\ a' \vec{i}(\vec{dl}) \\ a \\ \dots \end{bmatrix} - C \cdot \begin{bmatrix} \dots \\ a' \vec{i}(\vec{dl}) \\ a \\ \dots \end{bmatrix} \quad (5.38)$$

It can be observed, that equation 5.35 and 5.36 are identical to the MTL equations including shield effects (equations 4.96 and 4.97). Therefore, the solution to the phasor MTL equation, can be obtained by the analogy to the state-variable equations for lumped systems, as it has been well detailed in the previous sections¹.

The system can be divided again into two parts. One unexcited and the effect of the incident field can be represented by several current and voltage sources located at $z = L$ as it is shown in figure 5.10.

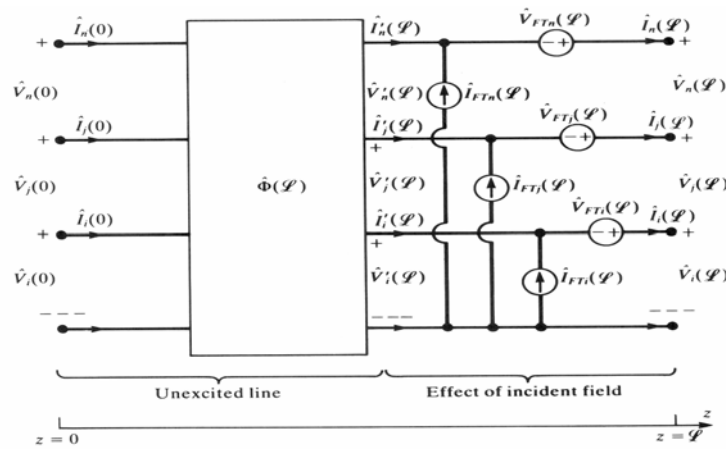


Figure 5.10: Representation of MTL model with incident-field illumination

The incident field effect add a convolution term to the usual chain parameter relation². Then, writing equations 4.40 out for a MTL system illuminated by an external field of total length L gives:

$$\begin{bmatrix} \hat{V}(L) \\ \hat{I}(L) \end{bmatrix} = \begin{bmatrix} \hat{\Phi}_{11}(L) & \hat{\Phi}_{12}(L) \\ \hat{\Phi}_{21}(L) & \hat{\Phi}_{22}(L) \end{bmatrix} \cdot \begin{bmatrix} \hat{V}(0) \\ \hat{I}(0) \end{bmatrix} + \begin{bmatrix} \hat{V}_{FT}(L) \\ \hat{I}_{FT}(L) \end{bmatrix} \quad (5.39)$$

where the total source voltages $\hat{V}_{FT_i}(L)$ and currents $\hat{I}_{FT_i}(L)$ are according to the equation:

1 Section 4.4
2 Equation 4.40

$$\hat{V}_{FT}(L) = \int_0^L [\hat{\Phi}_{11}(L-\tau) \cdot \hat{V}_F(\tau) + \hat{\Phi}_{12}(L-\tau) \cdot \hat{I}_F(\tau)] d\tau \quad (5.40)$$

$$\hat{I}_{FT}(L) = \int_0^L [\hat{\Phi}_{21}(L-\tau) \cdot \hat{V}_F(\tau) + \hat{\Phi}_{22}(L-\tau) \cdot \hat{I}_F(\tau)] d\tau \quad (5.41)$$

Now that the general solution of the phasor MTL equations has been obtained in terms of the chain parameter matrix and the incident field forcing functions, the terminal conditions to arrive at an explicit solution or the phasor line voltages and currents are incorporated to yield:

$$\begin{aligned} & [\hat{\Phi}_{11} \cdot \hat{Z}_S + \hat{Z}_L \cdot \hat{\Phi}_{22} - \hat{\Phi}_{12} - (\hat{Z}_L \cdot \hat{\Phi}_{21} \cdot \hat{Z}_S)] \cdot \hat{I}(0) = \\ & [\hat{\Phi}_{11} - \hat{Z}_L \cdot \hat{\Phi}_{21}] \cdot \hat{V}_S - \hat{V}_L + [\hat{V}_{FT}(L) - (\hat{Z}_L \cdot \hat{V}_{FT}(L))] \end{aligned} \quad (5.42)$$

$$\hat{I}(L) = \hat{I}_{FT}(L) + \hat{\Phi}_{21} \cdot \hat{V}_S + ((\hat{\Phi}_{22} - (\hat{\Phi}_{21} \cdot \hat{Z}_S)) \cdot \hat{I}(0)) \quad (5.43)$$

From these values and equations 4.62 and 4.63 the voltages at both ends of the lines can be calculated.

5.5.2 Uniform plane-wave excitation of the line

For the case of radiation of the line by an uniform plane wave from some distant source, the fields in the far field region of a radiating structure are spherical waves which locally resemble uniform plane waves. This assumption simplifies the evaluation of the sources in the above results.

In order to characterize the frequency-domain response of the line let us describe the incident uniform plane wave angle of incidence and polarization with respect to a spherical coordinate system as it is shown in figure 5.11

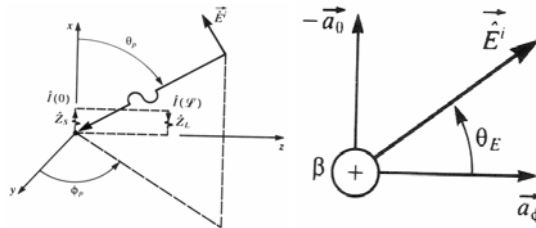


Figure 5.11: Characterization of incident field as uniform plane wave - Rectangular coordinate system.

The polarization of electric field vector is described in terms of the relation to the unit vectors in the spherical coordinate system, \vec{a}_θ and \vec{a}_ϕ . In terms of these components, the general expression for the phasor electric field vector can be written as:

$$\vec{E}_i = \hat{E}_o \cdot (e_x \cdot \vec{a}_x + e_y \cdot \vec{a}_y + e_z \cdot \vec{a}_z) \cdot e^{-(j \cdot \beta_x \cdot x)} \cdot e^{-(j \cdot \beta_y \cdot y)} \cdot e^{-(j \cdot \beta_z \cdot z)} \quad (5.44)$$

where the components of the incident electric field vector along the x,y and z axes of the rectangular coordinate system describing the line are:

$$e_x = \sin\theta_E \cdot \sin\theta_p \quad (5.45)$$

$$e_y = (-\sin\theta_E \cdot \cos\theta_p \cdot \cos\phi_p) - (\cos\theta_E \cdot \sin\phi_p) \quad (5.46)$$

$$e_z = (-\sin\theta_E \cdot \cos\theta_p \cdot \sin\phi_p) + (\cos\theta_E \cdot \cos\phi_p) \quad (5.47)$$

$$(e_x^2 + e_y^2 + e_z^2) = 1 \quad (5.48)$$

The components of the phase constant, β along those coordinate axes are:

$$\beta_x = -\beta \cdot \cos\theta_p \quad (5.49)$$

$$\beta_y = -\beta \cdot \sin\theta_p \cdot \cos\phi_p \quad (5.50)$$

$$\beta_z = -\beta \cdot \sin\theta_p \cdot \sin\phi_p \quad (5.51)$$

The phase constant is related to the frequency and properties of the medium as:

$$\beta = \omega \cdot \sqrt{\mu \cdot \epsilon} = \frac{1}{v_o} \cdot \sqrt{\mu_r \cdot \epsilon_r} \quad (5.52)$$

where v_o is the phase velocity in free space and the medium is characterized by permeability, μ and permittivity, ϵ , \hat{E}_o is the complex amplitude of the sinusoidal wave.

The results of the integral of equations 5.37, 5.38, 5.40 and 5.41 are very complex and they are well detailed in [3]. However, if the integrals 5.40 and 5.41 are solved as a sum of integrals (equation 5.53 and 5.54) in which each part of the line is electrically small, several assumptions and simplifications can be done to solve these equations.

$$\hat{V}_{FT(L)} = \sum_{i=1}^n \left(\left[\int_{l_i}^{l_{i+1}} \hat{\Phi}_{11(L-\tau)} d\tau \right] \cdot \hat{V}_{F_i} \left(\frac{l_{i+1}-l_i}{2} \right) + \left(\left[\int_{l_i}^{l_{i+1}} \hat{\Phi}_{12(L-\tau)} d\tau \right] \cdot \hat{I}_{F_i} \left(\frac{l_{i+1}-l_i}{2} \right) \right) \quad (5.53)$$

$$\hat{I}_{FT(L)} = \sum_{i=1}^n \left(\left[\int_{l_i}^{l_{i+1}} \hat{\Phi}_{21(L-\tau)} d\tau \right] \cdot \hat{V}_{F_i} \left(\frac{l_{i+1}-l_i}{2} \right) + \left(\left[\int_{l_i}^{l_{i+1}} \hat{\Phi}_{22(L-\tau)} d\tau \right] \cdot \hat{I}_{F_i} \left(\frac{l_{i+1}-l_i}{2} \right) \right) \quad (5.54)$$

For each portion of the integral, the line is electrically short, $L \ll \lambda$. This simplification allows to evaluate the values of \hat{V}_{F_i} and \hat{I}_{F_i} at any convenient point on each part of the line resulting this value constant. We have arbitrarily chosen to evaluate them at the midpoint of each portion. In case of one conductor of length L (electrically small at the frequency of interest) which is at a certain distance of its reference conductor and one conductor above the ground plane, the values of \hat{V}_F and \hat{I}_F are presented below:

Two conductors:

$$\hat{V}_F \left(\frac{L}{2} \right) \cdot L = A \cdot \hat{E}_o \cdot \left[\frac{\sin(\beta_x \cdot \frac{d}{2})}{(\beta_x \cdot \frac{d}{2})} \right] \cdot e^{-j \cdot \beta_x \cdot \frac{d}{2}} \cdot e^{-j \cdot \beta_z \cdot \frac{L}{2}} \cdot (j \cdot \beta_z \cdot e_x - (j \cdot \beta_x \cdot e_z)) \quad (5.55)$$

$$\hat{I}_F \left(\frac{L}{2} \right) \cdot L = -(j \cdot \omega \cdot c \cdot A) \cdot \hat{E}_o \cdot \left[\frac{\sin(\beta_x \cdot \frac{d}{2})}{(\beta_x \cdot \frac{d}{2})} \right] \cdot e^{-j \cdot \beta_x \cdot \frac{d}{2}} \cdot e^{-j \cdot \beta_z \cdot \frac{L}{2}} \cdot (e_x) \quad (5.56)$$

where $A = d \cdot L$ is the area between conductors, being d the distance between them.

For the case of a single conductor above the ground these sources are:

$$\hat{V}_F \left(\frac{L}{2} \right) \cdot L = 2 \cdot A \cdot \hat{E}_o \cdot \left[\frac{\sin(\beta_x \cdot h)}{(\beta_x \cdot h)} \right] \cdot e^{-j \cdot \beta_z \cdot \frac{L}{2}} \cdot (j \cdot \beta_z \cdot e_x - (j \cdot \beta_x \cdot e_z)) \quad (5.57)$$

$$\hat{I}_F \left(\frac{L}{2} \right) \cdot L = -(j \cdot \omega \cdot c \cdot 2 \cdot A) \cdot \hat{E}_o \cdot \left[\frac{\sin(\beta_x \cdot h)}{(\beta_x \cdot h)} \right] \cdot e^{-j \cdot \beta_z \cdot \frac{L}{2}} \cdot (e_x) \quad (5.58)$$

where A is the area between conductors and the ground plane (h.L) and h the distance from the conductor to the reference plane.

All of these equations and equations 5.42, 5.43, 4.62 and 4.63 have been implemented in a MATLAB program and they have been used in next section to calculate the effect of external electromagnetic fields in the PMTs and QIE connections of the Forward Hadron Calorimeter. The validation of the program and the model presented is explained in appendix A

5.5.3 Susceptibility to Electromagnetic fields of HF FEE.

As it has been showed above, to include the effect of external electromagnetic fields in the model of the multi-conductor cable¹, the outer system is modified. A series voltage generator $\hat{V}_F(z)$ proportional to the magnitude of the external magnetic field and a current generator $\hat{I}_F(z)$ proportional to the external electric field are included in the outer circuit. The modified circuit is solved in a similar manner than sections 4.6.3, first the shield current is calculated to define the coupling generators to the inner system and afterwards, the inner circuit is solved.

The example presented in this study assumes that the EM wave is propagating in the positive direction of z with the electric field polarized in the positive direction of x and the magnetic field perpendicular to the plane created by the cable and the metallic tray, which has been chosen as a reference plane. The case under study is referred as electromagnetic plane wave with an end-fire excitation as it is showed in figure 5.12.

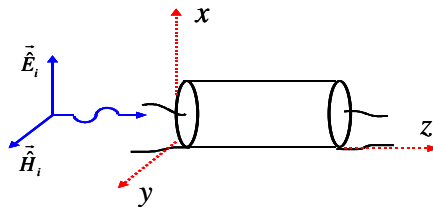


Figure 5.12: Electromagnetic plane wave with an end-fire excitation

For the end-fire excitation field, the normalized projections of the electric field vector on the rectangular coordinate system (e_x, e_y, e_z) are equal to $e_x = 1$ and $e_y = e_z = 0$.

The distributed voltages and currents in frequency domain $V_F(z)$ and $I_F(z)$ are calculated assuming a plane wave and a constant electric field E_o for all frequencies. Substituting these considerations into equations 5.57 and 5.58 results

$$\hat{V}_F\left(\frac{z}{2}\right) = 2 \cdot h \cdot \hat{E}_o \cdot \left[\frac{\sin(\beta_x \cdot h)}{(\beta_x \cdot h)} \right] \cdot e^{-\left(j \cdot \beta_z \cdot \frac{z}{2}\right)} \cdot (j \cdot \beta_z) \quad (5.59)$$

¹ See section 4.6.1

$$\hat{I}_F\left(\frac{z}{2}\right) = -(j \cdot \omega \cdot c \cdot 2 \cdot h) \cdot \hat{E}_o \cdot \left[\frac{\sin(\beta_x \cdot h)}{(\beta_x \cdot h)} \right] \cdot e^{-\left(j \cdot \beta_z \cdot \frac{z}{2}\right)} \quad (5.60)$$

The magnitude of the electric field applied is 100 $\mu\text{V}/\text{m}$ that corresponds to the limit of the emission level suggested by the EN 55022-B standard, and h is the cable height respect to the reference plane.

The per unit length parameter matrices¹ and terminal configurations² for the inner and outer systems are the same as section 5.4, except the terminal configurations of the external circuit, whose matrices are:

$$Z_L = \begin{bmatrix} 0 & 0 \\ 0 & 0 \end{bmatrix} \Omega, \quad V_L = \begin{bmatrix} 0 \\ 0 \end{bmatrix} \text{V Load level} \quad (5.61)$$

$$Z_S = \begin{bmatrix} R_{GND} & R_{GND} \\ R_{GND} & R_{GND} \end{bmatrix} \Omega, \quad V_S = \begin{bmatrix} 0 \\ 0 \end{bmatrix} \text{V Source level} \quad (5.62)$$

Figure 5.13 depicts the voltage at the output of the QIE when an electromagnetic field of 100 $\mu\text{V}/\text{m}$ is coupled to the cable connection for different values of the ground resistor, R_{GND} , when the capacitances C_p and C_c are not equal.

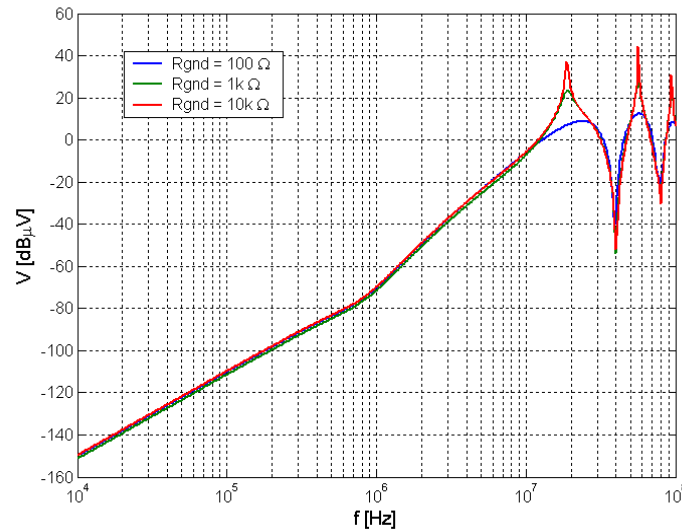


Figure 5.13: Output voltage of QIE in an unbalanced configuration, $C_p = 40\text{pf}$, $C_c = 30\text{pf}$, for different values of ground resistance $R_{GND} = 100 \Omega, 1 \text{ k}\Omega, 10 \text{ k}\Omega$

1 See equations 4.6, 4.8 and 4.14

2 See equations 4.106 and 4.107

The resistor R_{GND} has minimum influence rejecting this perturbation. This is different to the case of CM currents, where the CM rejection is quite susceptible to the resistance value. This difference can be explained by the different nature of the circuits. In the first case the ground resistance is in series with the noise source, however in the second one is in parallel decreasing a lot the beneficial effect of this resistance.

The influence of unbalances generated by the different position of the cables on the cable tray degrades the performance of the differential amplifier more than the capacitance unbalance. The effect of the cable heights is compared in figure 5.14 with the effect of different capacitances for a resistor $R_{GND} = 1 \text{ k}\Omega$.

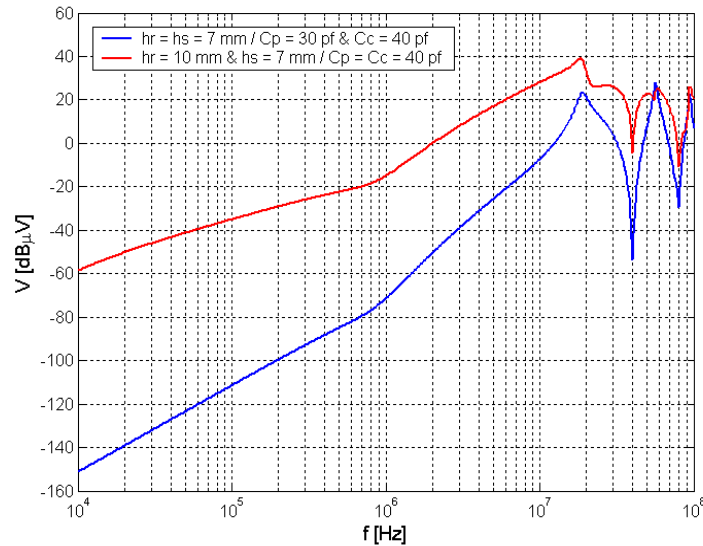


Figure 5.14: Output voltage of QIE for two different unbalanced configuration. Different high and unbalanced capacitances with a constant ground resistance of $R_{GND} = 1000 \Omega$

5.6 Summary

This chapter has presented a preliminary noise immunity analysis of the differential amplifier to be used by the FEE of CMS very forward calorimeter. The study of the sensitivity of the FEE to common mode spurious signals and EMI has been conducted by simulation using a line model based on the MTL theory. Results have shown the limitations of the topology to common mode rejection and EMI if it is implemented with separated coaxial cables. It was shown that the position of the cable respect to the reference plane has strong influence in the rejection of the differential amplifier. The rejection to spurious signals can be improved, in this particular case, by selecting a double coaxial cable with a single braided shield. This cable balances the outer circuit impedance for both internal twisted pairs.

Respect to the effect of the ground resistor R_{GND} , the results show that improves the common mode rejection of the system proportionally to its magnitude, decreasing at high frequency. However, this effect is practically neglected with the noise generated by external electromagnetic fields. This difference between both cases can be explained by the different nature of the circuits.

5.7 References

- [1] A.R. Djordjevic, T.K. Sarkar, R.F. Harrington "Time domain response of Multi-conductor Transmission Lines", Proc. IEEE PROC-75, N-6, pp 743-764, June 1987.
- [2] C.R.Paul, "Introduction to Electromagnetic Compatibility", NY: Wiley-Interscience, 1992, ISBN-0-471-54927-4
- [3] C.R. Paul, "Analysis of multi-conductor transmission lines", 1992, ISBN-0-471- 02080-X
- [4] Lorenz-Jung, Jan Luiken ter Haseborg, "Evaluation of measured complex transfer admittance for the characterization of shield in-homogeneities of Multi-conductor Cables", IEEE Transactions on Electromagnetic Compatibility, Vol 41, N-4, pp 358-363, November 1999.
- [5] Edward F. Vance, " Coupling to shielded cables ", 1987, ISBN 0-89874-949-2.
- [6] T. Williams, "EMC for Product Designers", 1997, ISBN-0-7506-2466-3
- [7] C. Goldstein, P. Mani, "CW and pulsed mode transfer impedance measurements in coaxial cables", IEEE Transactions on Electromagnetic Compatibility, Vol. 34, pp 50-57 February 1992.
- [8] Thomas Kley, "Electromagnetic coupling to and from shielded cables-optimizing factors", IEEE Transactions on Electromagnetic Compatibility, Vol. 34, pp 39-46 February 1992.
- [9] Thomas Kley, "Measuring the coupling parameters of shielded cables", IEEE Transactions on Electromagnetic Compatibility, Vol. 35, pp 10-20, February 1993.
- [10] Jasper J. Goedbloed, "Electromagnetic Compatibility", 1990, ISBN-0-13-249293-8.
- [11] M. Tyni , "The transfer impedance of coaxial cables with braided outer conductor", Pr. Nauk, Inst Telekomun Akust. Politech Wroclaw Ser. Konfi, pp 410-419, 1975.
- [12] S.Sali, "An improved Model for the Transfer Impedance Calculations of Braided Coaxial Cables", IEEE Transactions on Electromagnetic Compatibility, Vol. 33, N-2, pp 139-143, November1991.

- [13] A.Fourie, O. Givati, A.R.Clark, "*Simple technique for the measurement of the transfer impedance of variable length coaxial interconnecting leads*", IEEE Transactions on Electromagnetic Compatibility, Vol. 40, pp 163-166, February 1998.
- [14] A. Morriello, T.M. Benson, A.P. Duffy, C.F. Cheng, "*Surface transfer impedance measurement: a comparison between current probe and pull on braid methods for coaxial cables*", IEEE Transactions on Electromagnetic Compatibility, Vol. 40, pp 69-76 February 1998.
- [15] R. De Leo, G. Cerri, V. Mariani Primiani, R. Botticelli, "*A simple but effective way for cable shielding measurements*", IEEE Transactions on Electromagnetic Compatibility, Vol. 41, pp 175-179, August 1999.
- [16] Ashok K. Agrawal, Harold J. Price, Shyam H. Gur-baxami, "*Transient Response of Multi-conductor Transmission Lines Excited by Non-uniform Electro-magnetic Fields*", IEEE Transactions on Electromagnetic Compatibility, Vol. 22, N- 2,1980.
- [17] S. Tkatchenko, F. Rachidi, M. Ianoz, "*Electromagnetic field coupling to a line of finite length: theory and fast iterative solutions in frequency and time domains*", IEEE Transactions on Electromagnetic Compatibility, Vol. 37, N-4, pp 509-518, August 1993.
- [18] F. Rachidi, "*Formulation of the field-to-transmission line coupling equations in terms of magnetic excitation field*", IEEE Transactions on Electromagnetic Compatibility, Vol. 35, N-3, pp 404-407, August 1993.
- [19] C.R. Paul., "*A SPICE model for multiconductor transmission lines excited by an incident electromagnetic field*", IEEE Transactions on Electromagnetic Compatibility, Vol. 36, pp 342-354, November 1994.
- [20] C.W. Harrison, "*Generalised theory of impedance loaded multi-conductor transmission lines in an incident field*", IEEE Transactions on Electromagnetic Compatibility, Vol. 14, pp 56-63, May 1997.

Chapter 6

RF Susceptibility Test of FEE

The electromagnetic (EM) immunity [1][2] of a device, equipment or system is its ability to perform without degradation in presence of EM disturbances. The characterization of the front-end electronics to these disturbances [3] before the detector is integrated is highly important to guarantee the design goals and the good performance of the system. EMC immunity tests allow to determine the level of sensitivity of the FEE and give the possibility of taking corrective actions at an early design stage to ensure the good compatibility among the sub-systems during the integration of the detector. The procedure to conduct the radio-frequency (RF) immunity tests consists in the injection of perturbing currents through the input/output cables of the FEE to simulate the effect induced by conducted interference and external EM fields. This chapter addresses the results of the described tests when applied to the FEE of the CMS Hadron calorimeter (HCAL).

6.1 Introduction

The RF immunity tests are based on European standards [4] and aerospace rules. The goal of these tests is to define the immunity level of the FEE to the conducted disturbances coupled into the input cables, identify the key elements for the noise degradation of the FEE and settle on the noise level required at the output of the power supplies. Noise can be coupled to the FEE through the input power cables and slow control cables, as these are the two paths for conductive coupling due to the FEE output signal is transmitted to the counting room via optical fibre. RF noise currents can be induced in the cable shield by near and far external EM fields, forced to flow through the central conductors by the power supply outputs, etc. To emulate these interferences in a test environment, four tests have been proposed and conducted to study FEE immunity level due to inject currents via the input power cables of the FEE. In each of them the transfer function between the external perturbing signal and the output signal of the FEE is calculated. These tests are:

- Injection of shield currents.

- Injection of CM currents in the central conductors.
- Injection of DM currents in the central conductors.
- Injection of CM+DM currents in the central conductors

6.1.1 Injection of shield currents

High frequency currents flowing through the power cable shield can be generated by far and near electromagnetic fields coupled to the shield, or by high frequency ground currents flowing in the system. To emulate its effect on the FEE, a sine-wave current is injected into the power cable shield. This shield current also couples CM currents to the internal conductors through the surface transfer impedance and admittance of the cable. All these currents affect the performance of the FEE and its effect depends on the amount of noise current that can penetrate into the FEE (I_{pert}), as it is shown in figure 6.1. This plot shows the distribution of the noise currents in one of the HCAL RBX. This circuit is used to analyze the effects of these currents in the performance of the FEE. Shield currents are present in the CMS detector and it is necessary to evaluate the immunity of the system to them.

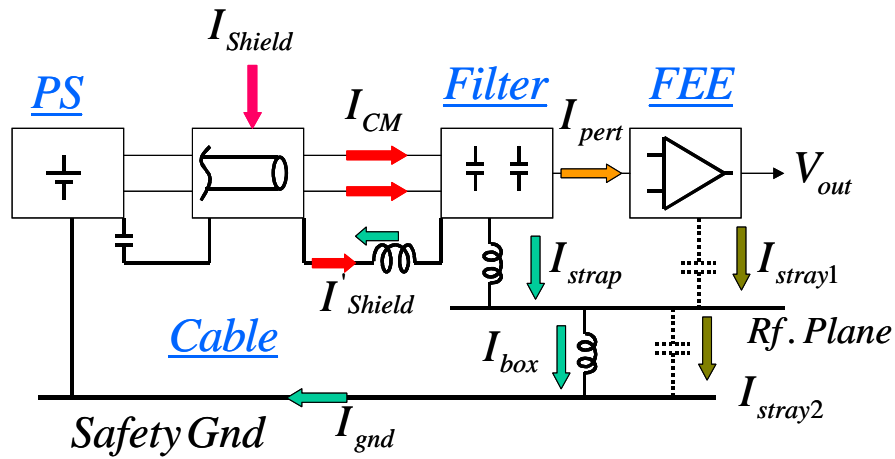


Figure 6.1: Shield current distribution into the FEE.

The immunity of the FEE to shield currents is quantified defining the transfer function between the FEE output voltage (V_{out}) and the current that is able to penetrate into the system, ($I_{CM} + I_{shield}$) (marked in red)

$$TF = \frac{V_{out}}{(I_{shield})} \quad (6.1)$$

This transfer function will basically depend on the ground connections of the system. The connection between the filter box and reference plane is the most important connection to obtain good immunity of the FEE against shield currents as this is the only path that can be used to filter the noise currents before they reach the FEE. The system immunity to the RF shield noise current increase when the current I_{strap} can be by-passed, lowering the effect of the perturbing current I_{pert} in the FEE.

6.1.2 Injection of CM currents in the central conductors

Power supplies and FEE can generate CM currents that flow through the central conductors of a power cable. These currents can affect the performance of the FEE, depending on the amount of noise that can penetrate into the FEE (I_{pert}), as mentioned before. In the CMS detector it is intended to install SMPS that have high CM current emission levels, and hence the study of the immunity of the system to these currents is one of the most important studies to be performed on the FEE.

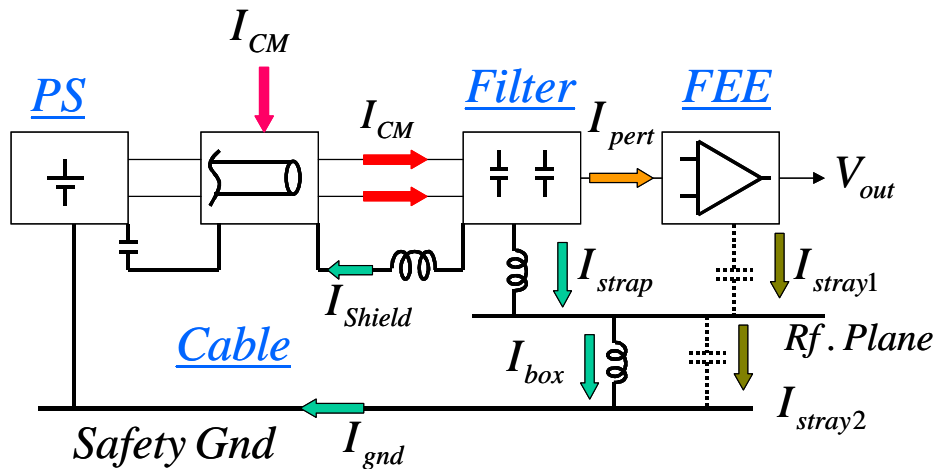


Figure 6.2: CM current distribution into the FEE.

Figure 6.2 shows the block diagram of the selected circuit to study the immunity of the HCAL FEE to CM currents as well as the distribution of the CM currents in the HCAL RBX. The immunity of the FEE to CM currents is quantified defining the transfer function between the FEE output voltage (V_{out}) and the CM current that is able to penetrate into the system, ($2 \cdot I_{CM}$) (marked in red)

$$TF = \frac{V_{out}}{2 \cdot I_{CM}} \quad (6.2)$$

This transfer function depends mainly on the ability of the system to filter these noise currents at the entrance of the power cables to the FEE box. For CM currents, the cable shield and the straps are the two parts available to bypass these currents and hence avoid that this perturbation flows through sensitive areas of the FEE. Most of the CM currents return through the shield, but the input filter must provide a low CM impedance to set the CM circuit around the filter.

6.1.3 Injection of DM currents in the central conductors

Both power supplies and the FEE can generate DM currents that flow through the central conductors of a power cable. In the CMS detector, any PS units generate DM noise and therefore the study of the immunity of the system to these currents is also very important.

DM currents can affect the performance of the FEE, depending on the amount of noise that can penetrate into the FEE (I_{pert}), as shown in figure 6.3. This plot shows the selected circuit to study the distribution of the DM currents in the HCAL RBX and defines the DM transfer function.

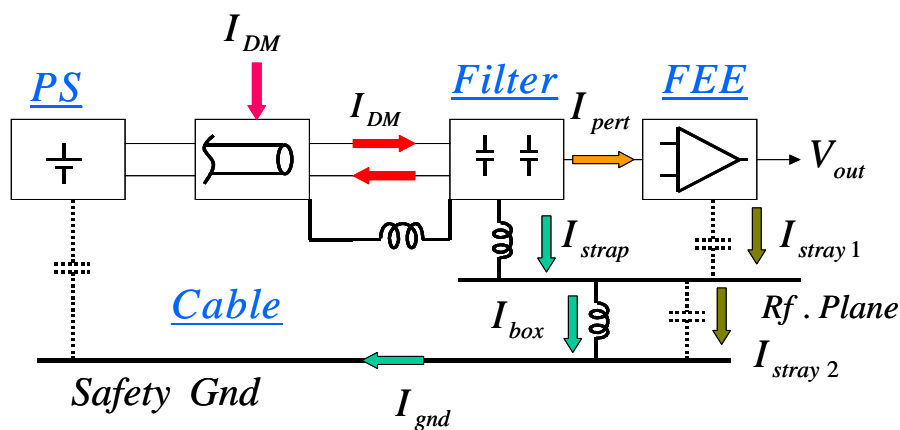


Figure 6.3: DM current distribution into the FEE.

If this plot is analyzed in detail there are two differences when compared with the previous ones. To increase the CM impedance of the system layout, the ground connection of the power supply and the normalized common impedance box is disconnected. In this case, the injected current in the active power cable is forced to return through the complementary power cable and the CM noise injected to the FEE is negligible. This configuration is extremely sensitive to resonances in the circuit and introduces several limitations when evaluating the DM transfer function.

The immunity of the FEE to DM currents is quantified defining the transfer function between the FEE output voltage (V_{out}) and the DM current flowing through the central conductor of the cable (I_{DM}) (marked in red).

$$TF = \frac{V_{out}}{I_{DM}} \quad (6.3)$$

This transfer function depends mainly to the ability of the RBX to filter this noisy current as well as the capacitors placed on the backplane at FEE the level, which practically filter all DM currents that escape the input filter. For this reason the efficiency of the input filter is not very important as this is not the only device that is used to filter the DM noise currents prior to the FEE.

6.1.4 Injection of CM+DM currents in the central conductors

This test is performed to analyze the effect of currents, combining common mode and differential mode components, on the FEE immunity and also to define normalized specifications for the output noise of the power supplies. Figure 6.4 shows the circuit and the current distribution in the system during this test.

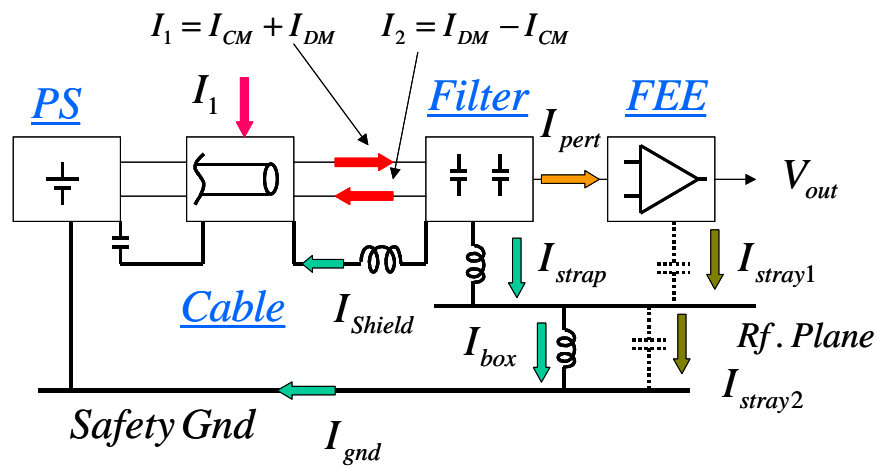


Figure 6.4: Positive lead current distribution into the FEE.

In this example, the immunity of the FEE to the positive lead noise currents is quantified defining the transfer function between the FEE output voltage (V_{out}) and the noise current (I_1) in figure 6.4 (marked in red).

$$TF = \frac{V_{out}}{I_1} \quad (6.4)$$

Assuming the total current flowing in each power cable can be expressed as:

$$I_1 + I_2 \cong I_{shield} + I_{gnd} = I_T \quad (6.5)$$

where I_1 and I_2 are the currents flowing through the central conductors, and I_{shield} and I_{gnd} are the return currents through the shield and the ground plane. The currents flowing through the central conductors can be decomposed in two orthogonal components:

$$I_{cm} = \frac{I_1 + I_2}{2} \quad \text{and} \quad I_{dm} = \frac{I_1 - I_2}{2} \quad (6.6)$$

If the injected current I_1 can be decomposed in two components I_{cm} and I_{dm} , multiplying each current by the respective TF, and adding the resulting output voltages, the calculated TF following this method should be equal to the TF obtained by the present measurement.

6.2 Experimental set-up

An experimental set up was implemented to study the immunity of the FEE. Figure 6.5 shows a schematic of the experimental set-up to define the FEE immunity.

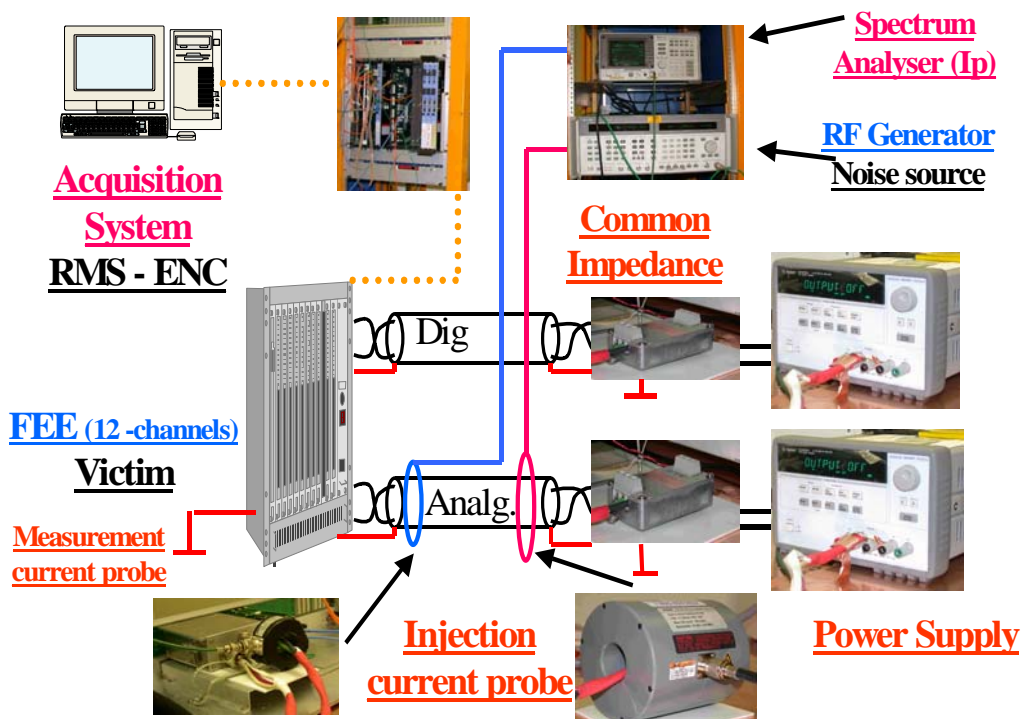


Figure 6.5: FEE immunity test set-up.

The basic idea of the test set-up is to keep the topology as close as possible to the final one. The FEE and the auxiliary equipment are placed on a copper plane, 1 meter above the floor. This copper sheet (2x2 meters) is the reference ground plane. A Bulk injection current probe (Fischer F-120-9A)¹, a RF amplifier (Dressler 250/75A) and a RF signal generator (HP 8664B) are used to inject the perturbing signal to the FEE, while an inductive current clamp (EMCO-91550-1) and a spectrum analyzer (HP-8594E) are used to monitor the current injected. The output signal of the FEE is measured by its own acquisition system. The connection between the bulk injection probe and the amplifier is made through a RF attenuator to improve the ratio between the injected current and the harmonics generated by the amplifier in 10dB.

To represent the effect of very long cables, normalized common impedances (CI) (Common Mode and Differential Mode impedance) based on lumped components are used to standardize the measurement. Figure 6.6 shows the common impedance used in these test.



Figure 6.6: Common impedance - HCAL power cable.

The common impedance presents a stable and well-defined impedance ($\pm 25\%$) throughout the desired frequency range. The chosen values of the CI components are estimated following the measurement of the HCAL power cable parameters². This CI presents three frequency areas in which the impedance behavior of the CI is different. At high frequency the CM and DM impedance of the CI approaches the CM and DM characteristic impedance of the lines. The chosen values of the common impedance in each branch of the line that match the DM and CM characteristic impedance of the cable are 21.4Ω for DM and 30.4Ω for CM. A more detailed analysis of the cable characteristic impedance matrix is presented in appendix I. At low frequency the value of this impedance is equal to the resistance of cable, whereas the transition frequency range between the low and high frequency is defined by inductance of cable.

1 See appendix C

2 See chapter 4

The values of each branch of the CI for the HCAL power cable in the range 10 kHz to 50 MHz are measured with a network analyzer (HP 4195A) and are shown in figure 6.7.

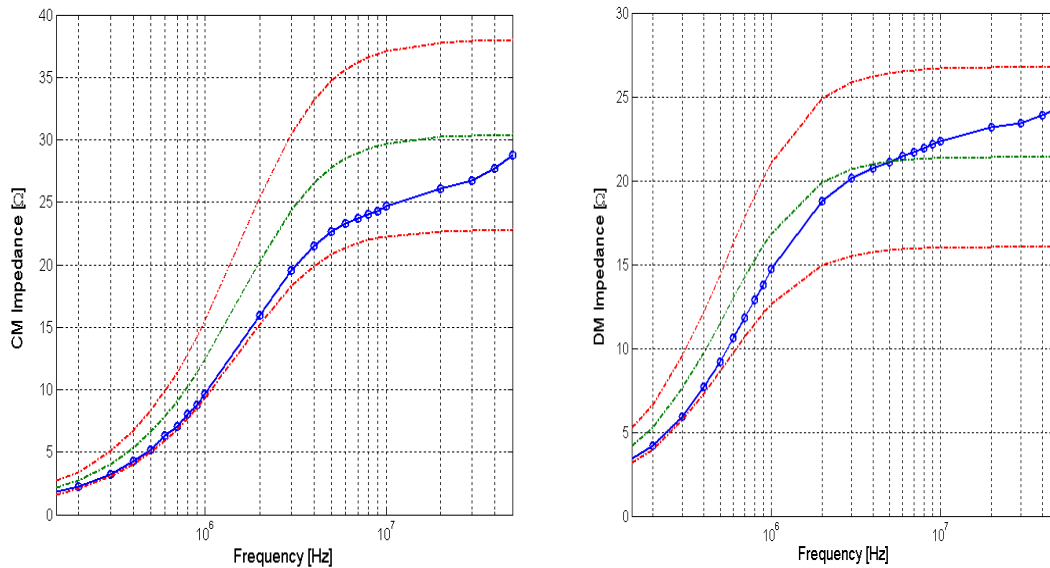


Figure 6.7: Variation of the Nominal and measured values of the CI respect to the frequency - CM and DM configuration.

6.2.1 HCAL FEE prototype

The RF immunity test is carried out on a prototype of the HCAL front-end electronics. Although it has been described at the beginning of the presented document¹ and in [5], some additional details are presented.

In this prototype, the sensitive amplifier is a charge integrator sampled at 34 MHz (the final version operates at 40 MHz). It amplifies and digitizes the signal generated by a hybrid photo-multiplier located a few centimeters from the amplifier. Later, the sampled signals are collected, serialized and sent out of the detector via optical links to the acquisition system. At that location, the FEE output data are processed and converted into deposited energy value that is stored until the first trigger level signal arrives.

CM and DM signals are injected through the power cables and the output signals of 12 channels are acquired. These channels are distributed in two identical boards, each of them connected to the backplane. Figure 6.8 shows the board layout of the

¹ Section 1.7

6.2. Experimental set-up

HCAL-FEE. Analogue signal conditioners and digitization electronics are located on these boards, which constitute one of the most sensitive components of the HCAL electronics.

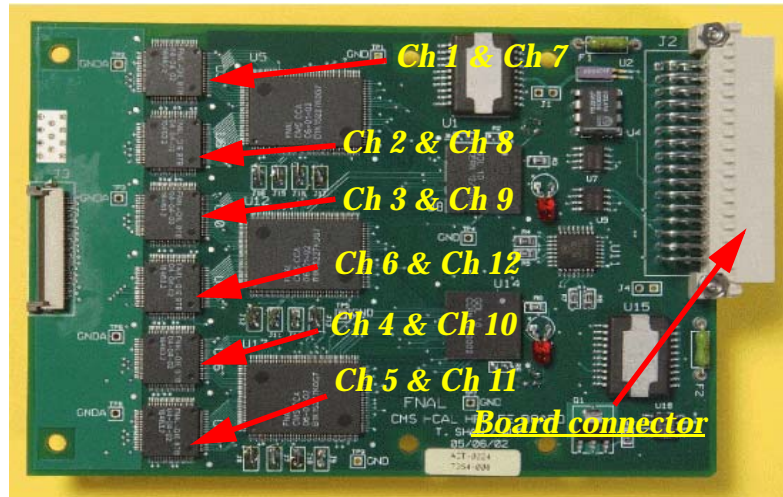


Figure 6.8: HCAL-FEE board layout [6].

The root mean square (RMS) of the acquired data is used to evaluate the performance of the FEE operating under the perturbing signal. Figure 6.9-a depicts the output signal in the time domain when no perturbing signal is applied, while figure 6.9-b shows the histogram of the signal. Figure 6.10 depicts the output signal and its histogram when the FEE is perturbed by a sine wave current of 10 MHz.

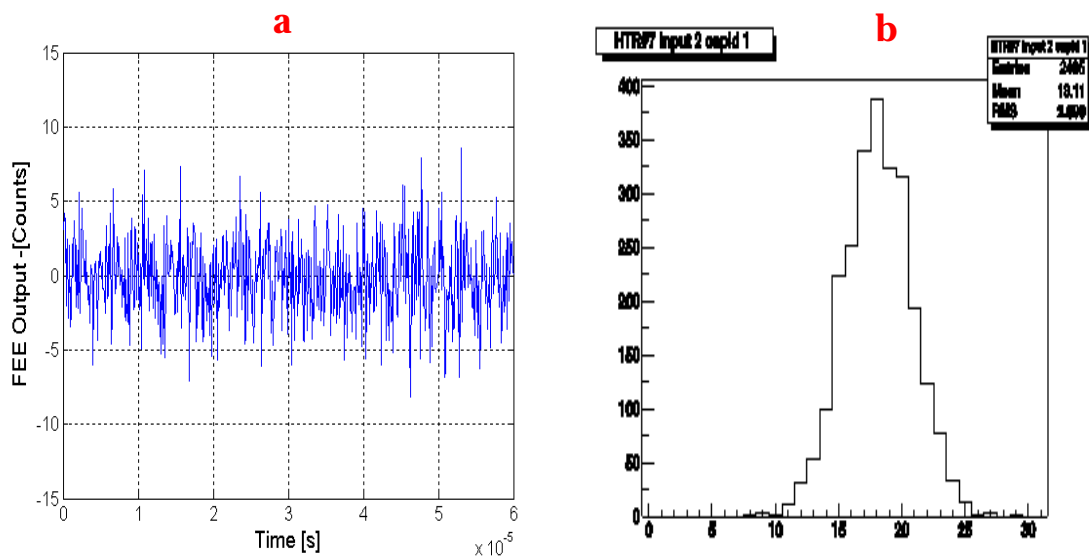


Figure 6.9: Time domain and histogram of the output of channel 2 HCAL - FEE when is not perturbed.

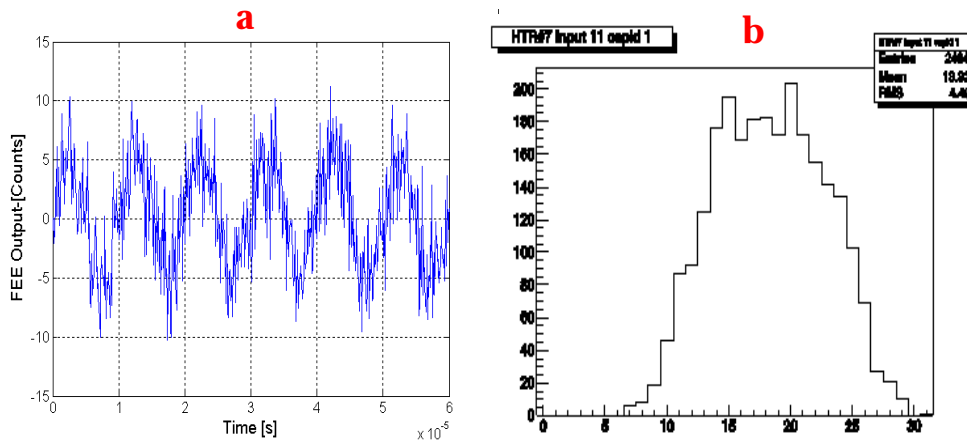


Figure 6.10: Time domain and histogram of the output of channel 11 HCAL - FEE when is perturbed

During the test, the RMS value of the output signal is used to evaluate the noise of the FEE. A level of 2.16 counts is the target value for this design for the RMS output voltage corresponding to the amplifier thermal noise. It is equivalent to an Equivalent Noise Charge (ENC) at the input of the amplifier equal to 0.72 fC or 4500 electrons¹. In these prototypes, when no RF perturbation is injected, the output noise level for all channels varies between 2.64 to 2.94 counts.

To increase the immunity of the FEE a RF capacitor between active and return analog power lines is placed at the input of the FEE. This DM capacitor works also as CM filter as the negative input of the FEE is connected to the signal reference plane to simulate the effect of a CM and DM filter as the return line is connected to ground following one of the ground configurations detailed in chapter 2. This is shown in figure 6.11.

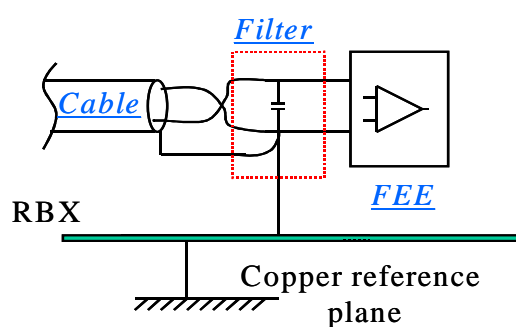


Figure 6.11: CM and DM filter- Analog power input line ground connection.

¹ During the test, the chip works in calibration mode, that means 1 count correspond to 0.33 fC

During the test a perturbing current with a frequency between 150 kHz and 50 MHz and different amplitudes is injected in the analogue power line of the FEE. A perturbation on the digital part of the FEE does not induce gradual performance degradation, but instead generates a clock loss that requires to reset the system to re-start. However, the order of magnitude of the perturbation observed that deteriorates the digital line is much higher than the perturbation in the analog part. Thus limiting the analysis to the analog one is a good approach to analyze the FEE sensitivity to conducted noise. During the test, the perturbing signal-to-noise ratio is kept above the background noise by $33 \text{ dB}\mu\text{V}$, as it is shown in figure 6.12.

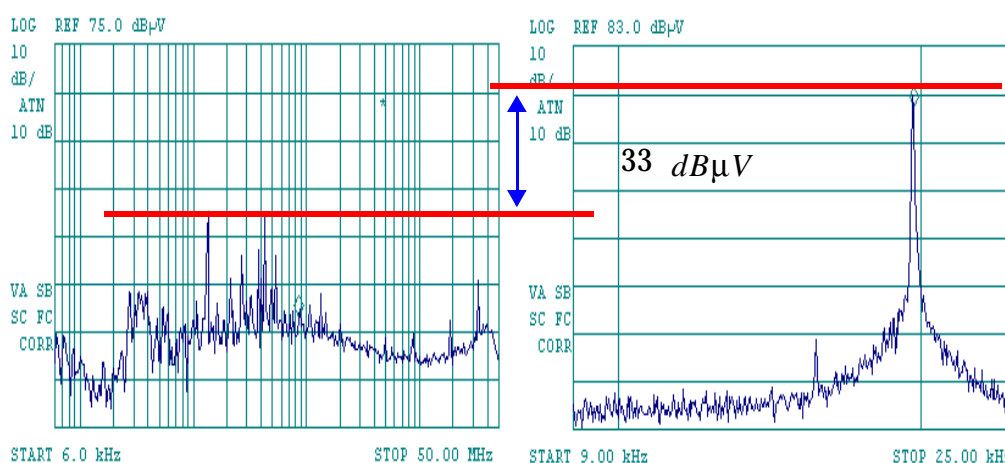


Figure 6.12: Perturbing signal to background noise ratio

6.3 Susceptibility to shield currents

For this test a sine-wave current is injected to the power cable shield to emulate the shield currents generated by far and near electromagnetic fields coupled to the shield or by high frequency ground currents flowing in the system.

6.3.1 Noise distribution

The main characteristic of this test is that the perturbation does not distribute equally across all channels. Figure 6.13 depicts the RMS value of the amplifier output voltages for all channels when a perturbing current of 6 mA RMS (at 5 MHz and 10 MHz) is injected. These values are compared with the output of each channel when no perturbation is injected (reference).

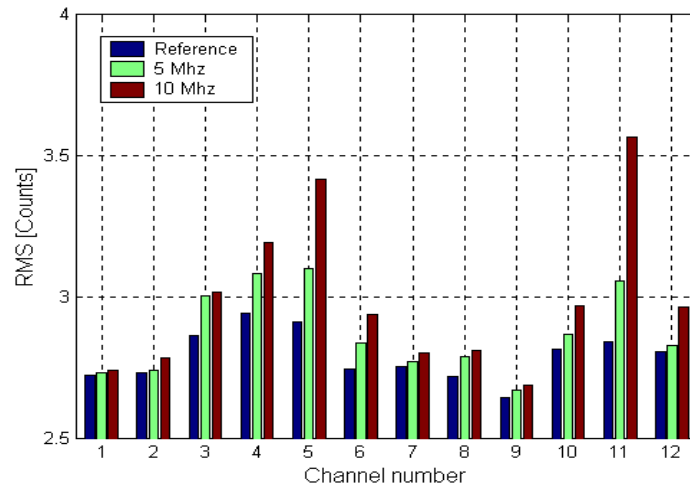


Figure 6.13: Noise distribution per channel for an injected current of 6 mA - Reference, 5 MHz & 10 MHz - Measured values.

Channels 1 to 6 are placed on board A and channel 7 to 12 belongs to board B, as it is shown in figure 6.8. It is clear that some areas of the FEE are more susceptible to noise than others. The worst area is around channels 5 and 11 and the less sensitive area is near channels 1 and 7. The origin of this problem is found in the ground connection between the amplifiers boards and the photo-detector board. This issue was solved after analyzing these test results by improving the signal integrity between the amplifiers and the photo-detector.

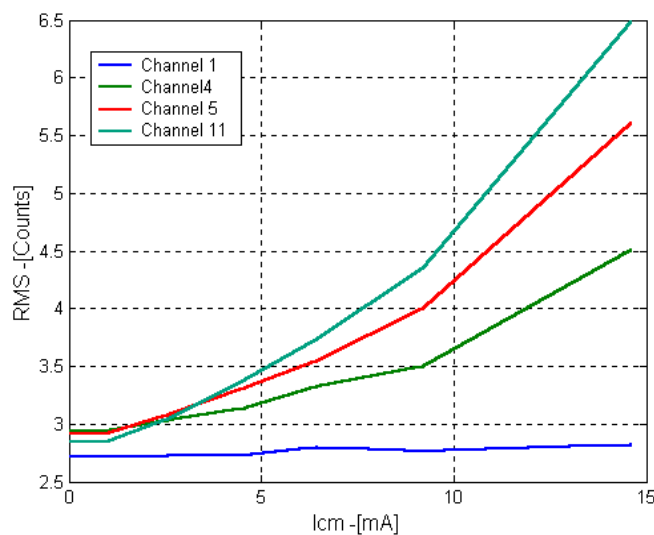


Figure 6.14: Variation of the RMS value of the output noise versus the magnitude of injected current at 10 MHz - Measured values.

6.3. Susceptibility to shield currents

Figure 6.14 shows the variation of the RMS value of the amplifier output voltage versus to the change in magnitude of the current injected at 10 MHz for channels 1, 4, 5 and 11. These channels represent the worst case (channel 5 & 11), the best case (channel 1) and a normal case (channel 4). At low current values, the output signal is dominated by the thermal noise contribution of the amplifier, while at high currents, it is dominated by the injected signal in the noisy channels.

The frequency response of all these channels to a perturbing current of 6 mA RMS is shown in the figure 6.15. At low frequencies, the current amplitude is not large enough to disturb the channels and the output signal is dominated by the thermal noise. At high frequencies, the perturbing signal is dominant defining the frequency response of the charge amplifier to the coupled CM noise into each channel. From this plot, it is possible to observe the loss of gain of the amplifier at around 17 MHz and 34 MHz. The gain lost at 34 MHz corresponds to the intrinsic behavior of the amplifier due to the sampling at that frequency. Notches in the frequency response at 17MHz and also at 8.5MHz appear due to the data organization in time domain. Each amplifier, after integration during $1/34\mu s$, send the data to the acquisition system with a time separation of $4/34\mu s$. This process is equivalent to a decimation by 4 of signal sampled at 34MHz, giving the zero response at 8.5MHz and 17MHz.

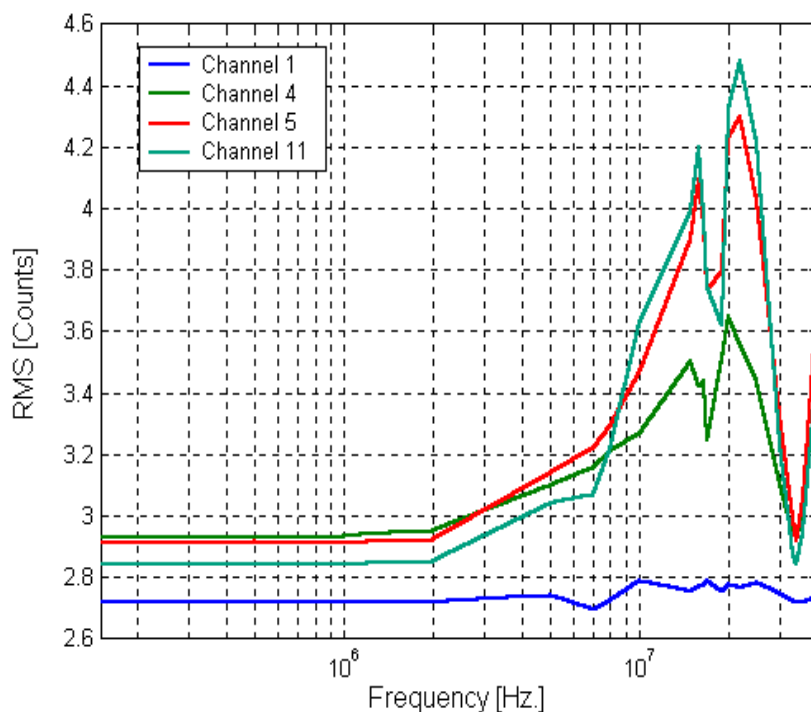


Figure 6.15: Variation of the RMS value of the output noise versus the frequency of the injected current ($I_p=6\text{ mA}$) - Measured values.

6.3.2 Transfer function

Based on the previous data, it is possible to identify the transfer function between the output voltage and the perturbing input signal. The transfer function is defined as the ratio between the output voltage of the FEE and the injected perturbing current. The output voltage of the FEE can be referred to as number of counts at the output of the ADC or it can be referred to as the equivalent noise charge (ENC) at the input of the amplifier, both units being related by a scale factor.

$$T_f = \frac{ENC}{I_p} \quad (6.7)$$

The transfer function quantifies the sensitivity of the amplifier to noise currents and allows estimating the noise contribution of any perturbing signal in the system. The transfer functions of channel 4, 5 and 11 between 1 MHz and 50 MHz are shown in figure 6.16. Lower frequencies values are not shown because the output of the FEE is dominated by thermal noise and the transfer function is poorly estimated.

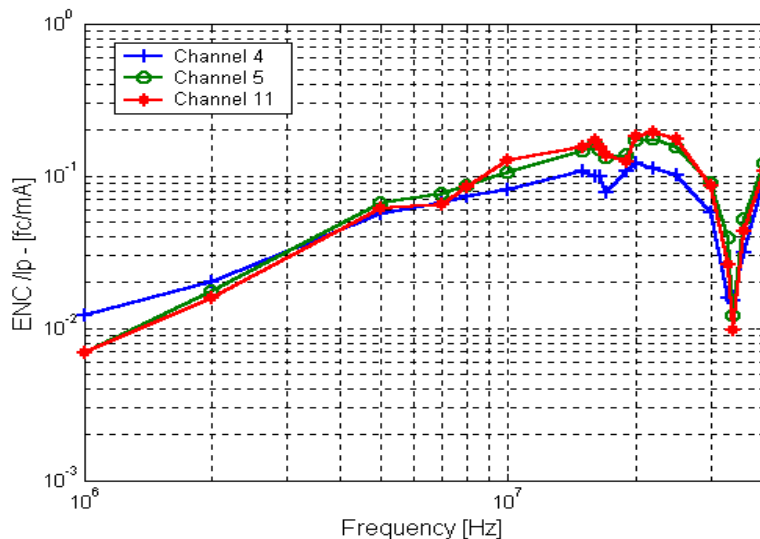


Figure 6.16: Transfer function of channel 4,5 and 11 - Measured values.

The transfer function values in the range of frequencies between 150 kHz and 100 MHz can be estimated by mathematical model of the FEE frequency response. This model is estimated by combining the transfer function of the QIE¹ with an external component. The curve is parameterized based on this external component and fitted to the measured values using the least square method.

¹ See chapter 1 - Section 1.7

6.3. Susceptibility to shield currents

The QIE transfer function is represented assuming the model of a sampled integrator in combination with a low-pass filter that represents the frequency response of the input stage of the device. The low frequency gain of these blocks is equal to one, including the low frequency gain of the system in the external parameter. The following equations describe the main blocks of the transfer function.

$$QIE = \frac{\sin\left(\omega \cdot \left(\frac{\tau}{2}\right)\right)}{\omega \cdot \left(\frac{\tau}{2}\right)} \quad (6.8)$$

$$\text{Filter} = \frac{1}{1 + \left(\frac{j \cdot \omega}{\omega_b}\right)} \quad (6.9)$$

$$\text{External parameter} = (j \cdot \omega \cdot L_m) \quad (6.10)$$

$$TF = \left| \frac{\sin \omega \cdot \frac{\tau}{2}}{\omega \cdot \frac{\tau}{2}} \right| \cdot \left| \frac{1}{1 + \left(\frac{j \cdot \omega}{\omega_b}\right)} \right| \cdot |j \cdot \omega \cdot L_m| \quad (6.11)$$

Where τ represents the sampling period of the QIE (1/34 MHz), ω_b the cut-off frequency of the input stage (~ 70 MHz) and L_m the parameter of the model. The last value depends on the channel and the ground layout as described in the next section. As an example, the measured values of channel 5 (in blue) and the fitted function (in red) are shown in figure 6.17.

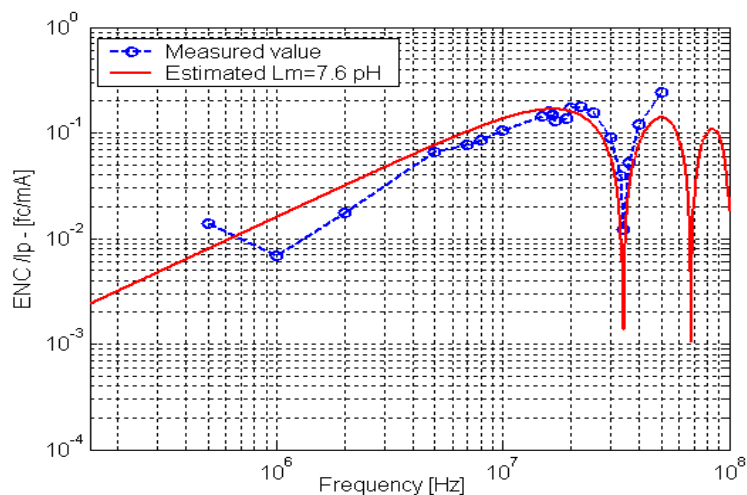


Figure 6.17: Channel 5 transfer function - Measured and fitted values.

If the previous plot is compared with the ideal behavior of the QEI with a filter as shown in figure 6.18, it is clear that the FEE presents a poor CM rejection at a high frequency, because above the sampling frequency there is a contribution of the noise to the output of the FEE that decreases the good performance of the FEE.

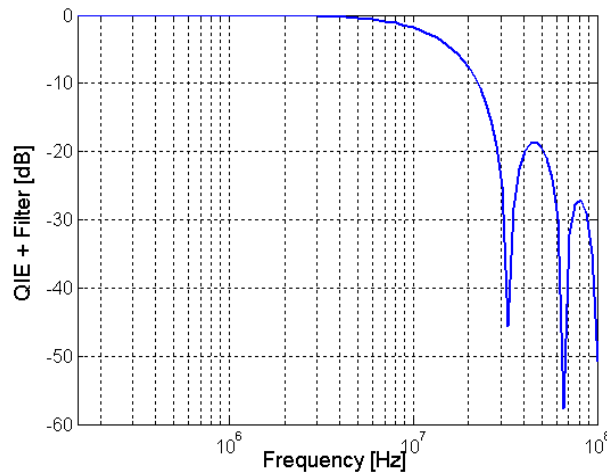


Figure 6.18: QIE with filter block frequency response - Simulated values

6.3.3 Grounding configurations.

The shields of the power cables are connected to the RBX through a metallic box, which encloses the power filter boards. The shield is connected to the metallic box by the EMC gasket included in the cable strain relief and the box is grounded locally to the RBX through a short metallic strap. The RBX is connected to the HCAL ground, which is simulated during the test by a copper plane, through a strap. This layout is shown in figure 6.19.

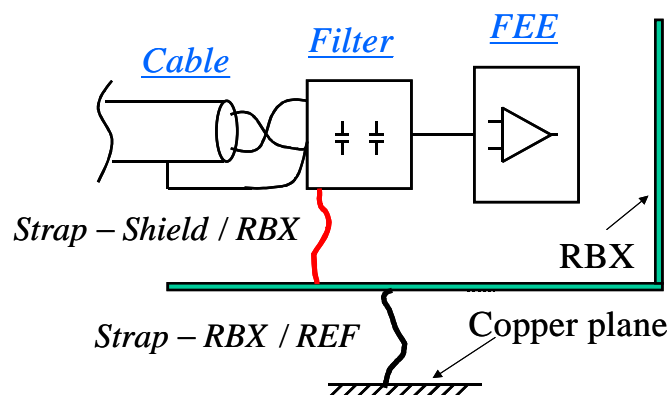


Figure 6.19: Ground connection layout between power cable, RBX and copper plane.

During the test, the strap connection between the filter box and the RBX (marked in red in figure 6.19) is changed to study their influence on the FEE performance. This connection is made with a copper strap, 15 cm long. The length and the routing of the strap connection to the RBX are changed. This modification produces a variation on the inductance of the ground connection. The results of three different layouts are presented.

- GND 1: The first layout is shown in fig. 6.20a. The ground connection is done with a long strap. It is routed to the connection point as far as possible from the metallic structure of the RBX.
- GND 2: The second layout, the strap is routed to the connection point as close as possible to the metallic structure of the RBX following the shortest path to that point (figure 6.20b without copper tape)
- GND 3: The third layout is similar to the second one, but a copper tape is used to fix the strap to the RBX (figure 6.20b). This layout decreases the length of the strap to a minimum.

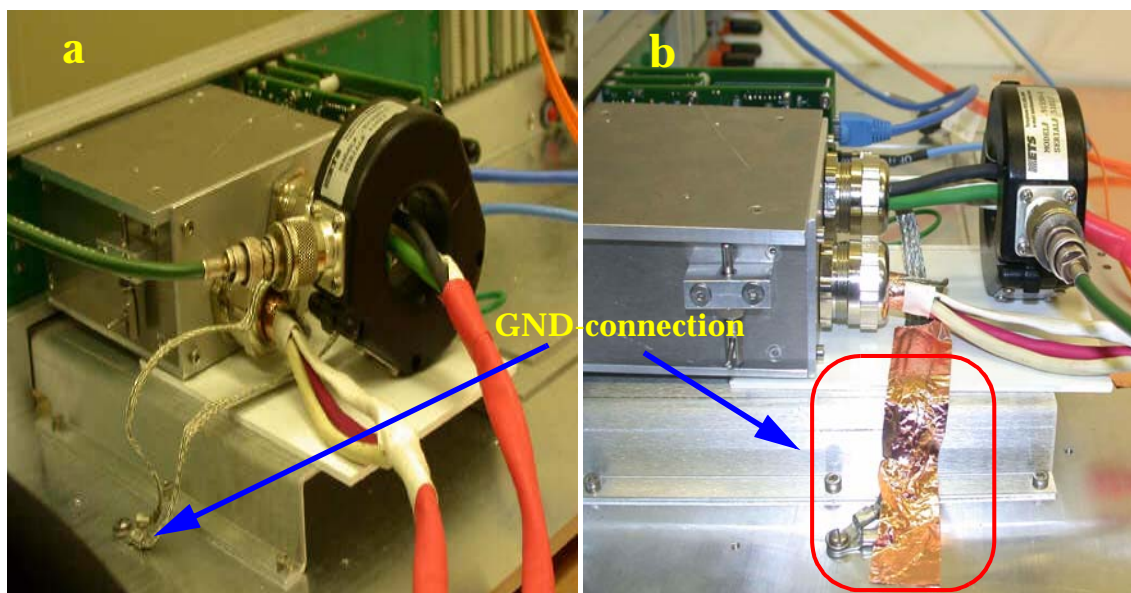


Figure 6.20: Ground shield connection layouts.

The results previously presented correspond to the second set-up (GND 2), in which the strap is routed as close as possible to the RBX to the ground connection, whereas the test results for the first configuration (GND 1), which is shown in figure 6.20a are shown in figures 6.21 and 6.22. In the first plot, the frequency response of some sensitive channels to a perturbing current of 6 mA RMS is depicted, while figure 6.22 shows the transfer function for several channels of the FEE.

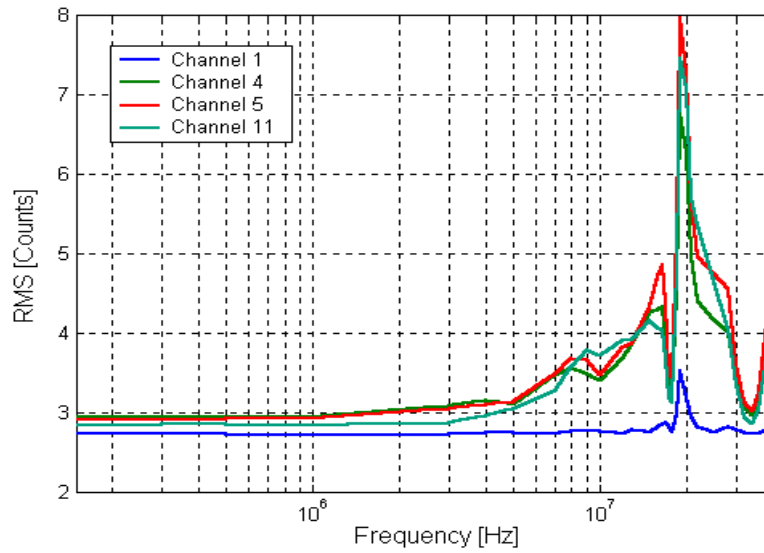


Figure 6.21: Variation of the RMS value of the output noise respect to the frequency of the injected current ($I_p=6$ mA) - Measured values - GND 1 configuration.

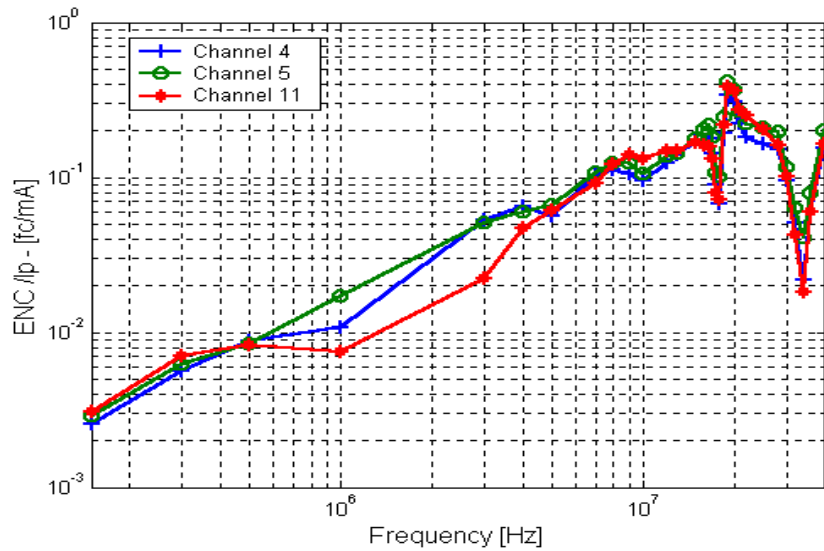


Figure 6.22: Transfer function of channel 4,5 and 11 - Measured values - GND 1 configuration.

Figure 6.23 shows the measured values and fitted curve for channel 5. Qualitatively, similar results have been obtained with the third layout.

6.3. Susceptibility to shield currents

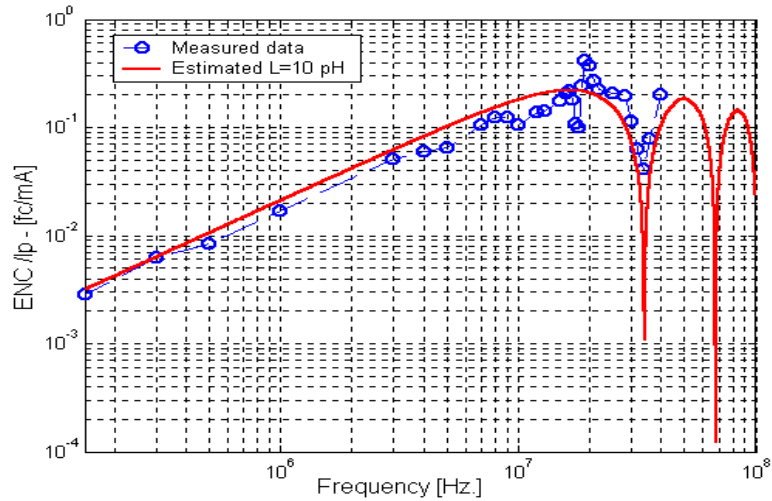


Figure 6.23: Channel 5 transfer function - Measured and fitted values - GND 1 configuration.

The results are very similar to the test results obtained for the GND2. Identical comments can be applied for this test and the fitted results of the measured values.

To compare the effect of the strap connection between the power cable shield and RBX, the fitted curves of channel 5 for the three different configurations are analyzed.

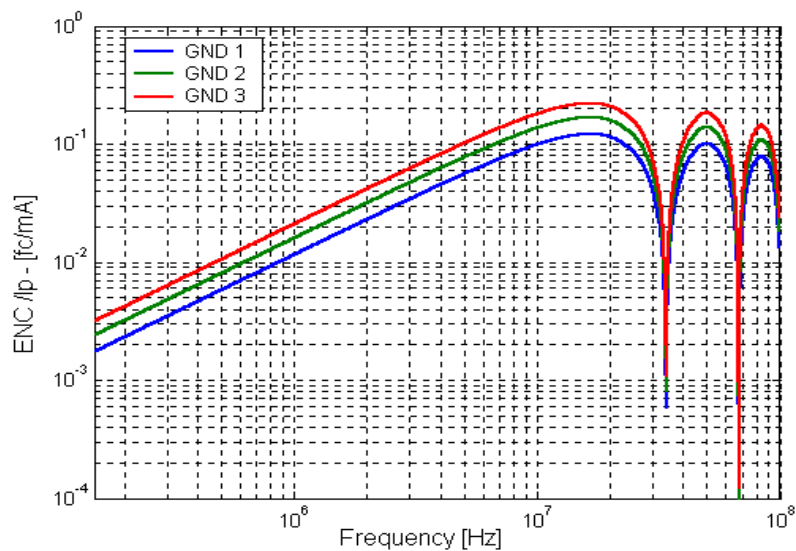


Figure 6.24: Channel 5 transfer function - Fitted values - GND 1, GND 2 and GND 3 configurations.

Figure 6.24 shows the transfer function of channel 5 of the three configurations under study. The first configuration correspond to the GND 1 ($L_m = 10pH$), the second correspond to the GND2 ($L_m = 7.60pH$) and the third one correspond to the GND3 ($L_m = 5.5pH$).

Based on these curves, the third layout (GND 3) is the best configuration to make the ground connection of the shield. Essentially this connection is characterized by the shortest and less inductive strap and produces the lowest value of ground impedance connection for the frequency range¹ of interest. The system presents a higher rejection to shield currents because most of these currents can be by-passed from the RBX and hence they do not pass through the sensitive part of the FEE.

The ground layout represents an important issue because it defines the sensitivity of the FEE to noise coupled through the shields currents. These currents are generated by EM fields (near and far fields) as well as by HF ground currents. Based on this study, it is possible to define the main characteristics that should be followed for the ground connections:

- The straps should be short and flat.
- Routing path should be as close as possible to the metallic box.

6.4 Susceptibility to CM power currents

To study the effect of the common mode noise currents flowing through the central conductors of the power cable, a perturbing current is injected to both the active and return conductors. In practice, this CM noise is generated by the power supplies.

6.4.1 Noise distribution

The perturbation does not distribute equally across all channels. Figure 6.25 depicts the RMS value of the amplifier output voltage of all channels when a perturbing current of 15 mA RMS (at 5 MHz and 10 MHz) is injected. These values are compared with the output of each channel when no perturbation is injected (reference).

1 Chapter 2

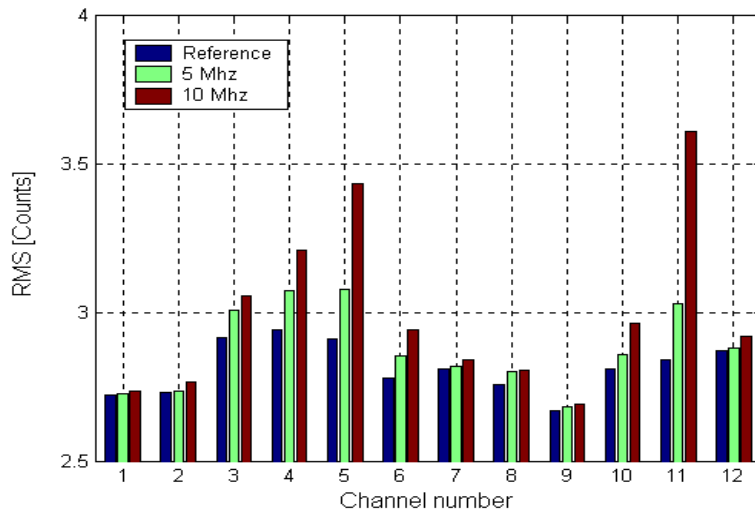


Figure 6.25: Noise distribution per channel for a injected current of 15 mA - Reference, 5 MHz & 10 MHz - Measured values.

The noise distribution is the same of the previous test, being most sensitive channels 4,5 and 11. However the magnitude of current applied to disturb the FEE is about three times bigger. Although it will be analyzed later, the FEE is less susceptible to common mode currents flowing through the active and return wires of the power cable than through the shield.

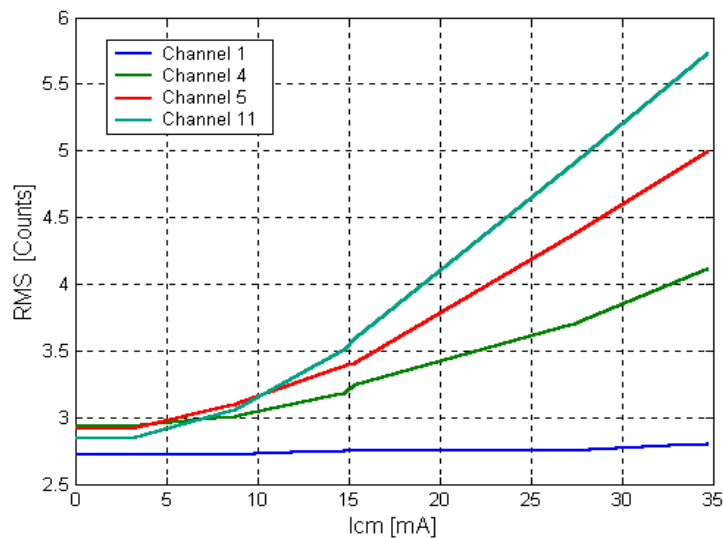


Figure 6.26: Variation of the RMS value of the output noise respect to the magnitude of injected current at 10 MHz - Measured values.

Figure 6.26 shows the variation of the RMS value of the amplifier output voltage versus the change in magnitude of the current injected at 10 MHz for channels 1,4,5 and 11. Figure 6.27 shows the frequency response of these channels to an injected current of 15 mA.

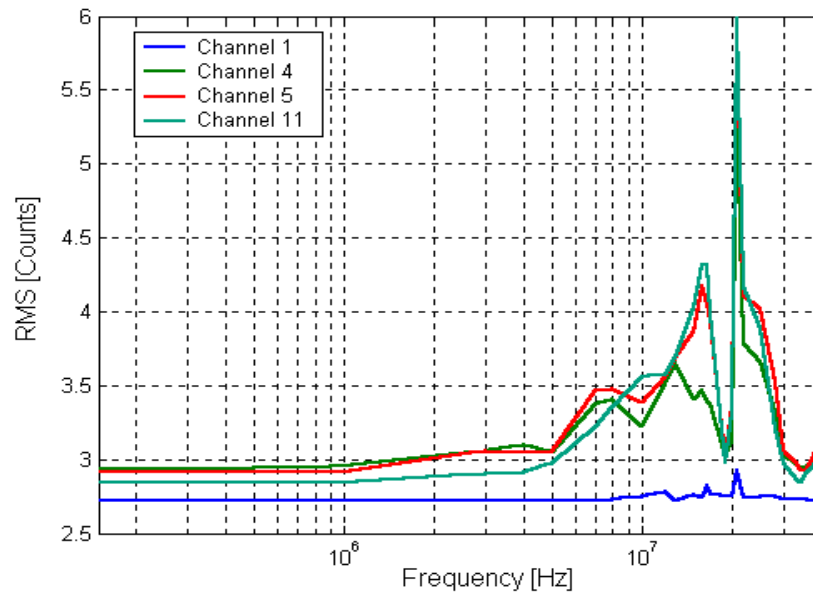


Figure 6.27: Variation of the RMS value of the output noise respect to the frequency of the injected current ($I_p=15$ mA) - Measured values

Figures 6.26 and 6.27 show that for low injection currents (at fix frequencies) and low frequencies (at a fix amplitude) the output signal is dominated by the thermal noise. However for high currents and high frequencies the perturbing signal is dominant. This analysis is similar to the previous test and identical conclusions can be extended to the behavior of the FEE perturbed by common mode currents flowing through the power cables.

6.4.2 Transfer function

Based on the previous data, it is possible to identify the transfer function between the output voltage and the common mode current flowing through both the active and return wires of the power cable. Figure 6.28 shows the transfer function of channels 4, 5 and 11 for a frequency range between 500 kHz and 40 MHz. As it was mentioned in the previous test, the estimation of the transfer function at lower frequencies is imprecise due to the signal to noise ratio being lower than one. The fitted values of transfer function for channel 5 are shown in figure 6.29.

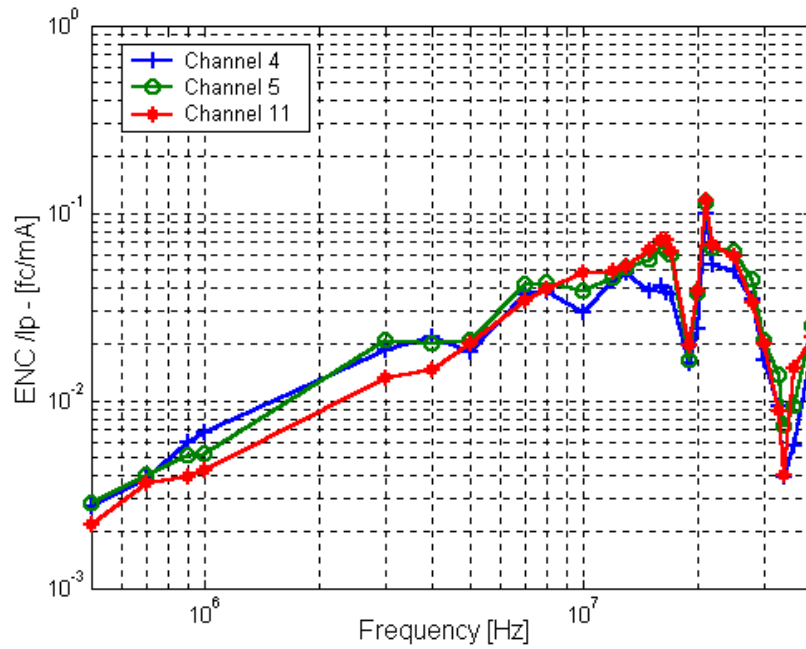


Figure 6.28: Transfer function of channel 4,5 and 11 - Measured values.

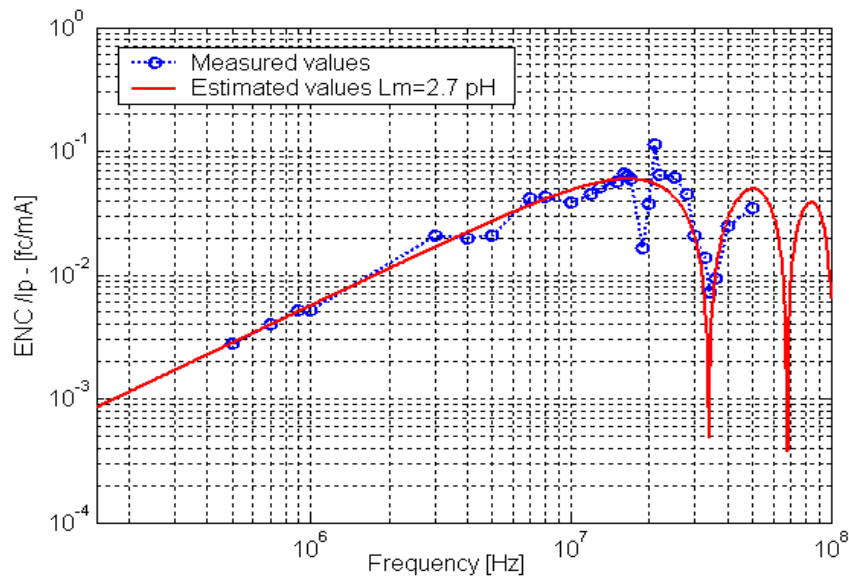


Figure 6.29: Channel 5 transfer function - Measured and fitted values.

Comparing the transfer function depicted in figure 6.29 with the transfer function of channel 5 to shield currents (figure 6.17), it is clear that the FEE is more susceptible to CM currents flowing through the shield than CM currents flowing through the

central wires. The ability of the system to filter these CM currents defines the susceptibility of the FEE. For current flowing through the power cable shield (figure 6.30), the only path to deviate the noise currents from the FEE is via the strap. For the case of CM currents flowing through the central conductors of the power cable, these can be bypassed from the FEE through both the shield and strap (figure 6.31).

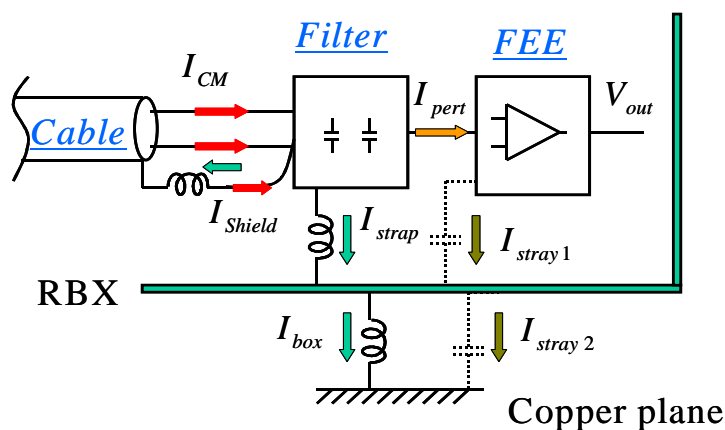


Figure 6.30: Shield current distribution at the input FEE.

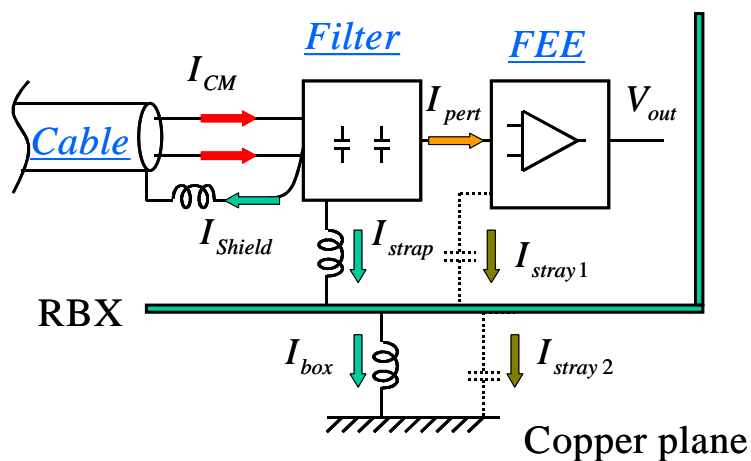


Figure 6.31: CM current distribution at the input of the FEE.

6.4.3 Common mode filter effects.

The CM filter¹ at the input power terminals protects the FEE from CM noise flowing through the power supply lines. It has also impact in the specification of the

¹ It is shown in figure 6.11

6.4. Susceptibility to CM power currents

common mode emission level of the power supplies. The transfer function for channel 5 without filter at the input power terminals is calculated for better understanding of the filter's influence on the susceptibility of the FEE. Figure 6.32 plots the measured and fitted transfer functions for channel 5 without filter, while in figure 6.33 it is compared with the transfer function of channel 5 with filter.

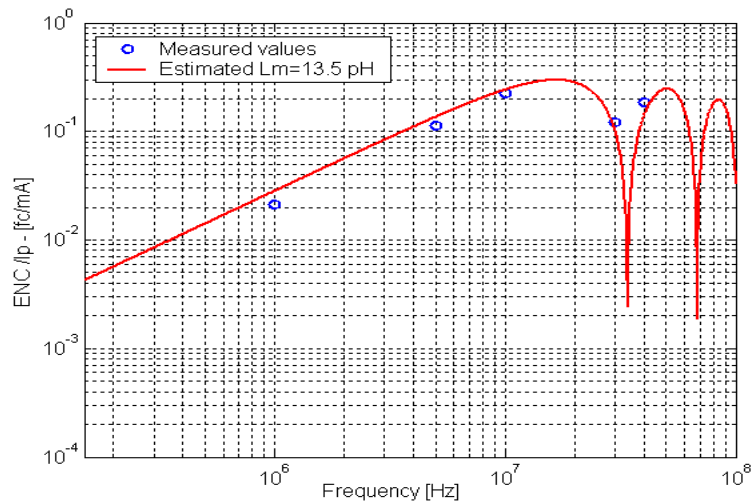


Figure 6.32: Channel 5 transfer function - Measured and fitted values - FEE without input filter.

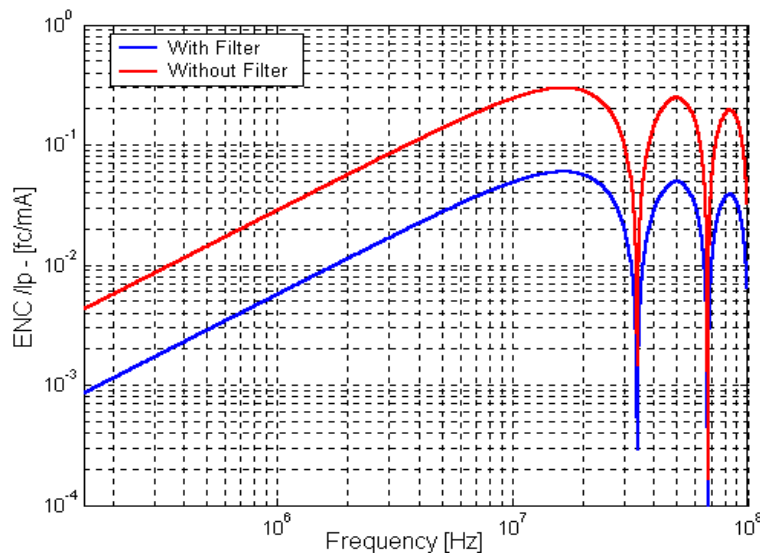


Figure 6.33: Channel 5 transfer function - Fitted values - FEE with and without input filter.

The FEE without CM filter is about 5 times more sensitive than the FEE with filter. It is clear that it is necessary to protect the FEE from the common mode noise currents by avoiding these currents can flow through the sensitive FEE path, deteriorating the performance of the system. The level of the attenuation of the CM filter showed in this analysis is relatively low, as the filter does not include any magnetic component to improve the attenuation to CM currents. In general in the CMS detector, the FEE can not use components with magnetic material due to the FEE operates under strong continuous magnetic fields.

As a conclusion, to protect the FEE from CM currents flowing through the power cables, the solution has to be addressed following two options; one is to use common mode filters at the input of the FEE and the other is limiting the noise emission of the power supplies to very low levels. In CMS the CM immunity of the FEE electronics must be improved by selecting a good cabling and imposing limits on the CM noise emission of power supplies. Power supplies with very low common mode emission can be found in linear power supplies and switching power supplies (SMPS) with special EMI filters. The first one presents poor efficiency, while SMPS requiring CM emission levels too low cannot be found in the market or they can be expensive due to they are custom designed. A solution balancing these two strategies could be the more appropriated for these cases. A simple CM filter built around RF capacitors located at the input of the power supply cables combined with twisted and shield cables will provide not only good CM rejection to CM current flowing through the central conductors but also will improve the rejection to currents induced by far and near EM field. In addition, requiring power supplies with low CM emission will help to achieve the performance goal of the FEE and will reduce the EM radiation from the distribution cables.

6.5 Susceptibility to DM power currents

To study the effect of differential mode noise currents flowing through the power cables, the perturbing current is injected into the active power cable. In addition, to decrease the CM current of the system layout, the ground connection of the power supply and normalized common impedance box is disconnected¹. In this case, the injected current in the active power cable is forced to return through the return power cable.

The measurements on this configuration present two constraints, which limits the values that can be measured. First, the layout is very sensitive to the strap's resonant frequency that connects the RBX to the copper plane². This resonant

1 See figure 6.3

2 See chapter 2

frequency disturbs a lot the measurement, resulting the values measured to fix the transfer function of the differential mode noise being invalid.

The second problem is that at high frequency the stray capacitance associated with the system¹ starts to play an important role increasing the value of I_{gnd} . Therefore the rejection to the common mode noise of the configuration decreases. Both problems limit the frequency range of the measurement. The box and injected current at several frequencies are measured to fix one of these limits. The results are shown in table 6.1 and 6.2.

At 5 MHz	$dB\mu V$	$dB\mu A$	mA
I_{DM}	92.24	78.7	8.6
I_{strap}	52.58	39.04	0.083
I_{box}	66.01	52.47	0.42

Table 6.1 DM current distribution at 5 MHz.

At 10 MHz	$dB\mu V$	$dB\mu A$	mA
I_{DM}	92.2	78.51	8.6
I_{strap}	69.05	55.36	0.63
I_{box}	75.33	61.64	1.2

Table 6.2 DM current distribution at 10 MHz.

At 5 MHz the amount of CM current that flows in the system is around 4% of the total current injected (differential mode around 96%), however at 10 MHz this number changes to 13.4%. Therefore the DM noise that is going to disturb the FEE maybe considered valid up to this frequency range.

Figure 6.34 shows the transfer function of channel 5, where the estimated function is fitted with values measured at lower frequencies than 10 MHz.

1 See figure 6.3

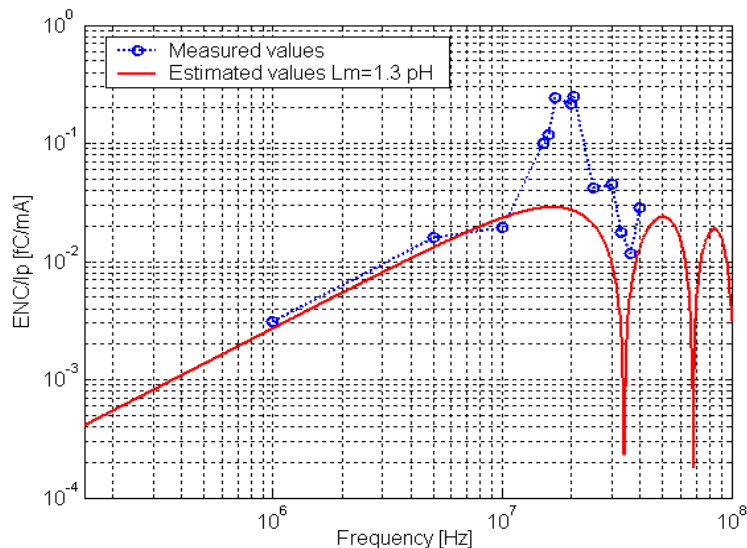


Figure 6.34: Channel 5 transfer function - Measured and fitted values.

Also, this plot shows two big peaks around 18 MHz and 21 MHz, which correspond to the resonance frequencies of the strap connection between the RBX and the copper plane. These resonances in this test set-up appear because the normalized common impedance box is disconnected from ground and it does not damp the resonance as in the previous set-ups. This resonance can be moved to higher frequencies using multi-strap connections between the RBX and the ground plane to reduce the parasitic inductance.

6.6 DM and CM noise contributions to FEE output

This main goal is to analyze the effect of currents, combining common mode and differential mode components, on the FEE immunity and also to define normalized specifications for the output noise of the power supplies.

The main goal of this analysis is to find out the main responsible of the degradation of the FEE performance (CM or DM noise in the central conductors) and also to define the normalized specifications for the output noise of the power supplies.

6.6.1 Noise distribution and TF of CM + DM currents.

The first step of this analysis is to determine the transfer function between the noise at the input positive power lead and the output of the FEE. During this test a perturbation current is injected through the active wire of the power cable.

The noise distribution is similar to the previous test. Figure 6.35 and 6.36 show the RMS value of the several channels versus the change in magnitude of the injecting current at 10 MHz and versus the change in frequency for a 15 mA injecting current

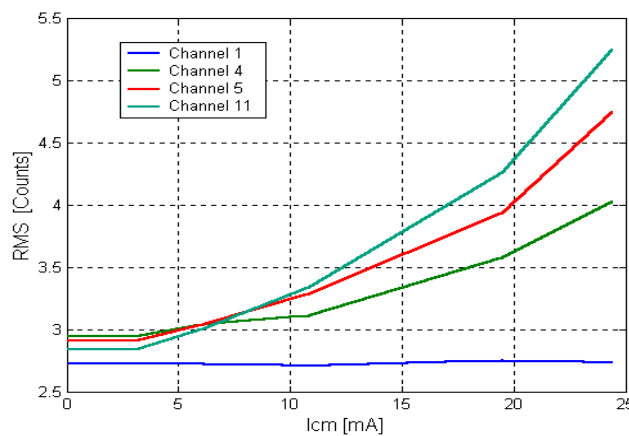


Figure 6.35: Variation of the RMS value of the output noise versus the magnitude of injected current at 10 MHz - Measured values.

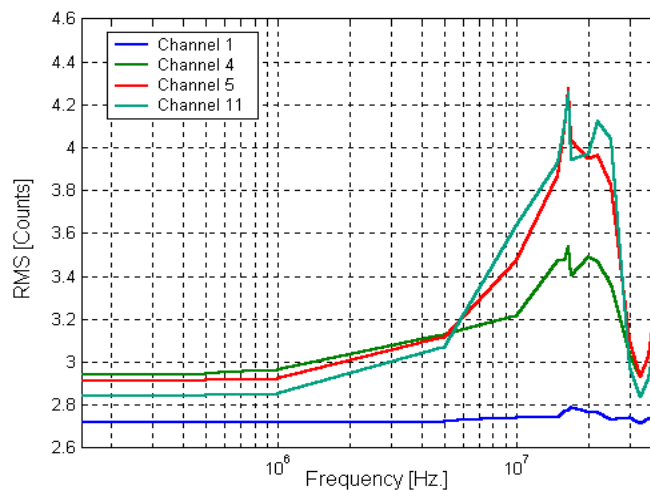


Figure 6.36: Variation of the RMS value of the output noise versus the frequency of the injected current ($I_p=15$ mA) - Measured values.

Similar to previous analysis, it is possible to get the transfer function between the output voltage of the FEE and the noise currents flowing through the cables. Figure 6.37 shows the transfer function of channels 4,5 and 11 for a frequency range between 500 kHz and 40 MHz, while figure 6.38 depicts the measured and fitted transfer function for channel 5.

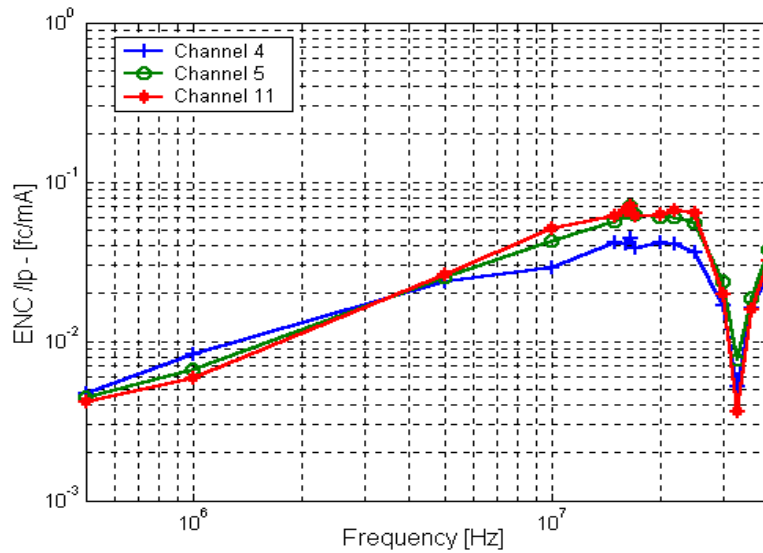


Figure 6.37: Transfer function of channel 4,5 and 11 - Measured values.

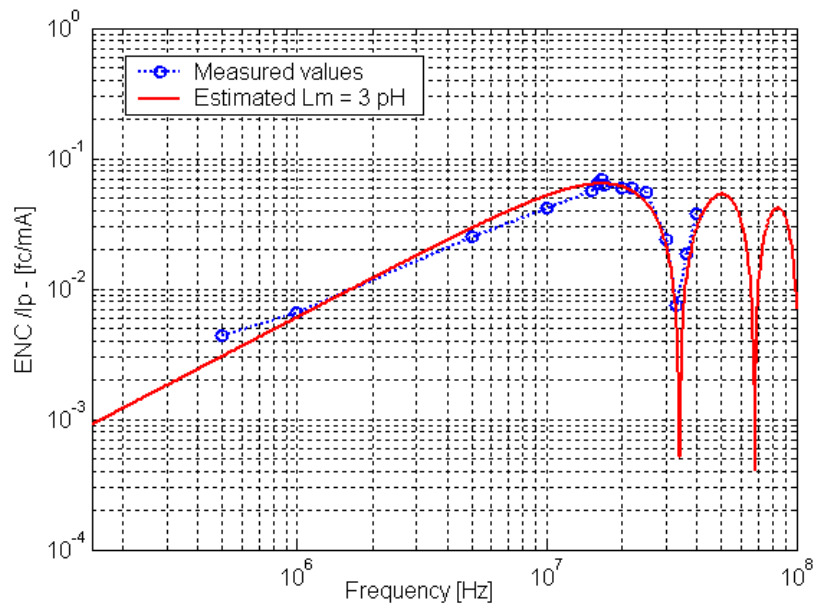


Figure 6.38: Channel 5 transfer function - Measured and fitted values.

6.6.2 External noise contributions to the overall FEE noise

To analyze the effect of currents, with CM and DM components, on the FEE immunity we compare this measures with the previous one where the CM and DM components were injected independently. The current in the active line I_1 and the CM current I_{cm} , depicted in figure 6.39, are measured at 10MHz. Based on these values, the DM current magnitude may be calculated as the difference between the active current and CM current amplitudes. The evaluation of the DM noise current is possible because the CM current and DM current are in phase. This is because both DM and CM circuit present similar impedances at the input of the FEE. All the current magnitudes mentioned above are shown in table 6.3.

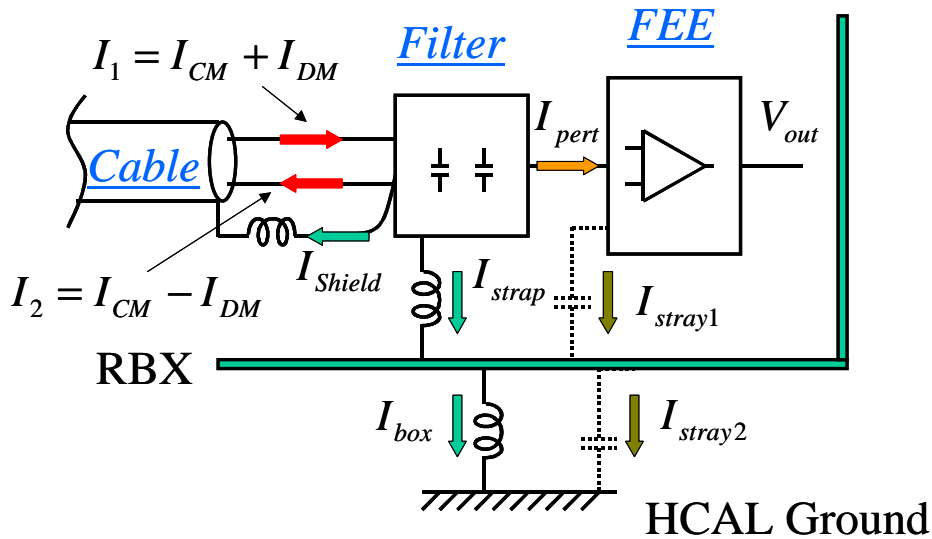


Figure 6.39: Layout of positive input lead immunity test of HCAL-FEE.

At 10 MHz	$dB\mu V$	mA	% - CM/DM
$ I_1 $	96.1	13.2	100
$ I_{cm} $	93.57	9.862	-
$ I_{cm} = I_{cm} /2$	-	4.931	37
$ I_{dm} = I_1 - I_{cm} $	-	8.269	63
$ I_{box} $	77.78	1.601	-

Table 6.3 Current distribution at 10 MHz - DM+CM immunity test.

Figure 6.40 shows the transfer function of CM, DM and positive lead modes. Based on this plot, it is possible to define two important properties of the configuration of the FEE:

- CM currents produce more noise at the FEE output than DM currents.
- It seems that the main responsible for the degradation of the system, when a current is injected in the positive lead, is the CM noise flowing through the system.

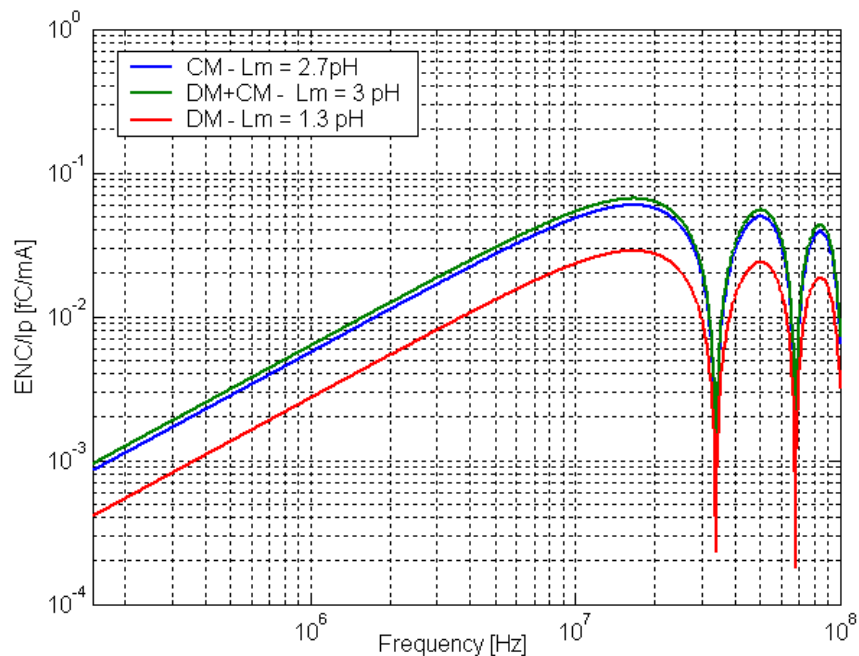


Figure 6.40: CM, DM and CM+DM Transfer function of channel 5.

The final contribution due to a noise current flowing through a power conductor depends on the magnitude of the CM and the DM components defined by the impedances of the circuit and the noise transfer function for each current mode. To verify that, a perturbing signal of 19.5 mA at 10MHz is injected in the active power conductors giving an output noise at channel 5 equal to 3.81 counts. This value is compared with the noise estimation obtained by decomposing the current in its CM and DM components and applying the CM and DM transfer functions previously measured.

The current injected is decomposed in the two orthogonal modes, defined mainly, by the impedance of the RBX. The common mode component of this current is equal to 7.3 mA (37%), while the differential mode component is 12.2 mA (63%). The proportion between CM and DM components is more or less the same for different current amplitudes and different frequencies up to 20 MHz.

Based on the CM and DM transfer function at 10 MHz previously calculated, the noise at the output of channel 5 generated by these currents are:

$$Counts - ch5_{CM} = 0.048 \frac{fC}{mA} \times 3 \frac{counts}{fC} \times (7.3 \times 2) mA = 2.101 \text{ counts} \quad (6.12)$$

$$Counts - ch5_{DM} = 0.023 \frac{fC}{mA} \times 3 \frac{counts}{fC} \times 12.2 mA = 0.841 \text{ counts} \quad (6.13)$$

The total numbers of the counts at the output of channel 5, including the thermal noise of the amplifier is:

$$Ch5 = \sqrt{(2.101 + 0.841)^2 + (2.91)^2} = \sqrt{(2.942)^2 + (2.91)^2} = 4.1 \text{ counts} \quad (6.14)$$

This value is in close agreement with the measured value, which is 3.81 counts. The error is around 7.5%. The first term of the square root (2.942) defines the contribution of the external noise to the total FEE output noise. Based on this number, it is possible to mention that the 71% of the contribution of the external noise is generated by CM currents and the 29% has its origin in DM currents, when the DM current is 1.7 times larger than the CM current. So, it is possible to conclude that the main responsible of the degradation of the FEE noise immunity are the CM currents.

6.6.3 Normalized noise level required at the output of the PS

Based on the transfer functions estimated when CM or DM current is injected, the effect on the FEE output noise has been analyzed when the sensitive electronics is powered up by switching mode power supplies (SMPS). Although, only a few standards define the conductive noise level at the power supply output, the noise level required at SMPS outputs for optimal performance of the FEE should be established.

Using the HCAL sub-system as reference, the effects of conducted emissions for three different FEE topologies have been studied to identify the standardized noise level required at the power supply output. The topologies used during this studies, correspond to a FEE with good EMI configuration (A), a FEE without EMI input filter (B), and a FEE with a bad EMI design, (C). Theses configurations are characterized by the parameter value (Lm) used in this chapter to parameterize the transfer functions. The values of these parameters for conducted emissions on the positive terminal are 3 pH for configuration A, 15 pH for configuration B and 75 pH for configuration C and for the CM emissions are 2.7 pH for configuration A, 13.5 pH for configuration B and 67.5 pH for configuration C. Figure 6.41a shows the transfer functions of the conducted noise at the input positive terminal of the three

configurations of the FEE and figure 6.41b shows the transfer function of CM at the input of the FEE of the three configurations of the FEE.

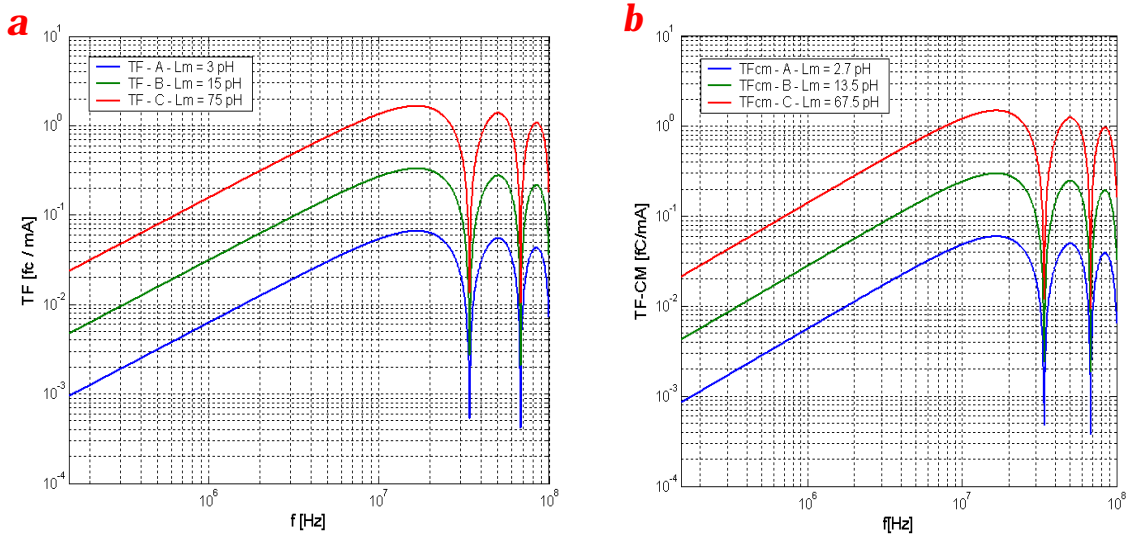


Figure 6.41: a) TF of positive input current b) TF of CM input current for A,B and C FEE configurations.

The conducted emissions assumed correspond to three different theoretical power supply units whose emissions are equal to the level defined by the standards EN 55022 class A or class B, and the switching frequency of each PS units is set to different magnitudes as; 100 kHz, 200 kHz and 300 kHz. Figure 6.42a shows the output voltage spectrum at the positive terminal of the PS switching at 200 kHz complying with the EN 55022 class A standard, while figure 6.42b shows the CM emission of this PS following the level defined by CM-EN 55022 - class A.

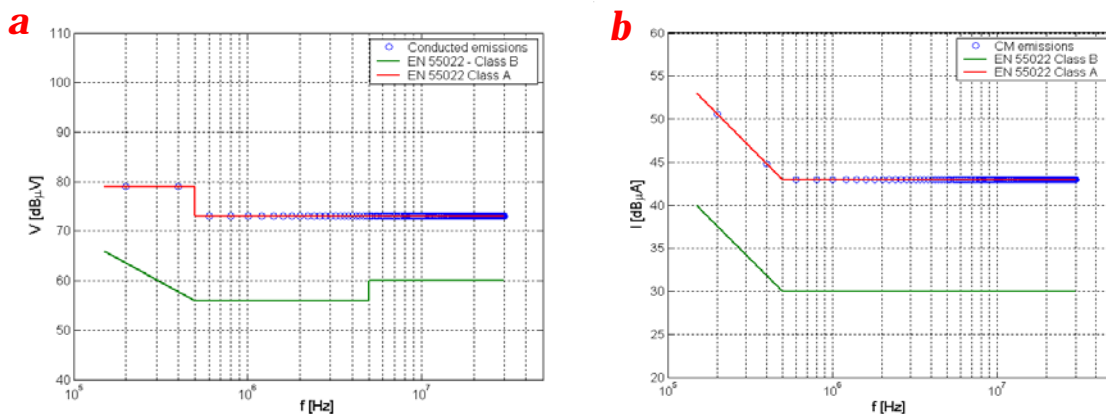


Figure 6.42: Conducted noise emissions of a theoretical PS units switching at 200 kHz.

EN 55022 - A	A	B	C	EN 55022 - B	A	B	C
100 kHz	2.91	3.12	6.41	100 kHz	2.91	2.92	3.17
200 kHz	2.91	3.02	4.97	-	2.91	2.91	3.04
300 kHz	2.91	2.98	4.39	-	2.91	2.91	3.00

Table 6.4 Estimated output noise for channel 5 generated by conducted emissions at the positive terminal of the FEE.

CM / EN 55022 - A	A	B	C	CM / EN 55022 - B	A	B	C
100 kHz	2.92	3.33	8.64	100 kHz	2.91	2.95	3.43
200 kHz	2.91	3.12	6.44	-	2.91	2.92	3.18
300 kHz	2.91	3.05	5.51	-	2.91	2.91	3.09

Table 6.5 Estimated values of FEE channel 5 generated by CM emissions at the input terminal of the FEE.

Tables 6.4 and 6.5 summarize the estimated output noise for channel 5 for different conducted emissions and different FEE configurations. These values have been calculated using the DM+CM TF and CM TF previously defined in figure 6.41. FEE units characterized by a high noise immunity show good performance when they are biased by power supplies whose conducted output noise comply with EN55022 class A. In opposition, FEE units with poor noise rejection require power supplies with very low noise output voltage. These power supplies have either to comply with military or FCC - Class B standards or they have to be linear power supplies. Similarly, table 6.5 shows the same tendency for power supplies having dominant CM output noise emission. This table shows that the combination of high CM emission at the power supply and poor CM rejection at the FEE gives a poor overall performance even in the case that no DM noise emission or ripple exists. It shows how important is to define the maximum level of emission for CM currents.

For the previous analysis it has been considered that power supplies emit noise in whole frequency range defined by the standards. In general, DM emissions are more important at low frequencies whereas the CM is more important above the MHz range. Also, analyzing more in detail the immunity curves, it is clear that the FEE is more susceptible to noise at high frequency than at low frequency and the noise contribution extends above 30MHz that is the maximum frequency set by the

EN 55022 standard for conductive noise. It seems that the noise level fixed by the European standards do not define the optimal requirements for the HCAL sub-system, being necessary to define a new emission level that adapts better to the noise sensitivity of this FEE.

The definition of the noise level will be based on the inverse curve of the transfer function that defines the immunity level of the FEE. The noise level required at the output of the power supply is defined by a constant curve above 20 MHz and below of this frequency, the level increase at 20 dB per decade up to 100 kHz. To fix the level of the proposed limit curve, a new noise analysis is carried out. The effect on the output noise of the FEE biased by a PS with an output conducted emission as defined by the proposed limit is calculated. It is assumed the power supply switches at 100kHz and the frequency range for the noise spectrum is extended between 100 kHz to 50 MHz, because there is an important noise contribution at the output of the FEE above 34 MHz. A criteria to define the level of the proposed limit can be fixed when the output noise of channel 5 is equal to 3 counts for the conduction emission in the positive terminal (noise contribution equal to 25% of the thermal noise) and 2.97 counts to define the level for the CM noise (20% of the thermal noise). Following these criteria the level depends on the characteristic of the FEE being necessary to establish a curve for each FEE configuration. Figure 6.43 shows the levels of the proposed limit corresponding to the different FEE configurations and compare those limits with the European standards. Figure 6.43a depicts the limits for the terminal current, while figure 6.43b shows the limits for the CM currents.

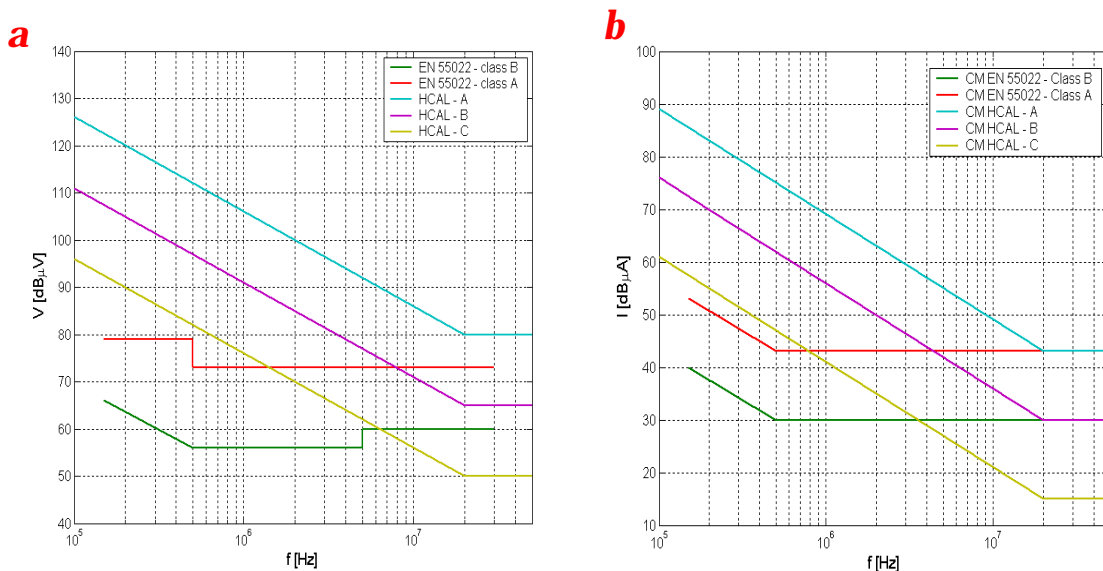


Figure 6.43: European (EN 55022 - Class A & B) and HCAL standard levels for positive input terminal noise and CM input noise.

In general, this plot shows a big difference between the requirements for the HCAL FEE and the levels imposed by the standards. For good EMI configurations the level required at the output are much more relaxed than the European norms. However, if bad configurations of the FEE are designed the level required are very restrictive, being for certain frequency range extremely low. Also, there is an important difference respect to the European standards at high frequency. Due to the FEE is sensitive above 30 MHz it is necessary to extend the emission frequency spectrum considered up to 50 MHz. This is a particular consideration for the HCAL FEE, for other sub-systems the spectrum considered could be extended to higher frequencies or not depending upon the FEE sensitivity. The FEE output noise (total number of counts of channel 5) for different power supplies switching at 100 kHz with output noise characteristics level equal to each of the standards levels defined above and different FEE configurations (A,B and C) are summarized in the table 6.6. The base noise for this channel is 2.91 counts.

DM+CM	A	B	C	CM	A	B	C
EN 55022 - A	2.91	3.12	6.41	CM EN 55022 - A	2.92	3.33	8.64
EN 55022 - B	2.91	2.92	3.17	CM EN 55022 - B	2.91	2.93	3.43
HCAL - A	3.03	5.69	24.6	CM HCAL - A	2.97	4.25	15.81
HCAL - B	2.91	3.01	5.23	CM HCAL - B	2.91	2.98	4.53
HCAL - C	2.91	2.91	3.03	CM HCAL - C	2.91	2.91	2.97

Table 6.6 Estimated values of FEE channel 5 generated by conducted emissions at the positive terminal and CM emissions at the input FEE.

As an example of the application of this new standards levels the conducted emission of a VICOR DC-DC converter is evaluated. Figure 6.44a shows the conducted emission at the output of the Vicor converter without EMI filter and figure 6.44b shows the CM emissions of the same unit. The noise emission of the VICOR converter complies with the emission level defined by HCAL-A. When this converter bias the FEE HCAL-A, the noise output of channel 5 is dominated by the thermal noise (Ch5-A = 2.91 counts) and the FEE performance is not affected. However, this emission level is quite far to comply with any of the European standards. A similar analysis is valid for the CM. The noise level of this Vicor converter is close to comply with the curve level defined by HCAL-B. For frequencies in the low-range of the spectrum, the output noise is large than the limit, while for higher frequencies, the noise lower, given this combined effect an overall noise at the FEE output of 3.05 counts. This converter does not comply with the level defined by HCAL-C, given a total noise of 5.28 counts.

6. RF Susceptibility Test of FEE

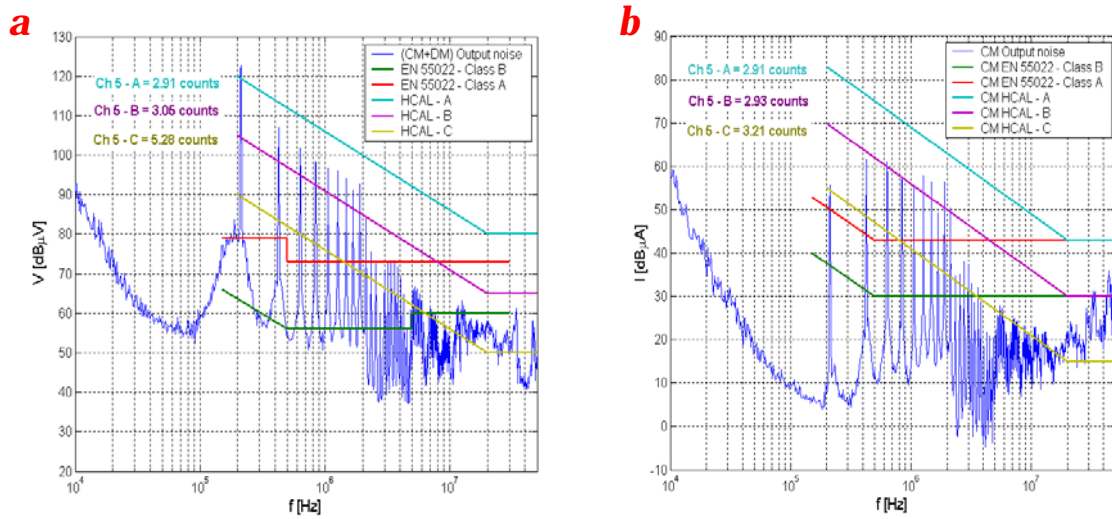


Figure 6.44: Conducted and CM emissions of Vicor converter compared with different standardized levels.

If the Vicor converter includes an output filter, the emission level is depicted in figure 6.45. For this case, the output noise emission complies with both the HCAL-A and HCAL-B levels, while at some frequencies it does not comply with the HCAL-C level. In this last case, if the FEE HCAL-C is biased by this converter with filter the output noise is equal to 2.96 count, being an acceptable performance.

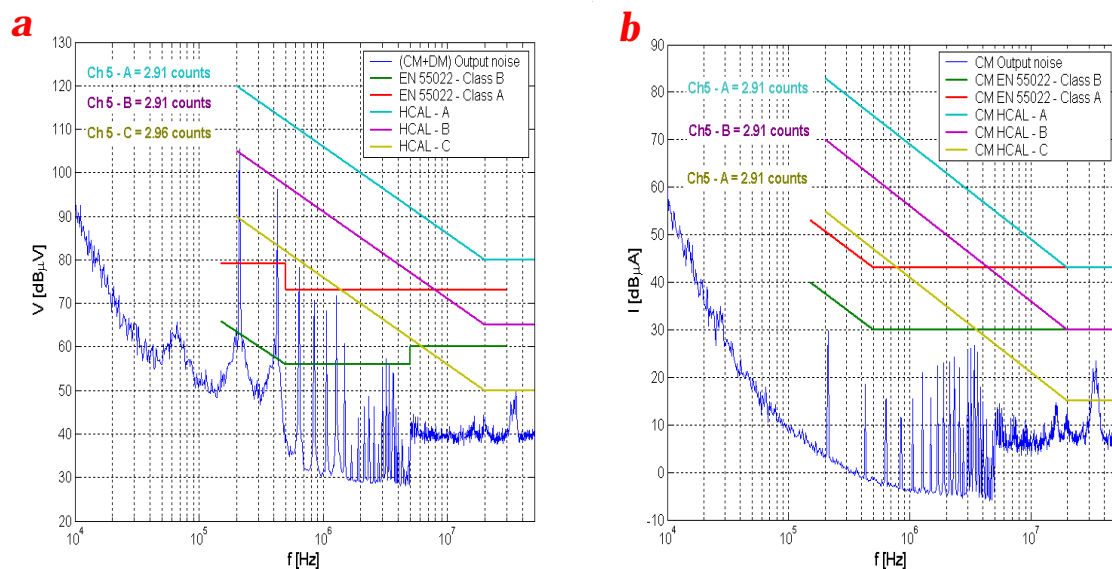


Figure 6.45: Conducted and CM emissions of Vicor converter with EMI output filter compared with different standardized levels.

It is necessary to remark that none of these emissions fits the requirements fixed by European standards, however even FEE with bad EMI configurations might work without any problem. It is very important to define the immunity level of the FEE for the different sub-systems. Each of them will be different and the application of the standards without the knowledge of this level can lead to serious problems. However, if immunity level curves are defined, it is possible to set a new level or define the European standards level that fits better to the requirements of the detector. For the present example the selected level would be Class A for good EMI immunity and Class B for FEE without very good EMI immunity. For the case of very bad EMI topologies, it would be necessary to apply more restrictive levels like FCC class B or military one. In all cases the standard level would be extended in frequency up to at least to 50 MHz.

6.7 Summary

The susceptibility of the HCAL FEE to noise currents in LV power supply inputs is defined by the susceptibility of the system to CM currents, DM currents and shield currents. The susceptibility is quantified by the transfer function between the output of the FEE and the perturbing current.

The principal cause of the degradation of the FEE immunity is CM currents. These CM currents can be coupled into the FEE by shield currents, by CM flowing through the cables and by the DM to CM conversion. The DM mainly contributes to the degradation of the FEE because of DM to CM conversion.

There are several actions that can be applied to improve the FEE immunity to noise currents.

- Select good ground connections
- Use CM filters
- Use of shielded power cables

The first one is defined by the low impedance of the ground connections in the whole frequency range, from a few Hz up to several tens of MHz. It is recommended to use very short and multiple straps to make the ground connections as well as to take care to route these ground connections as close as possible to the ground or reference plane. These recommendations are focused in creating a low impedance-grounding path for the system, which helps to bypass the noise currents from the sensitive parts of the detector. Also, it is recommended to weld these connections or use very tight connections which ensure a very good contact to ground of the FEE.

The second recommendation is focused on filtering the common mode noise flowing through the conductors. This filter must be implemented with RF

capacitors because the high magnetic field at the FEE area does not allow the use of magnetic chokes. These simple filters are not as good as a real EMI filter, however they improve the performance of the system in presence of common mode noise. This solution used in combination with the limitation to low levels of the common mode noise generated by the power supplies, which can be easily achieved, complete the implementation of a robust system with low noise output voltage.

The final recommendation is oriented to avoid the noise radiation through the cables and to give a low impedance path to CM noise currents to avoid them entering into the FEE. The use of un-shielded power cables, should not be used, as it will force the selection of power supplies with very low CM emission levels at the output, which it is not practical for technical and budgetary reasons.

The immunity curves of the system can be used to define a new noise level required at the output of the power supply. For HCAL FEE this level results very different from the level defined by the European standards. The definition of a standardized noise level at the output of the power supplies without the knowledge of the immunity curves of the system can lead to problems. It is important the definition of this level for all the sub-systems of the detector. Later, based on this curves, it is possible to define the emission level for the power supplies or select the European, American or Military standards that fits better to the requirements of the detector. In any case, the standardized level should be extended above the 30MHz limit because the FEE is very sensitivity in that frequency range.

6.8 References

- [1] Clayton R. Paul, *"Introduction to Electromagnetic Compatibility"*, NY Wiley Interscience, 1992, ISBN-0-471-54927-4.
- [2] T. Williams, *"EMC for Product Designers"*, 1997, ISBN-0-7506-2466-3.
- [3] F. Artech, C. Rivetta and F. Szonsco *"Electromagnetic compatibility plan for the CMS detector at CERN"*, Proc. 15th International Zurich Symposium and Technical Exhibition on Electromagnetic Compatibility, Zurich, Switzerland, pp. 533-538, February 2003.
- [4] International Standard IEC-61000-4-6, *"Electromagnetic compatibility (EMC) Testing and measurement techniques - Immunity to conducted disturbances, induced by radio-frequency fields"*, Basic EMC publication (Ed. 2000).
- [5] T. Shaw et. al., *"Front End Readout Electronics for the CMS Hadron Calorimeter"*, Proc. IEEE Nuclear Science Conference 2002, Viginia, USA, Vol 1, pp 194-197, November 2002.
- [6] Dan Green, *"HCAL Status"*, Oral presentation, CMS Week June 2003.

Chapter 7

Susceptibility to transient perturbation

This chapter addresses the analysis of transients in the power supply system of CMS. Transients in power distribution lines can be generated by variations of the current consumption of the FEE due to changes in operation mode, random failures, equipment turn on/off, etc. They can induce over-voltage and voltage dips in the LV-DC and AC distribution system, which can affect the performance and the reliability of the front-end electronics. During this analysis the CMS power supply distribution is divided in two areas. The first one corresponds to the AC distribution (between the counting room and the periphery of the detector) and the other to the DC distribution (between the periphery and the FEE). The transient limits for the first area are well defined by the standards, this is a typical AC distribution. However, limits for the second one are not clear and they depend on the characterization of the FEE to this kind of transients, power supply distribution topology, cost and risk. This chapter is focused mainly on this part. The main goal is to describe possible sources of transients and the implications that they have on the FEE performance. The chapter does not present neither the final transients levels of CMS nor the voltage level to be applied to the FEE during the transients susceptibility test because these values depend on the final topology of the power supply distribution system of CMS, which has not been defined yet.

7.1 Introduction

The low and high voltage distribution system in CMS is based on a primary 400Hz AC system. As it was described in chapter 2, it is composed of independent motor-generator sets for each sub-detector that converts the 50Hz AC mains to a 400Hz three-phase 400V system. The AC 400Hz-distribution system feeds AC/DC converters located around the detector to power up sub-detectors. These units are simply three phase step-down transformers with rectifiers and LC filters in the secondary. They convert the AC high voltage into appropriate DC low voltages that

are locally distributed around the detector. In this case, local LV regulation is performed in the front-end electronics at the board level using radiation tolerant low voltage drop regulators. Other sub-systems will convert the AC to 48V DC and distribute this intermediate voltage to DC-DC switching converters that supply the final power to the FEE. The HV power supplies are located in remote areas away from the detector as high energy particle radiation can induce on these systems catastrophic failures. In general, this voltage distribution involves cables with length larger than 100 meters.

The environmental condition at the detector is full of transient interactions. Fast and slow transients and voltage dips, can be found in the power supply distribution. Transients can induce EM interactions that affect the performance or reliability of the front-end electronics. The order of magnitude of the transient as well as the duration is a design parameter that is defined by the configuration of the power supply distribution and the susceptibility of the FEE. It has serious impact on the selection of the system protection (rates, reaction time etc.). The design of the system [1] should be focused to allow higher transients level for short time periods. Figure 7.1 shows the design goals of a typical power supply distribution system.

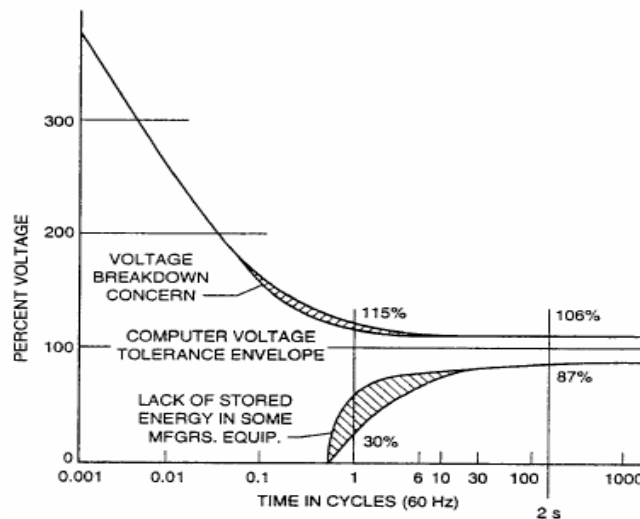


Figure 7.1: Design goal for a power supply distribution system fix by IEEE-Std 1100-1992.

Surges or slow transients are generated by switching transients or by lightning strokes injecting high voltage/currents via electromagnetic fields. The latter are not considered in the present study as the detector is placed 100 m underground and is well protected against these faults at surface level. Switching transients can be generated by power system switching, load changes, short circuit faults to the earthing system of the installation. The slow transient voltages are characterized by a fast rise time (a few μs) followed by a decay time of some tenths or hundredths of

μs . The energy involved in these transients is high and can cause the destruction of the electronic devices in the detector.

Fast transients are generated by switching transients (interruption of inductive loads, relay contact bounce, etc.). The fast transient is characterized by a very fast rise time (a few ns) followed by a decay time of some tenths of ns . In some cases, if the switching arc is unstable, as the contacts open, the current is often interrupted and re-ignited several times (bouncing) before the circuit is in open stable condition. The energy involved in these transients is not very high (a few mJ) but can cause malfunctions of the electronics devices in the detector.

Voltage dips and short interruptions are caused by faults in the network or in the installations, by a sudden large change of load, by inrush currents energizing transformers, etc. Voltage variations are caused by the continuously varying loads connected to the network. The duration of these transients are between a few ms up to several tenths of ms.

Since these disturbances are unavoidable in a distribution system with the power level required in CMS, it is necessary to include a combination of protection devices in the design of the sensitive electronic equipment. The potential impact of transients depends on its severity and the susceptibility of the equipment. Three types of occurrences are possible:

- Signal-data disruption: Circuits carrying signals are susceptible to surge interference via conductive, inductive, capacitive and electromagnetic coupling. They can affect the integrity of the signal.
- Gradual hardware stress and latent failures.
- Immediate hardware destruction.

This chapter addresses the study of transients in CMS. The generation, the propagation, order of magnitude and duration of the transient are studied as well as the solutions that can be used to improve the immunity of the electronics against these phenomena. These studies are based on Pspice simulations and some measurements on *FEE prototypes of HCAL and tracker sub-systems*. These analyses are used to obtain general rules, which help to tackle the transient problem in an early stage of the design and take the corrective actions, which ensures the immunity of the FEE against transients.

7.2 Voltage dips and short interruptions

7.2.1 Introduction

All electrical and electronic devices can be affected by voltage dips or short interruptions of power supply [2]. A voltage dip is defined as a sudden reduction of the voltage during a short period of time, from a few ms to a few seconds, at a point in the electrical system followed by a voltage recovery. Short interruption is defined as the disappearance of the supply voltage for a short period of time. It may be considered as voltage dips with 100% of amplitude. Typical waveforms of these transients are shown in figure 7.2. These transients are generated by faults in the network, by a sudden large change of load, by in-rush currents, etc. [3][4].

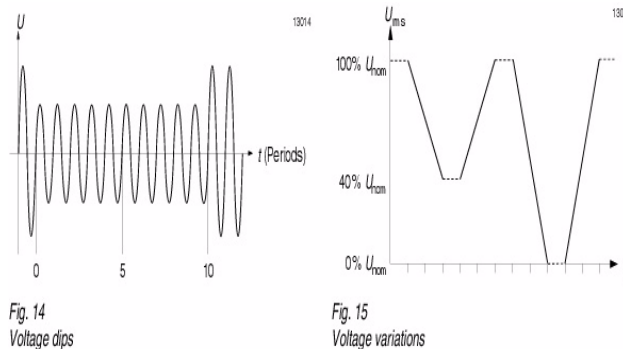


Figure 7.2: Voltage dips standards wave form and magnitude.

These phenomena are random in nature and may be characterized in terms of deviation from the rated voltage and duration. Voltage dips and short interruptions are not always abrupt, because of the reaction time of rotating machines and protection elements connected to the power supply network.

The step load changes are one of the most common sources of voltage disturbance. The basic cause of the voltage disturbance is simply the voltage drop caused by the abrupt load current change and the power system impedance. The inrush currents energizing transformers and filter capacitors in power supplies can reach values of about 10-20 times the nominal current if no limiting circuits are included in the equipment. The transformer start-up creates a magnetizing current transient, decaying to steady state after several cycles under worst-case conditions. This issue is particularly critical for transformers located in the periphery of the detector where the detector's fringe field pre-magnetizes the core of the transformers. In addition, when rectifier/capacitor power supplies are energized, the initial current charging the capacitor can cause similar levels of inrush currents. The fault currents

7.2. Voltage dips and short interruptions

represent an extreme case of transient current and thus AC or DC line voltage disturbance. Depending on the power system impedance, several order of magnitude of nominal load current may be available. Severe voltage reduction in adjacent equipment usually results until the fault is cleared.

7.2.2 HCAL FEE susceptibility test to voltage dips and short interruptions.

The goal of this test is to determinate the susceptibility of the equipment to short voltage interruptions and voltage variations of the primary power supply and to characterize the behavior of the LV regulators placed on the boards. Short interruptions and voltage variations are applied to the FEE. The degradation of the FEE performance and the loss of acquired data are evaluated. The test uses as guide the standard EN-61000-4-11/ IEC-1000-4-11 [5]. This test is focused on characterizing the transient levels for the area between the periphery of the detector and the detector itself. For the other area (AC distribution - Periphery of the detector to counting room) both amplitude and duration of the transients are perfectly defined by the standards and the applications of the standards are enough to fulfill the requirements of the detector.

This test was conducted to the same FEE system as described chapter 6. Voltage dips were applied independently to the voltage feeding each FEE power cable, using the transient generator (UCS-500) and two power supplies, which form the two voltages needed by the UCS-500 to create the voltage dip. The loss of data or loss of function was used as criteria to qualify the performance of the front-end electronics. The test has been carried out in the analog and digital part of the FEE. The test layout is shown in figure 7.3

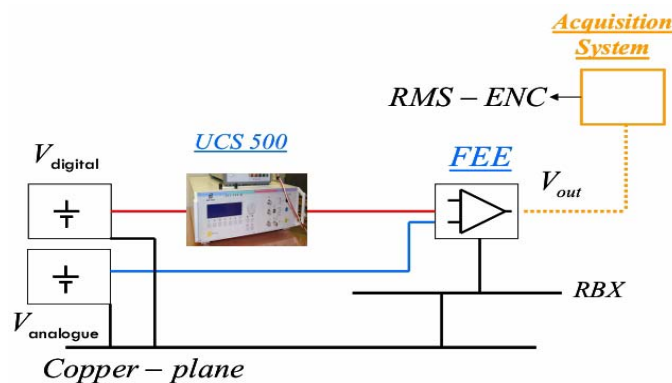


Figure 7.3: Voltage dip test layout.

The voltage at the back-plane (input of the LV regulator - V1) and at the output of the LV regulator (V2) have been measured to study the behavior of the LV regulators during the voltage dips. This is shown in figure 7.4.

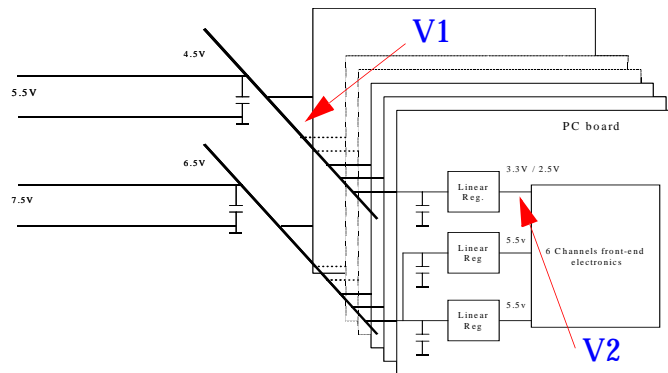


Figure 7.4: RBX layout - Measured voltages

Figure 7.5 shows the transient voltage at both the input and the output of the LV regulator during a voltage dip. There are three operation areas of the LV regulator. In the first one, corresponding to area A in figure 7.5, the LV regulator works properly because the input voltage is higher than the minimum input voltage required. The output voltage of the LV regulator is constant independent of the input voltage. In the second area, area B, the LV regulator cannot regulate the output voltage and behaves as an impedance. The output voltage drops at the same time as the input voltage. Later, in area C, when the voltage reaches a threshold the voltage regulator drops the output voltage to zero.

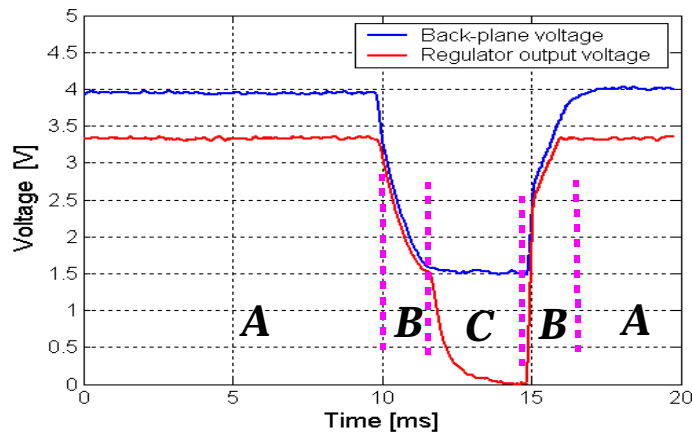


Figure 7.5: Input and output regulator voltage during a voltage dip.

Voltage dips were applied independently to both the analogue and digital power supplies feeding the HCAL-FEE and the loss of data or loss of function was used as criteria to qualify the performance of the system. The results of this test are shown in tables 7.1 and 7.2. The two upper rows resume the operation when the input voltage is applied continuously without any perturbation superimposed but with a

7.2. Voltage dips and short interruptions

magnitude lower than the nominal voltage. The rest of the table describes the operation when the input voltage is kept at the nominal value (6.5V for analogue, 4.5V for digital) and repetitive voltage dips with different amplitudes and durations are applied. When the voltage is applied to the analogue power supply, the only effect detected is a simple gain loss of the amplifier, which recovers when the dip finishes. When the voltage is applied to the digital power supply, two problems have been found. The first one is a loss of data and the second one is a clock failure. In case of clock failure, the FEE has to be re-setted. These faults define that the digital part of the FEE is more critical to these transients because in case that the clock signal is lost the system cannot be recovered and it is necessary to reset the sub-detector.

Minimum Voltage-V1 (Volts)	Voltage Dip (Volts)	Dip duration (ms)	Status	System recovery
5.15	-	Cte	OK	-
5	-	Cte	Gain loss	Yes
5.12	1.38	3	OK	-
5	1.5	3	Gain loss	Yes
4.8	1.7	3	Gain loss	Yes

Table 7.1 Results for voltage dips applied to the analogue power supply line - ($V_{dip} = V_{nom} - V_{min}$).

Minimum Voltage (Volts)	Voltage Dip (Volts)	Dip duration (ms)	Status	System recovery
3.2	-	Cte	OK	-
3	-	Cte	Loss of Data Clock fails	No Reset system
3.3	2.2	5	OK	-
3	2.5	5	Loss of Data	Yes
2.3	3.2	5	Loss of Data	Yes
3.3	2.2	10	OK	-
3	2.5	10	Loss of Data	Yes
1.88	3.62	10	Loss of Data Clock fails	No Reset system

Table 7.2 Results for voltage dips applied to the digital power supply line - ($V_{dip} = V_{nom} - V_{min}$)

The easiest method to achieve immunity to voltage dips is to make sure that the DC distribution has enough 'hold up' times. This is usually achieved by using higher values of capacitance on the DC bus bars and also by increasing the unregulated voltage to allow more headroom for the voltage dips. It is necessary to have enough energy storage, given the power consumption of the product, to ride through the frequent short dips and dropouts. If non-essential functions can be switched off during a 'hold up' event, or the microprocessors can be put into 'sleep mode', it will increase 'hold-up' time during voltage-dip. When the dips are so long that they become a sag or interruption and the unregulated energy storage cannot 'hold up' any longer, it is important to ensure that before the logic DC supplies go out of tolerance the product 'cleanly' (no memory is lost or corrupted and no unintended operations) and safely ceases operation and shuts down. Then, when the event has passed, operation can be cleanly and safely restored.

7.3 Surge or slow transients

7.3.1 Introduction

In the CMS detector, slow transients are generally generated by switching effects. A few examples are listed below:

- Inrush currents generated by energizing capacitors and transformers.
- Load changes in the power distribution system.
- Resonating circuits, such as long cables plus filter capacitors associated with switching devices.
- Short circuits and faults to the earthing system of the insulation.

The slow transient waveform is characterized [4][6][7][8] by a fast rise time (a few μs) followed by a decay time of some tenths or hundredths of μs . The energy involved in these transients is high (few mJ up to some Joules) and can cause the destruction of the electronic devices in the detector. In the case of the CMS detector, the victim circuit is characterized by very low impedance, which makes the ability of the noise sources to couple to the victim (FEE) much easier.

The power supply distribution system can be divided in two areas, one the 400Hz-AC power system and the other the DC power distribution system. The transient characteristics of each one are different, making necessary to tackle the transient problem separately. The AC power distribution system is extended between the surface level or counting room to the periphery of the detector (around 100 meters or 250 meters). It corresponds to the typical AC power distribution, which is well defined by the standards [2][9]. The test to be applied for defining the immunity of the equipment is defined by the standard IEC-61000-4-5. This standard

defines 5 different levels depending on the characteristic of the electrical environment where the equipment is going to be installed. A brief description of each class follows; a well-protected environment characterizes an electrical system classified as **Class 0**. In this system all incoming cables are provided with over voltage (primary and secondary) protection. The units of the electronic equipment are interconnected by well-designed earthing system. **Class 1** electrical system is defined by an environment partially protected, in which the electronic equipment has its own power supply completely separated from the other equipment and switching operations can generate interference voltages within the room. **Class 2** electrical system is characterized to have an electrical environment, where the cables are well separated even a short runs. An electrical environment where power and signal cables run in parallel characterizes an electrical installation classified as **Class 3**. This type of installation is earthed to the common earthing system of the power installation, which can be essentially subjected to interference voltages generated by the installation itself. Current due to earth faults, or switching operations may generate interference voltages with relatively high amplitudes in the earthing system. On the other hand, a **Class 4** electrical environment is characterized to have cables for both electronic and electric circuits running in parallel. Currents of kA range due to earth faults and switching operations may produce interference voltages of high amplitude in the earthing system of this kind of environments. For this environment the power supply network can be the same for both electrical and electronic equipment. Also, class 4 electrical environment are systems in which there is no systematically constructed earthing network outside the electronic equipment, and the earthing systems consist of pipes, cables etc. Finally, an electrical environment classified as **Class 5** corresponds to an electrical environment where the electronic equipment is connected to telecommunication cables and overhead lines in a non-density populated area.

According to the previous descriptions, all equipment placed in the AC area can be classified as either class 3 or 4. In this case, positive and negative pulses of amplitude equal to 2 kV (Line-Line) and 4 kV (Line-Ground) will be applied during surge tests following the test procedure well defined by the standards.

The DC power supply distribution system is located between the balconies (periphery of the detector) and the detector. The transients generated by the AC line are attenuated at the input of the DC system, being the transients generated by the DC system itself the only one that can affect the detector (FEE). This area is the most critical in terms of the protection selection because the high magnetic field and the radiation do not allow to use typical protection devices applied in normal environments. The transient analysis is focused in this area of the detector. This study is split in two parts, the former consists on the analysis of the transient effects generated by load changes, magnetic coupling and short-circuits in the DC area of the CMS detector. The magnitude, the duration and the energy involved in the transient are studied. This study is based on Pspice simulations of preliminary designs of power supply distributions to be applied in CMS sub-detectors. The

second part of the study is focused on the surge test. The goal of this study is to analyze the effects and internal voltage distribution in the FEE of surge perturbations. A surge signal of certain amplitude in DM and CM configuration of both positive and negative polarities is applied to a prototype of the HCAL sub-system, and the effects on a dummy board of the system are studied.

These examples are used to describe the implication that some PS distribution topologies have on the magnitude and duration of transients as well as the impact that these topologies have in terms of the protection selections, risks and costs. This analysis can be used as a base to define a transient immunity test, which allows to do the integration of the equipment in a safe way. This section does not pretend to give the test level to be applied to the detector because this level is defined by the final topology of the power supply distribution, which is not known yet. However, this study is the initial point to carry similar analysis with other sub-systems to define final tests to apply to the CMS detector electronic equipment.

7.3.2 Transients in DC distribution

The transients generated by a sudden load change, magnetic coupling and the energy storage in a cable during a short circuit are studied in this section. Two studies are carried out on the DC power supply distribution of the tracker sub-detector. The Tracker sub-system is powered by around 2000 power supplies units located 100 or 40 meters far from the detector with remote sensing to control the voltage at the FEE power terminals. Each power supply generates two very low voltages to power the FEE (+2.5 V, +1.25V) with a common power return and the high voltage (600V), which is used to bias the detector device. The front-end electronics is characterized by a very low over-voltage margin in the bias voltage, around 200 mV, which force to control accurately any transient generated in the LV line, such us load changes. The power supply units are connected to the detector using a very complex power cable where LV power wires, shielded twisted pair sense wires, shielded detector bias wires and shielded temperature sensor wires are placed together inside an aluminum shield. With this cable topology, transients generated by load changes or magnetic coupling between lines that carry different power levels may induce catastrophic failures in the FEE. The low over-voltage margin of the FEE and the environment, characterized by high radiation, where the tracker sub-detector is located limit the use of classical protection devices and force to study these transients in detail.

A final study is focused on transients generated by the energy stored in a cable during a short circuit. A large current runs in a cable during a short circuit energizing the cable. When the protection device opens the circuit, the stored energy induces an over-voltage at the end of the cable (distribution bus), which may produce serious damages to all the downstream FEE connected to the same bus.

The granularity of the DC power supply distribution system as well as the distance between the power supply units and the FEE have a direct relation to the order of magnitude of these transients, producing a direct impact in the selection of protections devices. This study is carried out in a generic power supply distribution system of the CMS detector. The main goal of this studies is to describe the characteristics of the slows transients in the DC power supply line to define the type of the test to apply to the equipment installed in this area.

7.3.2.1 The Tracker DC power distribution system

The tracker power supply system¹[10] is designed to supply power to a group of FEE with two different voltages and currents (+ 2.5 V / 11 A and + 1.25 V / 5 A) with a common power return. Also, these units supply the HV necessary to bias the detector (+600 V-10 mA). Due to constraints in the distribution channels of the detector, this long cable is divided in two sections of different lengths and wire sections. Some examples of over voltages generated by sudden load changes and magnetic coupling in one module of the power supply distribution system of the tracker detector are presented in this section. The frequency range of these transients is the order of 1 kHz-30 kHz, which allows to simplify the cable model presented in chapter 4. Equations 4.1 and 4.2 can be simplified for the tracker cable following an approximated model defined by the 'lumped' equations:

$$V_2 - V_1 = R \cdot \frac{z}{2} \cdot I_1(t) + L \cdot \frac{z}{2} \cdot \frac{d}{dt} I_1(t) \quad (7.1)$$

$$V_3 - V_2 = R \cdot \frac{z}{2} \cdot I_2(t) + L \cdot \frac{z}{2} \cdot \frac{d}{dt} I_2(t) \quad (7.2)$$

$$I_2 - I_1 = C \cdot z \cdot \frac{d}{dt} V_2(t) \quad (7.3)$$

where L,C and R are the matrices of the characteristic parameters per unit length, z is the length of the line and 1 is the beginning, 2 midpoint, and 3 endpoint of the line. Based on this simplification, each line can be represented in Psipce simulator. The simulated model corresponds to one module of the tracker detector, one power cable and one power supply unit. The module is formed by a group of FE-hybrids with 48 APVs. The nominal current consumption per line for the group is equal to 11 A for the 2.5V line and 5 A for the 1.25V line.

The LV channel of the FEE is simplified by the FE-hybrids and two identical input capacitors ($C_b = 483 \mu f$). A current source in parallel with a damping resistance is used to represent the equivalent circuit presented by the FE-hybrids at the input power terminals. The values of these resistances are estimated by measures of the

1 The tracker power supply system is described in chapter 1.

dynamic impedance of 4-APVs tracker outer barrel hybrids¹ [11]. The damping resistances for the model are equal to 0.6 Ω for the 2.5V line and to 1 $M\Omega$ for the 1.25V. The HV of the FEE is represented by a resistance of 1 $M\Omega$, which represents the high impedance of the detector, and by the HV input filter, which is represented by a resistance of 10 $k\Omega$ and a capacitor of 22 nF.

The LV power supply unit is formed by a battery (V1=6.4 V, V2 = 4.6 V), two output capacitor in parallel and two switches. The two output capacitors are identical and their nominal values are $C_{ps}=500 \mu F$. The HV power supply line is represented only by the outer capacitor, whose nominal value is 300 nf. This capacitor is charged initially to 600 V (nominal value of the HV line).

The cable model corresponds to two sections of tracker cable (one of 40 meters and the other of 60 meters). Only the three LV wires (2.5 V-1.25 V-LV common return) and two HV wires (+600V-HV return) have been included in the model. The per-unit length parameters at 11 kHz of 'section 1-40 meter' tracker power cable have been measured following the procedure explained in section 4.3.1. Pspice parameters of the lumped model are calculated based on these measurements. The values for the second section have been estimated from the values of section 1 in which the values of L and C have been kept constant changing only the resistance of the cable. All of these values are shown in table 7.3 and 7.4. The skin effect has not been considered in this analysis. The validation of the cable model presented is shown in appendix B.

Inductance	$\frac{\mu H}{m}$	Section 1 - 40 m Pspice lump values	Section 2 - 60 m Pspice lump values
L11	0.424	8.48 μH	12.72 μH
L22	0.632	12.64 μH	18.96 μH
L33	0.501	10.02 μH	15.03 μH
L44	1.188	23.76 μH	35.64 μH
L55	1.176	23.52 μH	35.28 μH
L12	0.272	k12 = 0.525	k12 = 0.525
L13	0.224	k13 = 0.486	k13 = 0.486
L14	0.225	k14 = 0.317	k14 = 0.317

Table 7.3 Pspice inductance values of tracker power cable - MSC (LV and HV wires).

¹ FE-hybrids curves are shown in appendix B

7.3. Surge or slow transients

Inductance	$\frac{\mu H}{m}$	Section 1 - 40 m Pspice lump values	Section 2 - 60 m Pspice lump values
L15	0.207	k15 = 0.293	k15 = 0.293
L23	0.235	k23 = 0.417	k23 = 0.417
L24	0.328	k24 = 0.378	k24 = 0.378
L25	0.312	k25 = 0.361	k25 = 0.361
L34	0.373	k34 = 0.483	k34 = 0.483
L35	0.358	k35 = 0.466	k35 = 0.466
L45	0.668	k45 = 0.565	k45 = 0.565

Table 7.3 Pspice inductance values of tracker power cable - MSC (LV and HV wires).

Capacitance	$\frac{nF}{m}$	Section 1 - 40 m Pspice lump values	Section 2 - 60 m Pspice lump values
C11	0.163	6.52 nF	9.78 nF
C22	0.187	7.48 nF	11.22 nF
C33	0.291	11.64 nF	17.46 nF
C44	0.061	2.44 nF	3.66 nF
C55	0.062	2.48 nF	3.72 nF
C12	0.040	1.6 nF	2.4 nF
C13	0.046	1.84 nF	2.76 nF
C14	0	0 nF	0 nF
C15	0	0 nF	0 nF
C23	0.005	0.22 nF	0.33 nF
C24	0	0 nF	0 nF
C25	0	0 nF	0 nF
C34	0	0 nF	0 nF
C35	0	0 nF	0 nF
C45	0.0183	0.732 nF	1.09 nF

Table 7.4 Pspice capacitance values of tracker power cable - MSC (LV and HV wires).

7. Susceptibility to transient perturbation

Resistance	$\frac{m\Omega}{m}$	Section 1 - 40 m Pspice lump values	$\frac{m\Omega}{m}$	Section 2 - 60 m Pspice lump value
R11	3.15	0.126 / 2 Ω	0.95	0.067 / 2 Ω
R22	4.65	0.186 / 2 Ω	1.78	0.125 / 2 Ω
R33	1.75	0.070 / 2 Ω	0.68	0.044 / 2 Ω
R44	24	0.96 / 2 Ω	24	1.44 / 2 Ω
R55	26	1.04 / 2 Ω	26	1.44 / 2 Ω

Table 7.5 Pspice resistance values of tracker power cable - MSC (LV and HV wires).

Figure 7.6 shows the Pspice model used in the tracker transient analysis.

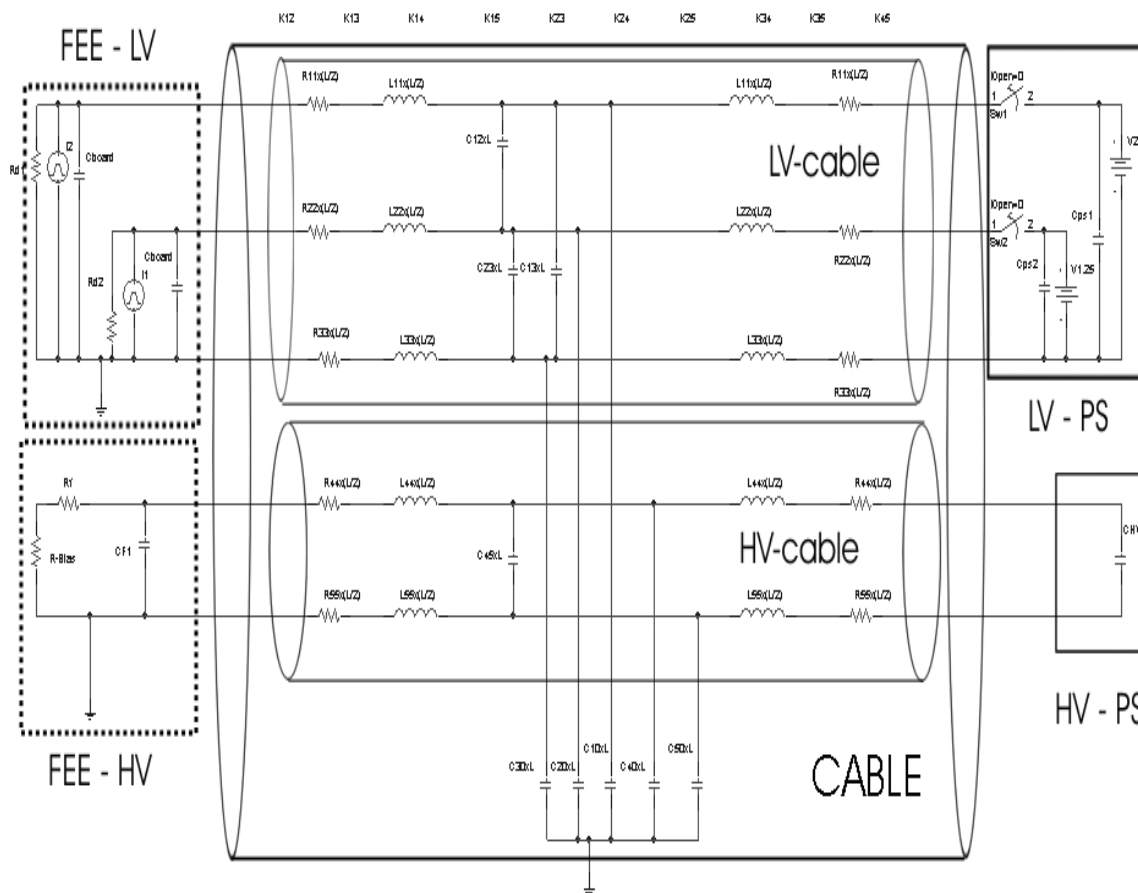


Figure 7.6: Tracker power supply distribution - Pspice circuit.

7.3.2.1.1 Sudden load changes

The first analysis presented corresponds to a sudden load change in the LV line. The power consumption in the V2.5 lines drops from 11 A to 9 A, and from 5 A to 0 A in the V1.25 line. This change of load produces an over voltage at the end of the line (FEE), generated by the energy stored in the cable and the high value of the voltage of the power supplies, which is necessary to compensate the voltage drop along the cables. The reaction of the closed-loop system against this transient cannot be faster than hundreds of μs because of the long length of the cable and the high value of the filter capacitors limits the bandwidth of the system. Figure 7.7 shows the transient generated in the LV lines under such conditions. The voltage at the FEE level pass the maximum over voltage recommended by the manufacturer of the APV25, which is around 2.8 V, producing the destruction of the FEE.

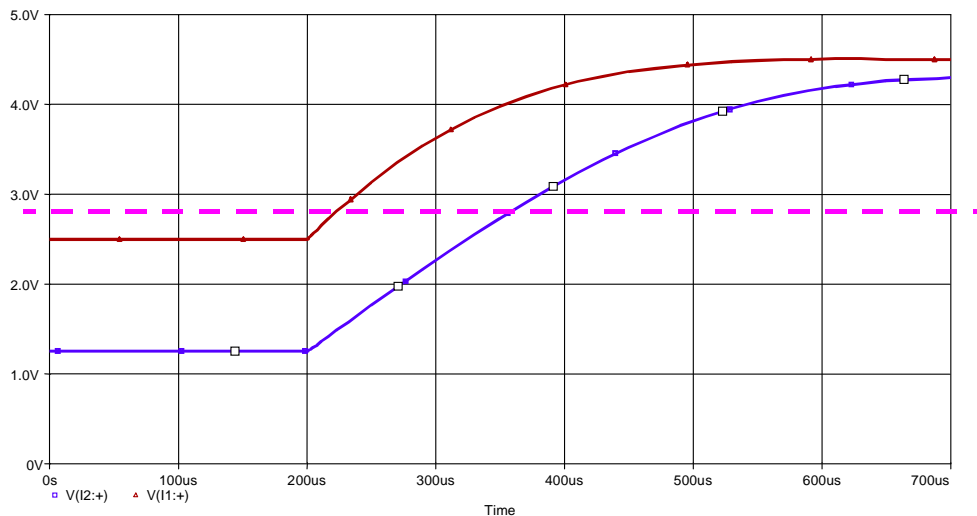


Figure 7.7: Simulation results of Over voltage on the V1.25 and V2.5 line in the Tracker sub-system generated by a load change of 11A to 9A-V2.5 line and 5 to 0 -V1.25 line.

One possible solution to avoid the destruction of the FEE by over voltage could be to open the power supplies when a transient is detected, and leave the circuit in open loop (un-regulated mode). However, the high value of the voltage of the power supplies necessary to compensate the voltage drop along the LV cables forces the transient to pass above the maximum value valid for the FEE. This phenomenon appears also in the case that bigger values of the capacitor at the input of the FEE are chosen. Figure 7.8 shows the over voltage generated for different values of the FEE capacitors ($C_b = 483 \mu f$, $C_b = 600 \mu f$ and $C_b = 1000 \mu f$).

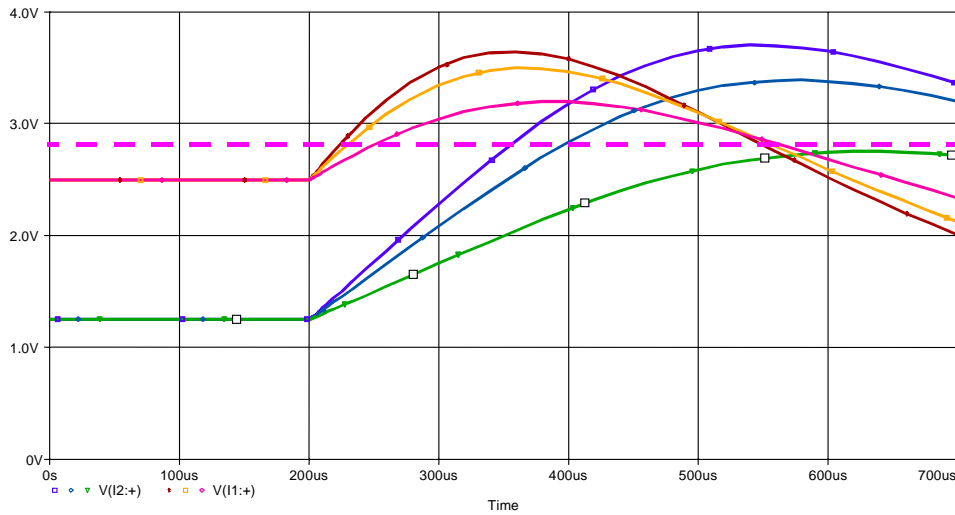


Figure 7.8: Simulation results of over voltage on the V1.25 and V2.5 line in the tracker sub-system generated by a load change of 11A to 9A-V2.5 line and 5 to 0 -V1.25 line for different values of FEE capacitors.

Other possible solution could be to place TVS (transient voltage suppressors) to absorb the transient and avoid the damage of the electronics. The energy that this device has to absorb during the transient is relatively small. However, there are two very important constraints that make it quite difficult to use them. First of all, the TVS should have a nominal voltage of 2.5 V, with maximum clamp voltage of 2.8 V, and second, this device has to be a RAD tolerant device, as the tracker is placed in an area with high radiation. Both characteristics force the device to be a custom design.

The problems pointed above force us to find other solutions to suppress the transients. The solution has to be focused on the design of power supply unit. One possible solution could be to use 2 quadrant power supply units. This type of units allows to apply a negative voltage at the output of the power supply when a transient is detected after a sudden change of load. This negative voltage accelerates the discharge of all energy stored in the cable decreasing, substantially, the maximum value of the voltage transient. Another solution, focused on the design of the power supply unit, could be to change the capacitor at the output of the power supply to a very small one (lower than $1 \mu F$). The function of this capacitor is to change the resonance frequency of the circuit. When a change of load is detected, the power supply unit opens and the cable inductance resonates with this capacitor. If a large value is selected for this capacitor (as the previous example presented), the over voltage pass the maximum value valid for the FEE. However, if a small value is selected for this capacitor, the transient response of the cable is fast discharging the excess of energy and keeping the maximum value of the transient voltage at the input of the FEE lower than the maximum value tolerated. Figure 7.9 shows the

evolution of the voltage on the FEE for different values of the output capacitor of the power supply unit. ($C_{ps} = 1 \mu f$, $C_{ps} = 100 \mu f$ and $C_{ps} = 500 \mu f$). This solution can be used in combination with a resistance at the power supply, which discharges the remaining energy in the system during the last section of the transient.

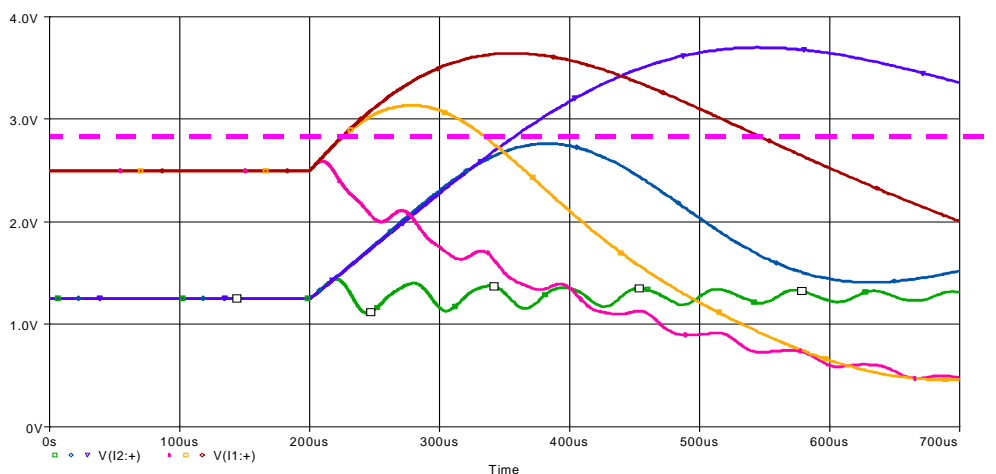


Figure 7.9: Simulation results of over voltage on the V1.25 and V2.5 line in the tracker sub-system generated by a load change of 11A to 9A-V2.5 line and 5 to 0 -V1.25 line for different values of PS capacitors.

7.3.2.1.2 Magnetic coupling transients

Cables or bundles of cables, which are placed in the same area, are susceptible to over-voltages induced by high current changes in one or more of these cables. These currents produce low frequency magnetic fields, which can be coupled to adjacent cables causing bad performance of the equipment connected to these cables. Different short-circuits in the HV system of the tracker sub-detector has been chosen to present the problems induced by these transients. When a short circuit occurs in the HV system, the PS unit reacts very fast and opens the power units. From that moment, the HV circuit becomes an un-regulated system in which the power supply is represented by the output capacitor, which is charged to 600 V. This circuit has been implemented in Pspice (figure 7.6) to study the influence of two different HV short circuits in the distribution line.

The first case corresponds to a balanced short circuit between both HV cables at the input of the HV-FEE (a short circuit in the HV input capacitor). In this case the short circuit current returns to the power supply through the HV return line of the cable. The second transient corresponds to an unbalanced short circuit at the input of the HV-FEE. In this transient the current cannot return to the power supply through the same cable¹. This kind of transient is not frequent and depends on the granularity and grounding layout of the tracker detector, which has not been decided yet.

7. Susceptibility to transient perturbation

However, for the present example it has been considered as a potential problem because it helps to understand better the problem of mixing cables, carrying different current levels in the same bundle.

The simulated model corresponds to a PS distribution unit of layer 4 of the tracker outer barrel (TOB). This unit supplies power to 24 APVs and the nominal current consumption per line is approximately 5 A for V2.5 line and 1 A for V1.25 line. The FEE-hybrid LV channel is simplified by two identical input module capacitors ($C_b=160 \mu f$) and by a current source in parallel with a damping resistance. The damping resistance for the model in the V2.5 line is equal two 1.1Ω and for the V1.25 is equal to $1 M\Omega$. Figure 7.10 and 7.11 represent the short circuit current in the HV line and the induced voltage at the 2.5V and 1.25V lines for balanced and unbalanced short-circuits, respectively.

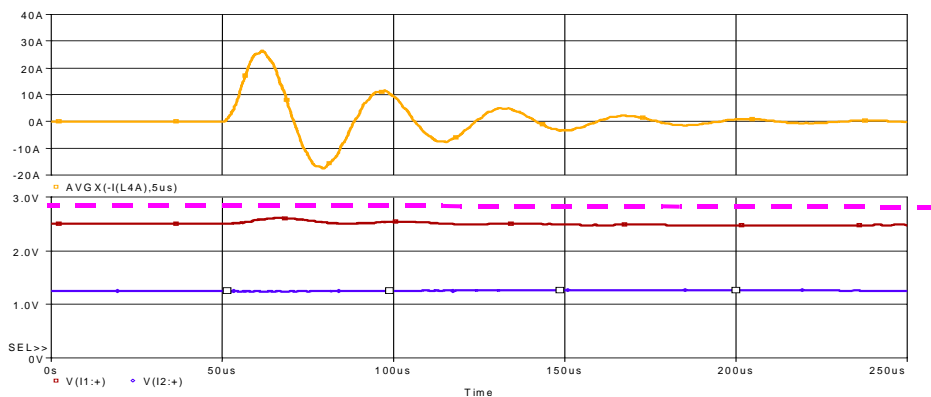


Figure 7.10: *Balanced short circuit current in the HV line and voltage at the 2.5V and 1.25V lines at the input of the FEE*

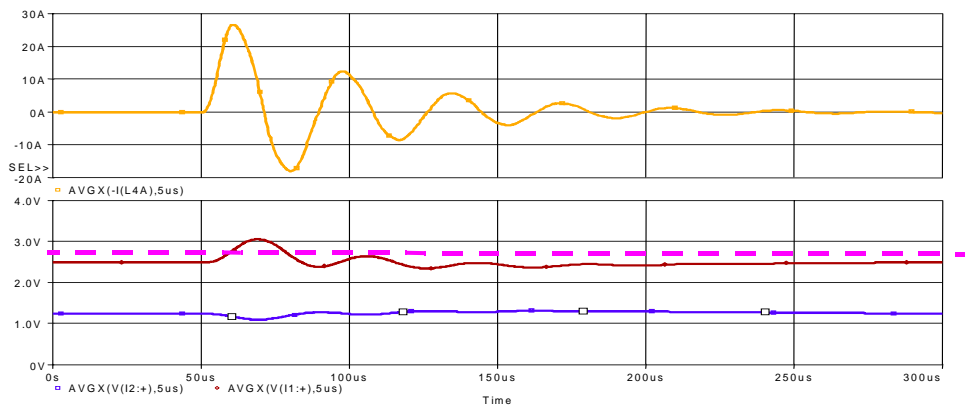


Figure 7.11: *Unbalanced short circuit current in the HV line and voltage at the 2.5V and 1.25V lines at the input of the FEE.*

1 In this case the current 'return' presents the same resistance as the normal one to have the possibility to compare the effects in both configurations.

7.3. Surge or slow transients

This transient cannot be easily cancelled using TVS or regulated by the PS units, as it was the case in the previous section. The easiest way to control the magnitude of the transient is to limit the coupling energy involved in the transient, which is defined by the capacitor at the output of the HV power supply unit and the geometrical configuration of the wires that belong to the same bundle. The geometry of the cables sets the value of the mutual inductance and defines the amount of energy coupled from the primary circuit (noise source - HV circuit) to the secondary circuit (noise victim - LV circuit). It is always recommended to separate cable bundles that work with different level of power.

The capacitor at the output of the power supply defines the maximum amount of energy present in the transient. This energy corresponds to the energy stored in the capacitor as it is shown in equation 7.4. In the present case, the HV is constant and equals to 600 V. The value of the HV output capacitor limits the value of this energy.

$$E_c = \frac{1}{2} \cdot C \cdot V^2 \quad (7.4)$$

Figure 7.12 shows the maximum voltage in the V2.5 line and maximum HV short circuit current for different values of the HV output capacitor for a balanced (figure 7.12a) and unbalanced short-circuit (7.12b).

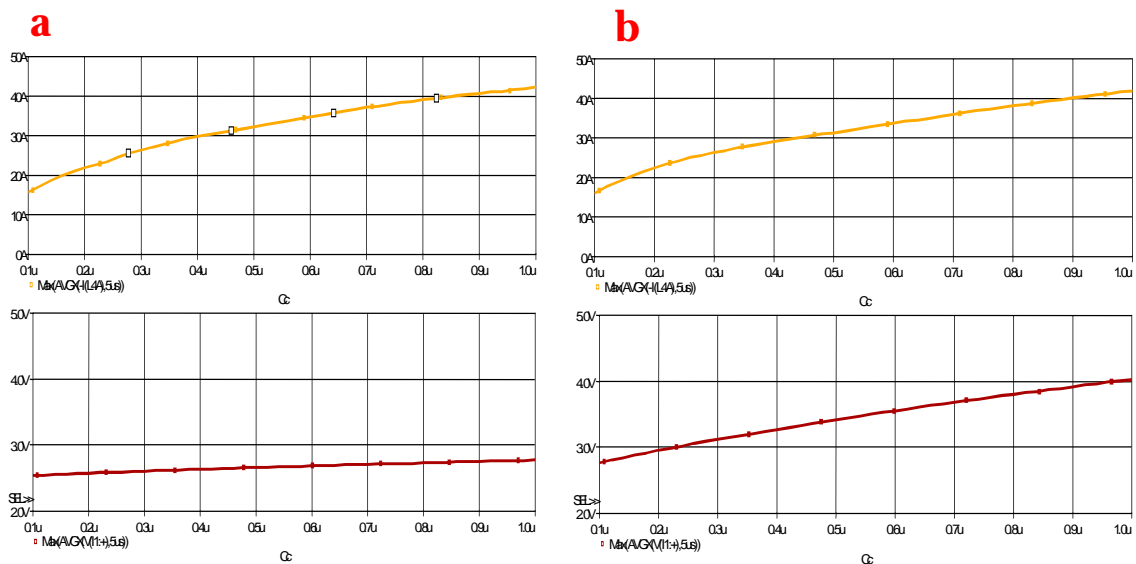


Figure 7.12: Maximum voltage on the 2.5 V line and shortcircuit current in the HV line for different values of HV output capacitor (balanced and unbalanced shortcircuit).

The worst case corresponds to the un-balanced short circuit. For the present example, limiting the value of the capacitor could be good enough to protect our system. However in some cases if the neighbor circuit presents high-energy transients (power line with fuses), the energy involved in the transient may be higher than the previous case, resulting in a serious problem for the detector. This

issue can be solved grouping the cables in bundles according to the power level transmitted and separating these bundles by a safe distance to ensure a low energy coupling among cables. In the literature it is possible to find a variety of papers [12][13][14] where this problem is studied in detail.

7.3.2.2 Multi-module DC distribution

Transients generated in a generic DC low-voltage distribution system are studied in this section. The topology analyzed corresponds to a distribution line carrying high current to a distribution bus where several groups of FEE are connected to the bus in parallel. This study addresses the implications of the detector granularity in the design of power supply distribution system and the selection of protection devices.

7.3.2.2.1 Model

As example of a generic power supply distribution system, we choose one which feeds 4 groups of generic FEE units at + 6.5 V. The power is supplied to the FEE unit through a long shielded power cable of 20 meters. Each FEE group consumes the same amount of current. For the present study, we assume that a short-circuit occurs at the input of one of the units. This failure blows the fuse protecting the faulted path. The length of the line is varied between 20 m, 50 m and 100 m, and the power consumption per unit changes between 5 A, 15 A and 25 A (total current - 20 A / 60 A / 100 A) in order to study the influence of these parameters in the short circuit characteristics (energy, short circuit current and duration). A schematic of the model presented is shown in figure 7.13.

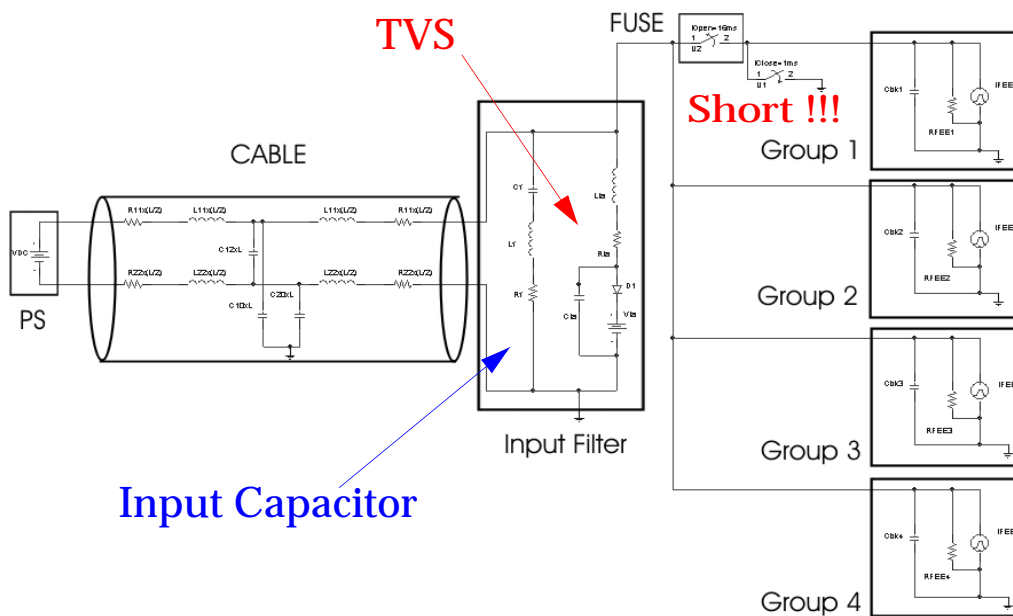


Figure 7.13: Generic power supply distribution system - Pspice circuit.

Although there are some papers [15] defining some fuse models for over current protection, we simulate during this study the fuse operation by means of switching devices included in the Pspice libraries. A close-switch is used to create the short circuit and an open-switch is used to simulate the fuse opening. A delay between both switches is included to simulate the opening time of the fuse. The opening time and resistance of the fuses are selected based on real fuse characteristics. The fuses selected (257075, 257020 and 257040) are fast acting fuses types from *Littlefuse Company* and the main characteristics of these fuses are given in appendix B.

Each FEE group is simplified by a current source in parallel by a damping resistance and a capacitor. The damping resistance for the model is equal to 80Ω and the capacitor is equal to $30 \mu F$. At the distribution bus a filter with several capacitors of $3000 \mu F$ is placed to remove part of the perturbing signals on the power supply line. The number of these capacitors varies between 1 for the 20 A line, 2 for the 60 A line and 4 for the 100 A line. The parasitic components of this capacitor have been included in the model. Their values are based on measurements performed on real filter capacitors of the HCAL sub-system.

The duration of these transients are of the order of μs , which allows to use the lumped model for the distribution line presented in the previous section. The cable model used corresponds to the HCAL power cable. The per-unit length parameters of the cable are calculated based on measurements performed at 10 kHz and used in the Pspice simulation.

During the present study the per unit length resistance values of the cable are modified when the length of the cable and/or the current increases in order to keep a constant voltage drop of 1.4 volts along the cables. That means that the section of cable is changed, accordingly, but the per unit length values of L and C keeps constant. This assumption is not true in real applications because if the section of cable changes the geometric configuration of cable changes and hence the per unit length values of the L and C. Nevertheless this assumption can be considered valid due to the goal of the study is to show the problematic with different configurations and not to estimate the exact value of the transient. The per unit length L, R, C and Pspice parameters are given in tables 7.6 to 7.7 and 7.8.

Inductance	$\frac{\mu H}{m}$	20m	50m	100m
L11	0.2433	$\frac{4.686}{2} \mu H$	$\frac{11.715}{2} \mu H$	$\frac{23.43}{2} \mu H$
L22	0.2426	$\frac{4.852}{2} \mu H$	$\frac{12.13}{2} \mu H$	$\frac{24.26}{2} \mu H$
L12	0.0097	k12=0.04	k12=0.04	k12=0.04

Table 7.6 Pspice and per-unit length inductance values of the power distribution cable.

Capacitance	$\frac{nF}{m}$	20 m nF	50 m nF	100 m nF
C11	0.1880	3.76	9.4	18.8
C22	0.1927	3.854	9.635	19.27
C12	0.0412	0.824	2.06	4.12

Table 7.7 Per unit length and Pspice capacitance values of the power distribution cable.

Resistance (Ω /km)	20 m	50 m	100 m
20 A	1.75	0.7	0.35
60 A	0.583	0.233	0.116
100 A	0.35	0.14	0.07

Table 7.8 Per unit length resistance values of the power distribution cable.

Resistance (R11 = R22)	All lengths
20 A	$\frac{0.035}{2} \Omega$
60 A	$\frac{0.011}{2} \Omega$
100 A	$\frac{0.007}{2} \Omega$

Table 7.9 Pspice resistance lumped values of power distribution cable.

7.3.2.2.2 Short circuit transient

When a short circuit occurs in one FEE group, major disturbances appear on the cable and at the distribution bus bar level. The current in the cable increases up to a maximum value fixed by the resistance of the cable and the short circuit contact resistance. Afterwards, for a short period of time this current remains steady in the

7.3. Surge or slow transients

cable until the fuse melts. This time depends on the clearing time of the fuse, which depends on the fuse selected. During this period, the high current causes a voltage dip at the input distribution board, where all other FEE groups are connected. Later, when the fuse melts, the cable current decreases and an over voltage appears at the input distribution board. This over voltage may cause malfunction or the destruction of the FEE connected to the same input distribution bus. Figure 7.14 shows the current in the cable and the distribution bus voltage during the short circuit for the case of a cable of 20 meters, carrying a nominal current of 60 amps.

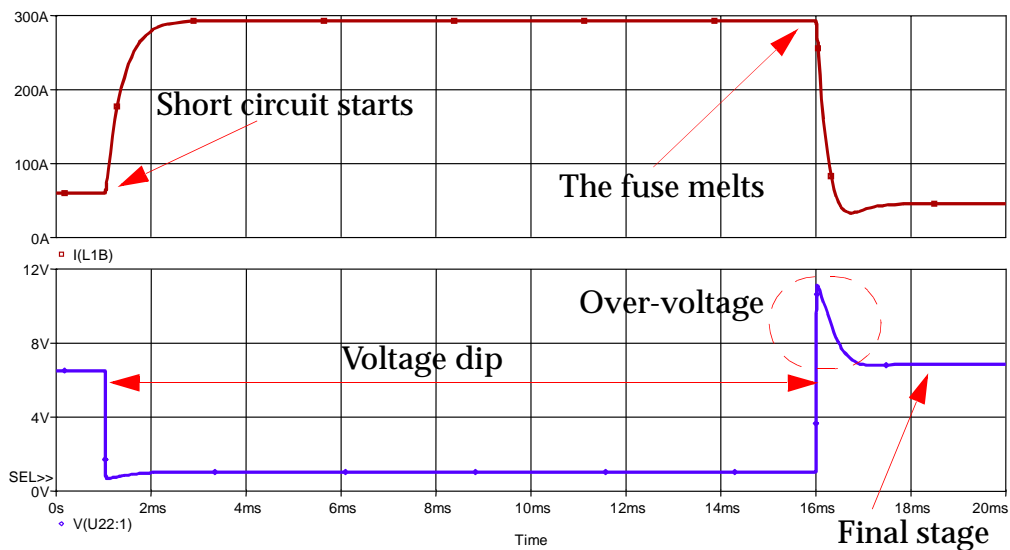


Figure 7.14: Cable current and FEE input voltage during a short circuit.

Several aspects are considered to characterize the transient during a short circuit:

- Short circuit current and voltage dip value.
- Over voltage (Value & duration).
- Excess of stored energy involved when the fuse melts.

The over voltage waveform at the time the fuse opens is characterized by its maximum value and duration. This duration is defined by the rise time value (t_r) and half time value ($t_{50\%}$), which is considered as the time difference between the moment in which the fuse opens and the moment in which the voltage decays to 50% of the voltage difference between maximum voltage and the final voltage. These values are given in detail figure 7.15.

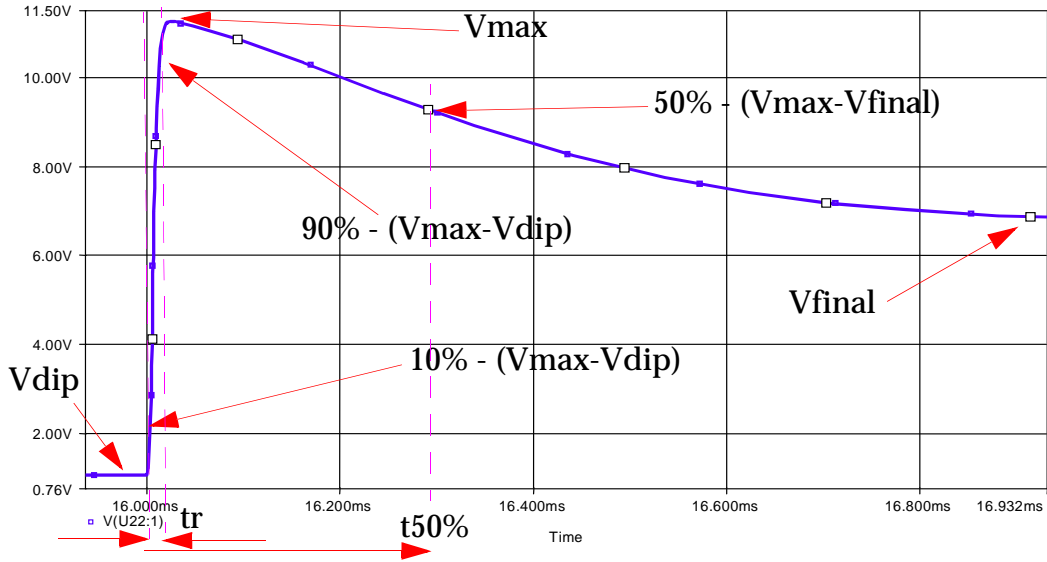


Figure 7.15: Over-voltage parameters

The excess of energy involved during the transient when the fuse opens helps to define and select the transient voltage suppressor device (TVS). This energy is defined as the difference between the energy stored in the cable and in the distribution bus capacitors when the fuse opens and the final stored energy in steady state.

$$Exc-E = \left(\frac{1}{2} \cdot I_{cc}^2 \cdot L + \frac{1}{2} \cdot V_{dip} \cdot C_d \right) - \left(\frac{1}{2} \cdot I_f^2 \cdot L + \frac{1}{2} \cdot V_f \cdot C_d \right) \quad (7.5)$$

where;

- I_{cc} is the short circuit current.
- V_{dip} is the voltage dip at the distribution bus.
- I_f is the current in the cable during the final steady state.
- V_f is the distribution bus voltage during the final steady state.
- C_d is the total capacitance of the distribution board
- L is the cable inductance, which is defined in this circuit as:

$$L = (L11 + L22 - (2 \cdot L12)) \cdot Lg \quad (7.6)$$

where Lg is the cable length. Table 7.10 summarizes all the parameters mentioned before:

Cable length	Cable Current			Distribution board voltage					Energy
	I_o (A)	I_{cc} (A)	I_f (A)	U_{max} (V)	t_r μs	$t_{50\%}$ μs	V_{dip} (V)	V_f (V)	$Exc.E$ (mJ)
20m	20	102	15	7.3	13	47	0.75	6.84	-
	60	293	45	11.25	9.27	322	1.06	6.84	245
	100	494	75	11.33	59	724	0.98	6.84	813
50m	20	102	15	8.07	18	564	0.75	6.84	46
	60	293	45	14.35	107	807	1.06	6.84	817
	100	494	75	16.84	295	1240	0.98	6.84	2438
100m	20	102	15	10.49	100	903	0.75	6.84	163
	60	293	45	19.52	289	1220	1.06	6.84	1776
	100	494	75	23.7	579	1810	0.98	6.84	5121

Table 7.10 Transient parameters during a short circuit in the generic PS distribution system

Based on the values shown in the table, it can be observed that the layout and granularity of the detector has a big impact in the transients generated by fuses in the detector. For a constant length, the higher the nominal current, the higher are over voltage and stored energy during the fault. For a constant current, the longer the length, the higher are the over voltage and stored energy during the fault.

The protection of the system against the over-voltage transients can be achieved by TVS for some sub-systems located in areas where the radiation level is not very high and the over-voltage margin of the FEE is relative large. The TVS is a silicon avalanche device and the more important parameters in its selection are:

- Reverse standoff voltage (V_r). This parameter should be equal to, or larger than, the peak operating level of the circuit (or part of the circuit) to be protected.
- The peak pulse current (I_p) is the maximum current that the TVS can withstand without damage. This value can be determined by dividing the peak transient voltage by the source impedance.
- The maximum clamping voltage (V_c) is the peak voltage that will appear across the TVS when subjected to the peak pulse current (I_p), based on a 1 ms exponential. This waveform is a 10/1000 microsecond waveform. This parameter basically fixes the maximum energy absorbed by the TVS.

The selection of the TVS involves the knowledge of the parameters such as limiting voltage, surge current and maximum energy dissipation.

The TVS data sheet, generally, are referred to a specific surge test that should be taken into account to select the TVS that fits better to our requirements. Based on the result shown in table 7.10 two TVS of 1500W and 5000 W with a reverse stand-off voltage of 6.5V (1.5KE7.5A and 5KP6.5A) from *Littlefuse* are selected for this analysis. The main characteristics of both TVS are for the 1500W device a maximum surge current of 132A and maximum clamping voltage of 11.3V referred to a current waveform of 10/1000 μs , while for the 5000W device a maximum surge current of 407A and maximum clamping voltage of 12.3 V referred to the same current waveform. These waveforms describe maximum abortion energy of these devices of 2 Jules and 7 Joules, respectively, which fits quite well with the requirements of the transients presented in the simulation model.

The circuit is analyzed including the selected TVS to verify the validity of the selection criteria presented above. For that purpose the TVS is modeled in Pspice circuit including its parasitic components. It can be modeled [16] using a resistance and inductance in series with a battery in parallel with a capacitor. The simulations presented have been performed with the first TVS selected, the 1.5KE7.5A. The model parameters of this TVS are $R_{ta} = 1.9m\Omega$, $L_{ta} = 11nH$, $C_{ta} = 10pf$ and $V_{ta} = 6.8V$. The Pspice model validation [17][18] is given in appendix B. During this simulation, the current through the TVS, the voltage, the power and the energy and the voltage have been calculated using Pspice simulation.

Figure 7.16 shows the simulated current and the voltage supported by the TVS during a short-circuit in the system in which the length of the cable is 50m and the nominal current is 60 A.

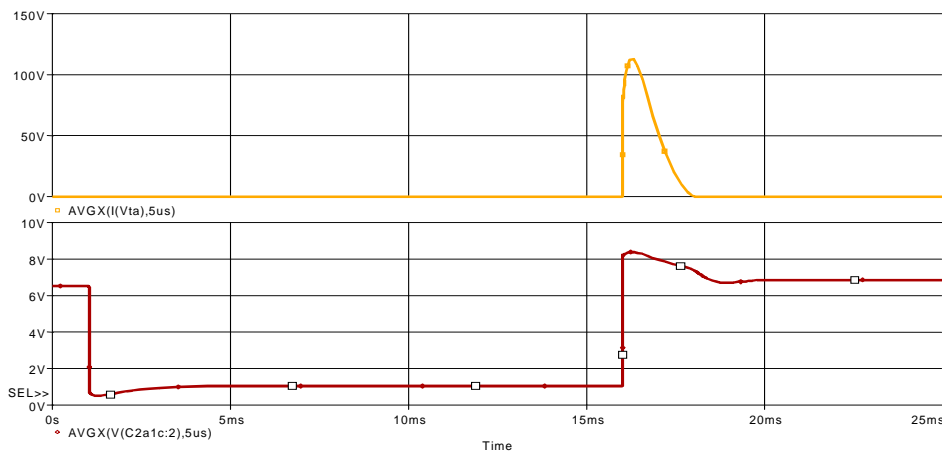


Figure 7.16: Current and voltage in the TVS during a short circuit for a 50 m long cable and nominal current of 60 A.

7.3. Surge or slow transients

Table 7.11 summarizes the simulated data of the TVS-1.5KE7.5A performance for some of fault cases analyzed previously.

Cable length	Cable current		TVS performance data			
	I_o (A)	I_{cc} (A)	I_{max} (A)	V_{cmax} (V)	P_{max} (W)	Energy dissipated TVS (mJ)
20m	60	293	80	8.13	610	205
	100	494	118	8.42	1000	712
50m	20	102	6	7.57	45	16.5
	60	293	112	8.38	945	913
100m	20	102	20	7.76	194	155

Table 7.11 TVS performance data during the short circuit.

The presence of high currents during the short circuit may be solved using current limiters or electronic fuses, which limits the maximum value of the current during the short circuit to a 30-50% of the nominal current. Table 7.12 summarizes the energy involved during the transient if fuses are replaced by current limitators.

Cable length	Cable Current		Energy
	I_o (A)	I_{cc} (A)	Exc.E (mJ)
20m	20	26	-
	60	78	-
	100	130	-
50m	20	26	-
	60	78	16.24
	100	130	69.41
100m	20	26	-
	60	78	63.19
	100	130	198.44

Table 7.12 Transient parameters during the short circuit in the generic PS distribution system with current limitators.

Based on the previous analysis, some power distribution layouts are characterized by large currents and stored energy during the short-circuit. The use of TVS as the only solution to avoid over-voltages on the power distribution lines is not probably the best strategy considering the radiation environment and the reduced space to locate the protection device. In those cases, the selection of an optimal granularity of the detector in combination with electronic fuses can avoid the use of large TVS.

7.3.3 Surge test for the CMS detector.

7.3.3.1 Introduction

Surge immunity tests are used to evaluate the performance of the equipment in presence of slow transients applied to the input/output cables and to define the protection devices necessary to attenuate its effects into the equipment. The surge immunity tests use generators with defined waveforms and test set-ups to achieve repeatable tests [19][20][21] that are representative of a set of characteristic transient that appears in the system. It is important to realize that these tests do not necessarily simulate exactly the real electromagnetic disturbances present in the system but they give the necessary information about its effect in the equipment to qualify its performance and robustness to a set of transient perturbations.

There are a great variety of standards that defines different normalized procedures to evaluate the immunity of the equipment to these transients. The two most common tests are defined by the standards EN-61000-4-5 and ANSI/IEEE C62.41-1980 [22]. These standard procedures define three normalized waveforms, which are divided in bidirectional waveforms and unidirectional waveforms. Figure 7.17 shows the wave-shape of a bidirectional waveform. This wave is based on the original voltage wave that was proposed by ANSI/IEEE C62.41-1980. It is representative of general surge voltages appearing in indoor power distribution systems. This wave shape rises in $0.5 \mu\text{s}$ and decays while oscillating at 100 kHz ('called ring wave'), each peak being about 60% of the presiding peak.

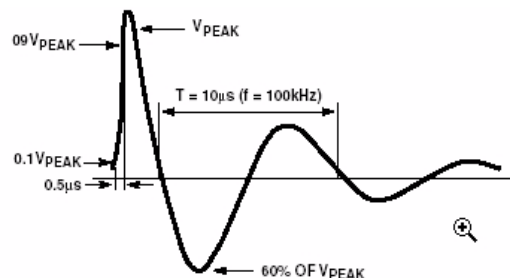


Figure 7.17: Bidirectional waveform for the surge immunity test.

7.3. Surge or slow transients

The unidirectional waveform is more typical for outdoor or unprotected systems, where the attenuation has not taken place and substantial energy or current is still available. One of these unidirectional impulse waveforms specified by the standards is shown in figure 7.18. This impulse is defined by the combination of two waveforms, $1.2/50 \mu s$ voltage impulse in open-circuit and a $8/20 \mu s$ current impulse into a short circuit, leading to its common name: 'the combination wave'.

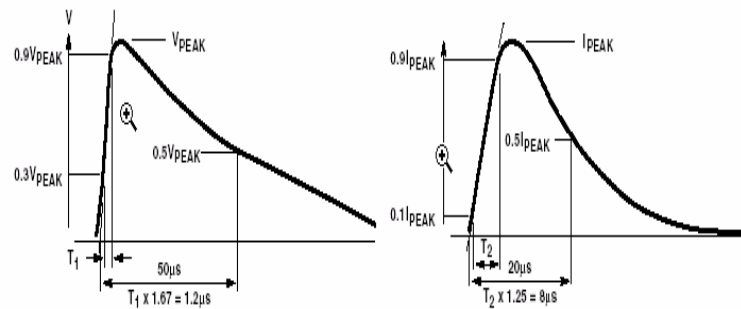


Figure 7.18: Unidirectional waveform for the surge immunity test.

The other unidirectional waveform is similar to the previous one but this is only specified by the open circuit voltage ($10/700 \mu s$) according to the standard publications [9].

A surge generator is used to inject the transient to the circuit. A coupling-decoupling network (CDN), which is located in the generator, is used to transfer the energy into the circuit. The amount of energy and waveform characteristic depends on the elements of this network as well as the internal impedance of the generator. Therefore all the components of the CDN and the internal impedance of the device are specified by the standards [9]. The CDN has an additional function that is protecting the auxiliary equipment used in the test and ensuring the pulse go into the equipment under test and not to other parts of the system Figure 7.19 shows the set-up used in this test.

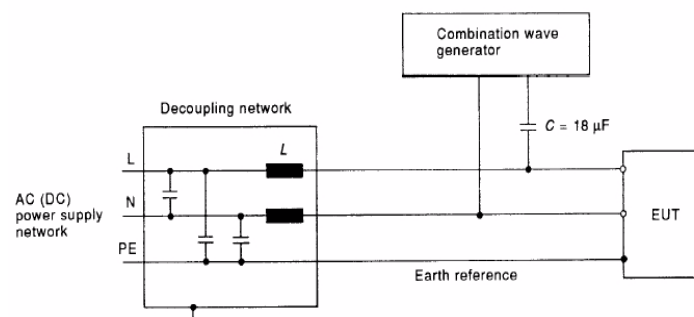


Figure 7.19: Typical set-up for the surge immunity test

Typical values of these network components are generally a capacitor of $9 \mu F$ or $18 \mu F$ for the capacitor, 10Ω or 40Ω for the resistor and an inductance of some mH.

The normalized waveform to be applied during the tests of the sub-detector electronics has to be representative of the transient perturbations characteristic of the different areas of the CMS detector. The definition of this normalized waveform to be used is important for the design of protective devices and also will define the reliability and cost of the system. Wrong surge test characteristics, like excessive duration of the perturbation, large voltage perturbation or very low source impedance, force a high-energy requirement on the protection device or transient suppressor.

7.3.3.2 Characterization of the HCAL FEE to surge test.

The goal of this test is to study the effect on the internal voltage distribution of surge perturbations. The FEE used for RF conducted noise immunity test has not been connected to the backplane because, at the time the test was performed, the destruction of this equipment implied serious problems for the project as it was the only prototype of the HCAL FEE.

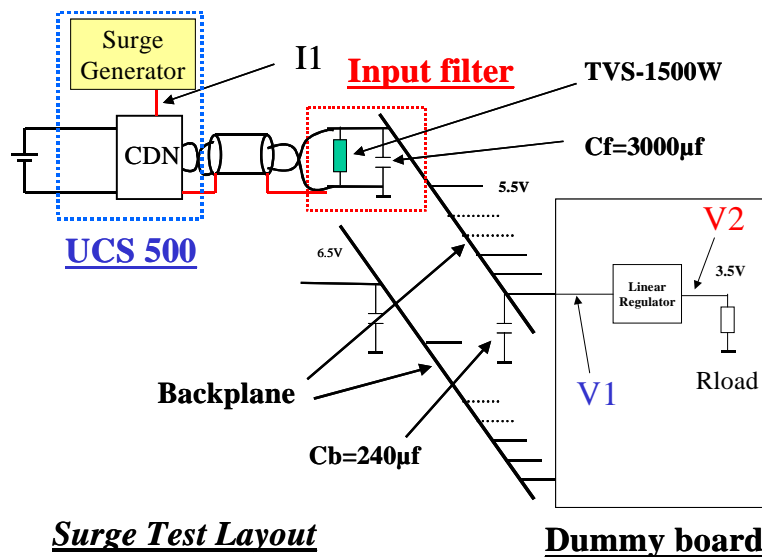


Figure 7.20: Surge test layout for the HCAL FEE.

Figure 7.20 shows the test layout. Unidirectional 1.2/50 voltage impulse waveforms of 200V peak with both positive and negative polarities in DM and CM configuration is applied to the system where the FEE is now replaced by dummy boards. Each dummy board consists of filter capacitors, the LV regulator and resistors to simulate the consume of the FEE board. The input power filter has a

transient voltage suppressor (TVS) of 1500 W and nominal voltage of 7.5 V. The backplane voltage (V1), the voltage at the output of the LV regulator (V2) as well as the current injected into the system (I1) has been measured using a digital Tektronix scope and a differential voltage probe. Figure 7.21 depicts the dummy board, while figure 7.22 shows a picture of the RBX layout during the test.

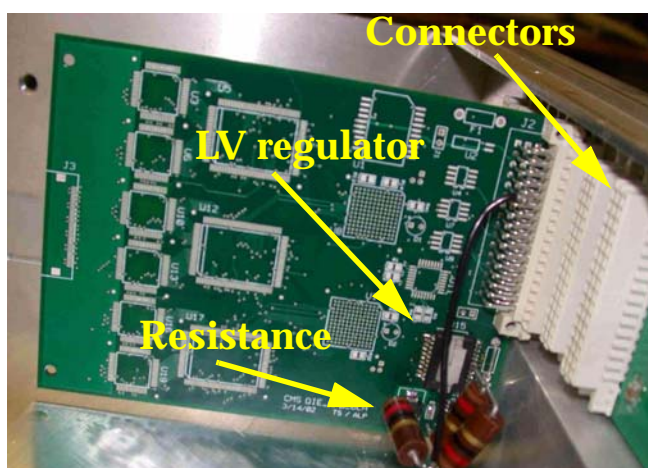


Figure 7.21: Dummy board layout during HCAL-FEE surge test.

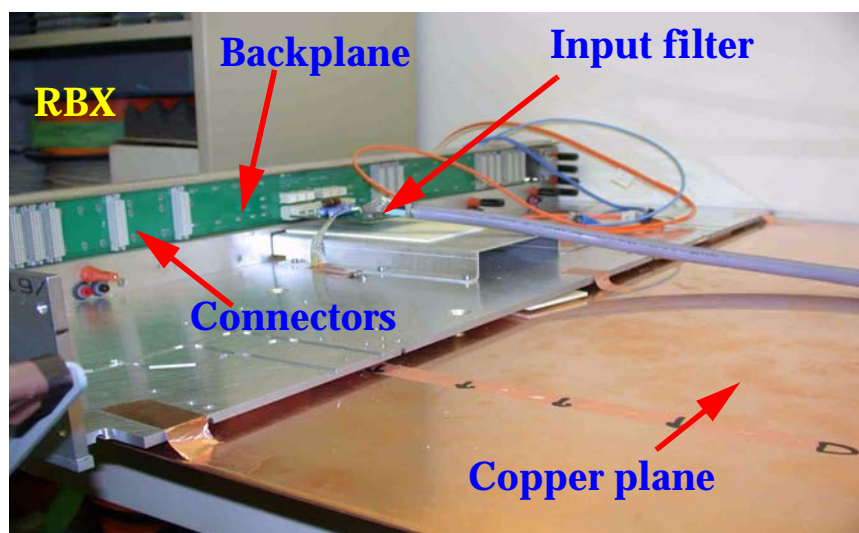


Figure 7.22: RBX layout and input filter during HCAL-FEE surge test.

7.3.3.2.1 DM surge immunity test.

A voltage surge of 200 V with both positive and negative polarities is applied to the system. The voltages are applied in DM and the current is injected through a capacitor of 18 μf without any resistance in series. This makes the total value of the

source impedance equal to 2 ohms. The current injected has a peak of 85 A for the positive polarity and 83 A for the negative one, as it is shown in figure 7.23.

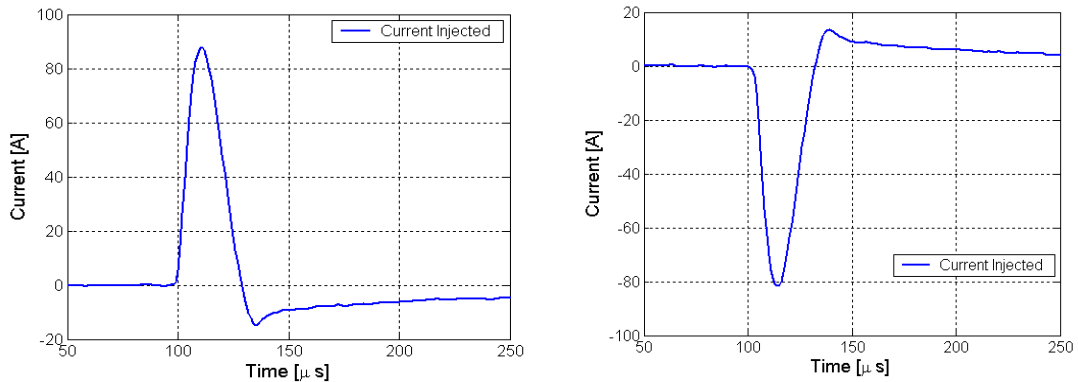


Figure 7.23: Current injected in the HCAL-FEE prototype during the DM surge test (positive and negative polarities).

The voltages at the input of the dummy board (back-plane voltage) and the output of the LV regulator when the transient is applied are shown in figure 7.24. For the positive voltage surge the system is protected without any problem. The TVS and the HF capacitor placed on the back-plane limit the peak voltage in the back-plane to 8 volts. The transient voltage is completely attenuated by the LV linear regulator giving clean 3.5V to bias the digital electronics.

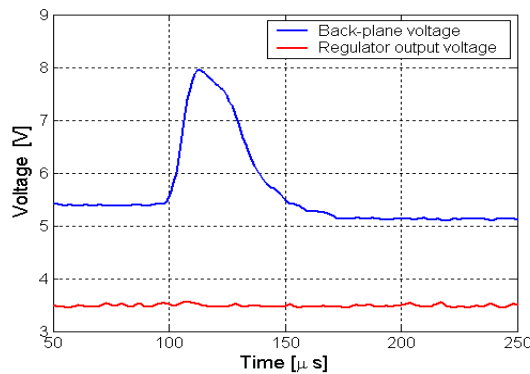


Figure 7.24: Backplane and regulator output voltage during the positive DM surge test.

For a surge with negative polarity (figure 7.25) the TVS and the voltage regulator do not work, generating on the 3.5V line a voltage dip of short duration, which could produce malfunction in the digital section.

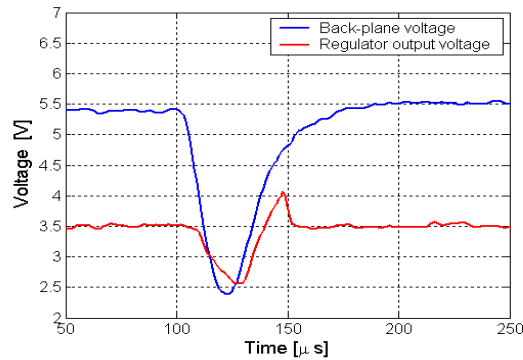


Figure 7.25: Backplane and regulator output voltage during the negative DM surge test

These effects may constitute a serious problem in the HCAL-FEE, however it is not clear that these transients appear in the CMS detector. Also, it is important to mention, that there are some TVS, which work with both polarities and the use of these devices may solve the problem.

7.3.3.2.2 CM surge immunity test.

A voltage surge of 200 V with both positive and negative polarities is applied to the system. The voltage is injected through a capacitor of $9 \mu\text{f}$ with a resistance in series of 10 ohms. This makes the total value of the source impedance equal to 12 ohms. The current injected has a peak of 15 A for the positive polarization, as it is shown in figure 7.26.

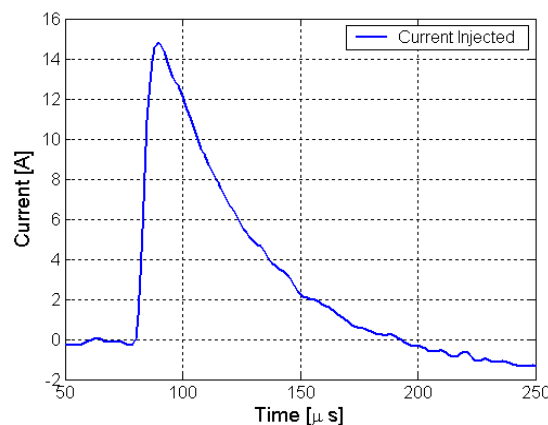


Figure 7.26: Current injected in the HCAL-FEE prototype during the CM surge test (positive polarity).

It is observed that for the same voltage applied the higher the value of the impedance the lower the value of the current. The current limitation generated by the impedance is important as it limits the over voltage generated by the current injected. This limitation causes a very low over voltage, which does not force the TVS to work and the transient is easily absorbed by the LV regulator. Figure 7.27 shows the backplane and linear regulator output voltage when a surge of 200 V in CM is applied to the dummy board.

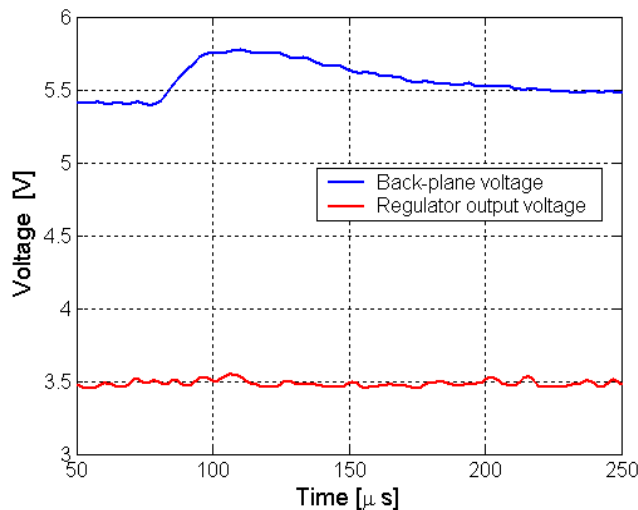


Figure 7.27: Backplane and regulator output voltage during the positive CM surge test

7.3.3.3 Protection stages for the CMS detector.

Surge transients can easily occur in the CMS detector. The amplitude, polarity and duration depend on the configuration and the layout of the power supply distribution system. It has an important impact in the selection of the protections of the system since TVSs are not ideal devices and present some parasitic parameters, which limit the amplitude of the current, power and energy absorbed by the TVS. In addition, as it has been presented in the previous sections, the transient is not totally absorbed by the TVS. The ceramic capacitors on the FEE and the LV linear regulators help to deal with these transients. This introduces an important point in the design of protections against transients, which is the protection stage.

If a transient cannot be attenuated using a single component, it is possible to combine different components and utilize their respective advantages to limit the transient in several steps. Figure 7.28 shows an example of the principle of staged protections. This example helps to limit an over voltage of 10 kV in three stages.

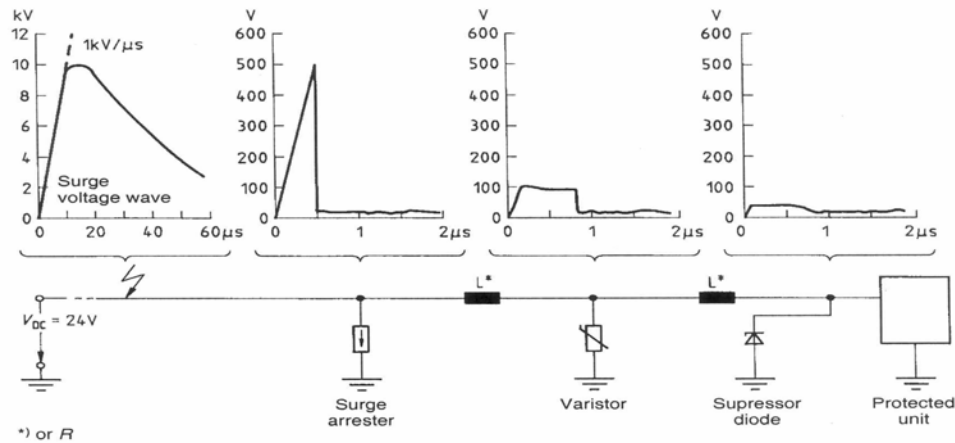


Figure 7.28: Protection stages against a surge of 10 kV

A similar system can be used to protect the FEE of the CMS detector. The first protection stage can be made at the counting room level, where TVS (surge arrestors or varistors), which are able to deal with high energy transients, can be placed. This device protects the AC-DC converters and DC-DC converters from the transients generated in the AC-400Hz line. In the case to distribute directly AC power to the periphery of the detector, these devices have to be placed on the periphery of the detector. A second protection stage is focused to protect directly the FEE. A combination of TVS, ceramic capacitors and LV linear regulators form this second protection unit. It focuses on the protection of the DC power supply line. However a bad selection on the distribution layout (cables bundle distributions and power supplies location), granularity (lines with high values of nominal current) and short-circuit protections (no current limitators), make it almost impossible to protect of the FEE against transients presented on this second part of the system. This will have a very important impact in terms of reliability and cost of the system.

7.4 Burst or fast transients

Electric arcs are generated between the mechanical contacts of circuit-breakers, when inductive loads like relay coils, timers, motors contactors etc. are connected or disconnected from the line. The over voltage generated between the contacts during this transient can be higher than the isolation voltage thus producing the spark re-ignition. Arc ignition and interruption leads to a burst process. This intermittent process finishes when the voltage stress presented on the switching contacts is below the electrical and thermal strength of the spark gap channel. Figure 7.29 shows the fast transient switching process.

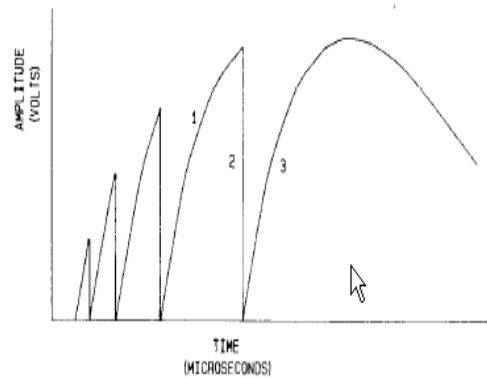


Figure 7.29: Burst effect.

This effect produces a repetitive and fast over voltage that propagates through the system and can affect the electronics devices connected to this unit. This transient is not especially important for its destructive effects but for the HF spectra content of the signal that can produce disturbances in safety devices (as electronic fuses, measurement devices or alarms) with its posterior consequences.

The fast transients contain high frequency harmonic components, which are expected to be easily attenuated as they propagate through the cables. In the CMS detector, the final location of electro-mechanical switches is not yet defined. A possible location is in the counting room (120 meters away from the detector) or at surface level (around 250 m far from the detector). Based on some studies presented in [23] these distances can produce between a 50% and 80% of attenuation of the amplitude of fast transients. This reduction in combination with the power level of these transients will produce very low and slow burst transients that can be easily filtered by HF capacitors and the LV regulator at the FEE board.

The EMC standards EN-6000-4 [24] define some test procedures to ensure the good performance of the system against this type of transients. The standard waveform into the 50 ohms load condition is characterized by a very fast rise time (5 ns) followed by a decay time of 50 ns . The test levels varies from 250 V to 5 kV and burst duration and period are also fixed by them, having values of 15 ms and 300ms respectively. Finally the repetition rate of the pulse is also defined by the standards and varies between 5 kHz and 2.5 kHz. The energy is injected into the system through a capacitor of 33 nF and the maximum energy injected into the system is limited to 4 mJ/pulse. Figure 7.30 shows the waveform defined by European standards.

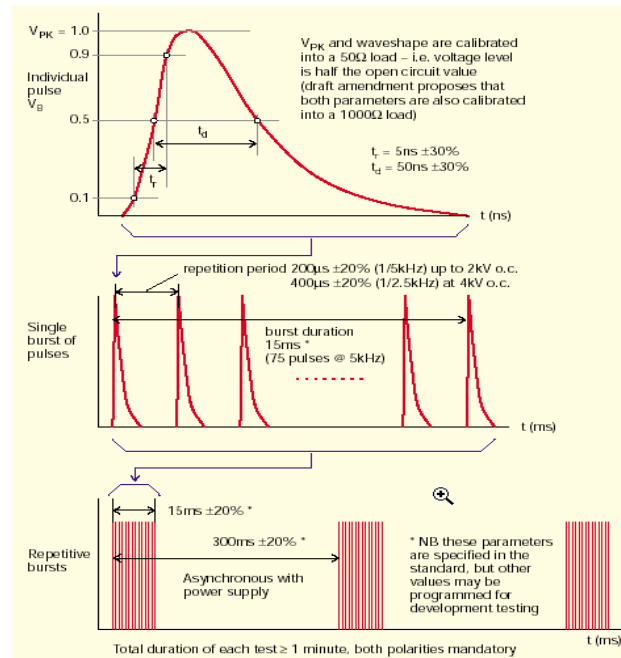


Figure 7.30: Burst test standard waveform.

7.5 Quenching effects

The tracker, ECAL and HCAL electronic systems are placed inside the superconducting solenoid¹, which forms a uniform magnetic field of 4 Tesla. This solenoid of 6 meters of diameter and 13 meters of length, has a nominal current of 19500 A and stores around 2.7 GJ of energy during normal operation. The inductance of the solenoid is 14.15 H

The charge and discharge of the magnet under normal conditions requires several hours and should not present any problem for the electronics devices. In two special cases the discharge of the magnet is performed in a relatively short period (10 minutes). These are the fast discharge and the quench discharge. The analysis of the effects induced in the CMS detector by these transients and the associated induced voltages by the magnet quenching are presented in this section.

A quench is known as the transition from the superconducting state to the normal conducting state of the conductor. If this phenomenon happens in the superconducting solenoid it is necessary to dissipate as fast as possible all the energy stored in the magnet to avoid the destruction of the superconducting cable. Figure 7.31 shows the discharging time of the magnet during a quench [25].

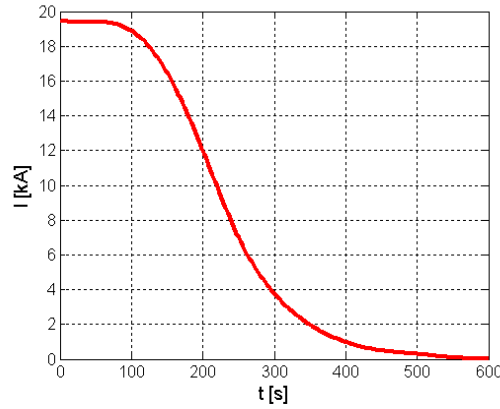


Figure 7.31: Solenoid current during an accidental quench.

To estimate the voltage induced in a certain region during a quench, the magnetic field value at an internal point of the solenoid, far away from the ends, induced by the solenoid current can be simplified as:

$$B(t) = \mu_o \cdot \frac{N \cdot i(t)}{Lg} \left[\frac{Wb}{m^2} \right] \quad (7.7)$$

where N is number of turns of the solenoid, Lg the length of the solenoid, the relative permeability of the media is 2 $\mu_r = 2$ and i(t) the current flowing through the solenoid. This field is calculated as:

$$B_{Th} = \mu_o \cdot \mu_r \cdot \frac{N \cdot i(t)}{Lg} \frac{Wb}{m^2} = 4 \cdot \pi \times 10^{-7} \cdot 2 \cdot \frac{2168}{12.5} \approx 4 Tesla \quad (7.8)$$

Assuming that in a specific area (S) perpendicular to the magnetic field the field is constant and the induced voltage is:

$$\Phi = \int B ds = B \cdot S \quad (7.9)$$

$$V = - \frac{d\Phi}{dt} = -S \cdot \frac{dB}{dt} \quad (7.10)$$

Combining both equations lead to voltage per unit area

$$\left| \frac{V}{S} \right| = K \cdot \mu_o \cdot \frac{N}{Lg} \cdot \frac{d}{dt} i(t) \quad (7.11)$$

Figure 7.32 shows the voltage induced per square meter in different areas of the detector (central part and at the end of the solenoid). The maximum voltage

induced corresponds to the central part of the detector which is the 4 tesla area and this value is around $43 \frac{mV}{m^2}$. For the end of the solenoid this value is around $21.5 \frac{mV}{m^2}$.

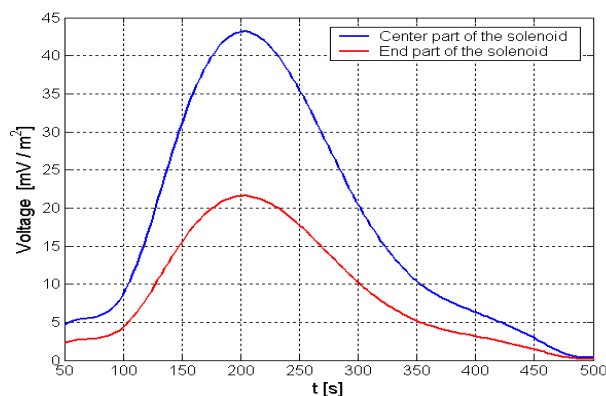


Figure 7.32: Voltage induced per squared meter in the internal and end part of the solenoid

These values are very low and may not cause any problem to the electronics circuits. However, the detector has several short-circuited structures, like pipes, copper or aluminum blocks, where part of the electronics are locally grounded (signal reference ground). Large currents may be induced in these blocks that may result in a damage of the electronics connected to these blocks.

7.6 Summary

Transients in power distribution lines can be generated by variations of the current consumption of the FEE due to load changes, random failures, turn On/Off of equipment, etc. They induce over-voltages and voltage dips in the LV-DC and the AC distribution system, which can affect the performance and the reliability of the FEE. The FEE immunity analysis to voltage dips, surge transients and fast transients has been analyzed in the present chapter to define the base line of a future EMC policy for the detector.

Voltage dip tests were conducted applying short interruptions and voltage variations to the HCAL-FEE and evaluating the degradation of the FEE performance and the loss of acquired data. These tests have shown that the FEE shows a gain loss of the amplifier when the perturbation is applied to the analogue power line, while when voltage dips are applied to the digital power line, the digital part of the FEE is very sensitive to these transients forcing to reset the system when the perturbation reaches the limit values.

The surge transient studies and tests have been focused on the characterization of the protection devices to be included in the FEE. The CMS detector can be divided in two areas; one corresponding to the AC power supply distribution system and the other corresponding to the DC power supply distribution system. The surge levels applied in these tests will be different for these two areas. The AC area may be classified as class 3 or 4 in EN 61000-4-5 and voltage levels defined by standards for the test signals are representative of perturbations in AC power distributions accomplishing the system integration in a safe way.

In the DC area the signal level to be applied during tests is not completely defined by standards but must be defined by each sub-system itself. Assuming the transients in the AC system are highly attenuated by the AC protection system and they do not propagate into the DC line, transients in the DC area are defined by the level of energy involved by the FEE and cable bundle granularity. Some preliminary studies have been conducted to quantify the energy level involved in these transients and to relate them to design considerations as granularity, type of protections, etc. Studies presented in this chapter concluded that good design considerations such as cables bundles grouped per power levels, small granularity, voltage regulators and current limiters, lead to easy and feasible solutions to protect the FEE against surge transients. Bad topologies may lead to difficult solutions to protect the system and can result in a potential problem during the normal operation of the detector. This research has shown that the best solution to protect the system is using the technique of protection per stages, which helps to deal with the limitations of real protection components. Each component of the protection stage attenuates partially the transient generated in the system. Transient voltage suppressors (TVS), capacitors and voltage regulators should be included in both the distribution system and the sensitive equipment connected to it. Proper coordination among these devices is necessary to divert the transient energy through the device with suitable rating. In addition when TVS are used, coordination with over-current protection should be evaluated. In low-voltage applications, the clearing time of fuses is affected by the connection of TVS at the distribution bus.

Fast transients studies are only presented but not studied in detail because this type of transients may occur in CMS in the AC distribution system and it is fully covered by the standard EN 61000-4-4.

It is not yet possible to fix the level and waveform for the detector as the final design of the power supply system is not defined. As a first approximation, the selected level and waveform may be based on the area where the equipment under test will be placed in CMS (AC area & DC area). In the DC area, the test level may be specified per sub-subsystem because the bundles of cables and protections are divided per sub-system. These levels will not be only based on the preliminary studies shown before. New simulations and test of the sub-detector electronics have

to be performed to get a statistical data about the type and the number of transients occurring in this kind of experiments.

7.7 References

- [1] IEEE-Std. 1100-1999, "*IEEE Recommended practice for powering and grounding electronic equipment*", Ed. 1999.
- [2] T. Gruz, "*Design Considerations for Powering 415-Hz Computer Systems*", IEEE Transactions on Industry Applications, Vol. 25, N-6, pp 1102-1109 November - December 1989.
- [3] Keith Armstrong, "*Design Techniques part 6 - ESD, Dips, Flicker, Dropouts electromechanical switching and factor correction*", EMC & Compliance Journal, <http://www.compliance-club.com/>.
- [4] Keith Armstrong, "*EMC Testing Part 3- Fast Transient Burst, Surge, Electrostatic Discharge*", EMC & Compliance Journal, <http://www.compliance-club.com/>.
- [5] International Standard-IEC-61000-4-11 "*Electromagnetic compatibility (EMC) - Testing and measurement techniques- Voltage dips, short interruptions and voltage variations immunity test*", Basic EMC publication (Ed. 1995).
- [6] C.R.Paul, "*Introduction to Electromagnetic Compatibility*", Wiley-Interscience, 1992, ISBN - 0 - 471-54927-4.
- [7] Tim Williams, "*EMC for product designers*", Paraninfo 1997 ISBN-0-12-55710-0
- [8] W. Rhoades, "*Congruence of low voltage power main transient designs*", Proc. National Symposium on Electromagnetic Compatibility, pp- 285 -293, May 1989
- [9] International Standard - IEC - 61000-4-5, "*Electromagnetic compatibility (EMC)- Testing and measurement techniques-surge immunity test*", Basic EMC publication (Ed. 2001)
- [10] R. D'Alessandro, G. Parrini, "*General guidelines for the tracker power supply system*", Private communication.
- [11] R. Hammarstrom, "*Mutual wire inductance in MSC prototype*", Private communication.
- [12] A. Ciccolella, F.G. Canavero, "*Stochastic prediction of wire coupling interference*", Proc. IEEE International Symposium on Electromagnetic Compatibility, pp-51 -56, August 1995.

- [13] G. T. Capraro, C. R. Paul, "*A probabilistic approach to wire coupling interference prediction*", Proc. 4th International Zurich Symposium on Electromagnetic Compatibility, Zurich, Switzerland, pp. 267-272, February 1981.
- [14] C. R. Paul, "*Sensitivity of crosstalk to variation in wire position in cable bundles*", Proc. 7th International Zurich Symposium on Electromagnetic Compatibility, Zurich, Switzerland, pp. 617-622, March 1987.
- [15] T. Robbins, "*Fuse model for over-current protection simulation of DC distribution systems*", Proc. International Telecommunications Energy Conference, INTELEC '93, Vol 2, pp 336-340, September 1993.
- [16] R. B. Standler, "*Transmission line models for coordination of surge-protective devices*", Proc. IEEE International Symposium on Electromagnetic Compatibility, Dallas, USA, pp 363-368, August 2003.
- [17] E.P. Dick R.W. Cheung, J.W. Porter, "*Generator models for over voltage simulations*", IEEE Transactions on Power Delivery, Vol 6, Issue 2, pp 728-735, April 1991.
- [18] R. Siegert, O. Mohammed, "*Evaluation of a hybrid surge testing generator configuration using computer based simulations*", Proc. IEEE Southeastcon '99, Lexington, USA, pp 193-196, 1999.
- [19] F.A. Fisher, F.D. Martzloff, "*Transient control level philosophy and implementation*", Proc. International Symposium on Electromagnetic Compatibility, Montreux, 1977.
- [20] R.B. Standler, "*Standard Waveforms for Surge Testing: Experimental Evaluation and Proposed New Criteria for Tolerances*", Proc. International Symposium on Electromagnetic Compatibility, Zurich, pp 115-124, March 1989
- [21] F.D. Martzloff, "*The development of a guide on surge voltages in low-voltage AC power circuits*", Application note 9769, Littlefuse Company.
- [22] ANSI/IEEE C62.41-1980, "*Guide on Surge Voltages in AC Power Circuits Rated up to 600V*", IEEE publication (Ed. 1980)
- [23] F. Martzloff, T.F. Leedy, "*Electrical fast-transient tests: applications and limitations*", IEEE Transactions on Industry Applications, Vol 26, Issue 1, pp 151-159, January February 1990.
- [24] International Standard - IEC - 61000-4-4, "*Electromagnetic compatibility (EMC) - Testing and measurement techniques-Electrical fast transient/burst immunity test*", Basic EMC publication (Ed. 1995).
- [25] B. Cure, "*CMS Coil Powering Circuit - Safety Issues*", Engineering design review EDR-MAG-02, slides, 29-30 March 2001.

Conclusions

The EMC study of a high-energy physics detector has been presented. This analysis is fundamental to ensure the integration and fully functionality of the electronic system of the detector. The main goal of this study has been to evaluate EMC problems at system level. The main topics analysed in this thesis have been:

- The grounding
- The conducted emissions and filtering of the PS
- The noise propagation effects on cables
- Immunity of the FEE
 - Immunity at design stage.
 - Immunity test of the FEE
- Transients on the PS distribution system

The main results and conclusions obtained from the analysis are detailed below:

1. EMC studies have started with the analysis of grounding and shielding issues that are the baseline for a good EMC policy. Based on electric safety, equipment protection and equipment performance, the main rules to be applied to the CMS detector have been determined.

2. Conducted emissions can affect the performance of the CMS detector. For that reason, it is necessary to conduct normalized tests (close to aerospace EMI rules and military standards) in order to measure the conductive emission level at the output and input of the power supplies. In some cases, EMI filters are needed to attenuate these emissions to acceptable levels.

- The filter selection is based on its insertion loss, which strongly depends on the external impedance connected to its terminals. Therefore, it becomes necessary to define adequate load and source impedances that allow selecting a robust filter to achieve the low emission levels imposed.
- Input filters interact adversely with DC-DC converters at low frequency, resulting in severe performance degradation or even instability. The instability limits the number of DC-DC converters to be connected to the same power distribution bus. This problem can be controlled defining the number of units connected to the same bus and the damping.

3. Long power cables installed in the detector produce undesirable effects on the noise propagation between the power supply (PS) units and the front-end electronics (FEE). These effects must be seriously considered as they strongly affect the performance of the CMS detector:

- For unbalanced loads, which are typical in high-energy physics, both CM and DM mode signals are amplified at the resonance frequencies of the cable. In particular, when a capacitor filter is included across the load terminals, the CM and DM currents flowing through the cable are amplified, but the DM and CM voltage across the load terminals are effectively attenuated. This input capacitor has the additional effect of decreasing the CM to DM and DM to CM conversion and reducing the amount of noise that can affect the performance of the FEE.
- FEE input filter with low impedance (capacitive input) amplifies CM currents from the power supplies, leading to severe radiation from the cable. To attenuate this effect, it is highly recommended to use shielded power cables. Moreover, this shield contributes to keep these noise currents away from the detector ground, reducing the interaction among sub-systems. The use of non-shielded cables can force to use power supplies with a very low conducted CM emission level to decrease the amount of noise radiated by the cables.
- For external shield currents, the factor that determines the amount of noise coupled to the central conductors is defined by the surface transfer impedance of shielded cable. The use of copper braid shields helps to decrease this coupling and therefore decreases the amount of noise affecting the performance of the FEE.

4. The susceptibility of the FEE is the most important part of the EMC studies. The susceptibility should be dealt at the design stage, where by means of simulations, it is possible to select the best FEE topology. As example, some studies have been carried out in the Forward HCAL-FEE, whose main conclusions are:

- The topology of the connection between the FEE and the detector presents several limitations to common mode rejection and radiated noise immunity if this one is implemented with separated coaxial cables. The rejection to spurious signals can be improved by selecting two coaxial cables with a single braided shield.
- The use of a ground resistor to isolate the HV to the input circuit of the FEE, improves the common mode rejection of the system proportionally to its magnitude, decreasing at high frequency. However, it has a negligible effect on the noise generated by external electromagnetic fields. This difference between both cases can be explained by the different nature of the circuits.

5. EMI tests are carried out to evaluate the susceptibility of the FEE. These tests allow taking the necessary corrective action in case of low noise immunity, as well as, determining the noise level required at the power supply outputs. Tests applied on a prototype of HCAL FEE have drawn the following main conclusions:

- The principal cause of the FEE performance degradation is the CM current. CM

currents are coupled into the sensitive path of the FEE by currents flowing through the shield, by the DM to CM conversion and by CM current generated by the power supplies. The DM currents contribute to the degradation of the FEE mainly through DM to CM conversion.

- In order to improve the immunity of the FEE to noise currents, there are several options such as: the selection of good grounding connections and the use of CM filters and shielded power cables.
- The immunity curves of the system can be used to define a new noise level required at the output of the power supply. For HCAL FEE this level results very different from the level defined by the European standards. The definition of a standardized noise level at the output of the power supplies without the knowledge of the immunity curves of the system can lead to problems. It is important the definition of this level for all the sub-systems of the detector. Later, based on this curves, it is possible to define the emission level for the power supplies or select the European, American or Military standards that fits better to the requirements of the detector. In any case, the standardized level should be extended above the 30MHz limit because the FEE is very sensitive in that frequency range.

6. For transient perturbations in the power distribution system, the CMS complex can be divided in two areas. The first one corresponds to the AC distribution (between the motor-generators and the counting room / the periphery of the detector) and the other the LV-DC distribution system (between the periphery of the detector and the FEE). Each of them is perturbed by transient voltages with different characteristics, making necessary to analyze this problem separately.

- The AC power supply distribution is well defined by the standards. According to these standards, all the equipment placed in the AC area can be classified as either class 3 or class 4 for surge transients and class 3 for burst. Tests and transient levels to be applied to measure the immunity to surges, bursts and voltage dips of the equipment are well established.
- Transients generated in the DC distribution system itself are the only one able to affect the FEE in the detector because the transients generated in the AC line are attenuated at the input of the DC system.
- The limits for the transients in the detector area depend on the front-end electronics immunity. From the measurements performed in a prototype of HCAL-FEE it is possible to define the baseline of future EMC policy of the detector.
 - Voltage dips tests applied to digital power cables showed that the digital part of the HCAL-FEE is very susceptible to these transients. Dips of a few volts (around 3 volts) and short duration (around 10ms) can produce a fail in the clock signal, being necessary to reset the whole system to recover. Voltage dips applied to the analogue line of the HCAL-FEE induced a temporary gain loss of the amplifier.
 - Surge tests have been focused on the characterization of the transient

protection devices included at the input of the HCAL-FEE and the effect of the applied signal in the FEE. These tests showed that the best solution to protect the FEE is using a protection system based on protection by stages. In this topology, each component of the protection chain attenuates partially the transient generated in the system. At HCAL we studied the combination of transient voltage suppressors, capacitors and voltage regulators to suppress the effect of the transient on the FEE bias voltage.

- Fast transients are not considered in detail as it is very unlikely to be present in this area of the CMS detector.

As a general statement, these studies conducted in the CMS detector show that the first step in the EMI control is the selection of good topologies for the three components of the system, the FEE, the PS and the cables. The former increases the immunity of the FEE, the second decreases the emission of the PS to acceptable levels and the third one is used to control the coupling paths. The selection of only one of these components as the only component oriented to cancel the EMI issues is a tremendous mistake. The system should be thought as an unique identity in which each component has a specific task, being the combination of all of them the final solution to ensure a good detector integration.

Thesis contribution and future work

This thesis has clearly fulfilled the proposed objectives:

- Description of the EMC environment of CMS and quantification of noise level and immunity of some sub-systems.
- Pre-definition of emission and immunity specifications for noise level.
- Definition of normalized tests for the equipment to comply with those levels.

The main contribution of this work has been the development of a methodology to face the EMC aspects of a HEP experiment following of a systematic approach. The thesis has created the baseline for the CMS EMC policy, which can be extended to other experiments. This is the first time this type of proposal is presented in a HEP environment.

The definition of the susceptibility to conducted noise and transients for the rest of the sub-systems will allow having all immunity levels of the detector. As a future work it is intended to implement this plan for the rest of the CMS sub-systems. This thesis opens several work lines that should be followed to define the future EMC policy in CMS. The EMC plan for CMS will have four basic steps that should be followed for all the sub-systems located in the AC and DC areas of the detector:

- Power supply/distribution block diagram
- Grounding Scheme
- Immunity tests
 - RF conducted noise (Common mode and Differential mode)
 - Harmonics Tests
- Emission tests
 - Immunity to radio frequency disturbances test.
 - Voltage dips, short interruptions and voltage variations immunity test.
 - Surge immunity test - Over-voltage
 - Burst immunity test

Basically this thesis presents a global analysis of EMC at macro-system level. A detailed analysis of every specific EMC issue like power supply emissions, filter design and cables effects is out of the scope of this work and constitutes by itself a subject of research. In this sense, this thesis opens several work-lines, which should

be followed in future studies if a general EMC policy wants to be addressed in the HEP community as it has been done in other communities such as aerospace, telecommunications and automobile. The main work-lines necessary are listed below, some of them constitute a subject to develop a new thesis.

- Data collection and characterization of immunity level of the FEE and the electronic equipment installed in HEP experiments.
- Characterization and parameterization (level, waveform, energy) of transient perturbations likely to be present in any experiment in HEP.
- Definitions of incompatibilities between the experiments and the accelerator.
- Study of EMI in the detector front-end electronics. EMI design oriented of the FEE.
- Noise and transient analysis in cable bundles.
- Development of protection devices for very low DC power voltage distribution in hostile areas, analysis of risk assessment.
- EMC impact in the upgrade of the detectors.

Conclusiones - Versión en castellano

En este trabajo se presenta el análisis de compatibilidad electromagnética en un detector de física de altas energías. Este estudio es fundamental para asegurar la integración y total funcionalidad de la electrónica del detector. La tarea principal de este estudio ha sido evaluar la problemática de EMC a nivel de sistema. Los temas principales analizados en la tesis han sido los siguientes:

- La puesta a tierra
- Emisiones conducidas y filtrado de las fuentes de alimentación
- Los efectos de la propagación de ruido en los cables
- Inmunidad del FEE
 - Inmunidad en la fase de diseño
 - Ensayos de inmunidad del FEE
- Transitorios en el sistema de potencia

Los principales resultados y conclusiones del análisis de estos temas se detallan a continuación:

1. Los estudios de EMC comenzaron con el análisis de la puesta a tierra y blindaje de los equipos del experimento. Estos factores determinan la base de una buena política de EMC. Una buena puesta a tierra y un blindaje óptimo se han de basar siempre en especificaciones de seguridad eléctrica, protección de los equipos y óptimo funcionamiento del sistema. En este primer análisis se detallan las principales características y recomendaciones válidas para el caso particular de CMS.

2. Las emisiones conducidas pueden afectar al buen funcionamiento del detector. Por esta razón, es necesario definir una serie de ensayos normalizados (similares a estándares aeroespaciales y militares) con el propósito de estimar el nivel de ruido exigido a la salida y a la entrada de las fuentes de alimentación. En algunos casos es fundamental el uso de un filtro de EMC con el fin de disminuir las emisiones a niveles aceptables para el detector.

- La selección de los filtros está basada en sus propiedades de funcionamiento y rendimiento, las cuales suelen venir definidas en función de sus pérdidas por inserción. Estas últimas dependen enormemente de las impedancias que aparecen en los terminales del filtro. Por lo tanto, es necesario definir las impedancias de carga y fuente adecuadas que permitan seleccionar el filtro más

adecuado a las necesidades o requerimientos del sistema, manteniendo suficiente margen de seguridad.

- Los filtros de entrada pueden interferir con los convertidores DC-DC en baja frecuencia. Como resultado de esta interacción se produce una brusca degradación del funcionamiento del sistema que puede dar lugar a inestabilidades. Este problema limita enormemente el número de unidades conectadas a una misma fuente primaria, que en el caso de CMS es un convertidor de alterna a continua. Este problema puede ser sencillamente controlado definiendo el número de unidades conectadas a la misma fuente primaria.

3. La propagación del ruido a través de los cables largos que unen las fuentes de alimentación y el FEE produce efectos no deseados que pueden degradar el correcto funcionamiento del detector. Por tanto, estos efectos deben ser tomados en consideración.

- Para el caso de cargas no equilibradas, muy típicas en física de altas energías, tanto las señales de modo común como las de modo diferencial se amplifican por efecto de las resonancias del cable. Concretamente, al colocar un condensador a la entrada del FEE, las corrientes de modo común y modo diferencial son amplificadas, mientras que, por contra, las tensiones generadas por estos modos en el terminal de entrada son atenuadas. Además, este condensador presenta un efecto adicional beneficioso, que consiste en la disminución de la conversión de modo común a modo diferencial, con lo que disminuye la cantidad de ruido que pudiera afectar al sistema.
- Sin embargo, el uso de este filtro capacitivo a la entrada del FEE puede conducir a una elevada radiación del cable, generada por el modo común inyectado en los cables por parte de las fuentes de alimentación. Con el fin de atenuar este efecto, se recomienda el uso de cables de potencia blindados. El blindaje de estos cables contribuye, por otra parte, a mantener la estructura de referencia del detector, así como otros sistemas, libres de estas corrientes de ruido. El uso de cables sin blindaje podría forzar el uso de fuentes de alimentación con niveles de ruido a la salida extremadamente pequeños, como única solución que mantenga bajo el efecto de radiación de los cables.
- Respecto a las corrientes externas del blindaje, el principal factor que determina la cantidad de ruido que se puede acoplar en los conductores centrales está definida por la impedancia superficial de transferencia del blindaje. El uso de blindaje del tipo entrelazado de cobre (copper braids) ayuda a disminuir la cantidad de ruido acoplado al sistema, mejorando el rendimiento de la electrónica.

4. La susceptibilidad del FEE constituye uno de los elementos más importantes en este estudio de EMC. La susceptibilidad debe ser analizada de antemano en la fase de diseño, donde mediante simulaciones, se puede seleccionar la mejor topología del FEE desde el punto de vista de EMC. Como aplicación de este tipo de estudios,

se ha realizado un análisis en fase de diseño del conjunto electrónica-detector del Forward Hadron Calorimeter, cuyas principales conclusiones son las siguientes:

- La topología usada en dicha conexión limita enormemente la capacidad del sistema para rechazar ruido de modo común y disminuye la inmunidad del conjunto al ruido radiado. El origen de esta problemática se encuentra en el uso de cables coaxiales separados, pudiendo solventarse en parte este problema usando un cable doble coaxial con un único blindaje de cobre común.
- El uso de una resistencia para aislar la componente de señal de la parte de alta tensión del detector mejora el rechazo del sistema al modo común proporcionalmente con el valor de esta resistencia, disminuyendo este efecto a alta frecuencia. Sin embargo, dicho efecto es despreciable en caso de que el ruido acoplado al sistema sea generado por campos externos. La diferencia entre ambos casos viene motivada por la diferente naturaleza de los circuitos implicados en ambos casos.

5. En una segunda fase del análisis de la susceptibilidad del FEE, se han realizado experimentos con el objetivo de definir la inmunidad del FEE al ruido conducido. Estos ensayos permiten evaluar la inmunidad de la topología aplicada en el FEE, tomar las medidas correctoras en el caso de presentar una baja inmunidad y determinar el nivel de ruido que será necesario especificar a la salida de las fuentes de alimentación. Una serie de ensayos de inmunidad que se realizaron en un prototipo del FEE han permitido obtener las siguientes conclusiones:

- Las corrientes de modo común son las principales responsables de la degradación del funcionamiento del FEE. Estas corrientes normalmente son generadas por corrientes de blindaje, por las fuentes de alimentación, así como por la conversión de modo diferencial a modo común.
- Existen diversas acciones que se pueden realizar con el fin de mejorar la inmunidad del FEE, como por ejemplo elegir muy buenas conexiones al plano de referencia, instalar filtros de modo común a la entrada de la electrónica y usar cables blindados de potencia.
- Las curvas de inmunidad del sistema se pueden usar para definir los nuevos niveles de emisión de ruido requeridos a la salida de las fuentes de alimentación. En el caso de HCAL-FEE estos niveles resultaron ser muy diferentes de los fijados por los estándares europeos. Esto lleva a concluir que la definición de un nivel de ruido basado en estándares sin el conocimiento de las características de inmunidad del FEE puede llevar a serios problemas. Sin embargo, si estos niveles de inmunidad son definidos, es posible que, basándose en ellos, se pueda elegir el estándar europeo, militar o espacial, que mejor se ajuste a las necesidades de nuestro sistema. En todo caso, el rango de frecuencias ha de ser extendido por encima de los 30 MHz, dado que el FEE es muy sensible en ese rango de frecuencias.

6. En el caso del análisis de transitorios, el sistema de distribución de CMS está dividido en dos partes principales. Una que corresponde al sistema de distribución

trifásica del detector (Generadores/Counting room - periferia del detector) y la otra que corresponde al sistema de distribución de corriente continua entre la periferia del detector y el FEE. Cada uno de ellos presenta transitorios de diferentes características, resultando necesario analizar el problema de los transitorios de forma separada.

- El sistema de distribución trifásica está perfectamente definido en los estándares. Los ensayos a aplicar para definir la inmunidad de los equipos contra sobre-tensiones, transitorios rápidos o caídas de tensión temporales están perfectamente definidos por los estándares. De acuerdo a estos estándares, todo equipo localizado en esta área se puede clasificar, tanto como clase 3 o clase 4, para el caso de transitorios lentos y como clase 3 para transitorios rápidos.
- Los transitorios generados en el sistema de distribución de continua son únicamente aquellos generados por el mismo sistema ya que los transitorios generados en el sistema de AC son atenuados a la entrada del sistema de continua.
- Los límites de los transitorios en el área del detector dependen únicamente de las características del sistema de distribución de esta área. Una serie de medidas y ensayos realizados en un prototipo del HCAL-FEE han permitido establecer una pautas que pueden ser usadas para fijar la base de la futura política de protección del detector contra los transitorios.
 - Ensayos de pérdida de tensión muestran que la parte digital del HCAL-FEE es la más sensible a este tipo de transitorios. Pérdidas de tensión de unos 3 voltios durante cortos periodos de tiempo, unos 10 ms, pueden producir fallos en la señal de sincronización que provoque un fallo general en todo el sistema, resultando necesario reinicializar el detector. En el caso de aplicar la pérdida de tensión a la línea analógica del HCAL-FEE tan sólo se produce una pérdida temporal de la ganancia del amplificador.
 - Con los ensayos y análisis de sobre tensión en esta área se ha tratado de caracterizar el sistema de protección necesario a la entrada del FEE. Los ensayos mostraron que el mejor sistema de protección es aquél basado en una protección por etapas. Cada componente de este sistema de protección atenúa parcialmente el transitorio generado en el sistema. El sub-sistema HCAL ha estudiado el uso de supresores de transitorios, condensadores y reguladores de tensión como cadena de protección del FEE contra los transitorios.
 - Los transitorios rápidos no son considerados en detalle al no estar tan claro su presencia en esta área del detector.

Como resumen general de la tesis hay que indicar, que estos estudios realizados para CMS muestran que la primera etapa en el control de perturbaciones electromagnéticas conducidas en el detector es una buena elección de las topologías de los tres principales componentes del sistema de distribución, FEE, fuentes y cables. La primera incrementa la inmunidad del detector, la segunda disminuye las

emisiones de las fuentes de alimentación a niveles aceptables y la tercera es usada para controlar los caminos de acoplamiento entre componentes. La selección de uno de estos componentes como único responsable de la cancelación de problemas de interferencias electromagnéticas es un enorme error. El sistema debe considerarse como una única identidad en la que cada componente tiene una tarea específica, siendo la combinación de todos ellos la solución final que asegura la correcta integración del detector.

Objetivos de la tesis & Futuros Trabajos -Versión en castellano

Esta tesis ha cumplido claramente los objetivos propuestos con el fin de abordar los problemas de interferencias electromagnéticas en el detector.

- Se ha descrito el ambiente electromagnético del detector
- Las especificaciones de emisiones e inmunidad al ruido en CMS han sido pre-definidas.
- Se han definido los ensayos normalizados que permitan integrar el detector de forma segura.

La principal contribución de esta tesis ha sido el desarrollo de una nueva metodología que permita hacer frente a cuestiones de EMC en experimentos de física de altas energías mediante un análisis sistemático de los fenómenos electromagnéticos dentro del detector. Esta tesis será tomada como base para desarrollar la futura normativa a seguir para integrar el detector de forma segura. Dicha metodología puede ser perfectamente aplicada a otros experimentos. Esta es la primera vez que este tipo de análisis y propuesta es presentado en física de altas energías.

La definición de la susceptibilidad al ruido conducido y a transitorios del resto de los subsistemas de CMS permitirán caracterizar el nivel de inmunidad del detector y finalmente establecer el nivel requerido por CMS. Como futuro trabajo se procederá a implementar un plan de EMC en el resto de subsistemas de CMS. El plan para CMS tendrá 4 etapas básicas, que deberán aplicarse a cada subsistema.

- Diagrama del sistema de distribución de potencia
- Esquema de la puesta a tierra de los equipos y electrónica.
- Ensayos de inmunidad
 - A ruido de radio frecuencia conducido
 - Ensayos de armónicos
- Ensayos de inmunidad
 - Inmunidad a ruido conducido de radio frecuencia
 - Inmunidad a pérdidas de tensión
 - Inmunidad a transitorios lentos

- Inmunidad a transitorios rápidos

Esta tesis ha intentado hacer frente a la problemática de EMC en física de altas energías, y más en concreto en el detector CMS. Básicamente presenta el problema del análisis global de EMC en el ámbito de macro sistema. Un análisis detallado de cada tema de EMC como emisiones de las fuentes de alimentación, diseño de filtros y efectos en los cables está fuera de los objetivos y el alcance de este estudio, constituyendo cada uno de ellos en sí mismo un tema de investigación. En este sentido, esta tesis abre diferentes líneas de trabajo que deben ser estudiadas en detalle si se quiere aplicar una normativa general para el mundo de física de altas energías, tal como han hecho otras comunidades, como la industria del automóvil, la industria aeroespacial, telecomunicaciones y en general toda familia de equipos electrónicos que se puedan encontrar en el mercado. Las principales líneas de trabajo necesarias para desarrollar los futuros estándares de EMC en física de altas energías se enumeran a continuación. Algunas de ellas pueden constituir en sí mismas un tema de tesis.

- Caracterización de la inmunidad de cualquier FEE y equipo electrónico instalado en un experimento de física de altas energías.
- Caracterización y parametrización de los tipos de transitorios (nivel, forma de onda, energía) que puedan presentarse en un detector de física de altas energías.
- Definición de incompatibilidades entre el acelerador y el detector.
- Estudios de EMC el FEE del detector. Diseño de FEE orientado a EMC.
- Análisis de ruido y transitorios en agrupaciones de cables.
- Desarrollo de sistemas de protección para distribuciones de potencia a muy baja tensión en ambientes hostiles. Análisis y evaluación de riesgos.
- Impacto de aspectos de EMC en la actualización del acelerador.

Appendix A - MTL

A.1 Internal impedances - Skin effect

The DC resistance of a conductor is computed by the typical equation.

$$R_{DC} = \frac{\rho \cdot l}{A} \quad (\text{A.1})$$

As the frequency increases, the current over the wire cross section tends to flow closer to the outer part of the conductor, producing an increase in the resistance of the conductor. This is known as the skin effect. For well developed skin effect the current can be considered to be uniform distributed over an annulus at the surface of the wire of depth, a skin depth δ .

$$\delta = \frac{1}{\sqrt{\pi \cdot f \cdot \mu_o \cdot \sigma}} \quad (\text{A.2})$$

On the other hand, the other component of conductor, which is affected by the skin effect, is the internal inductance. The internal inductance is the inductance arising due to the flux linkage inside the conductor for its own current. This values is quite small if it is compared with the self or mutual inductance of a conductor, and for the case of circular conductor is equal to $l_i = 50 \frac{nh}{m}$. In the case of internal inductance, the skin effect produces a decrease of the value of the internal inductance up to a certain frequency in which this value can be considered negligible.

The increase of the wire resistance and the diminution of the inductance for the HCAL and Tracker power are shown in figures 4.8,4.9,4.14 and 4.15.

To model this cable and include these effects in the frequency domain, the impedance of the conductor is divided in two parts; the internal and the external. The former corresponds to the values of the external inductance of the conductors (which are constant), and corresponds to the values of the conductor inductance at high frequency. The second to the values of the conductor resistance and internal inductance, which depends on the skin effect. This impedance can modeled in frequency domain as [1][2]:

$$Z = R_{DC} + R_{DC} \cdot \sqrt{\frac{f}{f_o}} \cdot (1 + j) \quad (\text{A.3})$$

The value of f_o corresponds to the frequency where $\delta = \frac{r}{2}$.

A.2 Characteristic impedance

The definition of the characteristic impedance of a multi-conductor transmission line involves the definition of a matrix. The concept is similar to the case of a single conductor line, but mathematically the calculation is more involved.

Based on equations 4.35 and 4.56, it may be obtained that:

$$\hat{V}(z) = (\hat{Y}^{-1} \cdot \hat{T} \cdot \hat{\gamma} \cdot \hat{T}^{-1}) \cdot \hat{T} \cdot (e^{-\hat{\gamma}z} \cdot \hat{I}_m^+ + e^{\hat{\gamma}z} \cdot \hat{I}_m^-) \quad (\text{A.4})$$

Under these considerations the characteristic impedance matrix is defined as:

$$\hat{Z}_o = \hat{Z} \cdot (\hat{T} \cdot \hat{\gamma}^{-1} \cdot \hat{T}^{-1}) \quad (\text{A.5})$$

For a single transmission line the parameters Z and $\hat{\gamma}$ are scalar and $\hat{T} = 1$. In this case, the definition of the characteristic impedance is.

$$\hat{Z}_o = \hat{Z} \cdot (\hat{\gamma}^{-1}) \quad (\text{A.6})$$

$$\hat{\gamma} = \sqrt{\hat{Z} \cdot \hat{Y}} = \sqrt{(r + j \cdot \omega \cdot L) \cdot (j \cdot \omega \cdot C)} = \alpha + j \cdot \beta \quad (\text{A.7})$$

where α is the attenuation constant and β is the phase constant per unit length. From equation A.6 and A.7, the final expression of the characteristic impedance for a single transmission line is obtained as:

$$Z_o = \sqrt{\frac{r + j \cdot \omega \cdot L}{j \cdot \omega \cdot C}} \quad (\text{A.8})$$

For the multi-conductor case, the characteristic impedance given by the expression A.5 is numerically evaluated. It corresponds to the HCAL power cable and the parameters are measured¹ at 1 MHz. The characteristic impedance matrix in Ω is:

$$\hat{Z}_o = \begin{bmatrix} 25.81 & 4.542 \\ 4.542 & 26.07 \end{bmatrix} \Omega \quad (\text{A.9})$$

¹ See chapter 4 - section 4.3

A.2. Characteristic impedance

A direct measurement of this characteristic impedance is possible similarly to the case of single conductors using a time domain reflectometer (TDR). Figure A.1 shows a TDR implemented in Pspice where a pulse generator of 1 A is applied between one line and the shield. The other side of cables is left floating as well as the other conductors. The voltage of the first incident wave is measured at the sending end for all conductors. This magnitude is coincident with the first row of the characteristic impedance matrix. Figure A.2 shows the results of simulation for HCAL power cable.

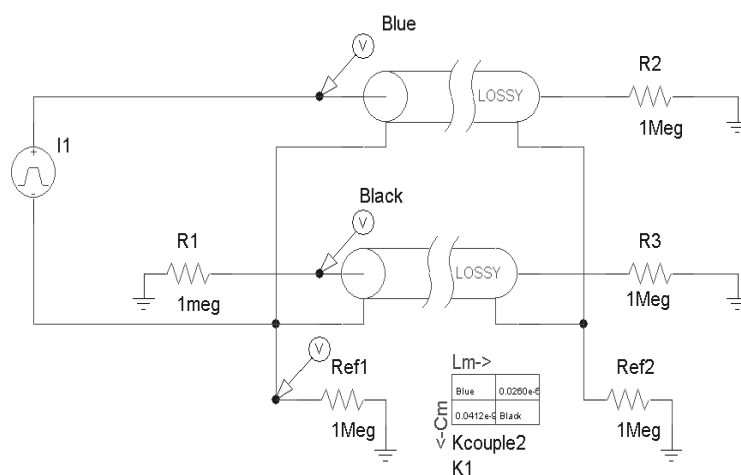


Figure A.1: TDR implemented in Pspice to measure the characteristic impedance matrix.

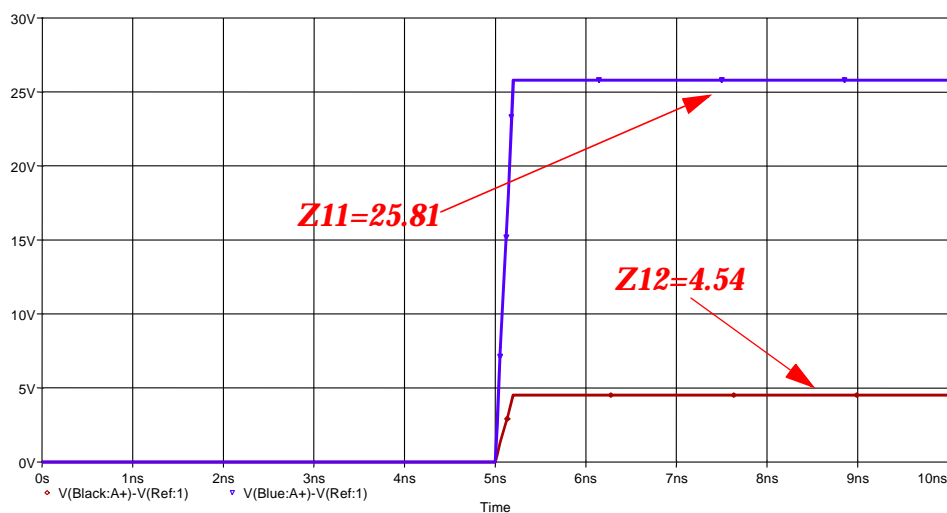


Figure A.2: Characteristic impedance matrix - First row.

A.2.1 CM and DM characteristic impedance matrix

For a pair of conductors, it is possible to decompose the currents in each wire I_1 and I_2 in a set of orthogonal current components. One of these components is called differential mode current and it is represented by two equal currents flowing through the cables in opposite direction. The other component is called common mode current and it is represented by identical currents and flowing in the same direction. This decomposition is shown in figure A.3 and defined by equations A.10 and A.11.

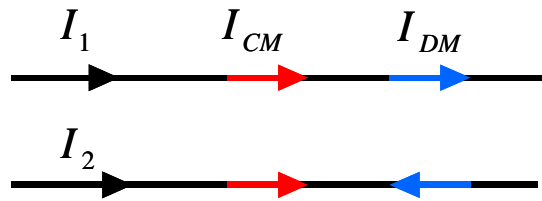


Figure A.3: CM and DM currents definition.

$$I_1 = I_{cm} + I_{dm} \quad (\text{A.10})$$

$$I_2 = I_{cm} - I_{dm} \quad (\text{A.11})$$

which can be expressed in matrix form as:

$$\begin{bmatrix} I_1 \\ I_2 \end{bmatrix} = W \cdot \begin{bmatrix} I_{cm} \\ I_{dm} \end{bmatrix} \quad (\text{A.12})$$

where W represent the transformation matrix from the normal mode of propagation to the CM and DM of propagation:

$$W = \begin{bmatrix} 1 & 1 \\ 1 & -1 \end{bmatrix} \quad (\text{A.13})$$

This equation is a nonsingular transformation between both modes of propagation. Therefore, the CM and DM currents can be calculated by:

$$\begin{bmatrix} I_{cm} \\ I_{dm} \end{bmatrix} = \frac{1}{2} \cdot \begin{bmatrix} 1 & 1 \\ 1 & -1 \end{bmatrix} \cdot \begin{bmatrix} I_1 \\ I_2 \end{bmatrix} \quad (\text{A.14})$$

A.2. Characteristic impedance

Based on the definition of both modes of propagation, it is possible to define a DM-CM characteristic impedance matrix applying a change of reference:

$$\hat{Z}_{(CM-DM)_o} = (W^{-1} \cdot \hat{Z}_o \cdot W) = \begin{bmatrix} 30.4 & -0.13 \\ -0.13 & 21.4 \end{bmatrix} \Omega \quad (\text{A.15})$$

As it has been developed before, a direct measurement of this characteristic impedance is possible similarly to the case of single conductors using a time domain reflectometer (TDR). Figure A.4, shows a TDR implemented in Pspice where two pulse generator of 1 A are connected between one line and the other in CM configuration.

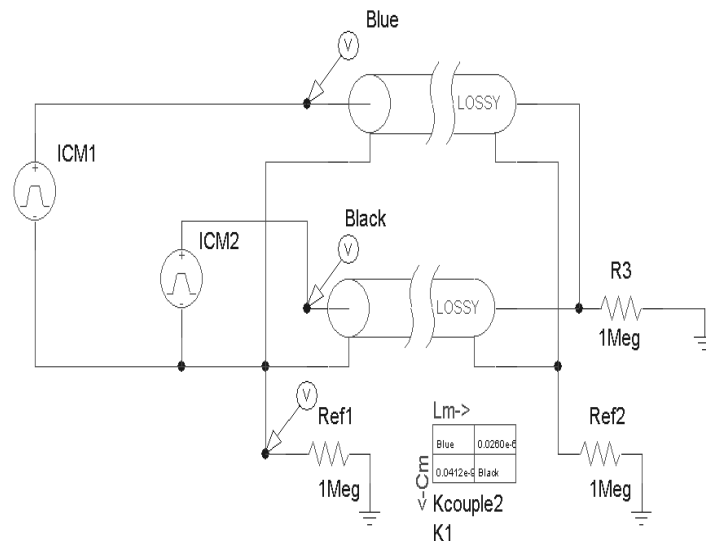


Figure A.4: TDR implemented in Pspice to measured the CM-DM characteristic impedance matrix - CM configuration.

The voltage of the first incident wave is measured at the sending end for all conductors and the transformation shown below is applied to calculate the CM and DM voltages:

$$V_{dm} = \frac{V_1 - V_2}{2} \quad (\text{A.16})$$

$$V_{cm} = \frac{V_1 + V_2}{2} \quad (\text{A.17})$$

These magnitudes are coincident with the first row of the CM-DM characteristic impedance matrix. Figure A.5 shows the results of simulation of HCAL power cable.

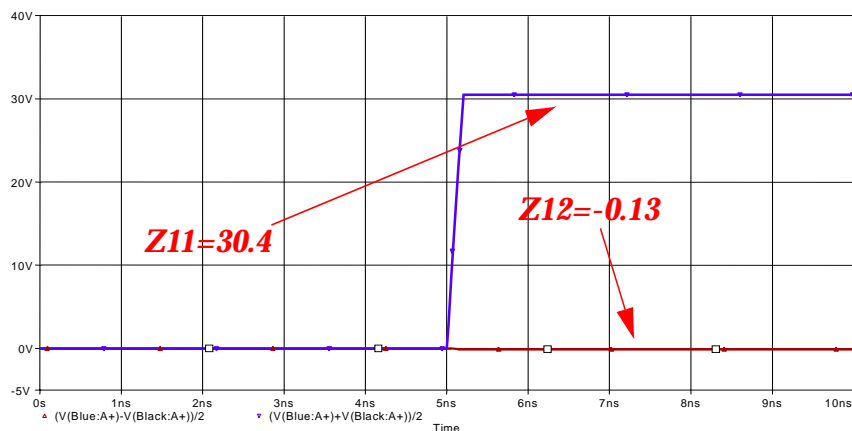


Figure A.5: CM-DM characteristic impedance matrix - First row.

Figure A.6a, shows a TDR implemented in Pspice in DM configuration. For this configuration a pulse generator of 1 A is connected between one line and the other. The voltage of the first incident wave is measured at the sending end for all conductors and the previous transformation is applied again. This magnitude is coincident with the second row of the characteristic impedance matrix. Figure A.6b shows the results of simulation of HCAL power cable.

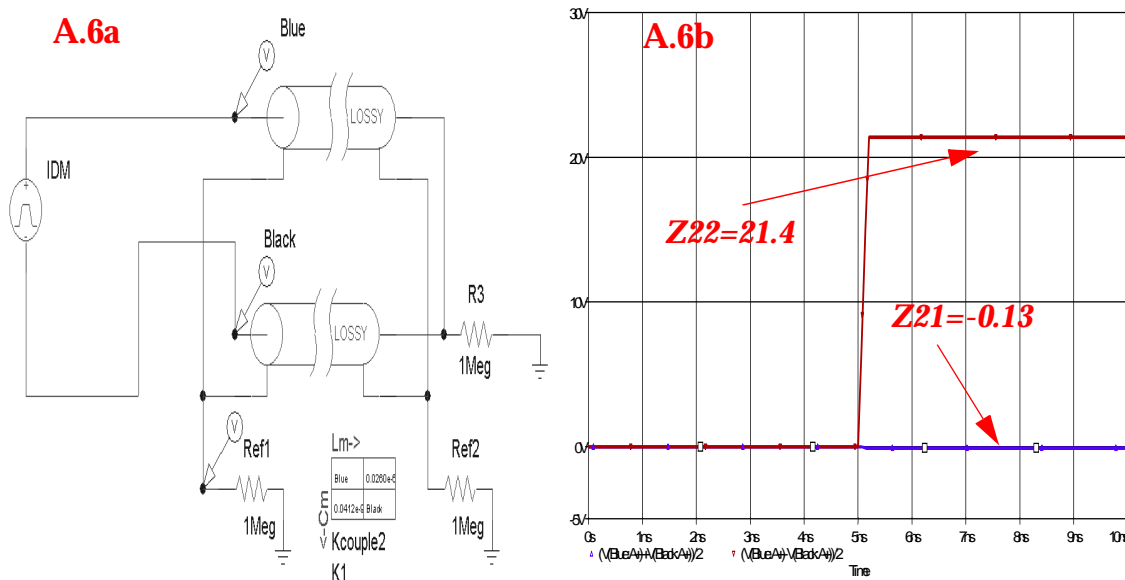


Figure A.6: TDR implemented in Pspice to measured the CM-DM characteristic impedance matrix - DM configuration - CM-DM characteristic impedance matrix - Second row.

A.3 MTL programs validation

As an example to validate the MATLAB program used in previous studies, two examples of multi-conductor system shown in [2] have been studied and the results of the MATLAB program are compared with the values measured and calculated.

A.3.1 Ribbon cable

This example consists on the study of the frequency domain solution of a three ribbon cables connected as it is shown in figure A.7.

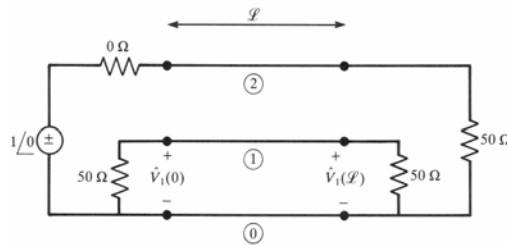


Figure A.7: Circuit under study.

The terminal configurations, characterized as a generalized Thevenin equivalent structures are:

$$\hat{V}_s = \begin{bmatrix} 0 \\ 1 \end{bmatrix} \quad (\text{A.18})$$

$$\hat{V}_L = \begin{bmatrix} 0 \\ 0 \end{bmatrix} \quad (\text{A.19})$$

$$\hat{Z}_L = \begin{bmatrix} 50 & 0 \\ 0 & 0 \end{bmatrix} \Omega \quad (\text{A.20})$$

$$\hat{Z}_S = \begin{bmatrix} 50 & 0 \\ 0 & 50 \end{bmatrix} \Omega \quad (\text{A.21})$$

The total length of the line is 2 meters and the per unit length parameters for this configuration are:

$$L = \begin{bmatrix} 0.7485 & 0.5077 \\ 0.5077 & 1.0154 \end{bmatrix} \frac{\mu H}{m} \quad (A.22)$$

$$C = \begin{bmatrix} 37.432 & -18.716 \\ -18.716 & 24.982 \end{bmatrix} \frac{pF}{m} \quad (A.23)$$

The resistance skin effect has been included by determining the frequency where the radius of one of the cables are equal to two skin depths, which according to the equation of A.2, where f_o is equal to 4.332 MHz.

$$R = \begin{bmatrix} 2 \cdot \left(0.19444 \cdot \left(1 + \sqrt{\frac{f}{(4.332 \times 10^6)}} \right) \right) & 0.19444 \cdot \left(1 + \sqrt{\frac{f}{(4.332 \times 10^6)}} \right) \\ 0.19444 \cdot \left(1 + \sqrt{\frac{f}{(4.332 \times 10^6)}} \right) & 2 \cdot \left(0.19444 \cdot \left(1 + \sqrt{\frac{f}{(4.332 \times 10^6)}} \right) \right) \end{bmatrix} \frac{\Omega}{m} \quad (A.24)$$

Figure A.8 shows the measured and MATLAB simulated values of the frequency response of the near-end crosstalk of the circuit presented. As it can be observed both results are very close.

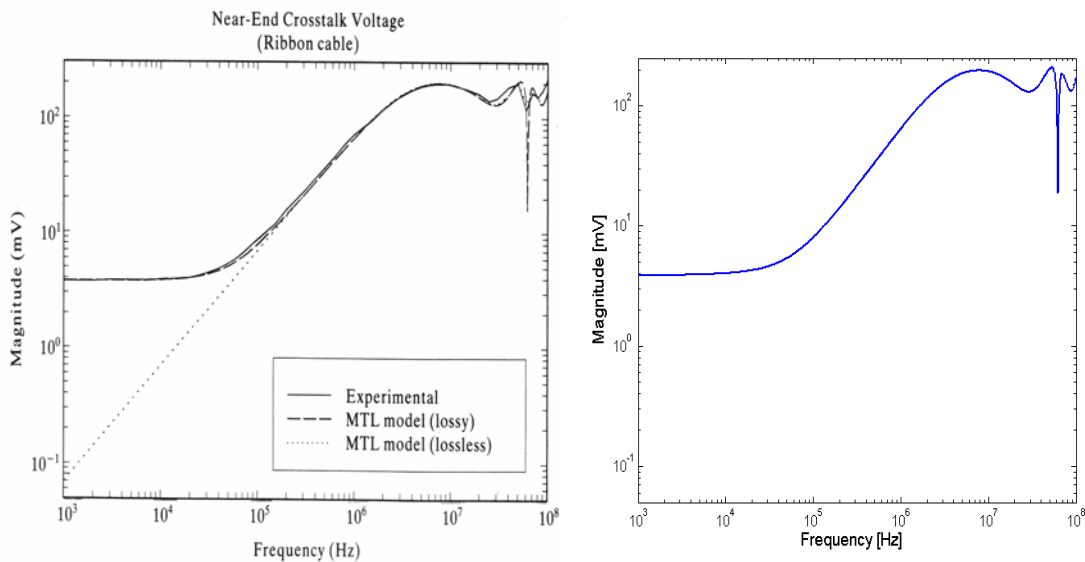


Figure A.8: Measured and MATLAB simulation values of the near-end crosstalk.

A.3.2 Field incident

For this sections the voltage induced on two conductors above an infinite ground plane (2 cm and 5 cm), when are illuminated by an uniform external plane wave of 1 V/m, traveling parallel to the ground plane is studied. This is shown in figure A.9.

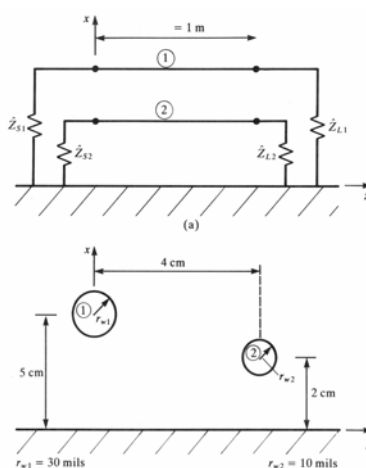


Figure A.9: Circuit under study.

The terminal configurations, characterized as a generalized Thevenin equivalent structures are:

$$\hat{V}_S = \begin{bmatrix} 0 \\ 1 \end{bmatrix} \quad (\text{A.25})$$

$$\hat{V}_L = \begin{bmatrix} 0 \\ 0 \end{bmatrix} \quad (\text{A.26})$$

$$\hat{Z}_L = \begin{bmatrix} 500 & 0 \\ 0 & 1000 \end{bmatrix} \Omega \quad (\text{A.27})$$

$$\hat{Z}_S = \begin{bmatrix} 100 & 0 \\ 0 & 500 \end{bmatrix} \Omega \quad (\text{A.28})$$

For the presented example, it has been considered a lossless line of 1 meter and the per unit length parameters for this configuration are:

$$L = \begin{bmatrix} 0.97538 & 0.0955 \\ 0.09555 & 1.0119 \end{bmatrix} \frac{\mu H}{m} \quad (\text{A.29})$$

$$C = \begin{bmatrix} 11.507 & -1.09 \\ -1.09 & 11.08 \end{bmatrix} \frac{pF}{m} \quad (\text{A.30})$$

Figure A.10 shows the measured and MATLAB simulated values of the frequency response of the near-end crosstalk of the circuit presented. As it can be observed both results are very close.

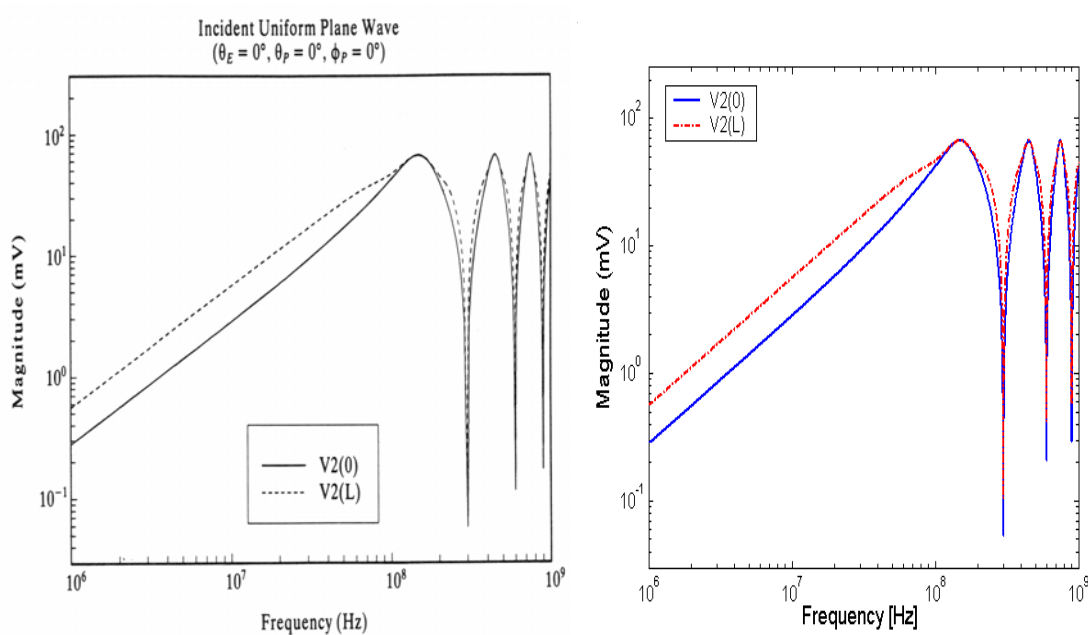


Figure A.10: Measured and MATLAB simulation values of the near-end crosstalk.

A.4 References

- [1] C.R. Paul, "Analysis of multi-conductor transmission lines", 1992, ISBN-0-471-02080 - X.
- [2] C.R. Paul, "Introduction to Electromagnetic Compatibility", NY: Wiley-Interscience, 1992, ISBN-0-471-54927-4.

Appendix B - Transients

B.1 Dynamic load impedances of Tracker FEE

The dynamic impedance of the APV25 during the transient analysis is calculated based on some measurements performed in Aachen by Waclaw Karpinski. These measured values are shown in figure B.1 and figure B.2. These plots show the U-I curves of a group of 4 APV25 -TOB hybrid.

The first plot shows the FE-hybrid dynamic impedance on the V250-line varies from about 3 to 7 ohms.

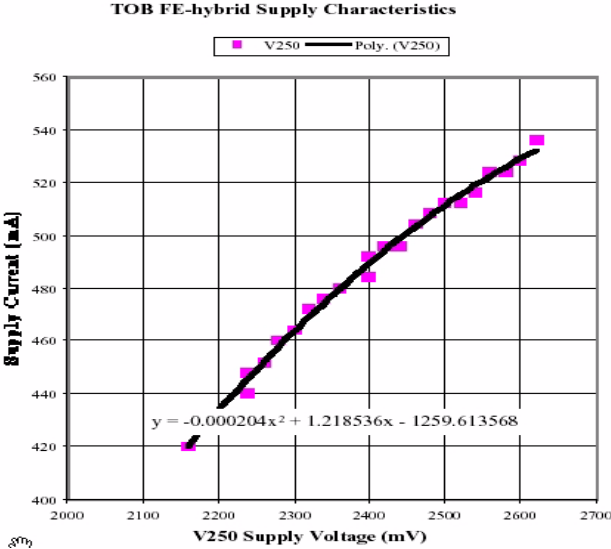


Figure B.1: TOB FE-Hybrid impedance - 2.5V line

Figure B.2 shows the FE-hybrid dynamic impedance on the V125-line. It varies from about 2.5 ohms to 8 ohms below 1.15 V. However, it behaves like a current source above 1.18 V and has an infinite impedance value.

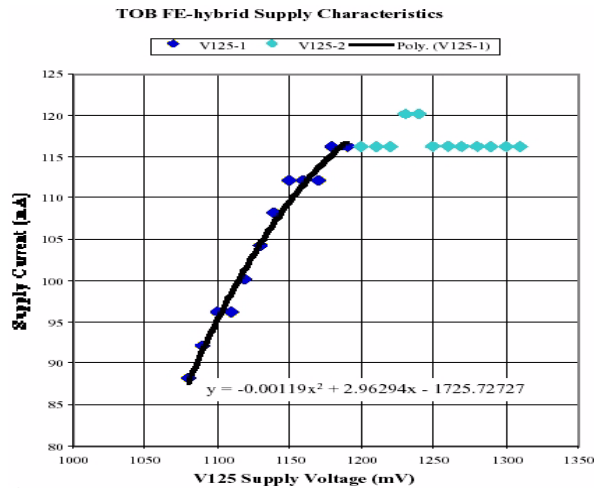


Figure B.2: TOB FE-Hybrid impedance - 1.25V line

B.2 Transient lumped model validation

To validate the lumped model of the cable used in the transients simulations analysis, Pspice simulations using 50 meters of the tracker power cable (MSC) have been performed using the transient lumped model. These results have been compared with real measurement performed by Robert Hammarstrom.

The configuration of the test is shown in figure B.3. The HV and sensor wires are left open during the test. The 2.5V line is loaded with a dynamic load which is set to 10 A at 2.5 V, with a damping resistance of 2.5 ohms and a capacitor of 125 μ f. This damping impedance is calculated based on the dynamic impedance of Hybrid-4APV25 shown in figure B.1. At load level, a dynamic current step is injected into the V2.5V line, which generates a step of 1 A in this line. The load power is supplied by a voltage source at 5 V.

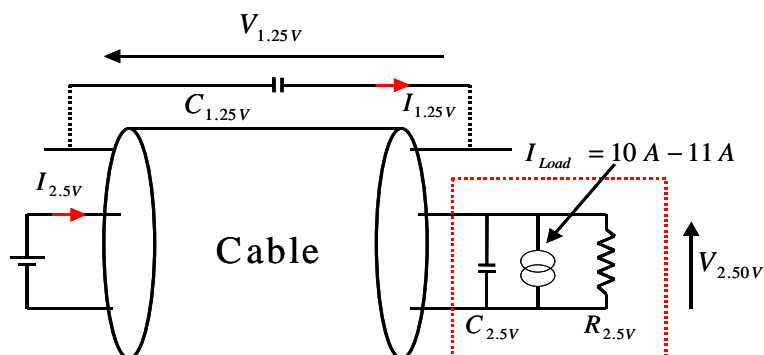


Figure B.3: Circuit used in these test.

B.2. Transient lumped model validation

For the test, the V1.25 line is left open in both sides of the cable and two steps of 1 A are applied to the line, one positive and the other negative. The voltage and the current on the V2.5 line are measured and compared with the Pspice simulation based on lumped transient model¹.

Figure B.4 and B.5 shows the simulated and measured values for the test. The voltage at load level is measured with channel 2 (V_1 -200 mV/div), the current in the V2.5 is measured with channel 4 ($I_{2.5V}$ -0.5 A/div) and the current step is measured with channel 1 (1 A/div). The time scale is $200 \frac{\mu s}{div}$.

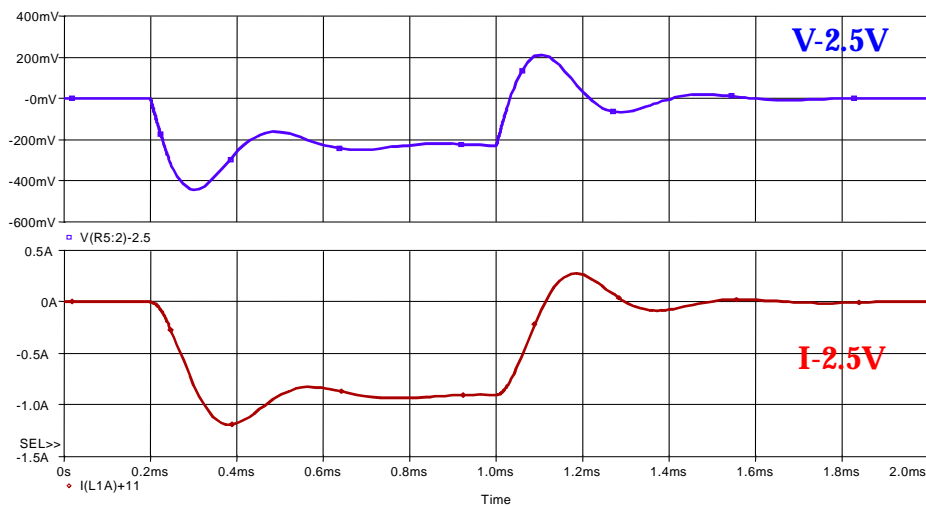


Figure B.4: Simulated voltage and current in the 2.5V line

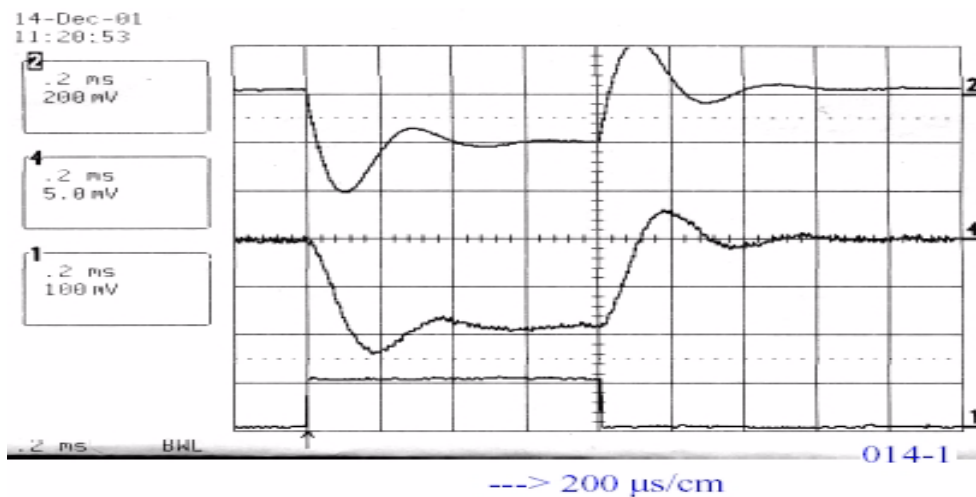


Figure B.5: Measured voltage and current in the 2.5V line

¹ See section 7.3.2

For the second test both sides of the 1.25V line are connected through a capacitor of $C_{1.25V} = 66\mu f$. Again, the V2.5V line is loaded with a dynamic load which is set to 10 A at 2.5V with a damping resistance of 2.5 ohms and a capacitor of $60\mu f$. The voltage and the current in the 1.25V line as well as the voltage on the 2.5V line have been measured.

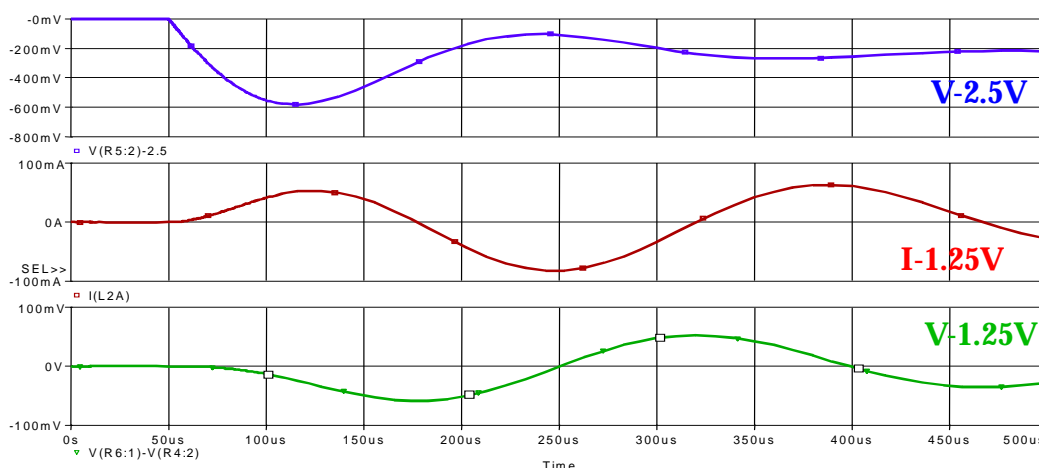


Figure B.6: Voltage and current at the 2.5V & 1.25V lines - Simulated values

Figure B.7 shows the measured values of the test. The voltage at load level is measured with channel 2 ($V_{2.5V}$ - 200 mV/div), the current $I_{1.25V}$ is measured with channel 4 ($I_{1.25V}$ - 0.1 A/div), the voltage at $V_{1.25V}$ line is measured with channel 3 ($V_{1.25V}$ - 100 mV/div) the current step is measured with channel 1 (1 A/div). The time scale is $50 \frac{\mu s}{div}$.

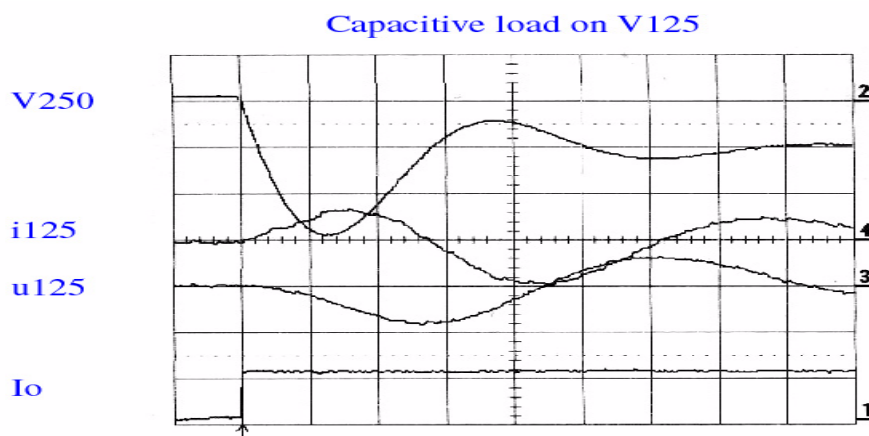


Figure B.7: Voltage and current at the 2.5V & 1.25V lines - Measured values

B.3 ATO fuse data sheet



ATO® Fuse Fast-Acting Type



Designed and originated by Littelfuse for the automotive industry, the ATO fuse has become the original equipment circuit protection standard for foreign and domestic automobiles and trucks. Readily identifiable and easily replaced, this fuse can be specified for a variety of low voltage electronic applications.

ELECTRICAL CHARACTERISTICS:

% of Ampere Rating	Ampere Rating	Opening Time
110%	1–40 Amp	100 Hours Minimum
135%	1–2 Amp	.50 sec., Min. ; 600 sec., Max.
	3–40 Amp	.75 sec., Min. ; 600 sec., Max.
200%	1–2 Amp	.10 sec., Min. ; 5 sec., Max.
	3–40 Amp	.15 sec., Min. ; 5 sec., Max.
350%	1–2 Amp	.020 sec., Min. ; 0.5 sec., Max.
	3–40 Amp	.080 sec., Min. ; 0.5 sec., Max.

AGENCY APPROVALS: Listed by Underwriters Laboratories (1–40 amperes). Certified by CSA (3–30 amperes).

DESIGN STANDARDS: U.L. Standard for Automotive Blade Type Fuses. SAE (Society of Automotive Engineers) J1284.

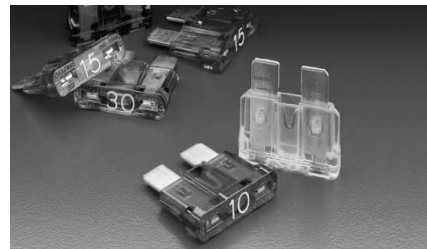
PATENTED

COLOR-CODING: Autofuse® fuses are color-coded for easy amperage identification.

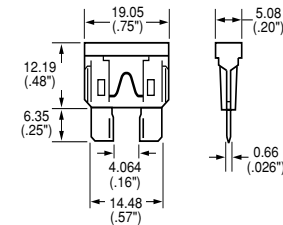
INTERRUPTING RATING:
1000A @ 32VDC

ORDERING INFORMATION:

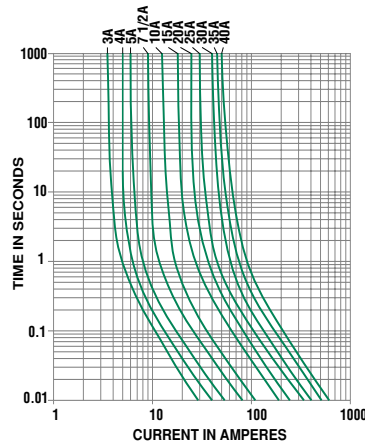
Catalog Number	Ampere Rating (A)	Voltage Rating (VDC)	Body Color Code	Nominal Cold Resistance Ohms	Minimum Melting I ² t (A ² Sec.)
257 001	1	32	Black	0.123	.4
257 002	2	32	Grey	0.050	1.4
257 003	3	32	Violet	0.031	7.4
257 004	4	32	Pink	0.023	14
257 005	5	32	Tan	0.018	26
257 07.5	7½	32	Brown	0.011	60
257 010	10	32	Red	0.0077	115
257 015	15	32	Blue	0.0048	340
257 020	20	32	Yellow	0.0033	520
257 025	25	32	Natural	0.0025	1080
257 030	30	32	Green	0.0019	1510
257 035	35	32	Blue Green	0.0016	2280
257 040	40	32	Orange	0.0014	3310



Reference Dimensions



Average Time Current Curves



Reference pg. 344, ATO® Fuse Clip for P.C. Board mounting.

Figure B.8: ATO fuse data sheet

B.4 TVS validation

A normalized pulse¹ of 340 V has been applied with a surge generator (UCS-500) on the input filter² of the real HCAL FEE to verify the validity of the parameters shown in the model. Figure B.9 shows the measurement voltage on the filter and figure B.10 shows the simulated voltage on the filter.

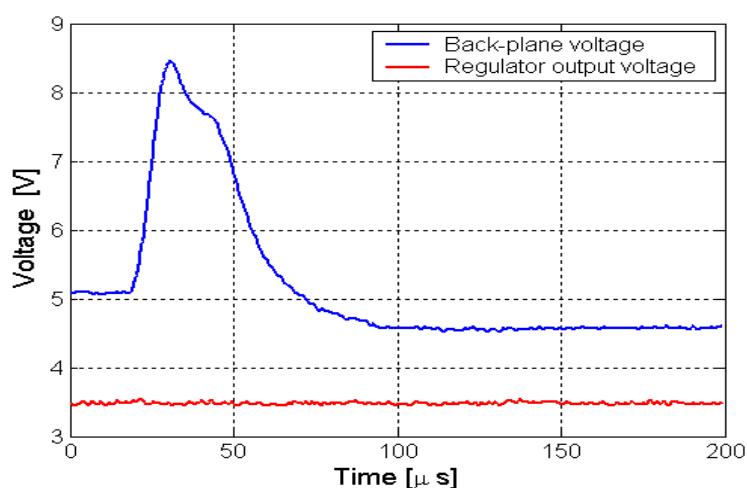


Figure B.9: Voltage at the input FEE filter - Measured values

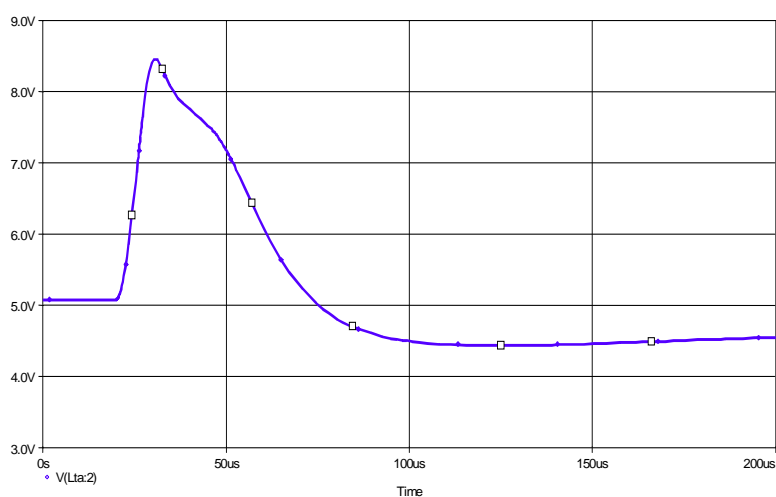


Figure B.10: Voltage at the input FEE filter - Simulated values

¹ See figure 7.18 and section 7.3.3.1

² See figure 7.20, section 7.3.2.2.1 and 7.3.3.2 for TVS and filter details

Appendix C - Current probes

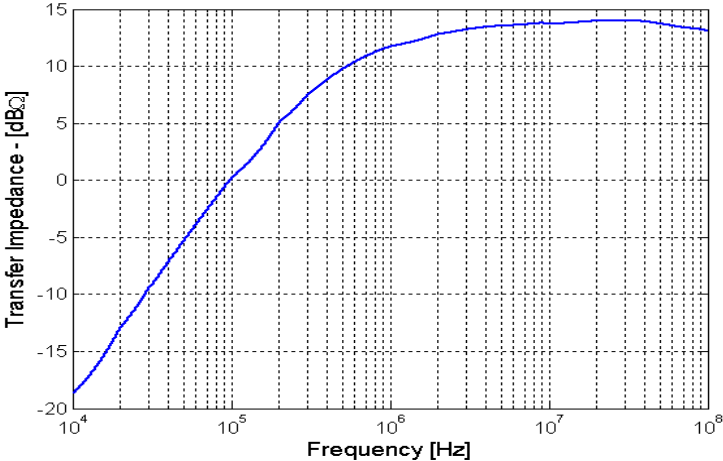


Figure C.1: Transfer impedance of current probe - EMCO-91550-1.

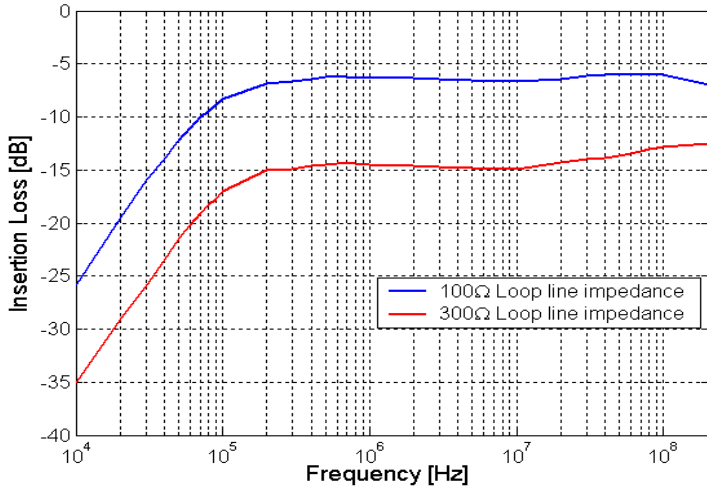


Figure C.2: IL of bulk injection current probe - Fischer F-120-9A.

Glossary

- **AC** - Alternative Current
- **ADC** - Analogue Digital Converter
- **ALICE** - A Large Ion Collider Experiment
- **ATLAS** - A Toroidal LHC Apparatus
- **CCU** - Communication and Control Unit
- **CERN** - European Center for Nuclear Research
- **CI** - Common Impedance
- **CM** - Common Mode
- **CMS** - Compact Muon Solenoid
- **CSC** - Cathode Strip Chambers
- **DC** - Direct Current
- **DM** - Differential Mode
- **DT** - Drift Tubes
- **ECAL** - Electromagnetic Calorimeter
- **EMI** - ElectroMagnetic Interference
- **EMC** - ElectroMagnetic Compatibility
- **ENC** - Equivalent Noise Charge
- **fC** - Femto-coulomb
- **FE** - Front End
- **FEE** - Front End Electronics
- **Gnd** - Ground
- **HCAL** - Hadron Calorimeter
- **HEP** - High Energy Physics
- **HF** - High Frequency
- **HPD** - Hybrid Photodiodes
- **HV** - High Voltage
- **IL** - Insertion Loss
- **LF** - Low Frequency
- **LHC** - Large Hadron Collider

- **LHCb** - Large Hadron Collider beauty
- **LIC**- Low Impedance Cable
- **LSB**-Less Significant Bit
- **LISN** - Line Impedance Stabilization Network
- **LV** - Low Voltage
- **MSC** - Multi-Service Cable
- **MTL** - Multi-conductor Transmission Line
- **RPC** - Resistive Paralell Chambers
- **PACE** - Pre-shower Analog Cms Electronics
- **PE** - Protective Earth cable
- **PLL** - Phase Lock Loop
- **PMT** - Photo-Multipliers
- **PS** - Power Supply
- **QIE** - Charge Integrator and Encoding chip
- **RBX** - Read Out Box
- **RF** - Radio Frequency
- **RMS** - Root Mean Square
- **SMPS** - Switch Mode Power Supply
- **STP** - Shieled Twisted Pair
- **TeV** - Teraelectron volt (energy)
- **TF** - Transfer Function
- **THD** - Total Harmonic Distorsion
- **TOB** - Tracker Outer Barrel
- **TVS** - Transient Voltage Suppresor
- **VME** - Versa Module Europe.
- **ZCS** - Zero Current Switch
- **ZVS** - Zero Voltage Switch